NASA/TM–2000–104606, Vol. 17

4X7 109

Technical Report Series on Global Modeling and Data Assimilation

Max J. Suarez, Editor

Volume 17

Atlas of Seasonal Means Simulated by the NSIPP 1 Atmospheric GCM

Julio Bacmeister, Philip J. Pegion, Siegfried D. Schubert, and Max J. Suarez

July 2000

The NASA STI Program Office ... in Profile

Since its founding, NASA has been dedicated to the advancement of aeronautics and space science. The NASA Scientific and Technical Information (STI) Program Office plays a key part in helping NASA maintain this important role.

The NASA STI Program Office is operated by Langley Research Center, the lead center for NASA's scientific and technical information. The NASA STI Program Office provides access to the NASA STI Database, the largest collection of aeronautical and space science STI in the world. The Program Office is also NASA's institutional mechanism for disseminating the results of its research and development activities. These results are published by NASA in the NASA STI Report Series, which includes the following report types:

- TECHNICAL PUBLICATION. Reports of completed research or a major significant phase of research that present the results of NASA programs and include extensive data or theoretical analysis. Includes compilations of significant scientific and technical data and information deemed to be of continuing reference value. NASA's counterpart of peer-reviewed formal professional papers but has less stringent limitations on manuscript length and extent of graphic presentations.
- TECHNICAL MEMORANDUM. Scientific and technical findings that are preliminary or of specialized interest, e.g., quick release reports, working papers, and bibliographies that contain minimal annotation. Does not contain extensive analysis.
- CONTRACTOR REPORT. Scientific and technical findings by NASA-sponsored contractors and grantees.
- CONFERENCE PUBLICATION. Collected papers from scientific and technical conferences, symposia, seminars, or other meetings sponsored or cosponsored by NASA.
- SPECIAL PUBLICATION. Scientific, technical, or historical information from NASA programs, projects, and mission, often concerned with subjects having substantial public interest.
- TECHNICAL TRANSLATION. English-language translations of foreign scientific and technical material pertinent to NASA's mission.

Specialized services that complement the STI Program Office's diverse offerings include creating custom thesauri, building customized databases, organizing and publishing research results . . . even providing videos.

For more information about the NASA STI Program Office, see the following:

- Access the NASA STI Program Home Page at http://www.sti.nasa.gov/STI-homepage.html
- E-mail your question via the Internet to help@sti.nasa.gov
- Fax your question to the NASA Access Help Desk at (301) 621-0134
- Telephone the NASA Access Help Desk at (301) 621-0390
- Write to:
  NASA Access Help Desk
  NASA Center for AeroSpace Information
  7121 Standard Drive
  Hanover, MD 21076–1320

NASA/TM–2000–104606, Vol. 17

Technical Report Series on Global Modeling and Data Assimilation

Max J. Suarez, Editor
Goddard Space Flight Center, Greenbelt, Maryland

Volume 17

Atlas of Seasonal Means Simulated by the NSIPP 1 Atmospheric GCM

Julio Bacmeister
Universities Space Research Associates

Philip J. Pegion
General Sciences Corporation, Laurel, Maryland

Siegfried D. Schubert
Data Assimilation Office, Goddard Space Flight Center, Greenbelt, Maryland

Max J. Suarez
Climate and Radiation Branch
NASA Seasonal to Interannual Predication Project
Goddard Space Flight Center, Greenbelt, Maryland

National Aeronautics and
Space Administration

Goddard Space Flight Center
Greenbelt, Maryland 20771

July 2000

Available from:

NASA Center for AeroSpace Information
7121 Standard Drive
Hanover, MD 21076–1320
Price Code: A17

National Technical Information Service
5285 Port Royal Road
Springfield, VA 22161
Price Code: A10

Abstract

This atlas documents the climate characteristics of version 1 of the NASA Seasonal-to-Interannual Prediction Project (NSIPP) Atmospheric General Circulation Model (AGCM). The AGCM includes an interactive land model (the Mosaic scheme), and is part of the NSIPP coupled atmosphere-land-ocean model. The results presented here are based on a 20-year (December 1979-November 1999) "AMIP-style" integration of the AGCM in which the monthly-mean sea-surface temperature and sea ice are specified from observations.

The climate characteristics of the AGCM are compared with the National Centers for Environmental Prediction (NCEP) and the European Center for Medium-Range Weather Foreacsting (ECMWF) reanalyses. Other verification data include Special Sensor Microwave/Imager (SSM/I) total precipitable water, the Xie-Arkin estimates of precipitation, and Earth Radiation Budget Experiment (ERBE) measurements of short and long wave radiation.

The atlas is organized by season. The basic quantities include seasonal mean global maps and zonal and vertical averages of circulation, variance/covariance statistics, and selected physics quantities.

Contents

List of Figures

GLOBAL MAPS 33

1 Introduction

The mission of the NASA Seasonal-to-Interannual Prediction Project (NSIPP) is to use remotely-sensed observations to enhance the predictability of El Nino/Southern Oscillation (ENSO) and other major seasonal-to-interannual signals and their global teleconnections. Fullfilling this mission requires state-of-the-art general circulation models of the coupled ocean-atmosphere-land system that can be used to assimilate observations and to demonstrate the utility of those observations through experimental prediction.

This report presents the climate characteristics of version 1 of the NSIPP Atmospheric General Circulation Model (the NSIPP 1 AGCM). This model, which is the atmosphere/land component of the full coupled atmosphere-land-ocean model, is currently being used in a wide range of atmospheric, coupled ocean/atmosphere and land/atmosphere simulation and predictability studies. Subsequent reports will summarize the predictability characteristics and interannual variability of this version of the AGCM.

The NSIPP AGCM was developed at Goddard. NSIPP 1 is a production version of the development cycle Aries 1_1/Patch 4. We note that the Goddard Earth Observing System (GEOS) model currently being used by the Data Assimilation Office (DAO) stems from the same development path. The GEOS model was, however, tailored for atmospheric data assimilation, while the NSIPP model was developed for climate simulation and prediction. This difference in application manifests itself largely in the tailoring and tuning of the physical parameterizations to ensure that certain key aspects of the atmosphere/land system are faithfully reproduced by the model. For example, in the development of the NSIPP AGCM, much attention has been devoted to the simulation of wind stresses over the tropical Pacific Ocean in order to obtain the proper atmosphere-ocean coupling when run in a coupled mode. Also, the middle latitude atmospheric stationary waves must be sufficiently unbiased in order to obtain the proper extratropical ENSO response and its variability (e.g., Schubert et al. 2000). In fact, it is these two aspects of the model climatology that motivated the recent model development, leading to Patch 4.

Although one may regard most changes in Patch 4 as fairly minor, they led to a much improved simulation over earlier versions. These changes include an increase in vertical resolution from 22 to 34 levels, with all new levels added near the surface; a modified version of the convection parameterization, with a more complete liquid water budget in updrafts; a modified version of the turbulence scheme, together with the elimination of dry convective adjustment; the use of filtered topography; and some minor modifications to the cloud disgnostic scheme. More details are presented in the next section.

The results presented are from a 20-year (December 1979-November 1999) "AMIP-style" integration of the NSIPP 1 AGCM. Here AMIP indicates that the model was run with monthly mean sea surface temperature and sea ice specified from observations following the experimental design of the Atmospheric Model Intercomparison Project (Gates 1992). The results are compared with the reanalysis performed by the National Centers for Environmental Prediction and the National Center for Atmospheric Research (the NCEP/NCAR Reanalysis, Kalnay et al., 1995) for the same time period. Other verification data include the European Center for Medium-Range Weather Foreacsting (ECMWF) reanalysis (Gibson et al., 1996), Special Sensor Microwave/Imager (SSM/I) total precipitable water, Xie ans

Arkin (1997) estimates of precipitation, and Earth Radiation Budget Experiment (ERBE) measurements of shortwave and longwave radiation.

The atlas is organized by season. The basic quantities include seasonal mean global maps and zonal and vertical averages of circulation, variance/covariance statistics, and selected physics quantities.

Section 2 describes the NSIPP 1 AGCM. Sections 3 and 4 describe the model integration and validation data, respectively. Section 5 gives an overview of the organization of the atlas. The results are discussed in Sections 6–8.

2 Description of the model

The AGCM is the atmospheric component of the NSIPP coupled prediction system. It uses a finite-difference dynamical core based on a C-grid in the horizontal and a standard sigma coordinate in the vertical. A detailed description of this core is given in Suarez and Takacs (1995).

Finite differences are second-order accurate, except for advection by the rotational part of the flow, which is done at fourth order. The momentum equations use a fourth-order version of the enstrophy conserving scheme of Sadourney (1975). The horizontal advection schemes for potential temperature and moisture are also fourth-order and conserve the quantity and its square (Takacs and Suarez, 1996).

The parameterizations of solar and infrared radiative heating rates are described in Chou and Suarez (1999) and Chou and Suarez (1994). The solar parameterization includes absorption due to O_3, CO_2, water vapor, O_2, and clouds, as well as gaseous and aerosol scattering. The solar spectrum is divided into eight Visible-UV bands and three near-IR bands. A k-distribution method is used within each band. The eight VIS-UV bands use a single k-interval, while the IR bands use ten intervals each. Effects of multiple scattering by clouds and aerosols are treated using the δ-Eddington approximation for the direct beam and Sagan-Pollock for diffuse radiation. The infrared parameterization includes absorption by water vapor, CO_2, O_3, methane, N_2O, CFC-11, CFC-12, and CFC-22, within eight spectral bands, but in the results prsented only water vapor, CO_2, and O_3 are included.

From the moist physics parameterizations, the GCM estimates a cloud fraction at each level. For the solar radiation calculation, the GCM levels are then grouped into three regions which are identified with high ($\sigma < 0.56$) middle ($0.56 < \sigma < 0.77$) and low ($\sigma > 0.77$) clouds. Within each of these regions, clouds are assumed to be maximally overlapped and the cloud fractions are scaled using a scheme that depends on solar zenith angle and optical thickness. This leaves us with a single cloud fraction in each of the three regions. The overlapping between these region is treated "exactly" by assuming random overlapping and combining the results of full transfer calculations for the eight possible cases.

Turbulence throughout the atmospheric column is modeled using the Louis et al.(1982) scheme. This is a local "K" scheme with Richardson number-dependent viscosity and diffusivity. In practice, we found that the scheme contributed to excessive annual mean stresses over the equatorial pacific, as well as to unrealistic seasonal variation of these stresses. These deficiencies were alleviated by using a smaller than usual value for the eddy-mixing length scale λ_0. We use λ_0=20 meters, compared to typical values of 80 to 160 meters in other implementations of the scheme. We also truncate mixing in the stable Ri regime, so that for Ri>3.0 vertical viscosity and diffusivity are exactly zero. This eliminates sporadic patches of significant momentum mixing in the middle troposphere, which we believe have an adverse effect on the simulation of surface wind stresses. These modifications to the standard implementation of the Louis scheme do not have noticeable negative impacts on other aspects of the model climate. We also note here that dry convective adjustment has been eliminated from the current version of the model.

The model uses the gravity-wave drag parameterization described by Zhou et al. (1996). The Zhou scheme incorporates only orographically forced gravity waves. Directional anisotropy of the orographic forcing is ignored. The scheme contains two important "tunable" parameters, the effective wavenumber k_{mw} for the waves, and a maximum surface amplitude for the waves h_{max}. These must be determined empirically. Currently we use $k_{mw} = 2.5 \times 10^{-5}$ m^{-1} and h_{max} = 400 m. The surface amplitude of waves is the lower of h_{max} and a local gridbox RMS topographic deviation derived from the GTOPO30 thirty arcsecond topographic data set (http://edcwww.cr.usgs.gov/landdaac/gtopo30/gtopo30.html). The GTOPO30 data have been binned by averaging the heights in 5 x 5 squares to produce a 2.5' dataset. It is with these data that the RMS amplitudes are computed.

In addition to the Zhou scheme, the model incorporates enhanced Rayleigh damping above σ=0.05. This damping is formulated as

$$\vec{F} = \gamma_0 \left(\frac{0.05 - \sigma}{0.05} \right)^2 (\vec{U} \cdot \vec{U})\vec{U}$$

where $\vec{U}$ is the model horizontal wind vector. The strength $\gamma_0 = (60 \text{ m s}^{-1})^{-2}(10 \text{ d})^{-1}$ is chosen to damp a 60 m s^{-1} jet in 10 days. This drag is a crude *ad hoc* representation of missing gravity wave drag in the middle atmosphere. It is intended primarily to reduce the strength of the polar night jet in the winter stratosphere in the interest of computational stability. This drag formulation does not produce realistic simulations of the stratospheric climate.

We find that our simulation of stationary planetary waves improves significantly when the topographic elevation data used by the model is first filtered to eliminate high spatial frequencies. This is accomplished using a 12-th order Coiflet filter. Coiflets are nearly symmetrical orthogonal wavelets with compact support and exact reconstruction. We filter by simply removing the highest frequency (octave) of the Coiflet transform of the topography and reconstructing. The compact support of the Coiflet filter reduces the ringing that plagues higher-order filtering techniques.

Penetrative convection originating in the boundary layer is parameterized using the Relaxed Arakawa-Schubert (RAS) scheme (Moorthi and Suarez, 1992), which is a simple and efficient implementation of the Arakawa-Schubert scheme. The version described in Moorthi and Suarez, RAS-1, is the standard parameterization used at Goddard. It has also been tested at NCEP, NCAR, and COLA, and has performed particularly well in simulating the atmospheric response to tropical SST anomalies — a crucial aspect of the coupled prediction problem. We have recently updated it by including a more detailed condensate budget in the updraft. This version, which we refer to as RAS 1.5, is the one used in the NSIPP 1 AGCM.

Clouds are obtained from an empirically-based, diagnostic scheme in which the cloud cover at each grid point depends directly on the results of the large-scale condensation and convection parameterizations. The scheme defines both large-scale and convective cloudiness. Large-scale cloudiness is determined in two steps. First, an intial cloud fraction is estimated using a simple diagnostic scheme based solely on relative humidity (RH). This scheme is similar to that of Slingo (1987). A high threshhold RH of 95% is used. Even with this high threshhold value, excessive cloudiness results over tropical and subtropical oceans. Thus, a second "destruction" step is invoked. We simply use the magnitude of subsidence drying produced by RAS to destroy a fraction of the large-scale clouds produced by the RH diagnostic,

$$C_{ls} = \max\left[\ C_{ls}^{*}\left(1 - \left[\frac{D_{cnv}}{D_0}\right]^2\right), 0\right]$$

where C_{ls}^{*} is the initial estimate from the RH-diagnostic, D_{cnv} is the 3-dimensional distribution of net convective drying from RAS, and D_0 is a tunable parameter, which we choose by examining the global radiation budget. In the simulations discussed here, this parameter has a value of 7 g kg^{-1} day^{-1}.

The land surface model (LSM) is the Mosaic LSM of Koster and Suarez (1992, 1996), The core of the LSM is a standard soil-vegetation-atmosphere-tranfer (SVAT) model. The most distinctive feature of Mosaic is that it subdivides each AGCM grid square into subregions, or tiles, of relatively homogeneous vegetation type and then calculates separate one-dimensional energy and water balances over each tile, with distinct stomatal control over transpiration rates. This model has performed well in tests against observations (Chen et al. 1997, Wood et al. 1998), and has been used in studies of land-atmosphere interactions (Koster et al., 2000, and references therein).

3 Description of the integration

All results presented here are from a single AMIP-style run begun on 1 January 1979 0Z and extending to 1 December 1999 0Z. The first eleven months of the run were discarded as a "spin up" period. We thus analyzed twenty years (December 1979 - November 1999) of integration.

For this run, the model was integrated at a resolution of 2° latitude by 2.5° longitude, using 34 sigma layers (Table 1).

Sea-surface temperatures (SST) and sea-ice fractions were specified based on the monthly Reynolds O-I dataset (Reynolds and Smith 1994). The land surface was fully interactive and consists of some 13000 tiles distributed over the atmospheric grid boxes that contain a non-zero land fraction. The tiles represent six different vegetation types, as well as land ice, bare soil, desert, and lakes. Lakes are treated as a freely evaporating surface (i.e., no surface, only aerodynamic, resistance) with a heat capacity equivalent to 2 meters of water.

Table 1: Sigma surfaces separating the 34 layers of the model.

L	σ	L	σ	L	σ	L	σ	L	σ
1	0.000	2	0.005	3	0.010	4	0.015	5	0.025
6	0.050	7	0.075	8	0.100	9	0.125	10	0.150
11	0.175	12	0.200	13	0.225	14	0.275	15	0.325
16	0.375	17	0.425	18	0.500	19	0.625	20	0.700
21	0.750	22	0.775	23	0.800	24	0.825	25	0.850
26	0.865	27	0.880	28	0.895	29	0.910	30	0.925
31	0.940	32	0.955	33	0.970	34	0.985	35	1.000

One peculiarity of this run is that, to avoid running with a sea-ice model, we have specified both sea ice fractions *and* temperatures. The former vary interannual, but sea-ice temperatures repeat the same seasonal cycle each year.

4 Validation data sets

For the upper air fields and their statistics, we compare with the NCEP/NCAR Reanalysis (Kalnay et al. 1994) averaged for the same period as the model simulation. For the moisture field and various physics diagnostics we compare with various satellite and in situ measurements described below.

Precipitation is compared with the combined satellite,gauge, and model estimates derived by Xie and Arkin (1997). These data are available for the entire period of the simulation from ftp://ftp.ncep.noaa.gov/pub/precip/cmap/monthly/.

Estimates of total precipitable water (TPW) are those generated by Wentz (1992) from the Special Sensor Microwave Imager (SSM/I) measurements. The radiative transfer algorithm uses three channels of microwave measurements (22V, 37V, 37H) and a scheme that accounts for absorption and emission in the atmosphere and uses a surface emissivity value over oceans appropriate for a wind-roughened sea surface. The scheme does not account for scattering by raindrops or by frozen hydrometers and is, therefore inaccurate for high rain rates. No data is produced over land or sea ice, because of the complexity of the surface emissivity.

To validate the top of the atmosphere radiation budget, we compare with the Earth Radiation Budget Experiment (ERBE) data collected by the ERBS, NOAA 9 and NOAA 10 satellites between November 1984 and February 1990. More information on ERBE may be obtained at (http://asd-www.larc.nasa.gov/erbe/ASDerbe.html). We limit our comparison to the 5-year period from 1985 through 1989.

Surface fluxes are compared with the first 10 years of the ECMWF reanalysis (Gibson et al., 1996).

5 Organization and calculations

Unless otherwise noted, quantities presented in this report are averaged over the 20 years of the integration. We will concentrate on seasonal means. Instantaneous values of the simulated upper air data were saved four times daily at 0Z,6Z,12Z, and 18Z. Surface and top-of-atmosphere (TOA) fluxes, precipitation, and cloudiness were accumulated at each time step and saved once daily.

Results are presented as zonal means and global maps of climatological means and sub-monthly variance/covariance statistics. For selected quantities we also show the zonal mean bias (departures from NCEP/NCAR reanalysis), and/or line plots of zonal means at selected pressure levels or of vertical means. The zonal means are computed at the following pressure levels (1000, 925, 850, 700, 500, 400, 300, 250, 200, 150, 100, 70, 50, 30, qnd 10 mb). While results are presented up to 10 mb, the model was not tuned to produce a very realistic stratosphere. In fact, the current values of Rayleigh friction produce a rather strong damping on the stratosphere, resulting in unrealistically weak high latitude westerlies and covariance statistics above about 50 mb.

The variance/covariance statistics are divided into "transient" and "stationary" components. The "transient" statistics are computed from 6 hourly deviations from monthly means of each year and each calendar month. Products are then taken and averaged for each season and for the twenty years of the analysis. The "stationary" statistics are computed from zonal departures of monthly means. these are then averaged for each season and for the twenty years of the analysis. We will use overbars to denote a calendar monthly mean, so that $u' = u - \overline{u}$ is the monthly deviation of u, and square brackets to denote a zonal mean, so that $u^* = u - \overline{u}$ is the zonal departure of u. Then the mean quadratic quantities are defined as:

$$TRANSIENT(u,v) = \left\{\overline{u'v'}\right\}, \qquad STATIONARY(u,v) = \{[\overline{u}^*\overline{v}^*]\},$$

where the braces represent an average over the three months of each season and all years. For all squared statistics, other than kinetic energy, we plot the square root, which is taken after all averaging.

Section 6 discusses the climatological means and bias of upper air fields. Section 7 discusses sub-monthly quadratic statistics, and Section 8 selected physics quantities.

6 Means of Upper Air Fields

The model produces a very good simulation of the general circulation of the troposphere, including the zonally asymmetric flow and stationary eddy patterns. In the following discussion, we emphasize deficiencies that remain in the simulation.

The model simulation of the seasonal mean zonal mean winds is generally quite good. Notable deficiencies include, weak high latitude stratospheric winter westerlies, an easterly bias in the upper troposphere/lower stratosphere of the tropics, and a westerly bias in the middle latitudes of the Southern Hemisphere. At 200 mb, the model produces a westerly node in the eastern tropical Pacific that is too strong. During JJA, the 200 mb Asian and North Pacific jets are too weak. There is a tendency for a westerly bias at 200 mb over the tropical western hemisphere during DJF and MAM. The model fails to capture the separation of the 200 mb African and East Asian jets during MAM. At 850 mb, the model generates too strong tropical easterlies over the eastern Pacific, and too strong westerlies in the Southern Hemisphere middle latitudes and the Asian summer monsoon region.

The seasonal cycle of the Hadley Cell is quite realistic, though the maximum rising motion during JJA occurs substantially lower in the atmosphere (below 500 mb) than the estimates from the NCEP/NCAR reanalysis show (400 mb). The model has a consistent cold bias throughout most of the stratosphere, the Southern Hemisphere high latitude upper troposphere, and the tropical upper troposphere. A substantial warm bias (greater than 8 degrees C) occurs during the winter in the stratosphere of the southern high latitudes. During all seasons the tropical and subtropical troposphere below 800 mb is too dry (maximum bias near 925mb), while between 700 mb and 500 mb the tropics are too wet. The moisture bias is reflected in the relative humidity (RH) bias, though the latter also show that the boundary layer relative humidity is too high, while away from the polar regions the upper tropospheric relative humidity is too low.

The North Pacific and North Atlantic surface highs tend to be too strong, especially during JJA. The North American upper tropospheric west coast ridge is too strong during DJF. The east Asian/west Pacific trough is too weak (and has a noticeable hump) during DJF, and it does not extend far enough into the eastern Pacific during MAM.

The model shows excessive noise over mountains in the 500 mb omega fields. Compared to the NCEP reanalysis, there is insufficient rising motion over the tropical eastern Pacific in the region of the ITCZ. The eddy stream function at 300 mb shows tropical/subtropical stationary waves that are too weak in the eastern hemisphere, while they are too strong in the western hemisphere during all seasons. The seasonal evolution of the 200 mb velocity potential is quite good.

7 Sub-Monthly Quadratics of Upper Air Fields

The model produces good tropospheric transient and stationary zonal and meridonal wind variances. However, the transient variances in both wind components (especially v) tend to be somewhat weak in the Northern Hemisphere. This leads to a substantial underestimate of the transient kinetic energy in the Northern Hemisphere troposphere during all seasons. The stationary zonal wind variance is too strong in the upper tropospheric tropics. The wind variances are much weaker than observed in the high latitudes of the stratosphere during winter.

There are large differences in the variance of the omega field, with the model showing considerably larger variance than the NCEP/NCAR reanalysis in the tropics and extratropics. It should be noted that the quality of the reanalysis are suspect for this field. The model produces very good geopotential height variances in the troposphere. Similar to the wind variances; however, the height variances are weaker than observed during the cold seasons in the high latitudes of the stratosphere. This is especially so for the stationary component during DJF in the Northern Hemisphere and during SON in the Southern Hemisphere. At 200 mb, the seasonal cycle of the height variance is quite good, though the variance is somewhat weaker than observed in the Northern Hemisphere middle and high latitudes.

The model produces excellent meridional fluxes of zonal momentum. Exceptions are the too strong stationary fluxes between 200 mb and 100 mb during JJA, and a tendency to overestimate the southward transient fluxes in the Southern Hemisphere. The model produces reasonable heat fluxes in the troposphere, though transient southward fluxes in the Southern Hemisphere are systematically higher than in the reanalysis. In the stratosphere, the stationary meridional heat flux is much too weak at high latitudes during DJF, while the transient component is too strong. The model generates very realistic meridional moisture fluxes.

8 Surface and TOA Fluxes

The model's global precipitation distribution is much improved from that produced by earlier versions. In particular, its tendency to produce unrealistic double ITCZs in the central and eastern Pacific has been greatly lessened. A strong vestige of the problem, however, remains in the MAM season. One of the more intractable problems with the precipitation distribution is a "gap" in the eastern Pacific ITCZ and an associated "bull's eye" in precipitation over Central America. This problem is apparent in all four seasons of the simulation.

The simulated precipitable water (vapor only) agrees quite well with the satellite estimate (SSM/I). As might be expected, however, it shows some of the same unrealistic features as the precipitation fields.

The zonal mean total radiation budget at the top of the atmosphere is simulated well. The most obvious deficiency is the excessive outgoing longwave radiation at almost all latitudes and all seasons. This results in a systematic "cold" bias in the net radiation, which is otherwise extremely well simulated. The "cloud radiative forcings" (CRF) highlight better the model's performance. In the OLR-CRF, the model does surprisingly well in the tropics—a result of our improved distributions of convective activity. In the middle latitudes, the model consistently underestimated the OLR-CRF, implying too little, or too low cloudiness in these regions. The solar CRF is extremely good, the main problem being too weak forcing in middle latitudes of the southern hemisphere during MAM. Aside from this, little differentiates it from the ERBE data.

The global distributions of CRF show clearly that some of the agreement in the zonal mean results from a compensation of errors along latitude circles, but they also show that much of the agreement is due to the model's improved distribution of tropical (convective) cloudiness and of the marine stratus and stratocumulus regimes. The latter is best seen in the solar CRF distributions.

Because of its importance to the ENSO problem, we have devoted considerable attention to the simulation of tropical surface stresses, particularly the seasonal cycle in the equatorial Pacific. As may be seen from the global distributions shown, both the zonal and meridional stress compare quite well with the ECMWF reanalysis. In fact, even the more difficult and oceanographically important curl of the wind stress is very close to the reanalysis.

The same cannot be said of the sensible and latent heat fluxes, both of which the model seems to overestimate very significantly, at least over oceans.

9 Summary

The atlas presents a very good simulation of the mean seasonal cycle of the tropospheric general circulation. The model is shown to have very good skill in simulating the horizontal and vertical distribution of both mean fields and variance/covariance statistics.

The results also identify a several deficiencies. Some of these, like the problems in the eastern Pacific ITCZ, may require increased horizontal resolution. Others, however, are things that we feel can clearly be improved within the current framework.

Nevertheless, we feel this is an acceptable model for NSIPP's purposes and have frozen it in the form presented here. A number of other experiments have already been conducted with it and many more will follow. These experiments address the model's sensitivity to sea-surface temperatures, its teleconnection patterns and modes of natural variability, the nature of its land-atmosphere interactions, and its performance in coupled integrations. In all of these areas, the model appears to be performing quite well, and results will be reported in the near future.

10 References

Chen, T.H. and 42 others, 1997: Cabauw experimental results from the Project for Intercomparison of Landsurface Parameterization Schemes (PILPS), *J. Climate*, **10**, 1194-1215.

Chou, M.-D. and M. Suarez, 1994: An efficient thermal infrared radiation parameterization for use in general circulation models. NASA Technical Memorandum, 104606, **10**, 84pp.

Chou, M.-D. and M. J. Suarez, 1999: A solar radiation parameterization for atmospheric studies, NASA Technical Memorandum, 104606, **11**, 40pp.

Gibson,R., P.Kallberg and S. Uppsala, 1996: The ECMWF reanalysis (ERA) project. ECMWF Newsletter, **73**, 7-16.

Gates, W. L., 1992: AMIP: The atmospheric model intercomparison project. *Bull. Amer. Meteor. Soc.*, **73**, 1962-1970.

Gruber, A. and A.F. Krueger, 1984: The status of the NOAA outgoing longwave radiation data set. *Bull. Amer. Meteor. Soc.*, **65**, 958-962.

Kalnay, E., M. Kanamitsu, R. Kistler, W. Collins, D. Deaven, J. Derber, L. Gandin, S. Sara, G. White, J. Woollen, Y. Zhu, M. Chelliah, W. Ebisuzaki, W. Higgins, J. Janowiak, K. C. Mo, C. Ropelewski, J. Wang, A Leetma, R. Renolds, R Jenne, 1995: The NMC/NCAR Reanalysis Project. *Bull. Amer. Meteor. Soc.*, **77**, 437-471.

Koster, R., and M. Suarez, 1992: Modeling the land surface boundary in climate models as a composite of independent vegetation stands. *J. Geophys. Res.*, **97**, 2697-2715.

Koster, R. and M. Suarez, 1996: Energy and Water Balance Calculations in the Mosaic LSM, *NASA Tech. Memo.* 104606, Vol. 9.

Koster, R. D., M. J. Suarez, and M. Heiser, 2000: Variance and predictability of precipitation at seasonal-to-interannual timescales, *J. Hydrometeorology*, **1**, 26-41.

Louis, J., M. Tiedke, J. Geleyn, 1982: A short history of the PBL parameterization at ECMWF. In: *Proceedings, ECMWF Workshop on Planetary Boundary Layer Parameterization, Reading, UK*, 59-80.

Moorthi, S. and M. Suarez, 1992: Relaxed Arakawa-Schubert: a parameterization of moist convection for general circulation models. *Mon. Weather Rev.*, **120**, 978-1002.

Reynolds, W. R. and T. M. Smith, 1994: Improved global sea surface temperature analyses using optimum interpolation. *J. Climate*, **7**, 929-948.

Rossow, W. B., and R. A. Schiffer, 1991: ISCCP cloud data products. *Bull. Am. Meteorol. Soc.*,**72**, 2-20.

Sadourney, R., 1975: The dynamics of finite difference models of the shallow water equations, *J. Atmos. Sci.*, **32**, 680-689.

Schubert,S. D., M. J. Suarez, Y. Chang and G. Branstator, 2000: The impact of ENSO on extratropical low frequency noise in seasonal forecasts. *Submitted to J. Climate.*

Slingo, J. M., 1987: The development and verification of a cloud prediction scheme for the ECMWF model, *Q. J. R. Meteorol. Soc*, **113**, 899-927.

Suarez, M. J. and L. L. Takacs, 1995: Documentation of the Aries/GEOS dynamical core Version 2, NASA Technical Memorandum 104606, **5**, 58pp.

Takacs, L. L.and M. J. Suarez, 1996: Dynamical aspects of climate simulations using the GEOS GCM, NASA Technical Memorandum, 104606, **10**, 56pp.

Wentz, F., 1994: User's Mannual, SSM/I Geophysical Tapes. Remote Sensing Systems, 11 pp.

Wood, E.F., and 28 others, 1998: The project for the intercomparison of land-surface parameterization schemes (PILPS) phase 2(c) Red Arkansas river basin experiment, 1, Experiment description and summary intercomparisons, *J. Global and Planetary Change*, **19**, 115-135.

Xie, P. and P. Arkin, 1997: Global precipitation, a 17-Year monthly analysis based on gauge observations, satellite estimates and numerical model outputs. *Bull. Am. Met. Soc.*, **78**, 2539-2558.

Zhou, J., Y. C. Sud, and K. M. Lau, 1996: Impact of orographically induced gravity wave drag in the GLA GCM, *Q. J. R. Meteorol. Soc*, **122**, 903-927.

ZONAL MEAN FIELDS

(DJF, MAM, JJA, SON)

Zonal wind

Meridional wind

Mass stream function

Omega

Temperature

Specific humidity

Relative humidity

Zonal wind bias

Temperature bias

Specific humidity bias

Relative humidity bias

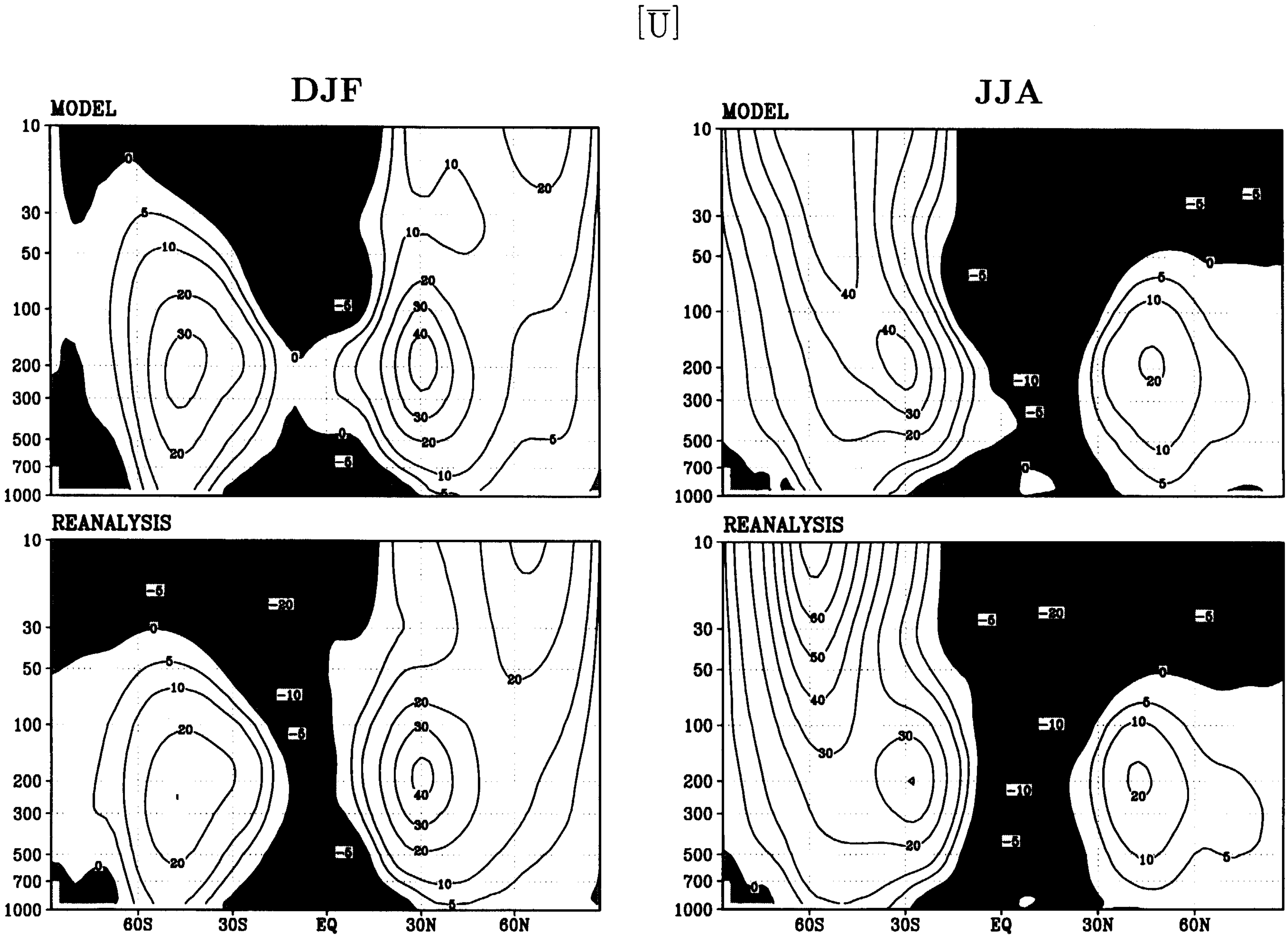

Figure 1: Zonal mean zonal wind (m s^{-1}) — Upper panels: Model; Lower panels: Reanalysis; Left panels: DJF; Right panels: JJA.

$[\overline{\mathrm{U}}]$

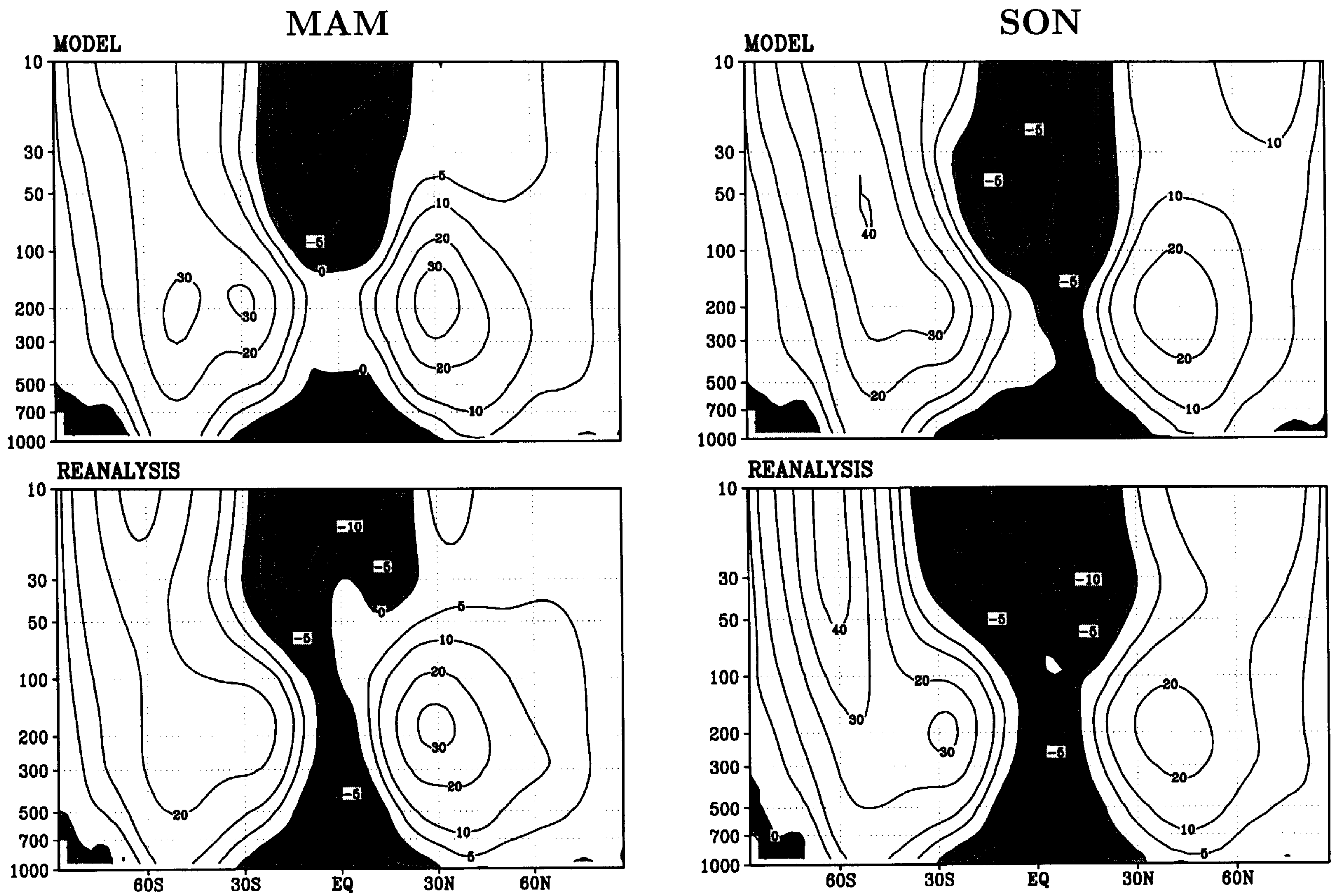

Figure 2: Zonal mean zonal wind (m s^{-1}) — Upper panels: Model; Lower panels: Reanalysis; Left panels: MAM; Right panels: SON.

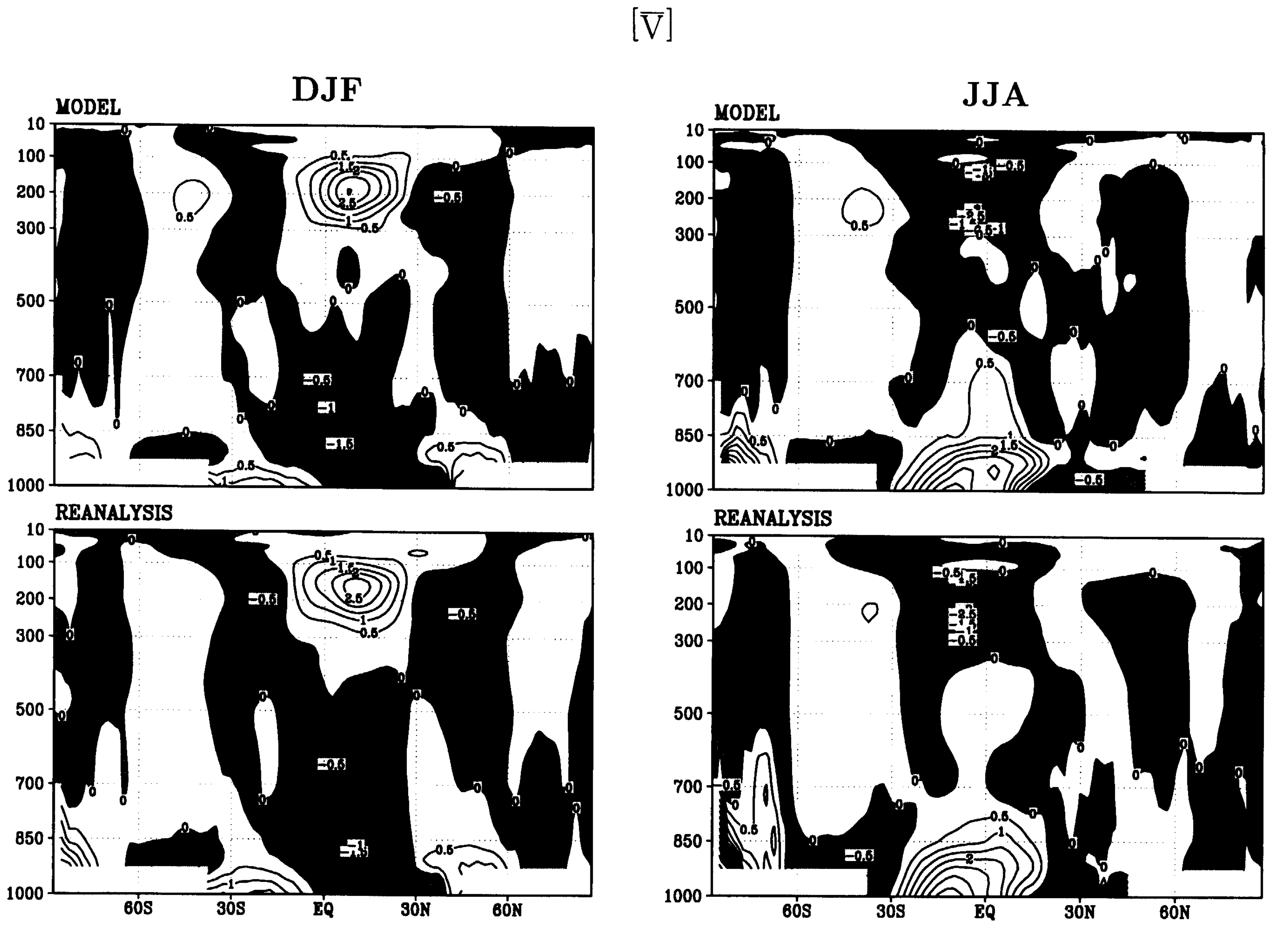

Figure 3: Zonal mean meridional wind (m s^{-1}) — Upper panels: Model; Lower panels: Reanalysis; Left panels: DJF; Right panels: JJA.

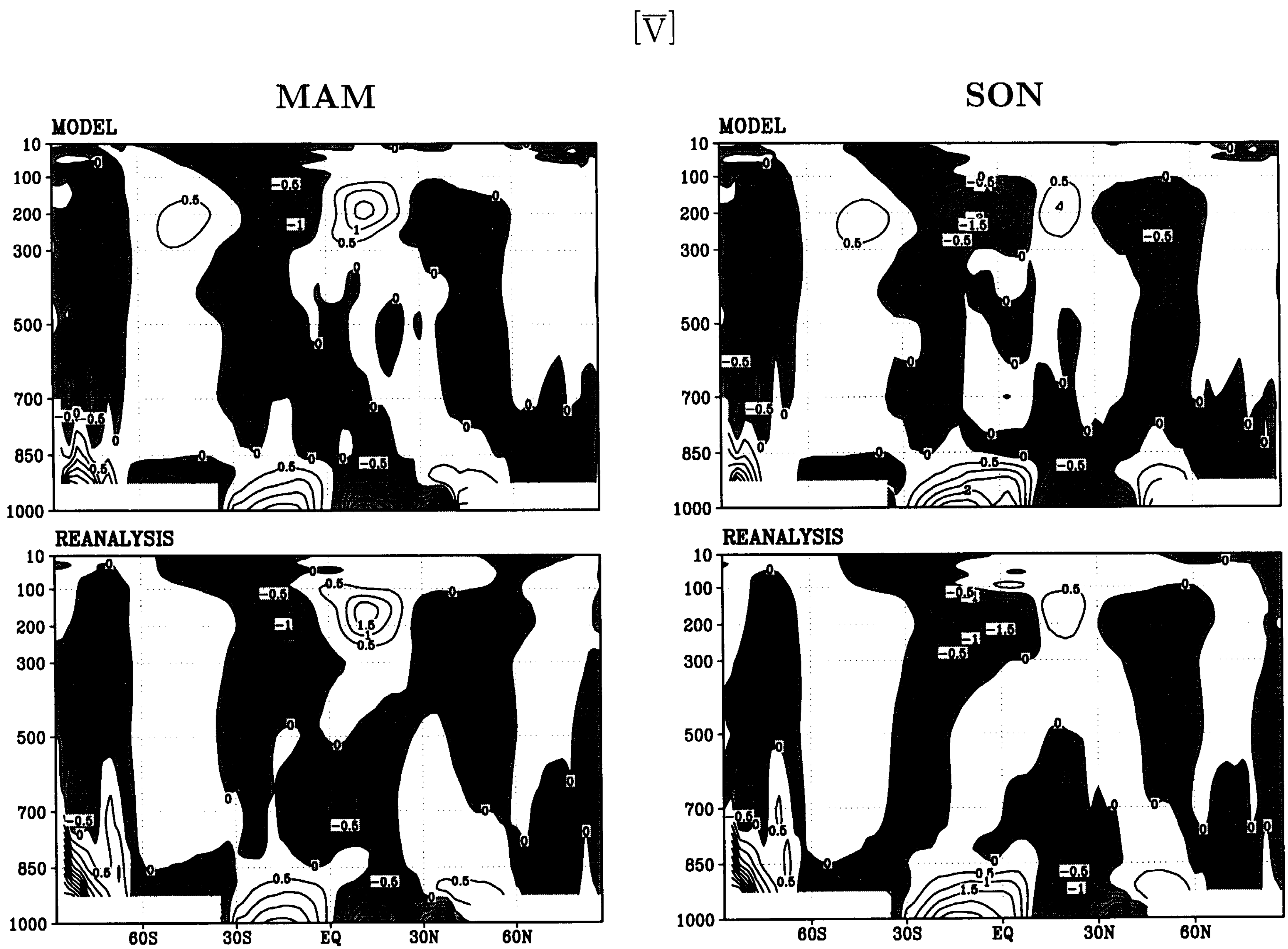

Figure 4: Zonal mean meridional wind (m s^{-1}) — Upper panels: Model; Lower panels: Reanalysis; Left panels: MAM; Right panels: SON.

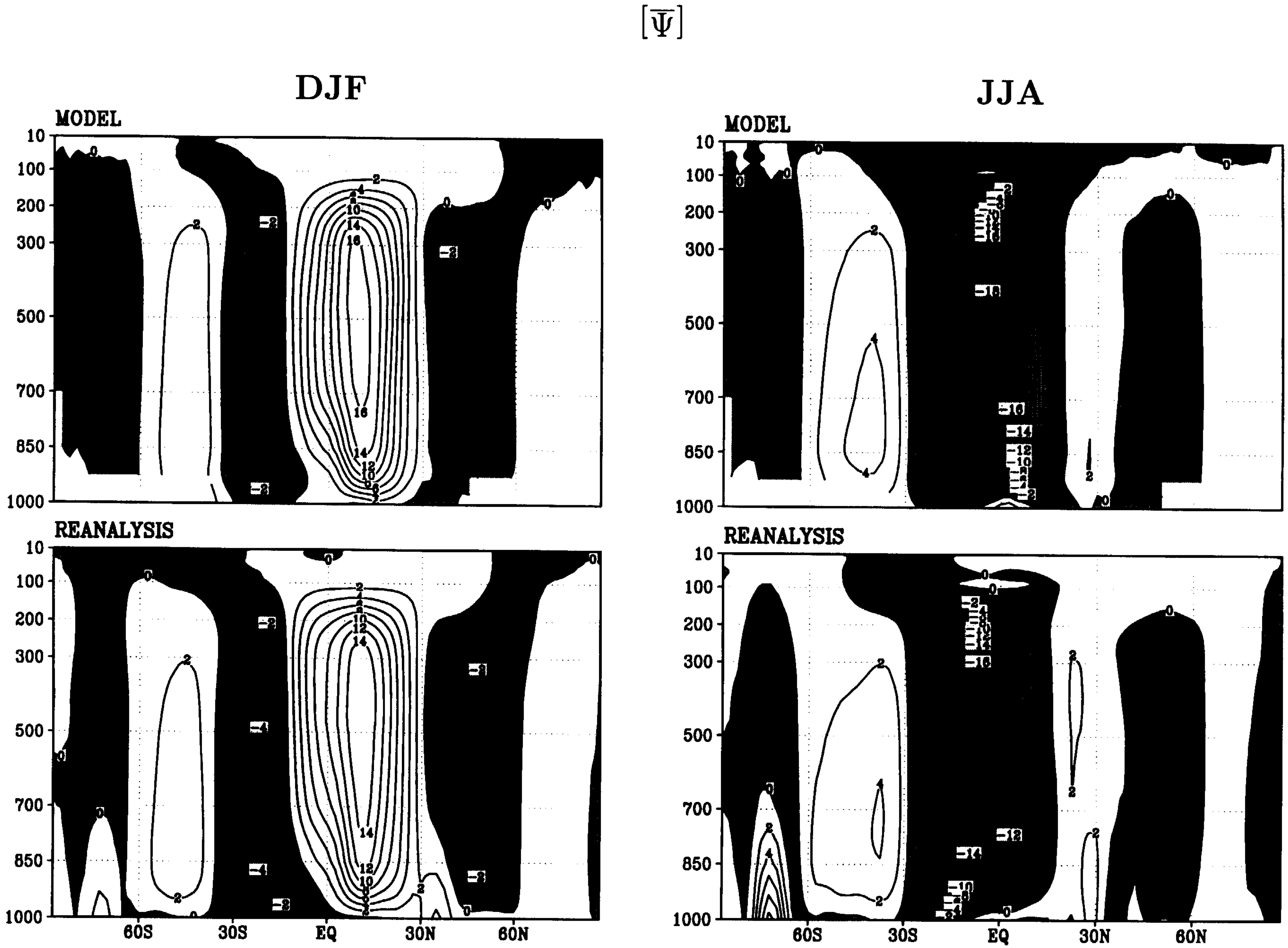

Figure 5: Zonal mean mass streamfunction (10^9 kg s^{-1}) — Upper panels: Model; Lower panels: Reanalysis; Left panels: DJF; Right panels: JJA.

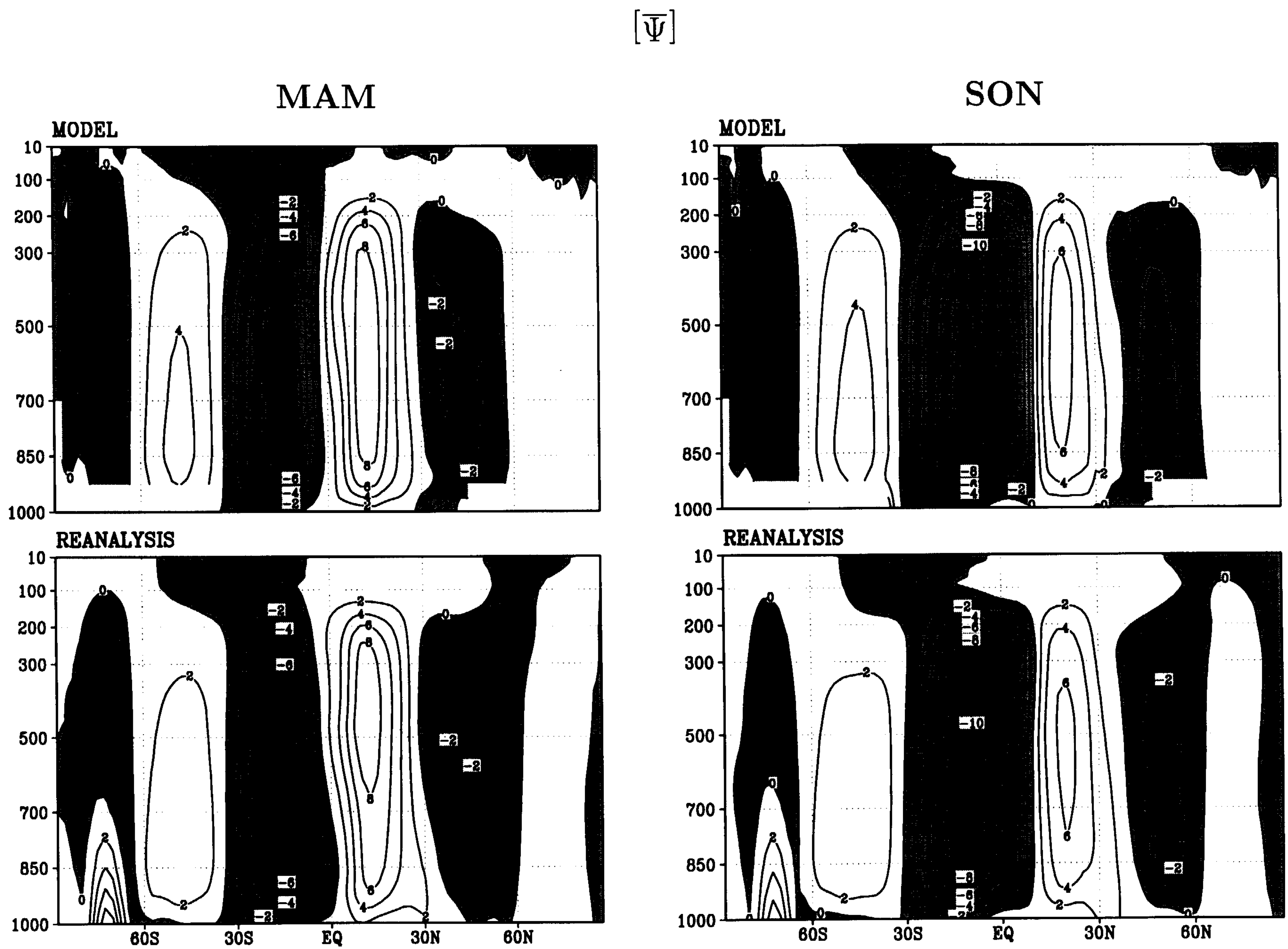

Figure 6: Zonal mean mass streamfunction (10^9 kg s^{-1}) — Upper panels: Model; Lower panels: Reanalysis; Left panels: MAM; Right panels: SON.

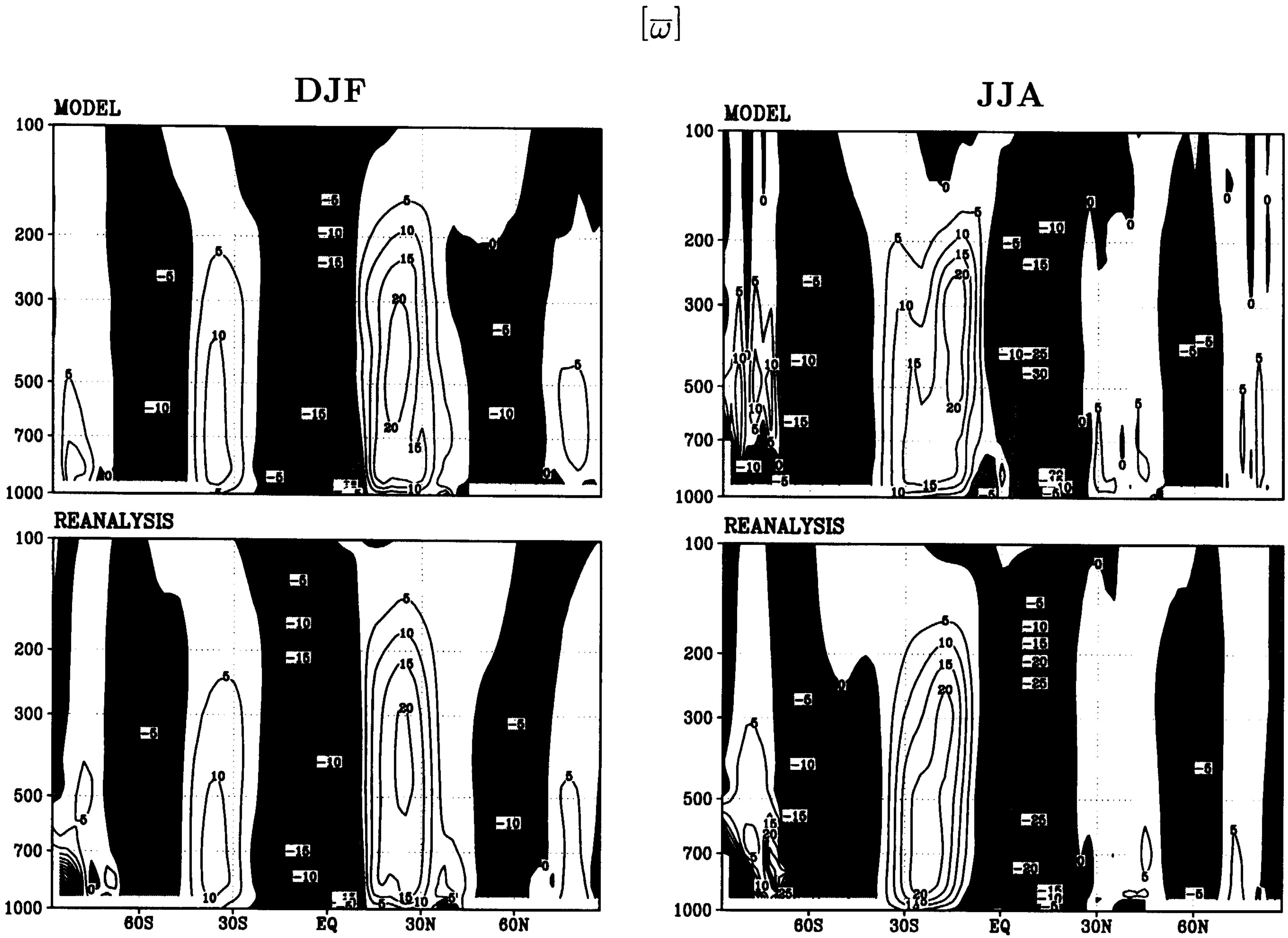

Figure 7: Omega (mb d^{-1}) — Upper panels: Model; Lower panels: Reanalysis; Left panels: DJF; Right panels: JJA.

$[\overline{\omega}]$

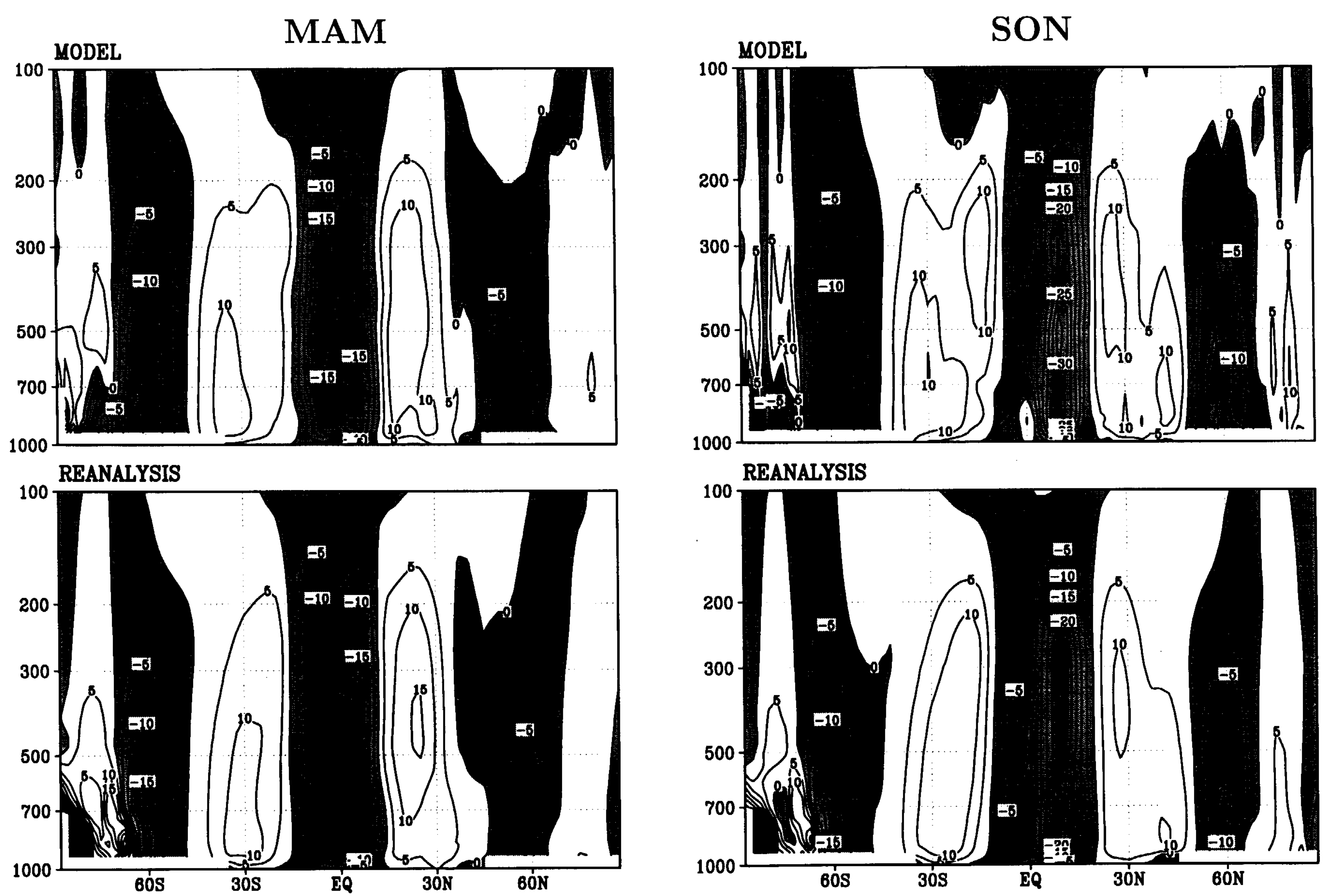

Figure 8: Omega (mb d^{-1}) — Upper panels: Model; Lower panels: Reanalysis; Left panels: MAM; Right panels: SON.

$[\overline{T}]$

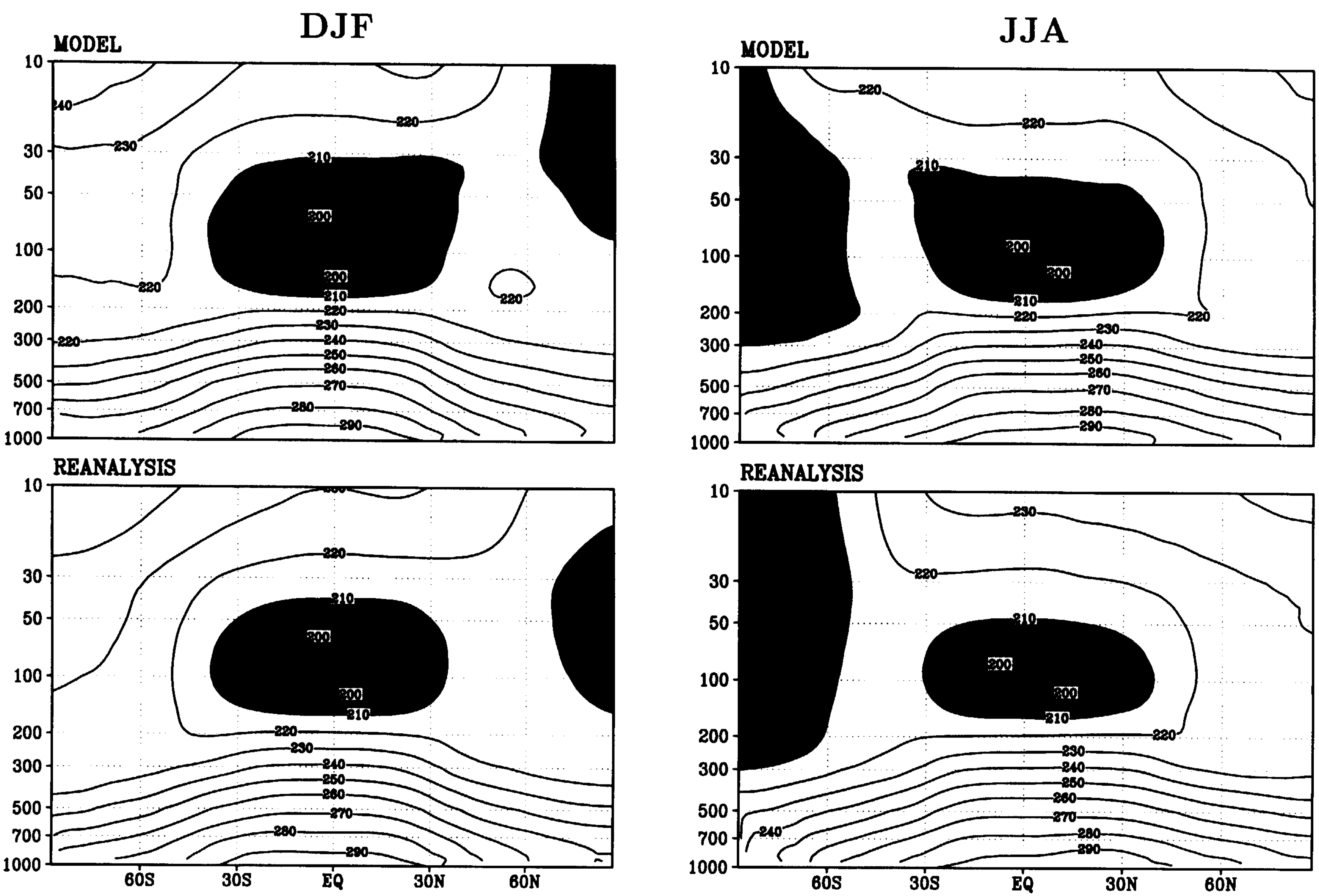

Figure 9: Zonal mean temperature (K) — Upper panels: Model; Lower panels: Reanalysis; Left panels: DJF; Right panels: JJA.

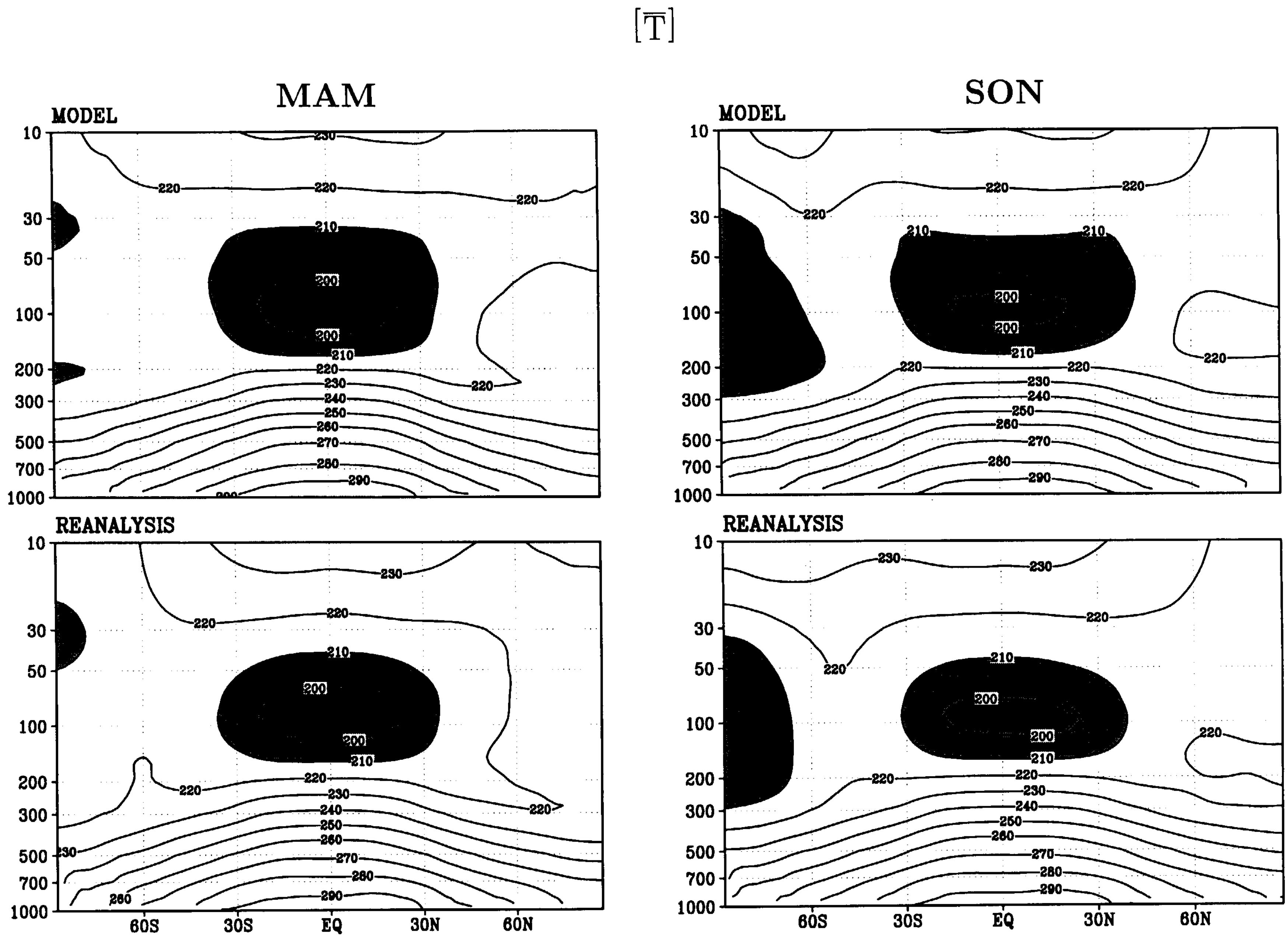

Figure 10: Zonal mean temperature (K) — Upper panels: Model; Lower panels: Reanalysis; Left panels: MAM; Right panels: SON.

$[\overline{q}]$

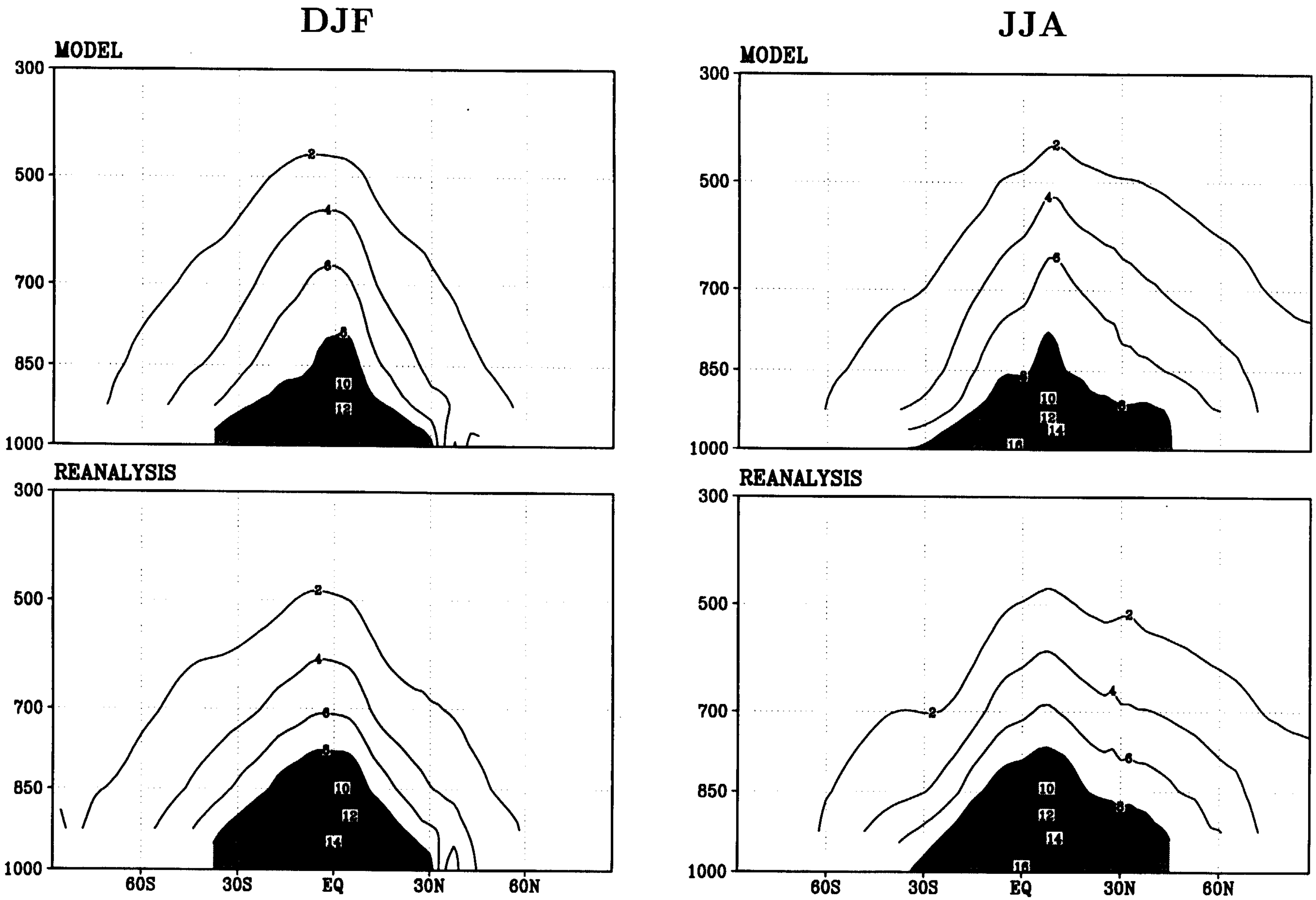

Figure 11: Zonal mean specific humidity (g kg^{-1}) — Upper panels: Model; Lower panels: Reanalysis; Left panels: DJF; Right panels: JJA.

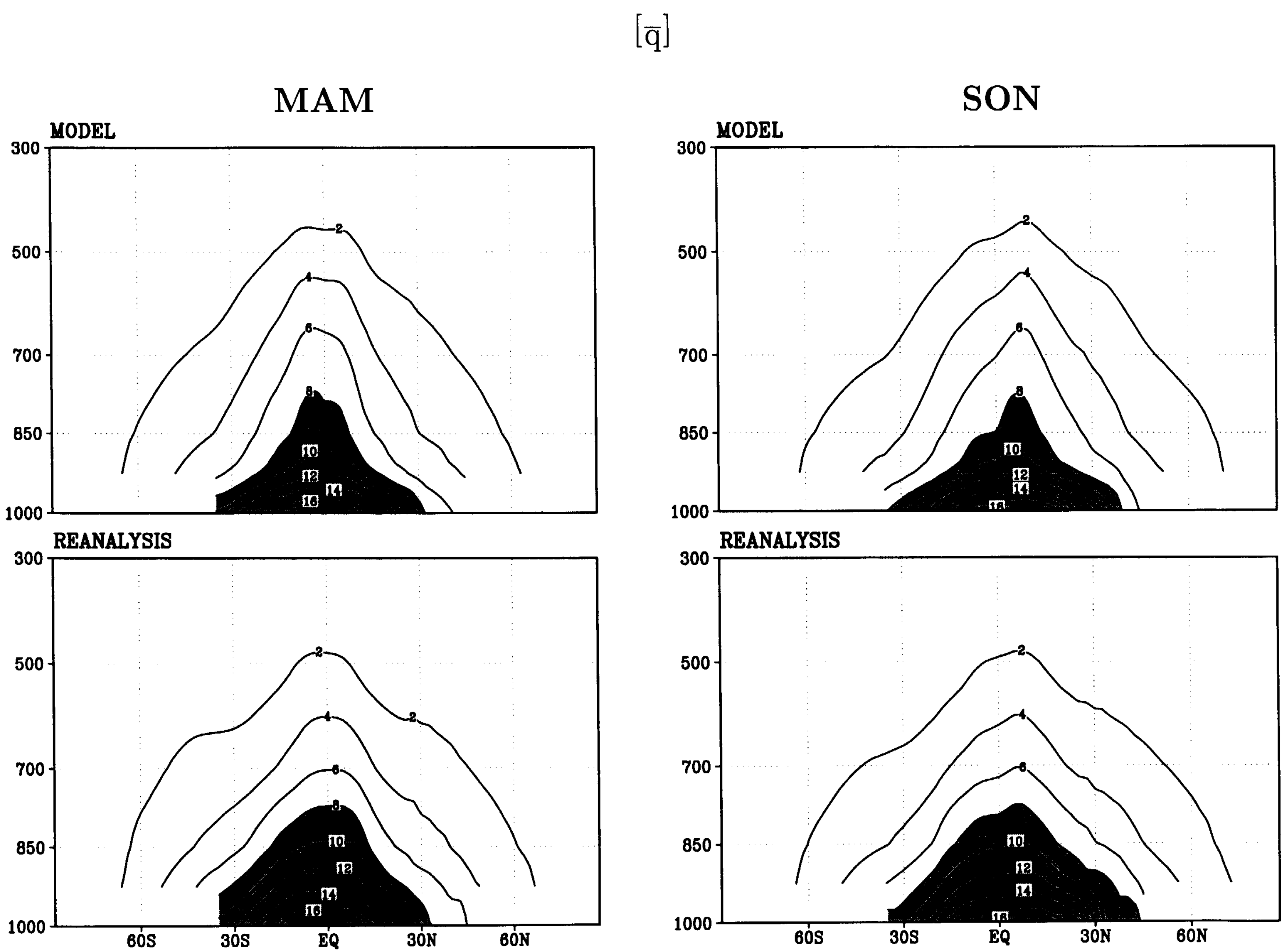

Figure 12: Zonal mean specific humidity (g kg^{-1}) — Upper panels: Model; Lower panels: Reanalysis; Left panels: MAM; Right panels: SON.

$[\mathrm{RH}(\overline{\mathrm{q}}, \overline{\mathrm{T}})]$

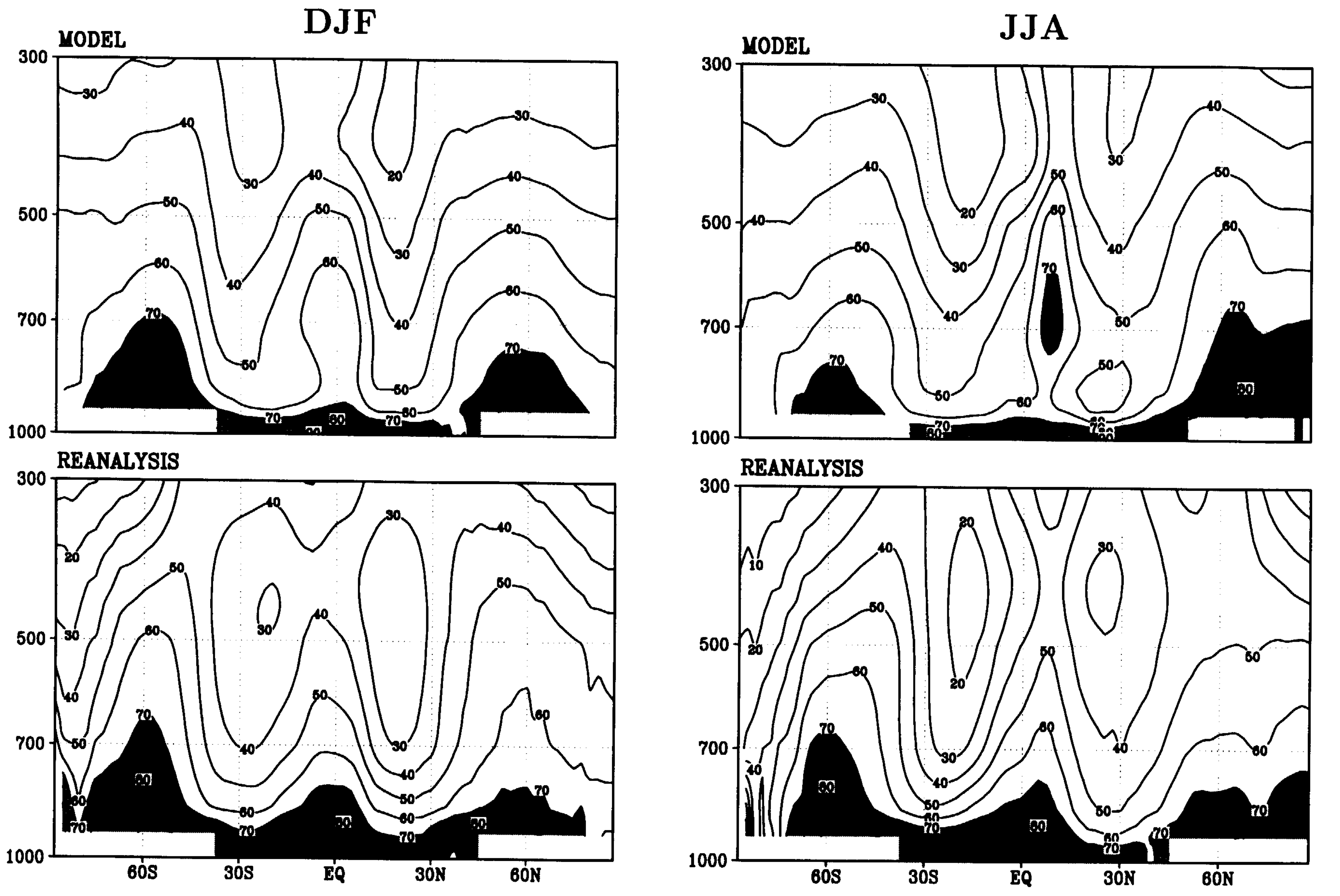

Figure 13: Zonal mean relative humidity (%) — Upper panels: Model; Lower panels: Reanalysis; Left panels: DJF; Right panels: JJA.

$[\mathrm{RH}(\overline{q}, \overline{T})]$

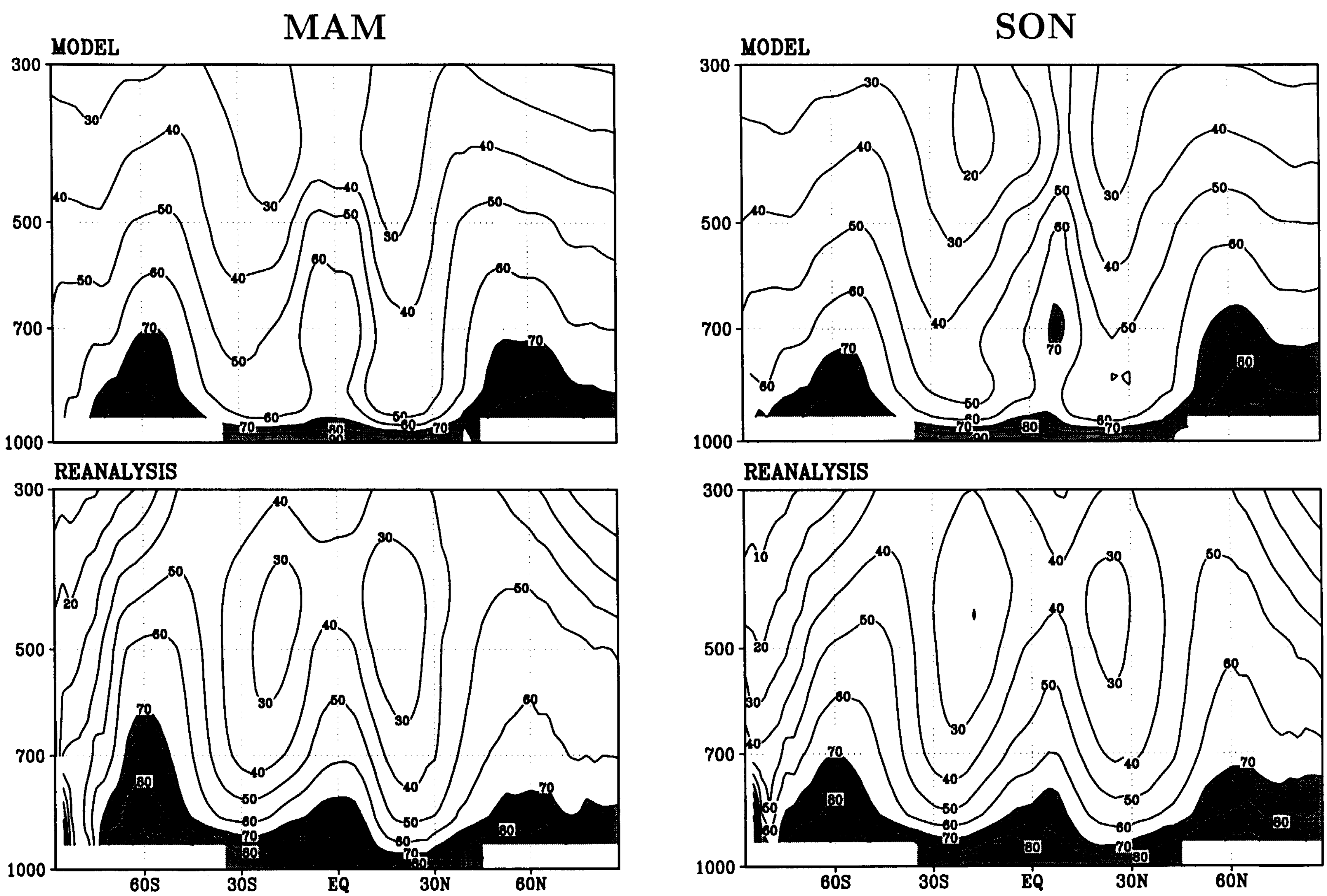

Figure 14: Zonal mean relative humidity (%) — Upper panels: Model; Lower panels: Reanalysis; Left panels: MAM; Right panels: SON.

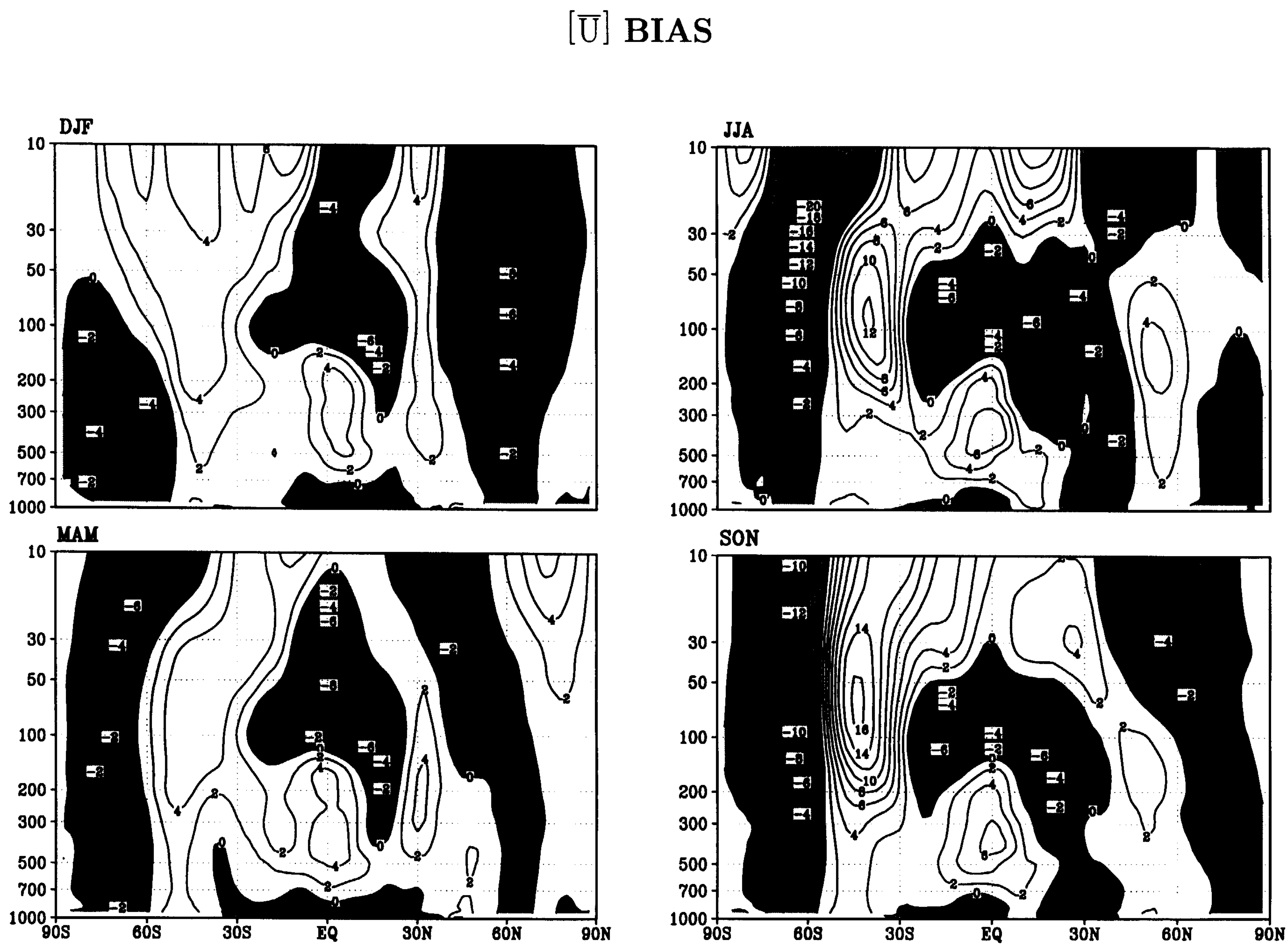

Figure 15: Zonal mean zonal wind bias (m s^{-1}) .

$[\overline{\mathrm{T}}]$ BIAS

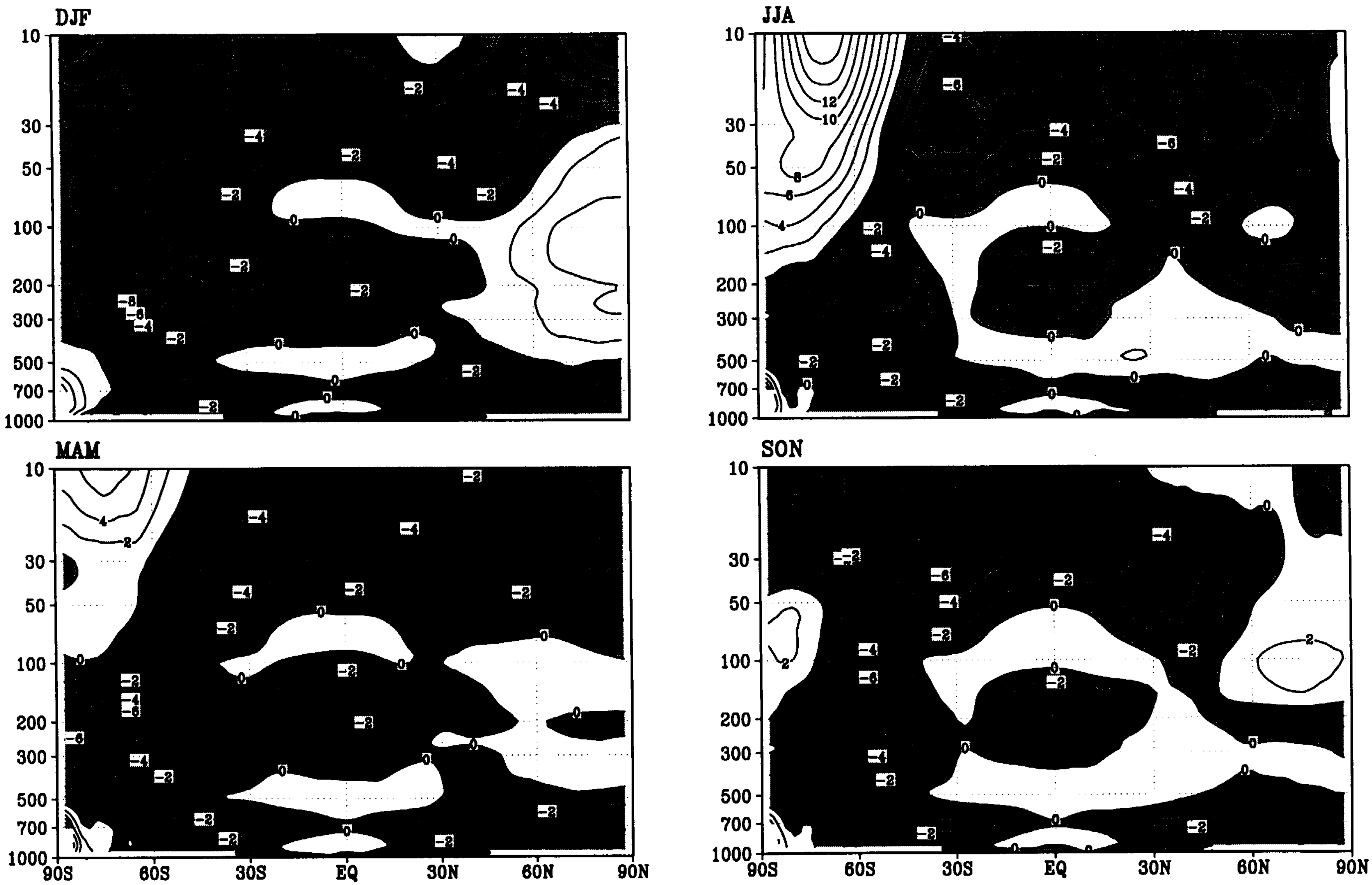

Figure 16: Zonal mean temperature bias (K) .

$[\overline{q}]$ BIAS

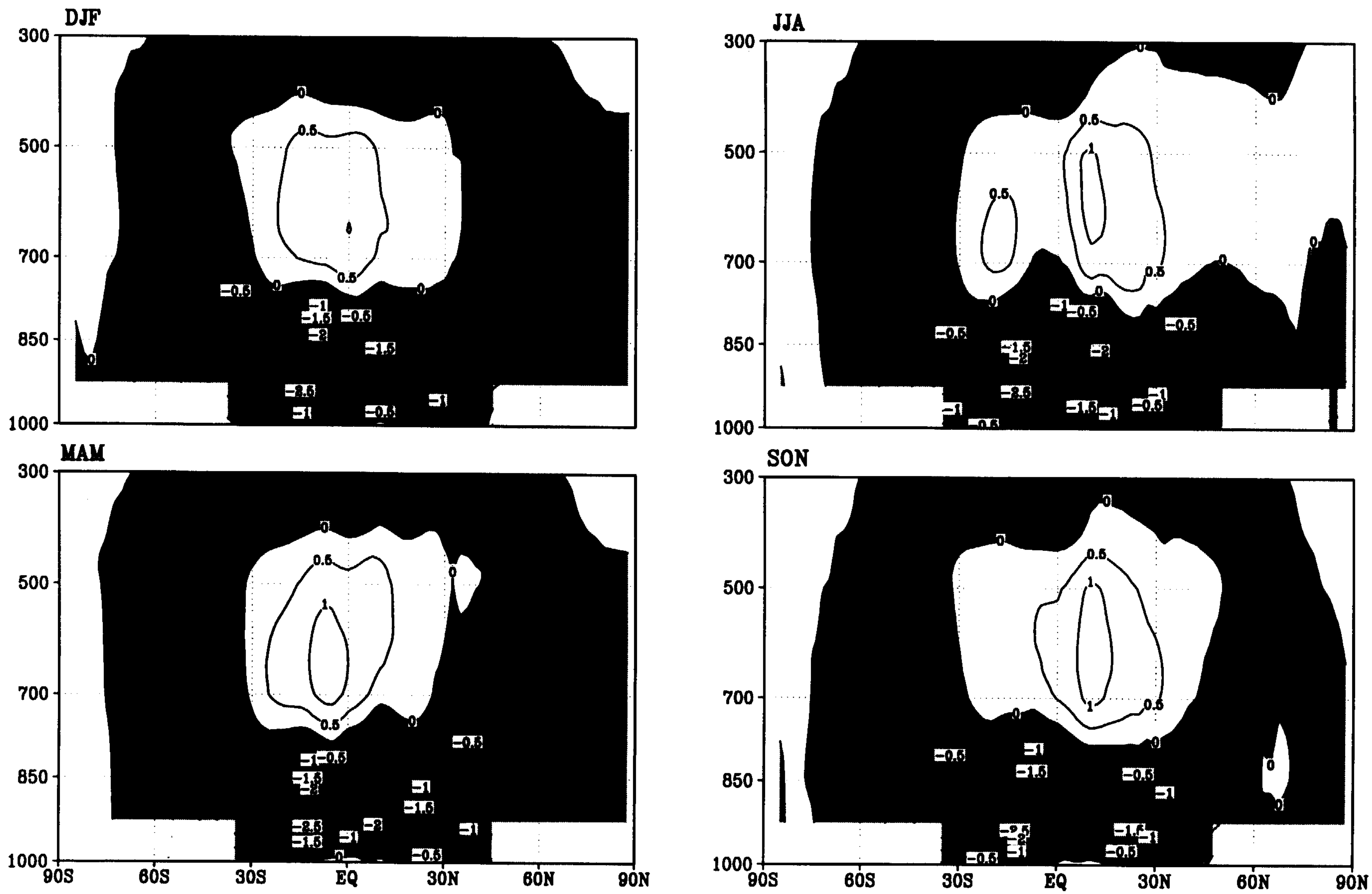

Figure 17: Zonal mean specific humidity bias (g kg^{-1}) .

$[\mathrm{RH}(\overline{\mathrm{q}}, \overline{\mathrm{T}})]$ **BIAS**

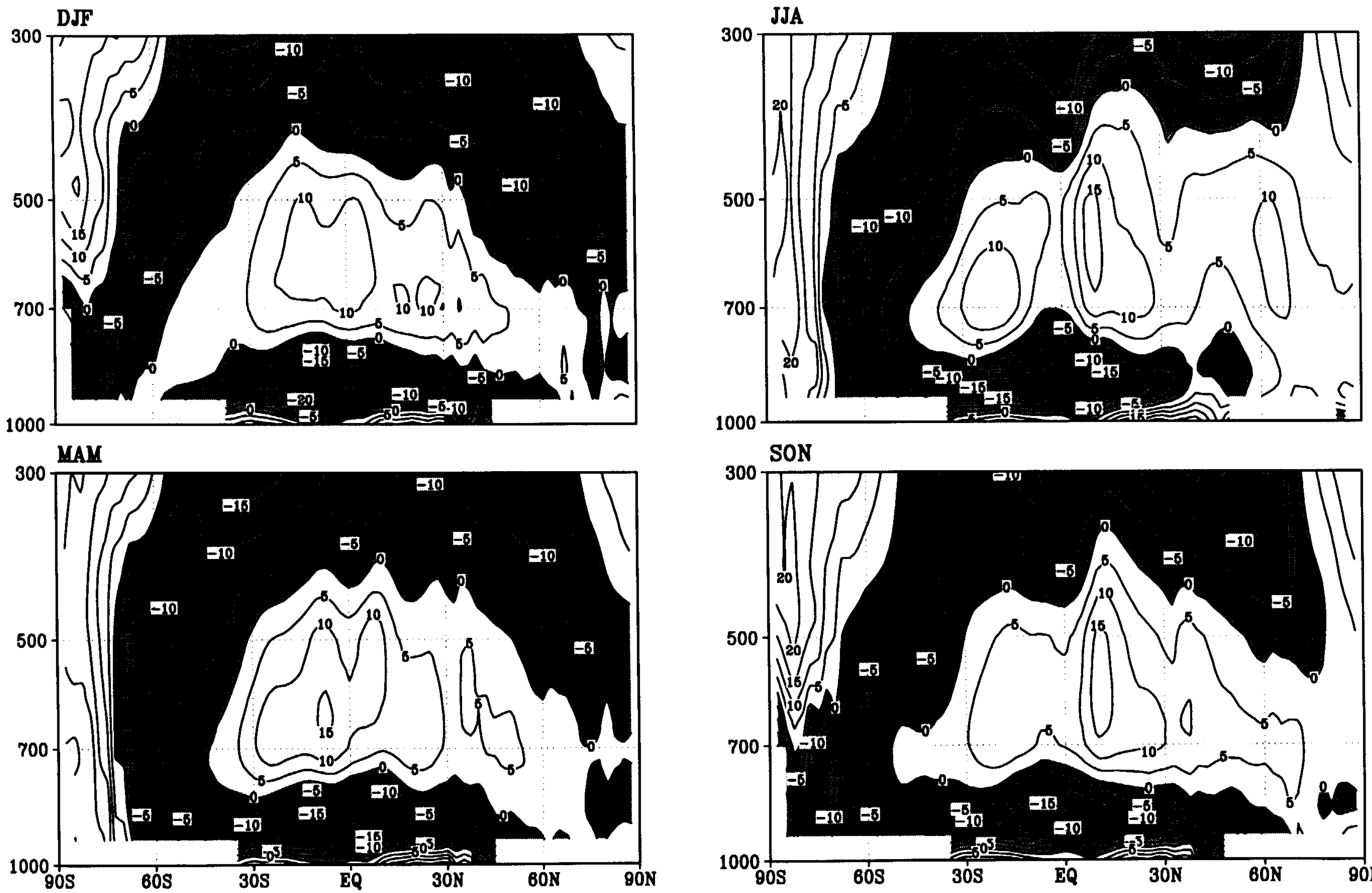

Figure 18: Zonal mean relative humidity bias (g kg^{-1}) .

GLOBAL MAPS

(DJF, MAM, JJA, SON)

Zonal wind 200 mb

Zonal wind 850 mb

Sea-level pressure

Eddy geopotential height 300 mb

Omega 500 mb

Eddy stream function 200 mb

Velocity potential 200 mb

ZONAL MEANS

Sea-level pressure

Zonal wind 200 mb

Zonal wind 850 mb

DJF $\overline{\mathrm{U}}_{200}$

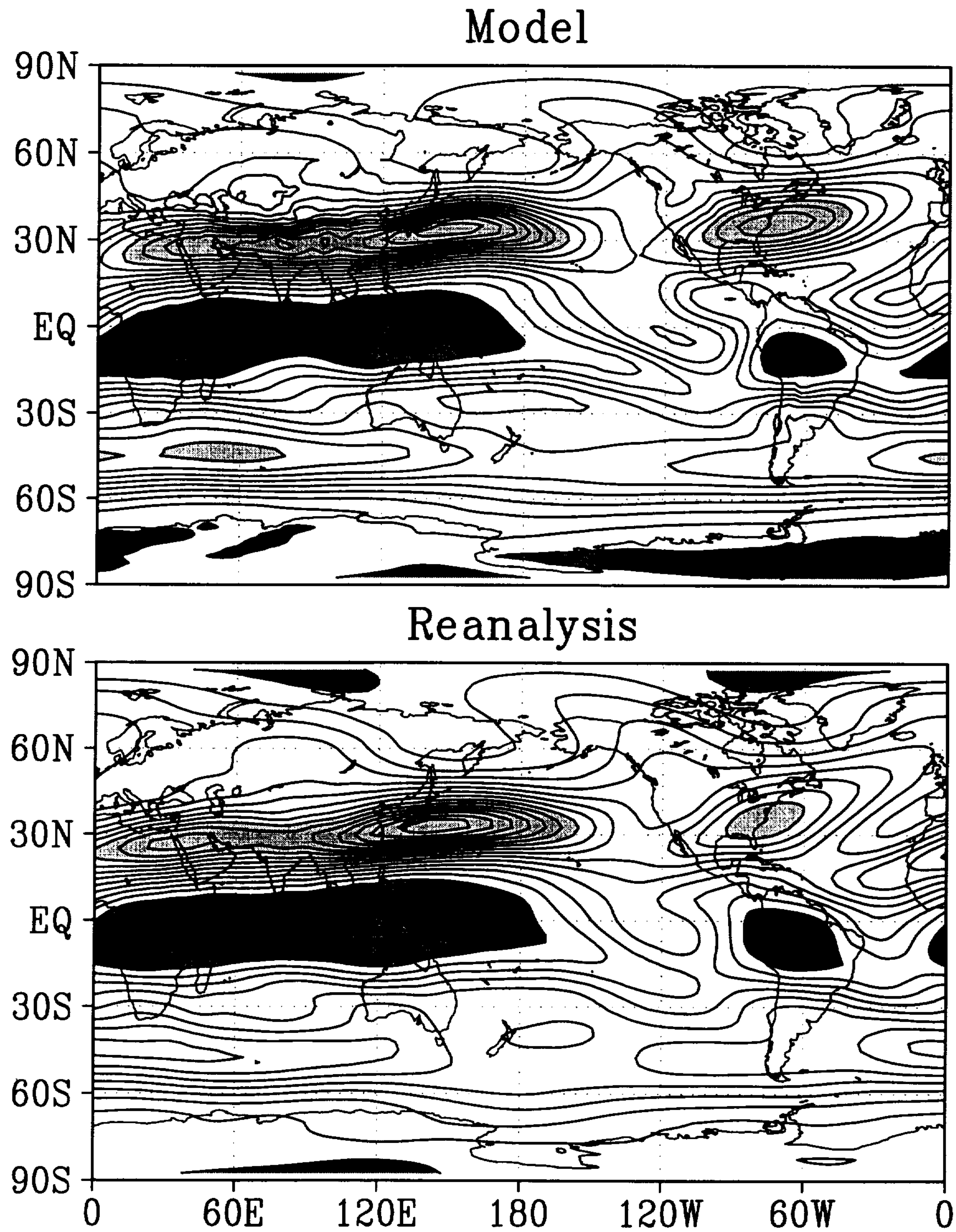

Figure 19: Zonal wind at 200 mb for DJF— Top: Model, Bottom: Reanalysis. Contour interval: 5 m s^{-1}. Easterlies indicated by dark shading, light shading indicates westerlies in excess of 40 m s^{-1}.

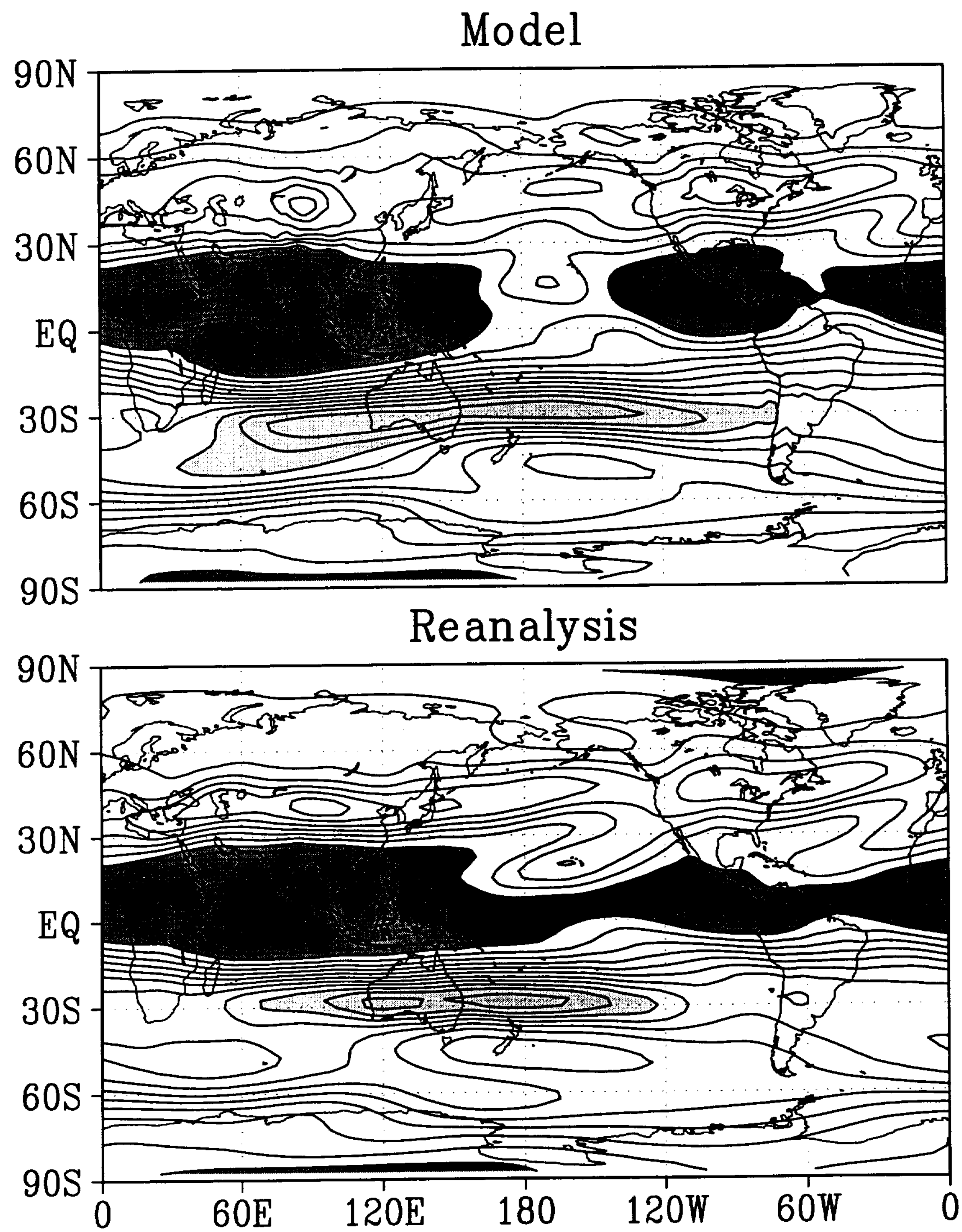

Figure 20: Zonal wind at 200 mb for JJA— Top: Model, Bottom: Reanalysis. Contour interval: 5 m s^{-1}. Easterlies indicated by dark shading, light shading indicates westerlies in excess of 40 m s^{-1}.

MAM $\overline{U}_{200}$

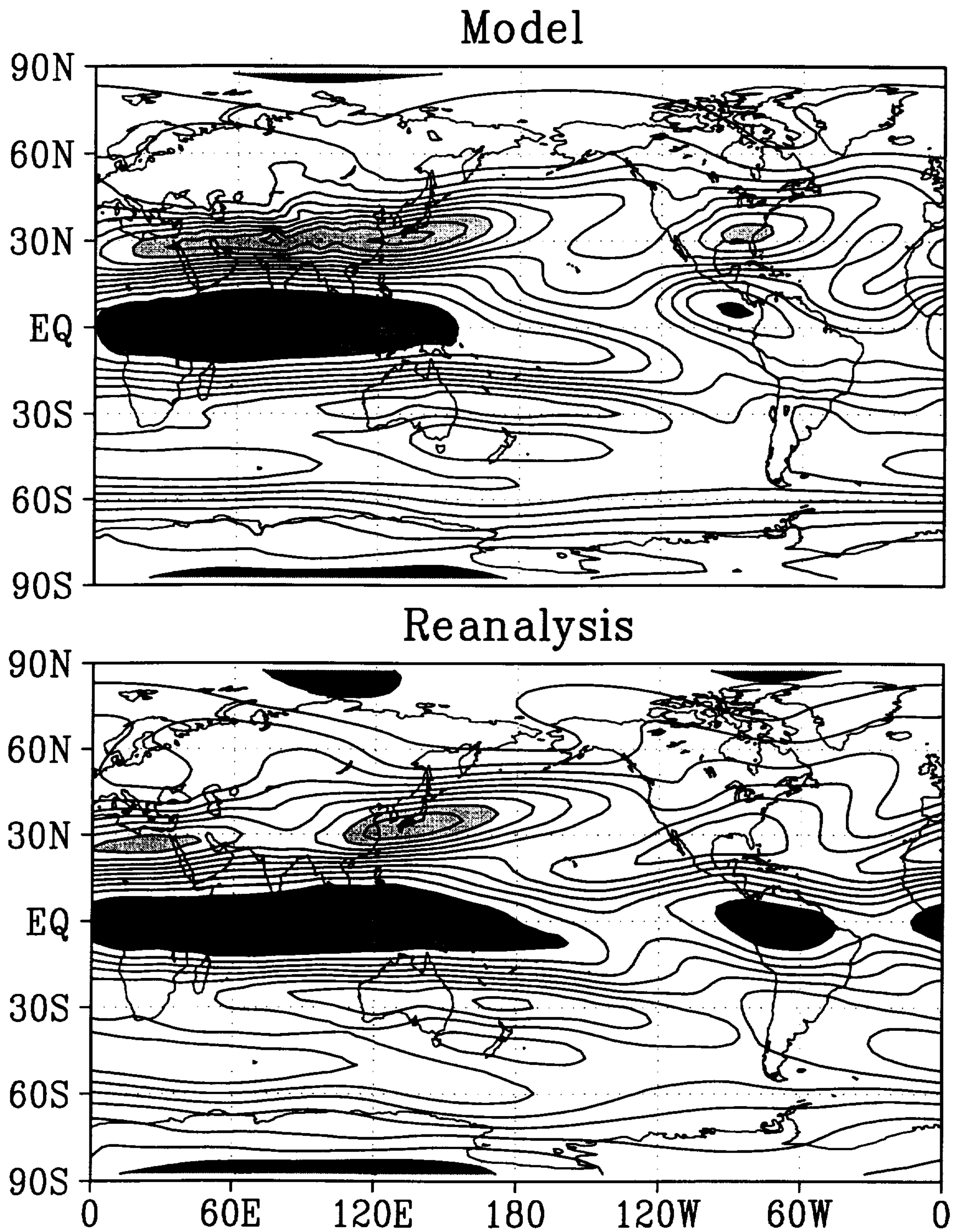

Figure 21: Zonal wind at 200 mb for MAM— Top: Model, Bottom: Reanalysis. Contour interval: 5 m s^{-1}. Easterlies indicated by dark shading, light shading indicates westerlies in excess of 40 m s^{-1}.

SON $\overline{U}_{200}$

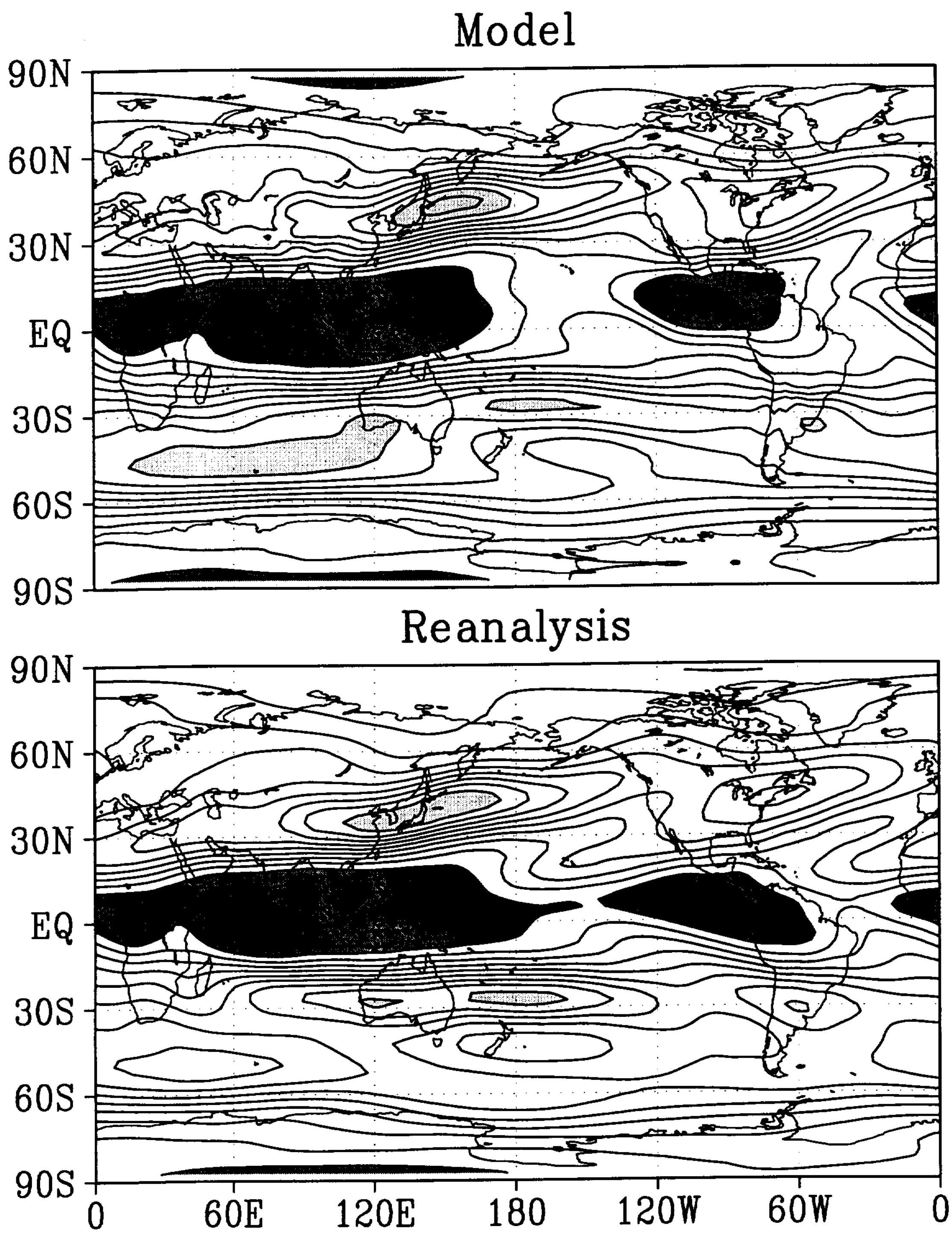

Figure 22: Zonal wind at 200 mb for SON— Top: Model, Bottom: Reanalysis. Contour interval: 5 m s^{-1}. Easterlies indicated by dark shading, light shading indicates westerlies in excess of 40 m s^{-1}.

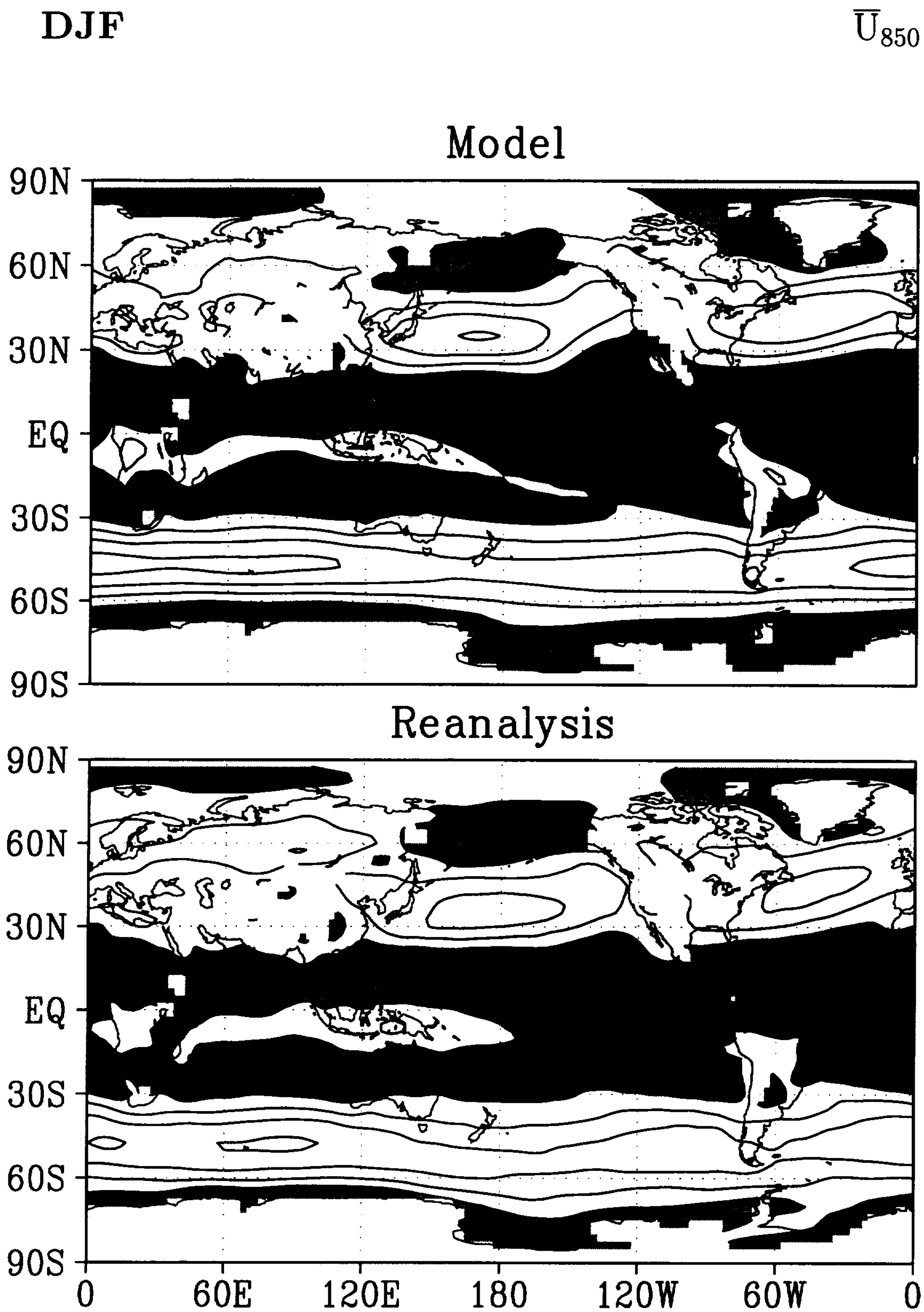

Figure 23: Zonal wind at 850 mb for DJF— Top: Model, Bottom: Reanalysis. Contour interval: 3 m s^{-1}. Easterlies are shaded.

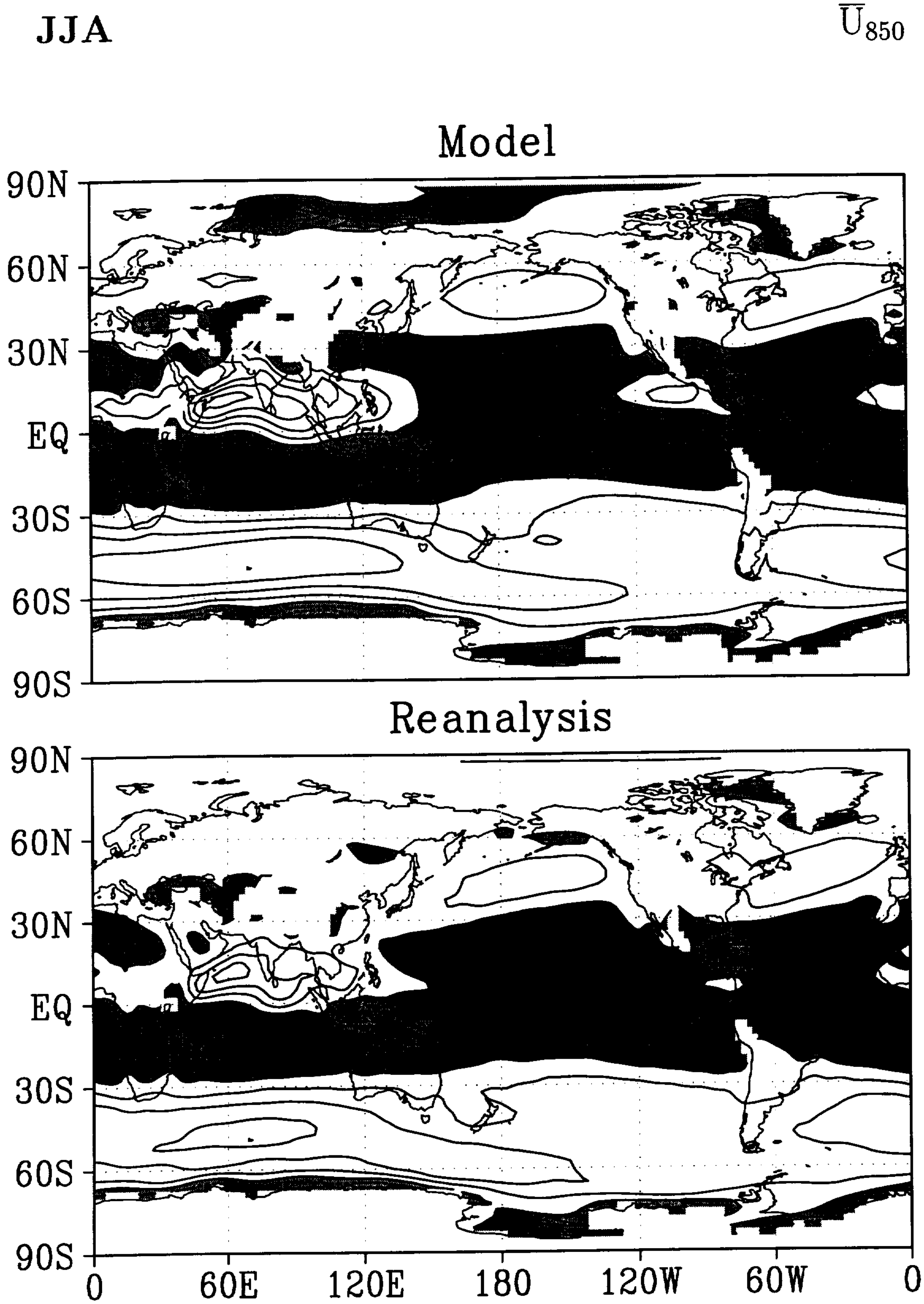

Figure 24: Zonal wind at 850 mb for JJA— Top: Model, Bottom: Reanalysis. Contour interval: 3 m s^{-1}. Easterlies are shaded.

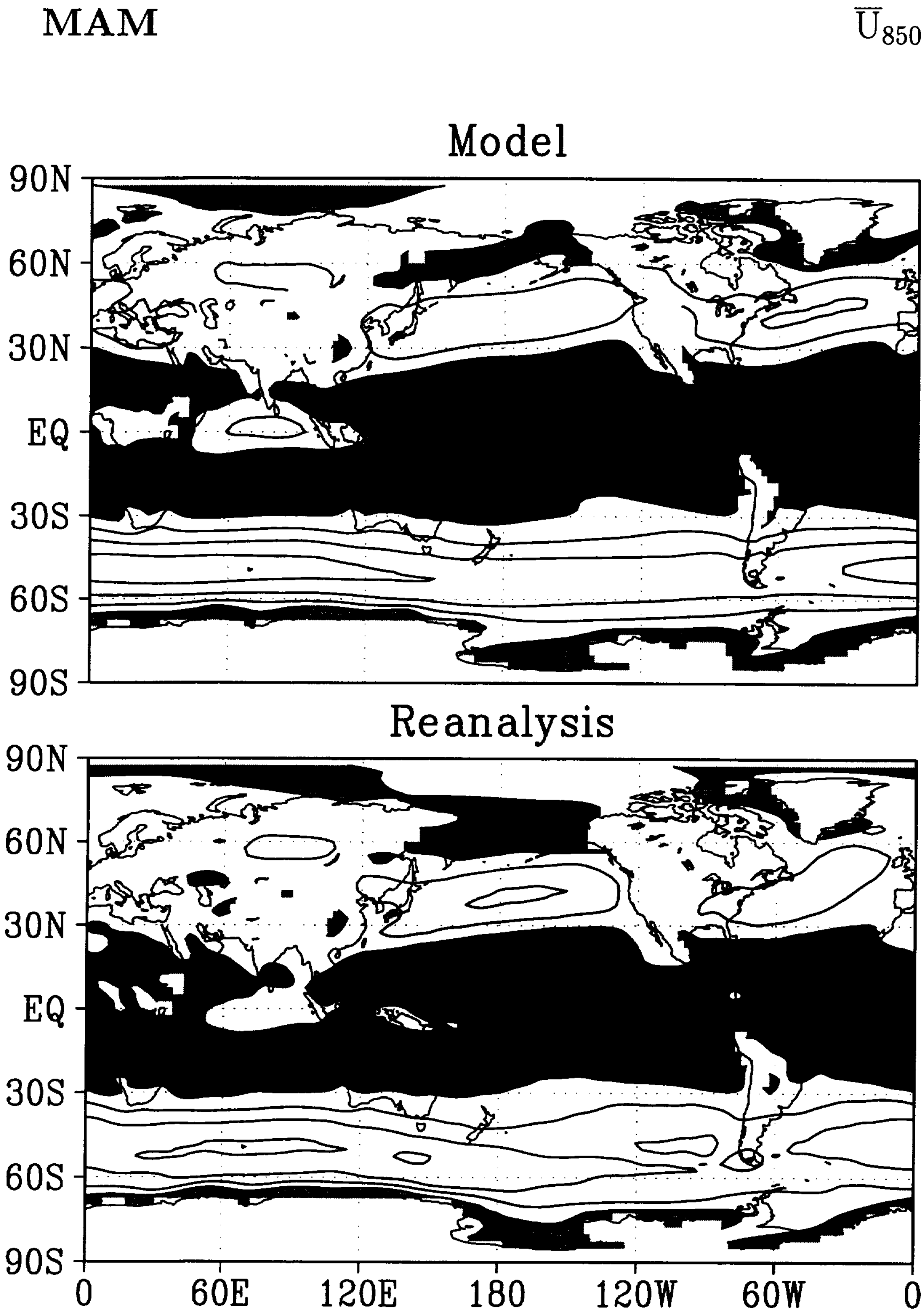

Figure 25: Zonal wind at 850 mb for MAM— Top: Model, Bottom: Reanalysis. Contour interval: 3 m s^{-1}. Easterlies are shaded.

SON $\overline{U}_{850}$

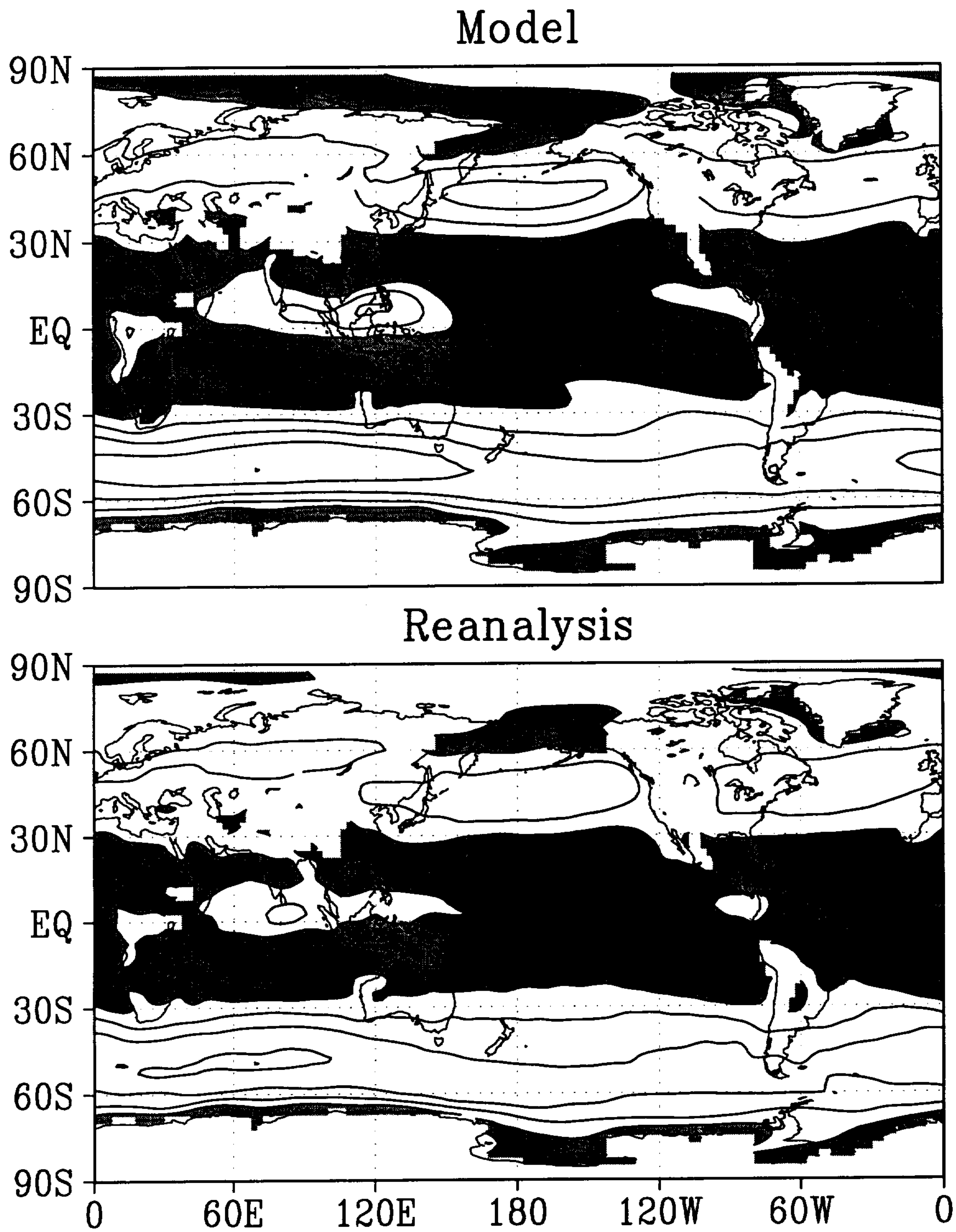

Figure 26: Zonal wind at 850 mb for SON— Top: Model, Bottom: Reanalysis. Contour interval: 3 m s^{-1}. Easterlies are shaded.

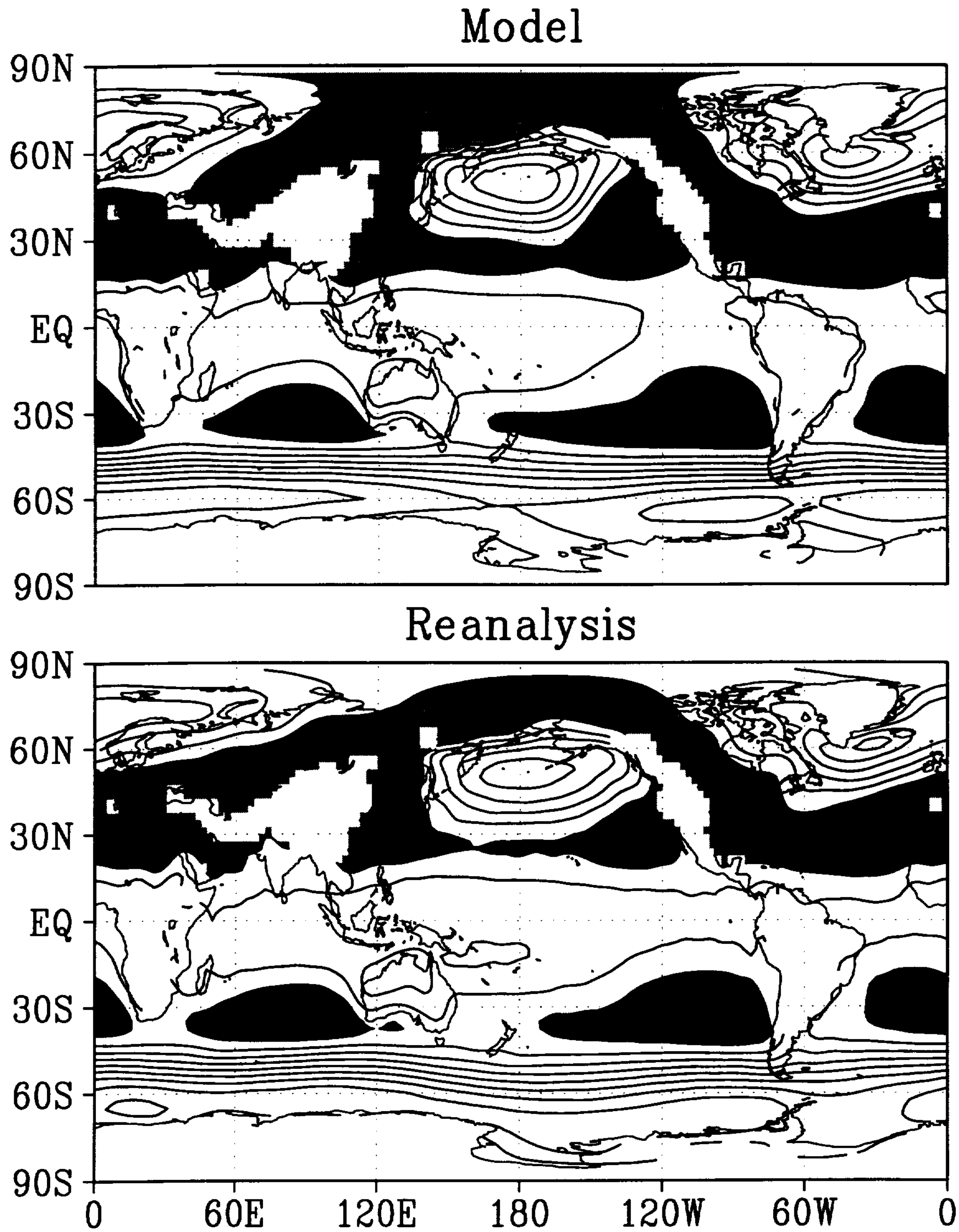

Figure 27: Sea-level pressure for DJF— Top: Model, Bottom: Reanalysis. Contour interval: 4 mb. Shading indicates pressures in excess of 1000 mb.

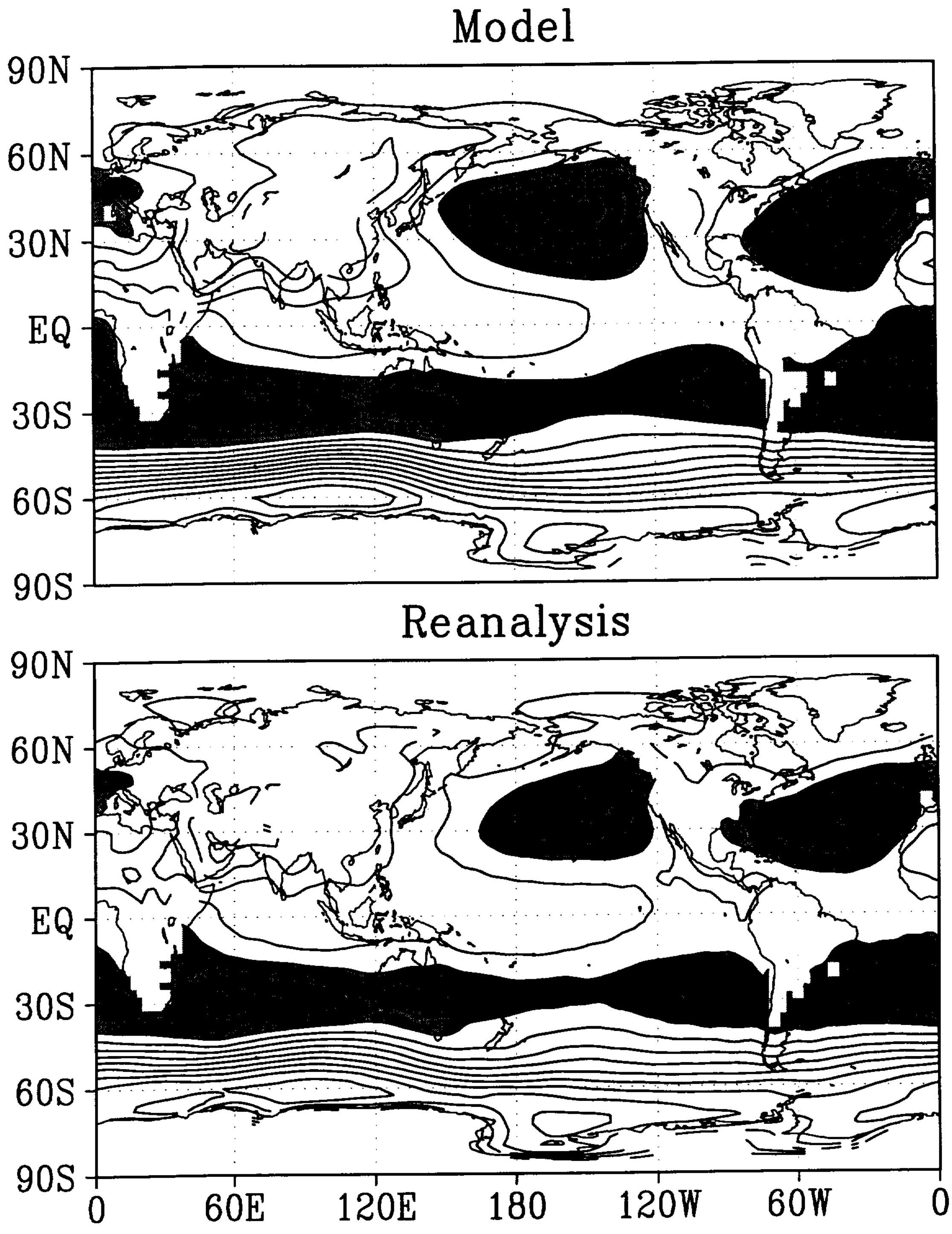

Figure 28: Sea-level pressure for JJA— Top: Model, Bottom: Reanalysis. Contour interval: 4 mb. Shading indicates pressures in excess of 1000 mb.

MAM $\overline{\text{SLP}}$

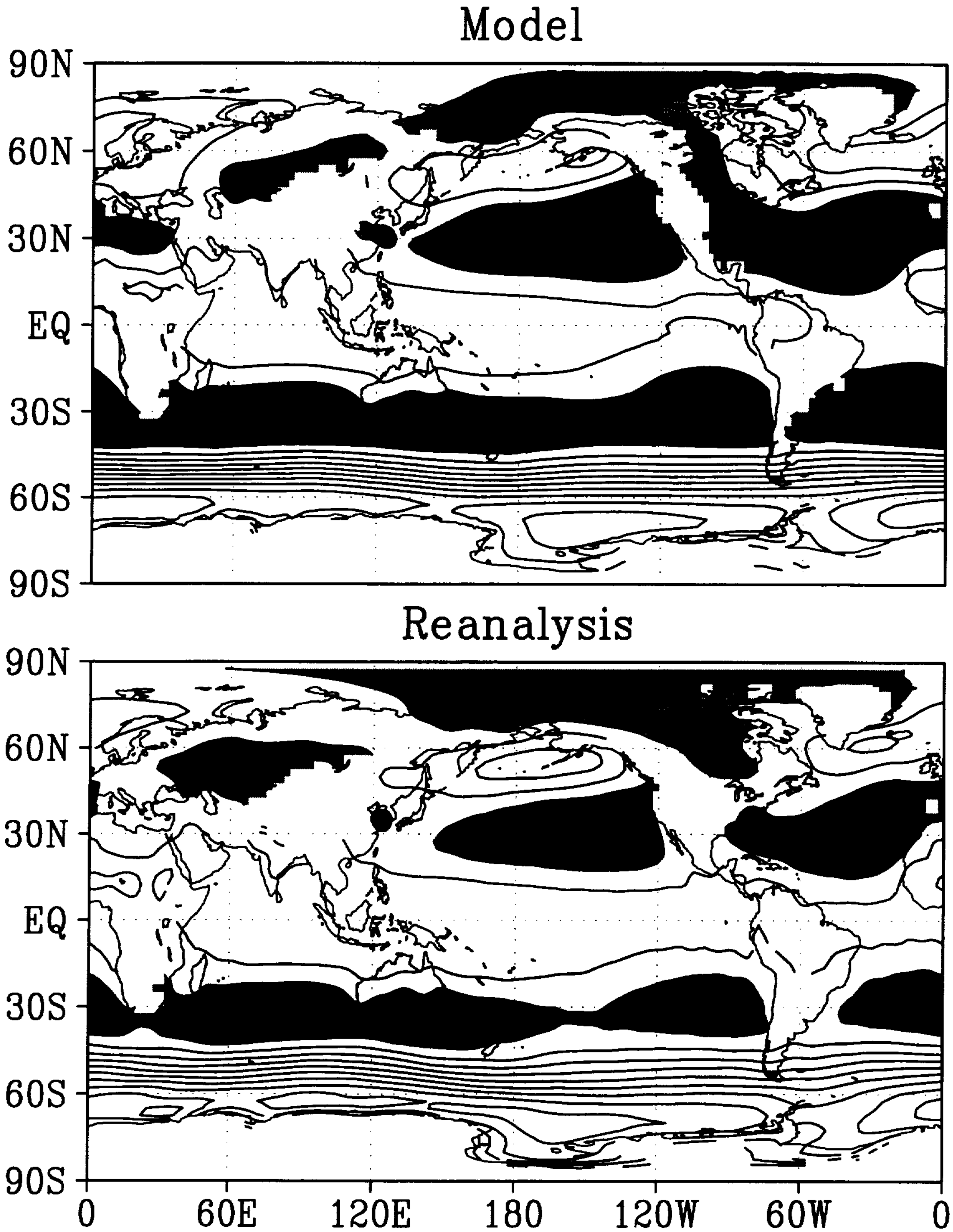

Figure 29: Sea-level pressure for MAM— Top: Model, Bottom: Reanalysis. Contour interval: 4 mb. Shading indicates pressures in excess of 1000 mb.

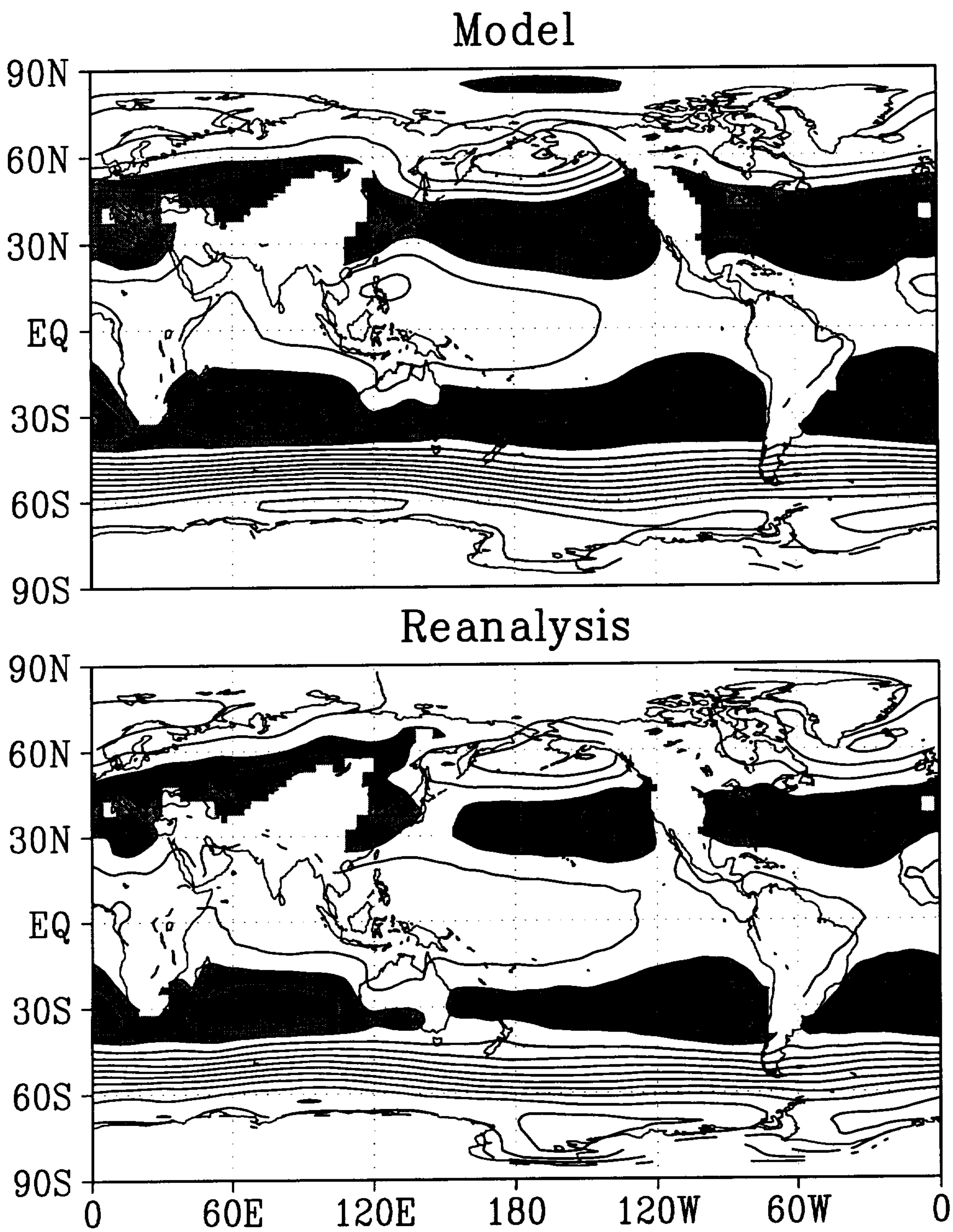

Figure 30: Sea-level pressure for SON— Top: Model, Bottom: Reanalysis. Contour interval: 4 mb. Shading indicates pressures in excess of 1000 mb.

DJF $\overline{Z^*}_{300}$

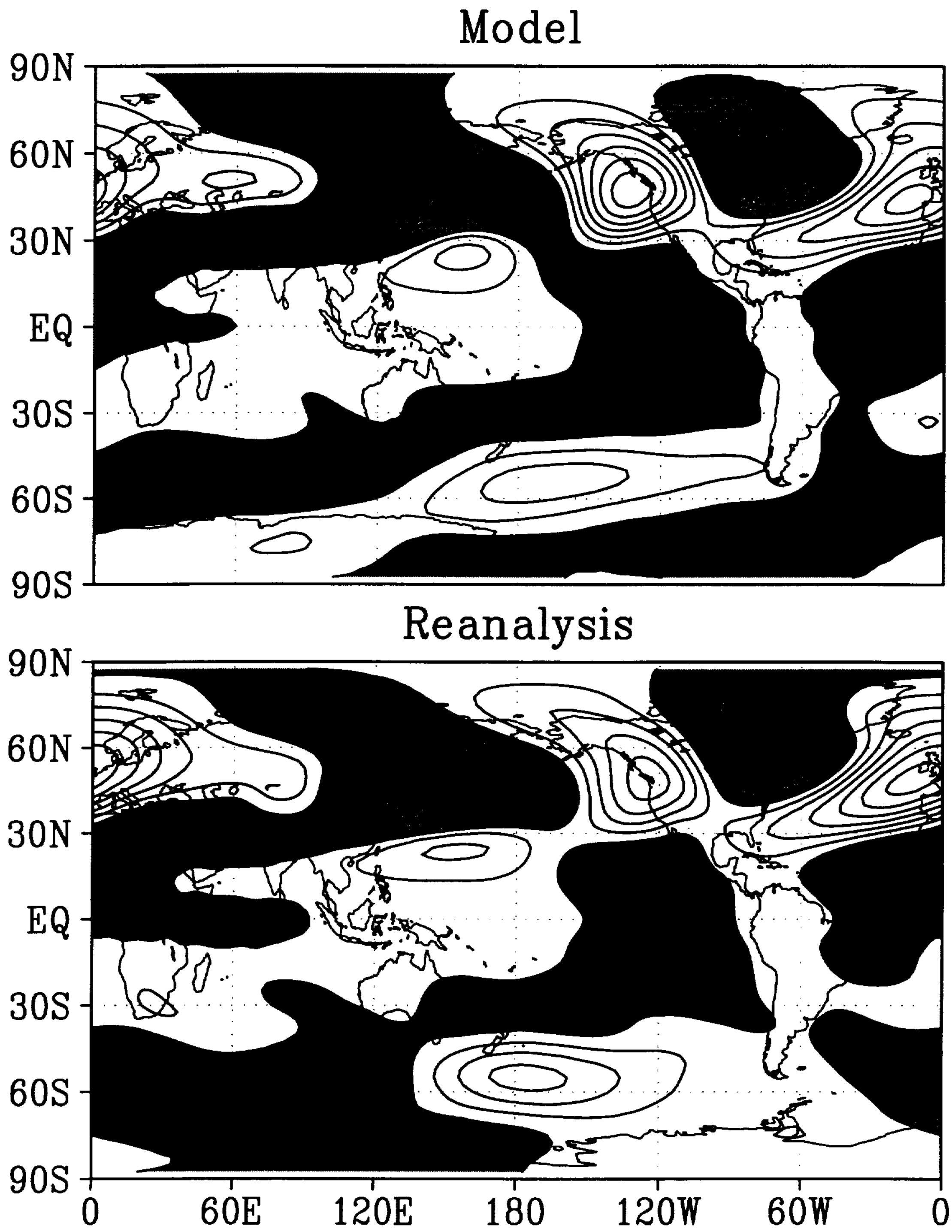

Figure 31: Eddy geopotential height at 300 mb for DJF— Top: Model, Bottom: Reanalysis. Contour interval: 40 m. Shading indicates negative values.

JJA $\overline{Z^*}_{300}$

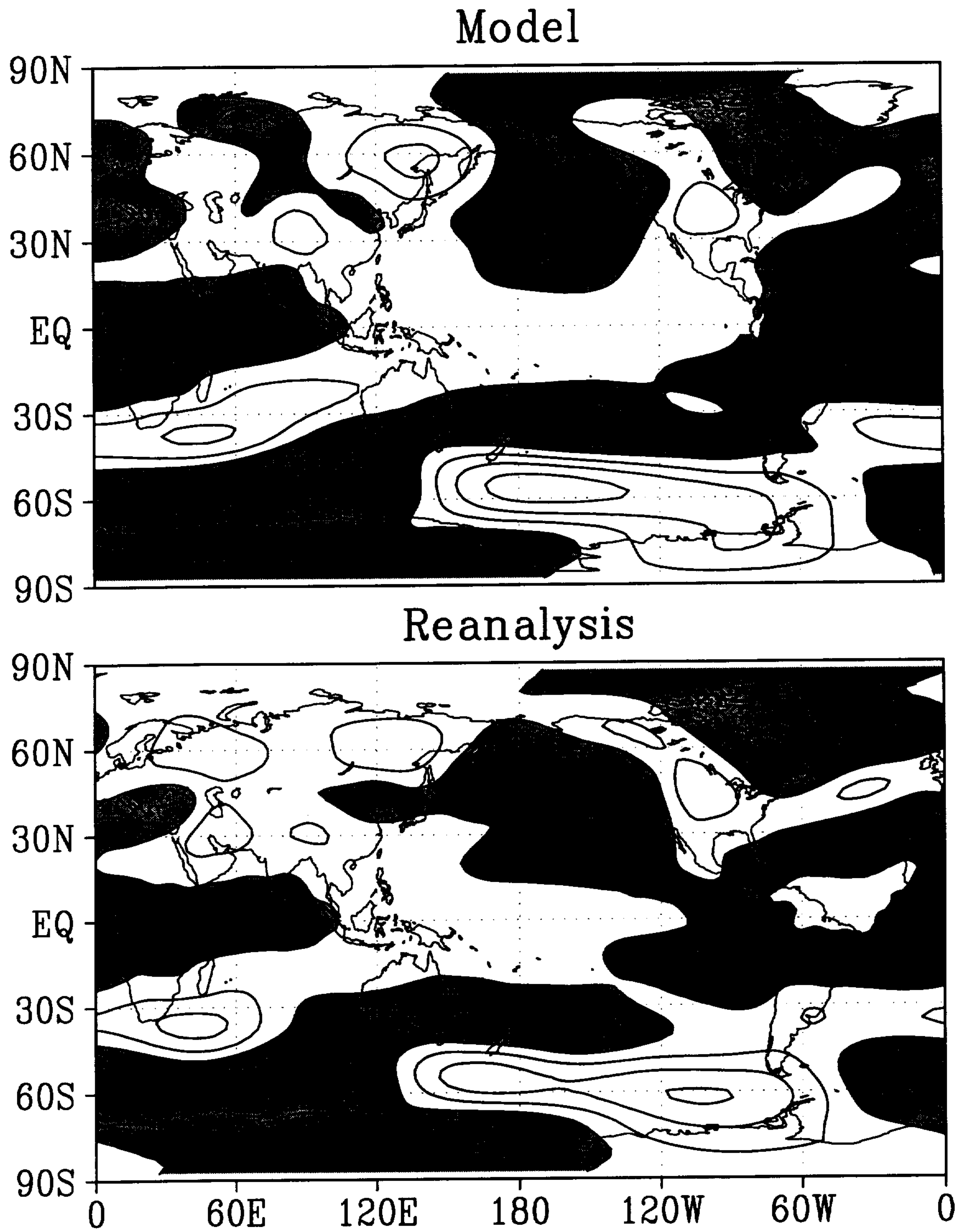

Figure 32: Eddy geopotential height at 300 mb for JJA— Top: Model, Bottom: Reanalysis. Contour interval: 40 m. Shading indicates negative values.

MAM $\overline{Z^*}_{300}$

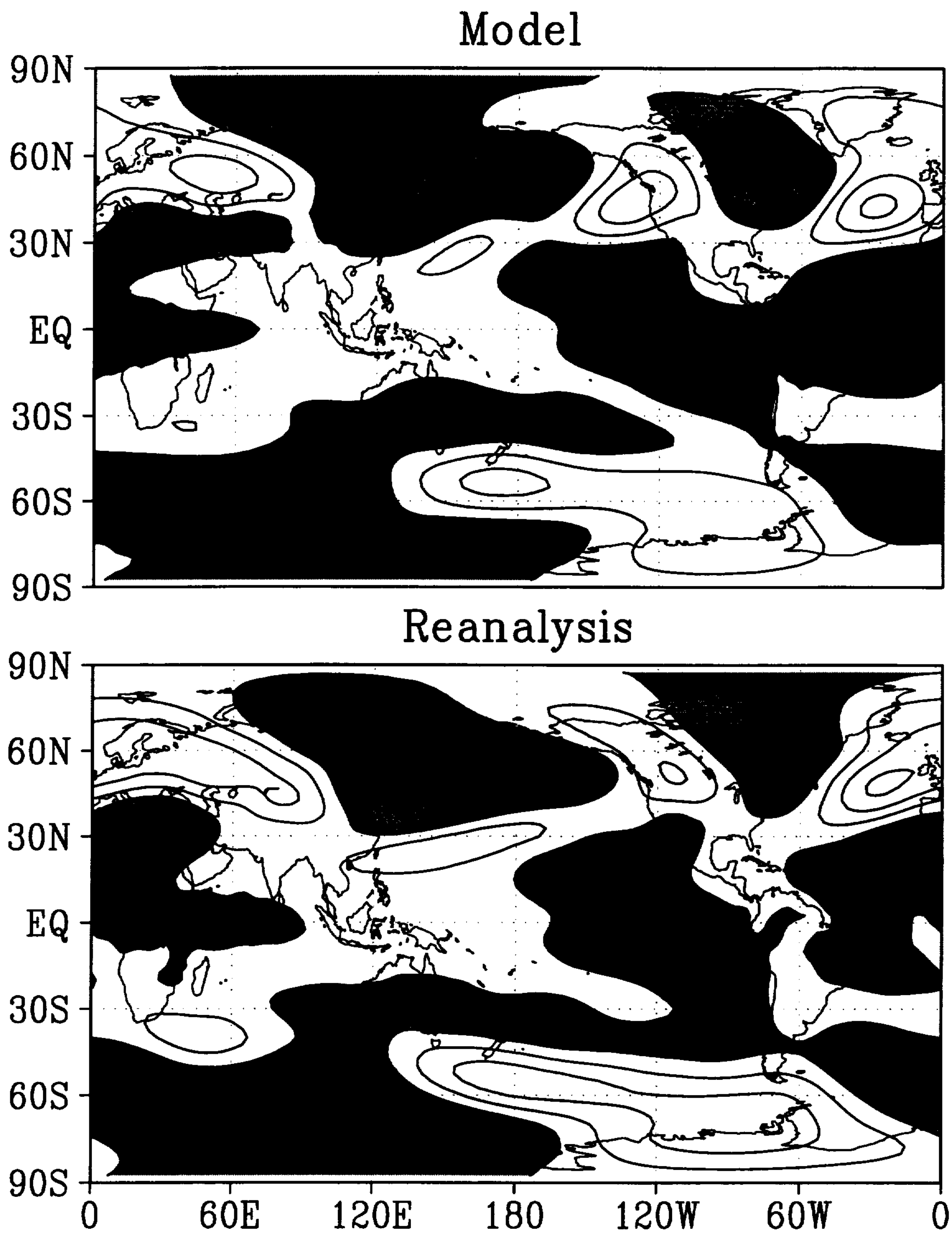

Figure 33: Eddy geopotential height at 300 mb for MAM— Top: Model, Bottom: Reanalysis. Contour interval: 40 m. Shading indicates negative values.

SON $\overline{Z^*}_{300}$

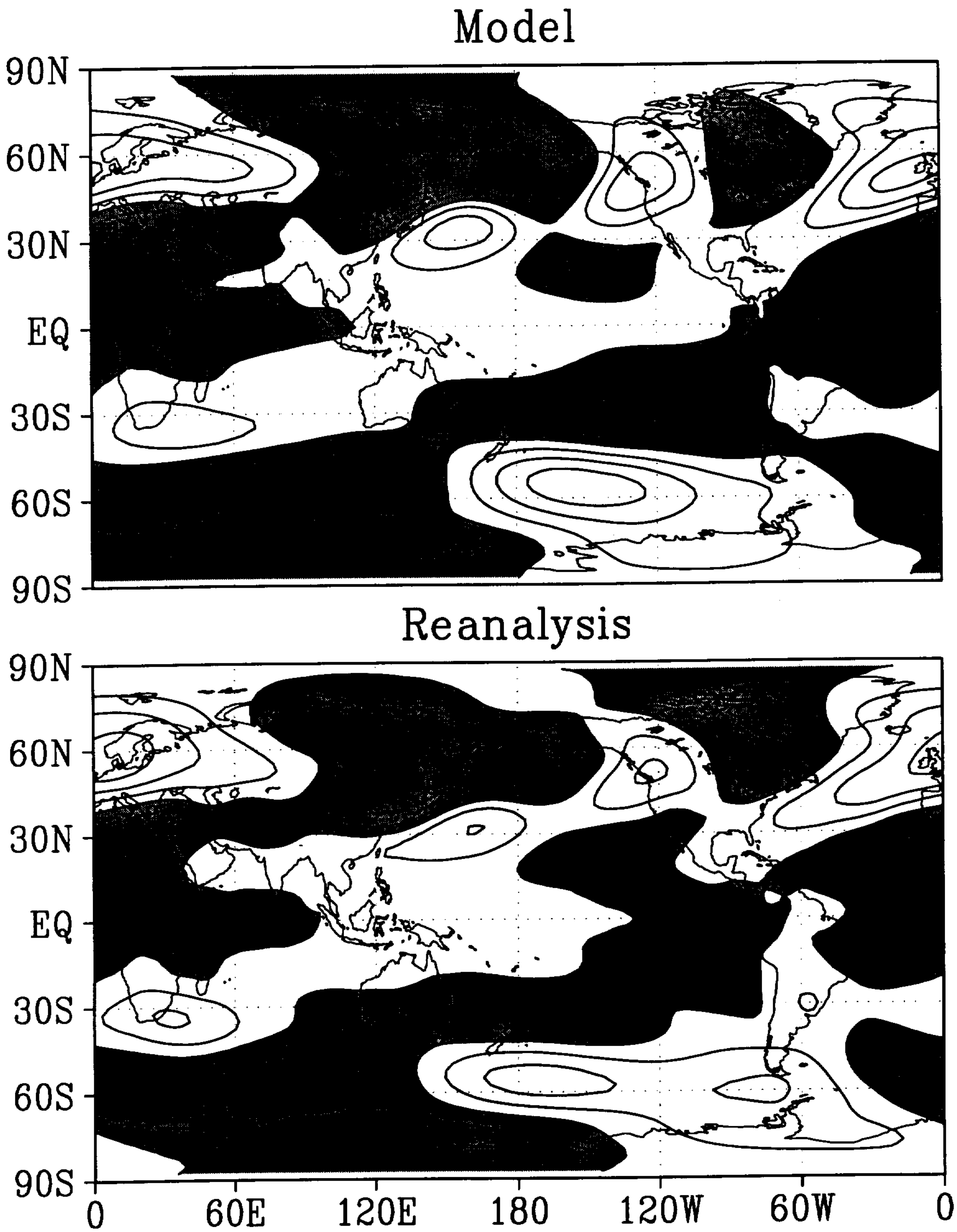

Figure 34: Eddy geopotential height at 300 mb for SON— Top: Model, Bottom: Reanalysis. Contour interval: 40 m. Shading indicates negative values.

DJF $\overline{\omega}_{500}$

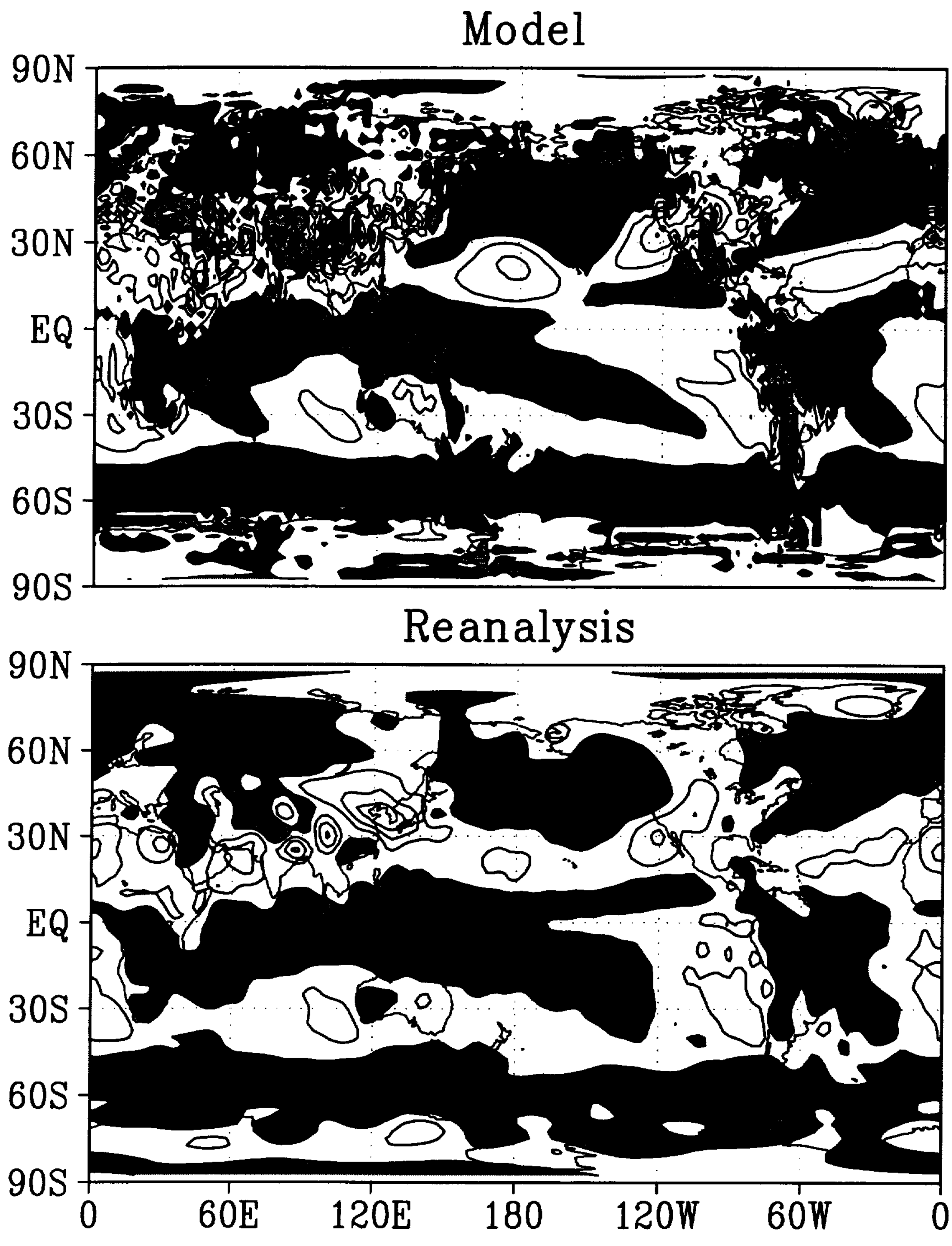

Figure 35: Omega at 500 mb (mb d^{-1}) for DJF— Top: Model, Bottom: Reanalysis. Contour interval: 4 mb d^{-1}. Shading indicates rising motion.

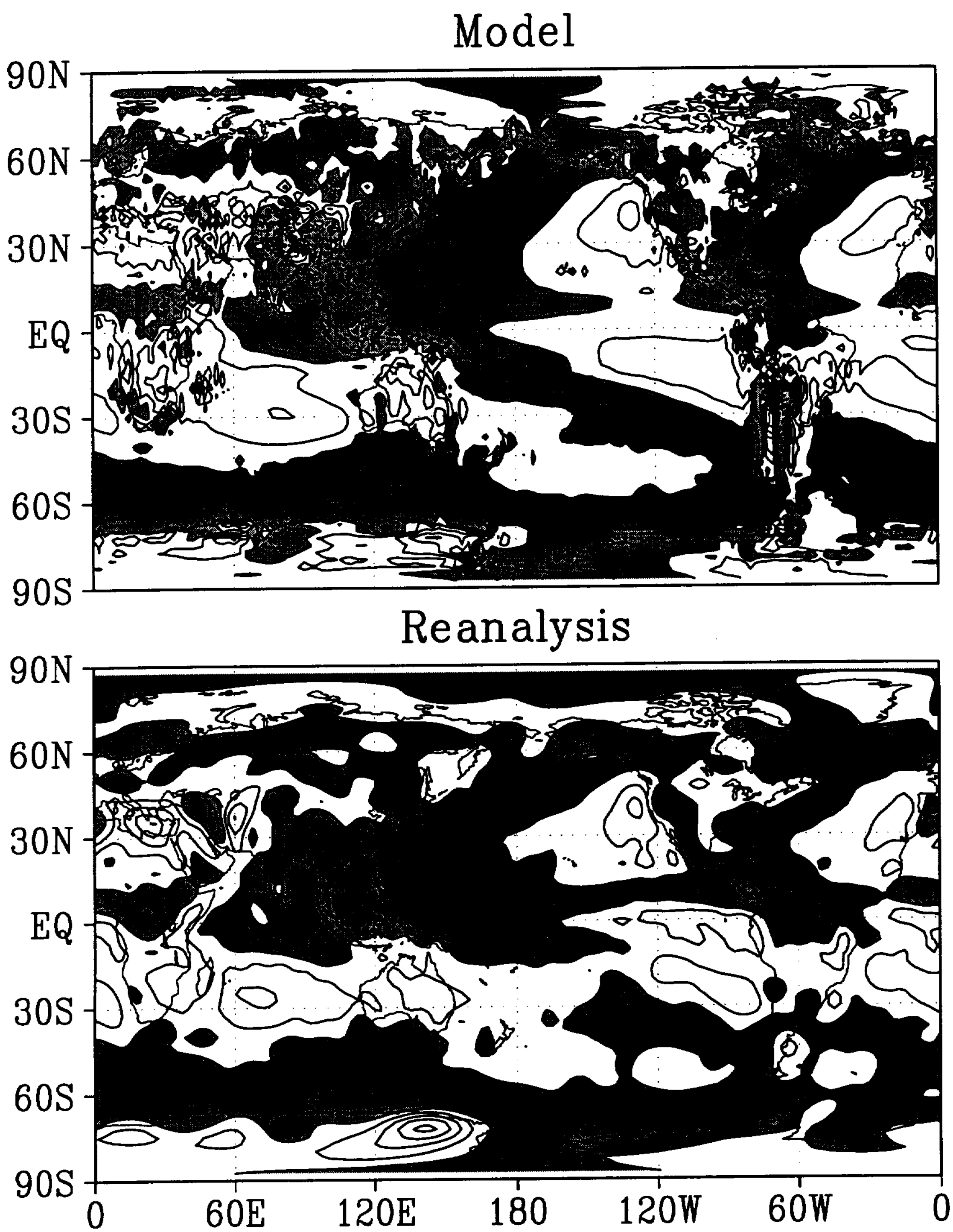

Figure 36: Omega at 500 mb (mb d^{-1}) for JJA— Top: Model, Bottom: Reanalysis. Contour interval: 4 mb d^{-1}. Shading indicates rising motion.

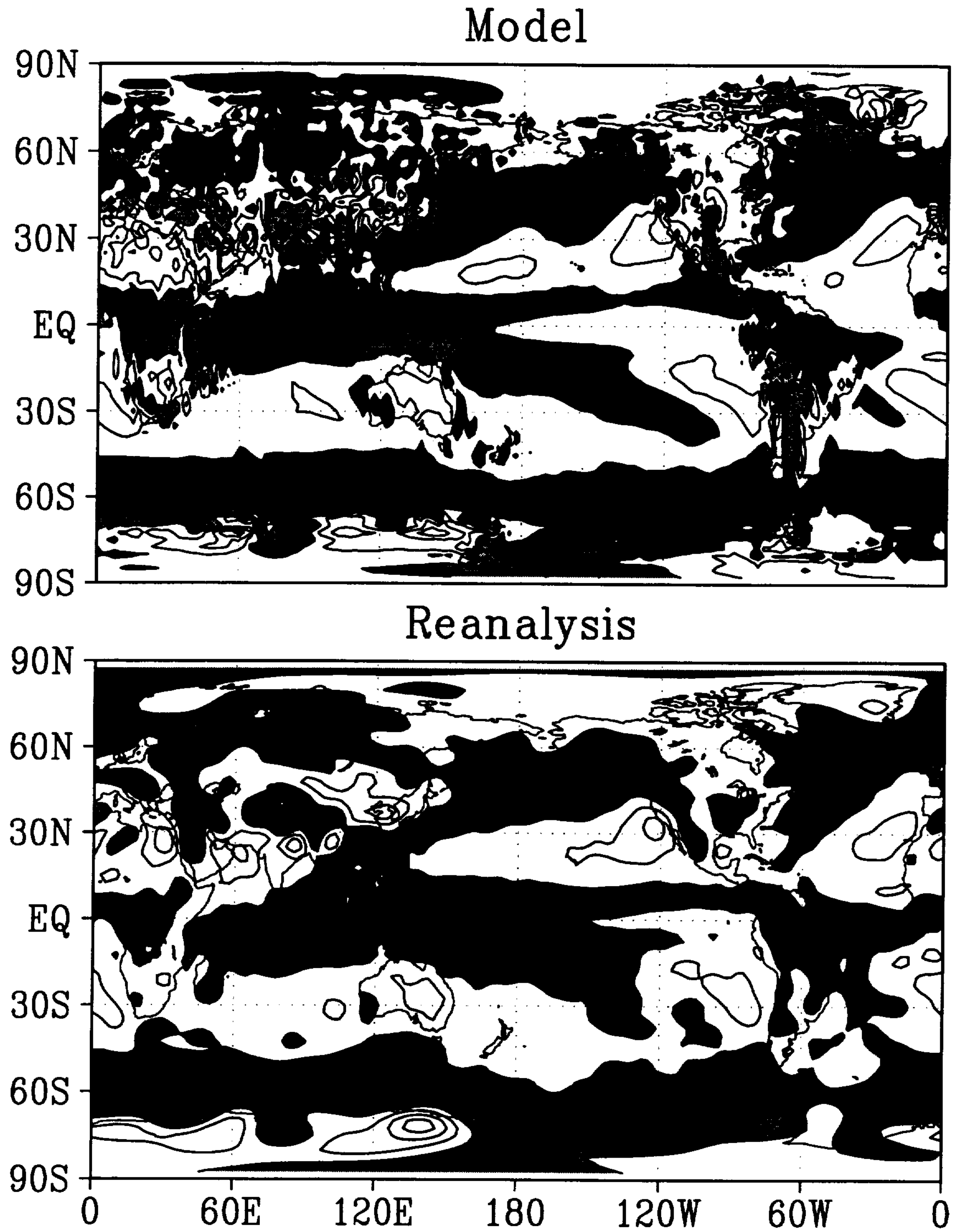

Figure 37: Omega at 500 mb (mb d^{-1}) for MAM— Top: Model, Bottom: Reanalysis. Contour interval: 4 mb d^{-1}. Shading indicates rising motion.

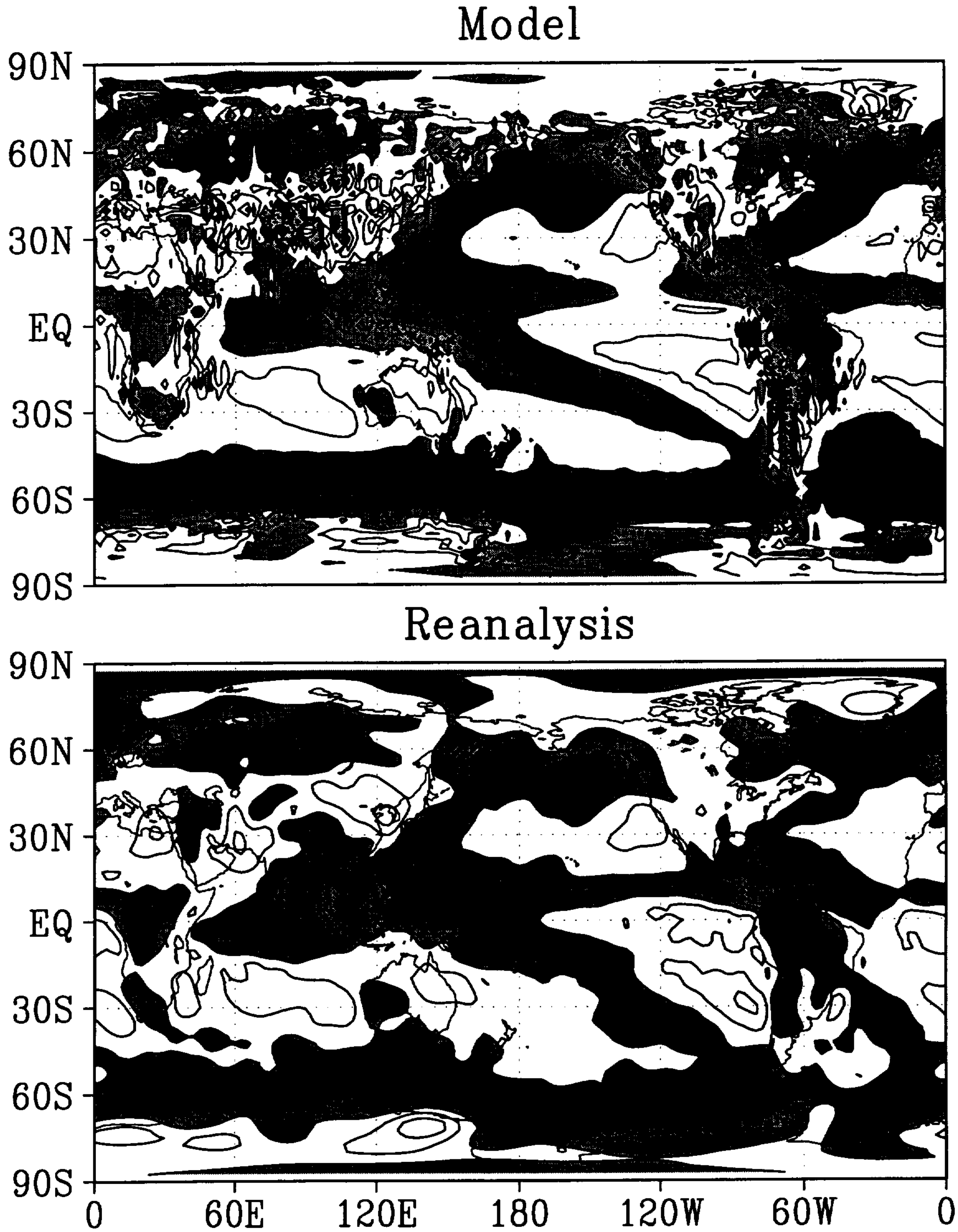

Figure 38: Omega at 500 mb (mb d^{-1}) for SON— Top: Model, Bottom: Reanalysis. Contour interval: 4 mb d^{-1}. Shading indicates rising motion.

DJF $\overline{\psi^*}_{200}$

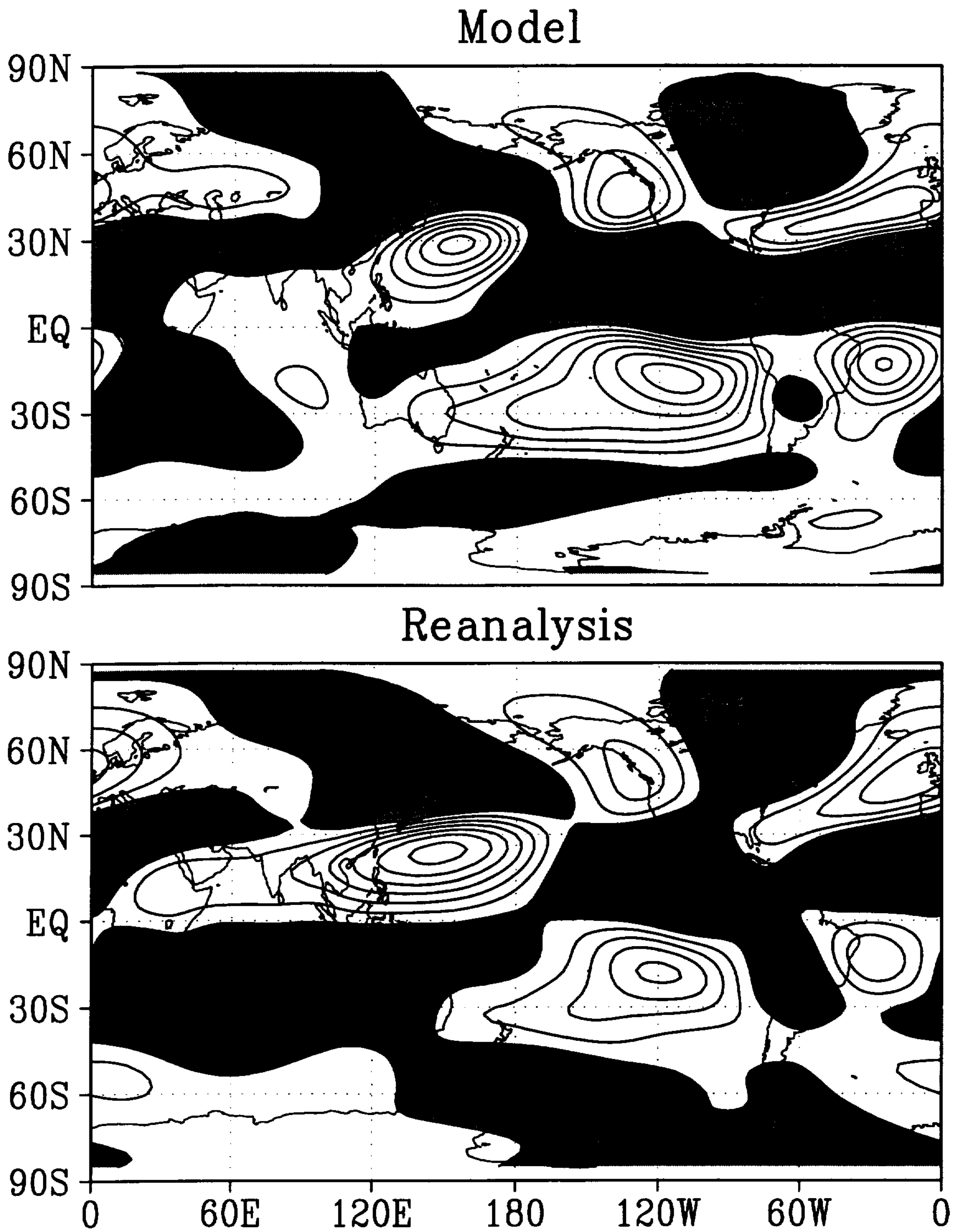

Figure 39: Eddy stream function at 200 mb for DJF— Top: Model, Bottom: Reanalysis. Contour interval: 5 $\times 10^6$ m^2 s^{-1}. Shading indicates negative values.

JJA $\overline{\psi^*}_{200}$

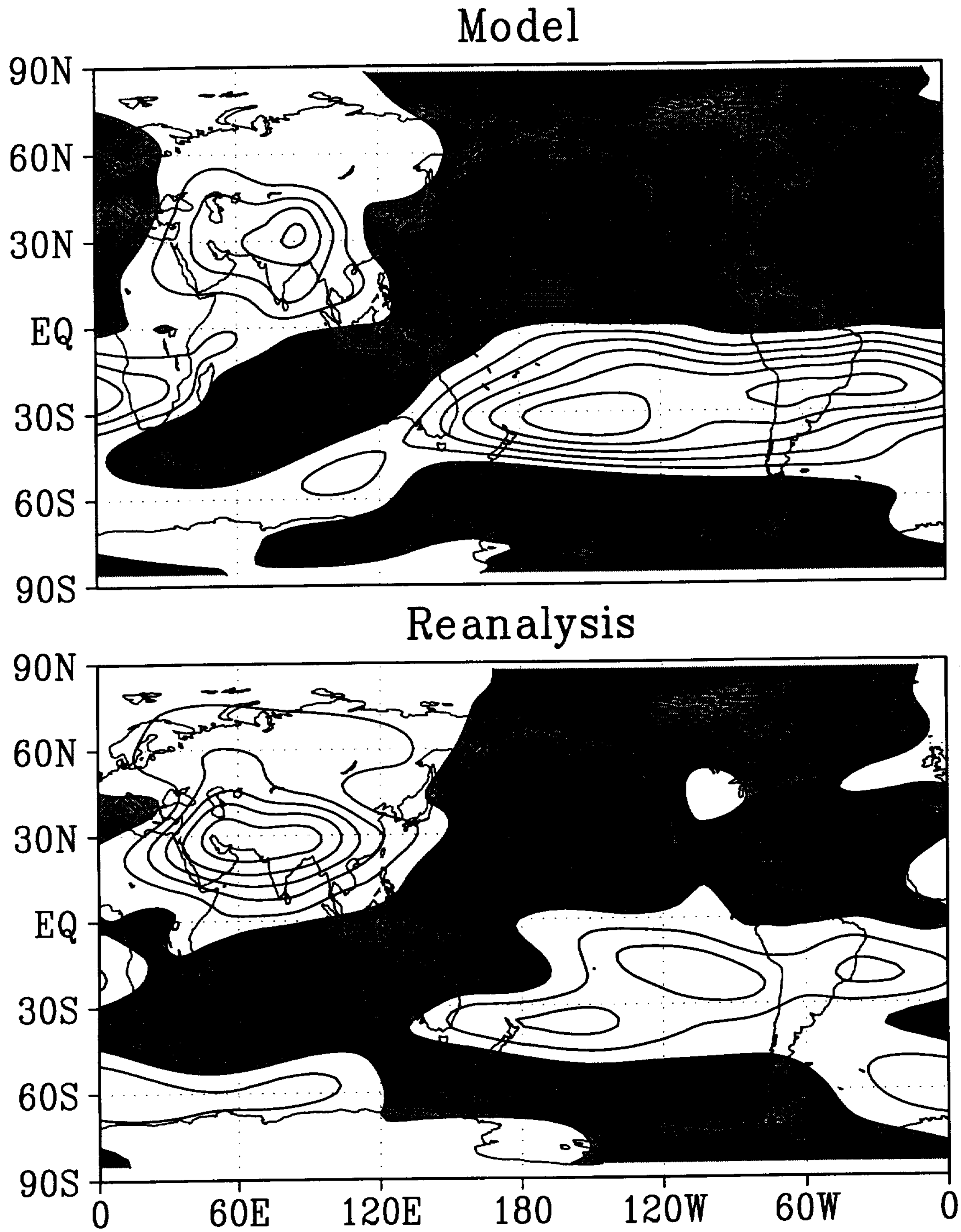

Figure 40: Eddy stream function at 200 mb for JJA— Top: Model, Bottom: Reanalysis. Contour interval: 5×10^6 m^2 s^{-1}. Shading indicates negative values.

MAM $\overline{\psi^*}_{200}$

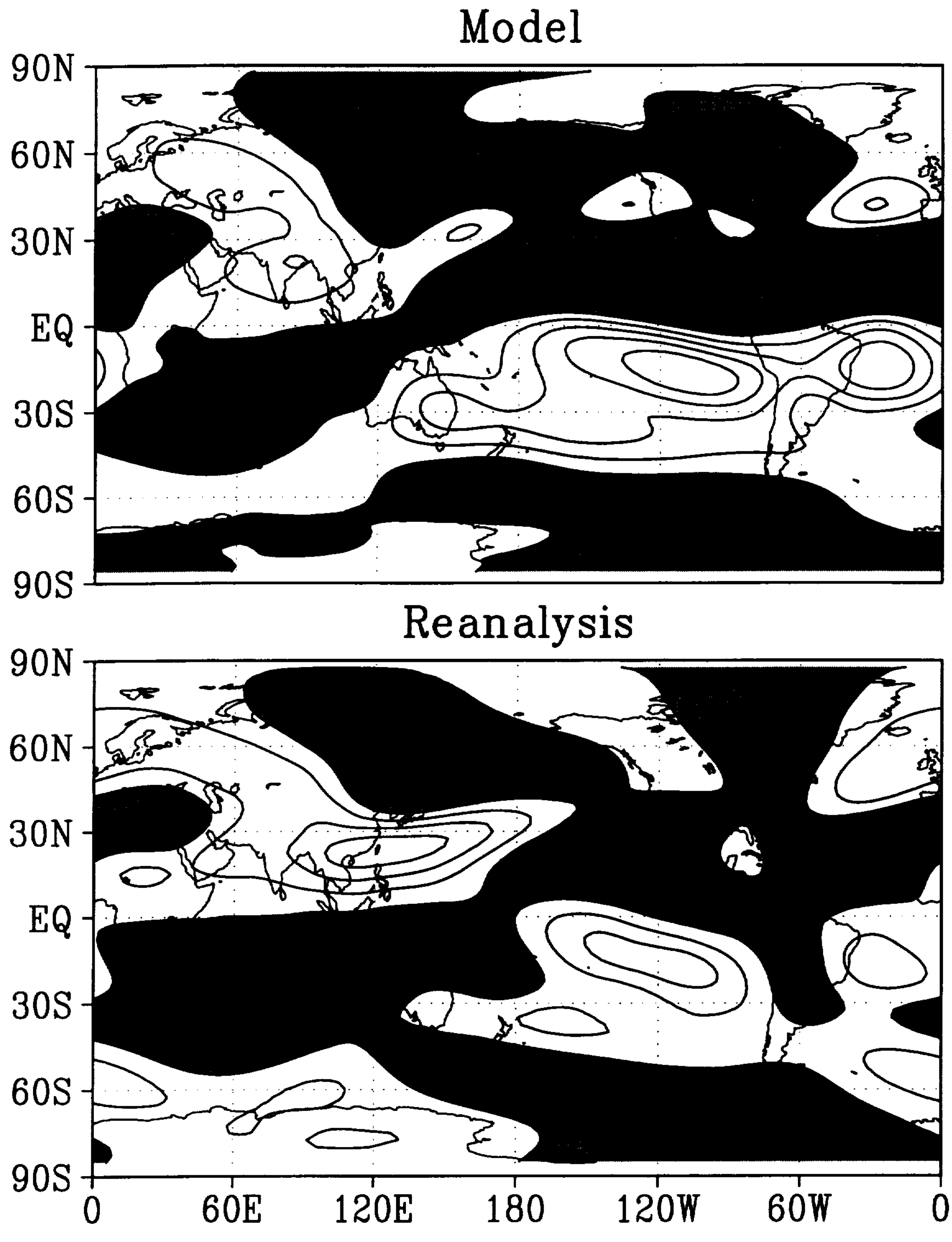

Figure 41: Eddy stream function at 200 mb for MAM— Top: Model, Bottom: Reanalysis. Contour interval: 5 $\times 10^6$ m^2 s^{-1}. Shading indicates negative values.

SON $\overline{\psi^*}_{200}$

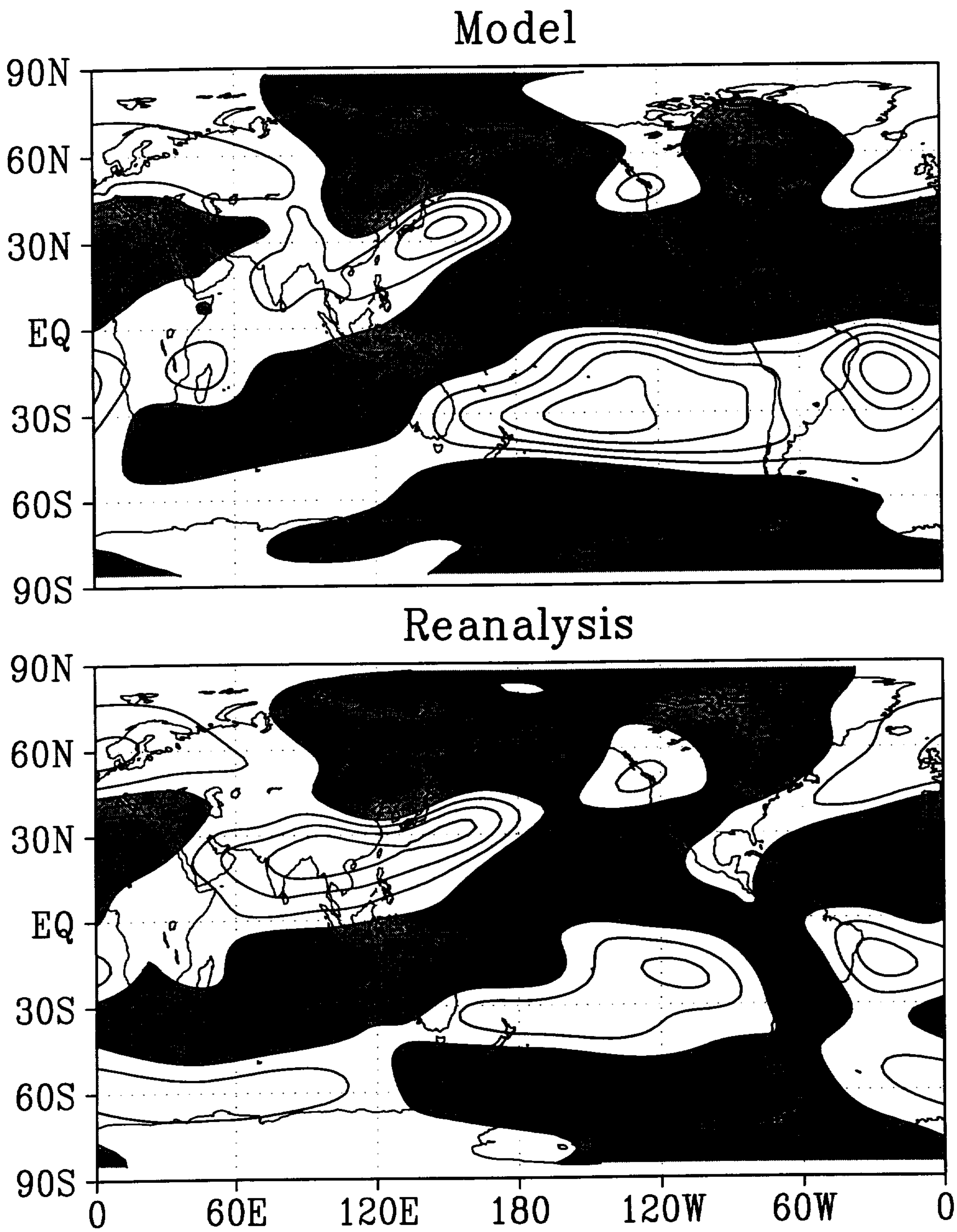

Figure 42: Eddy stream function at 200 mb for SON— Top: Model, Bottom: Reanalysis. Contour interval: 5 $\times 10^6$ m^2 s^{-1}. Shading indicates negative values.

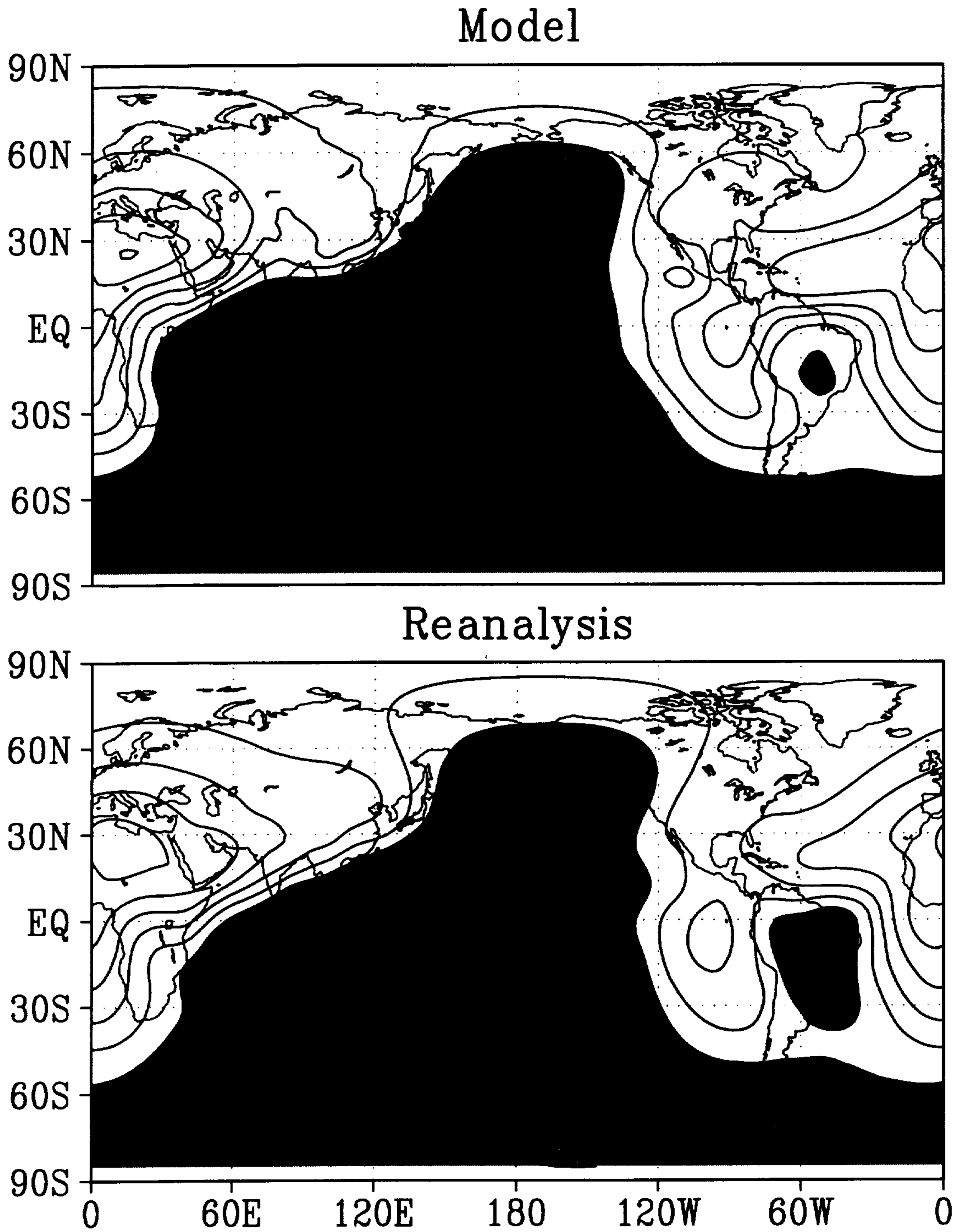

Figure 43: Velocity potential at 200 mb for DJF— Top: Model, Bottom: Reanalysis. Contour interval: 5 $\times 10^6$ m^2 s^{-1}. Shading indicates negative values.

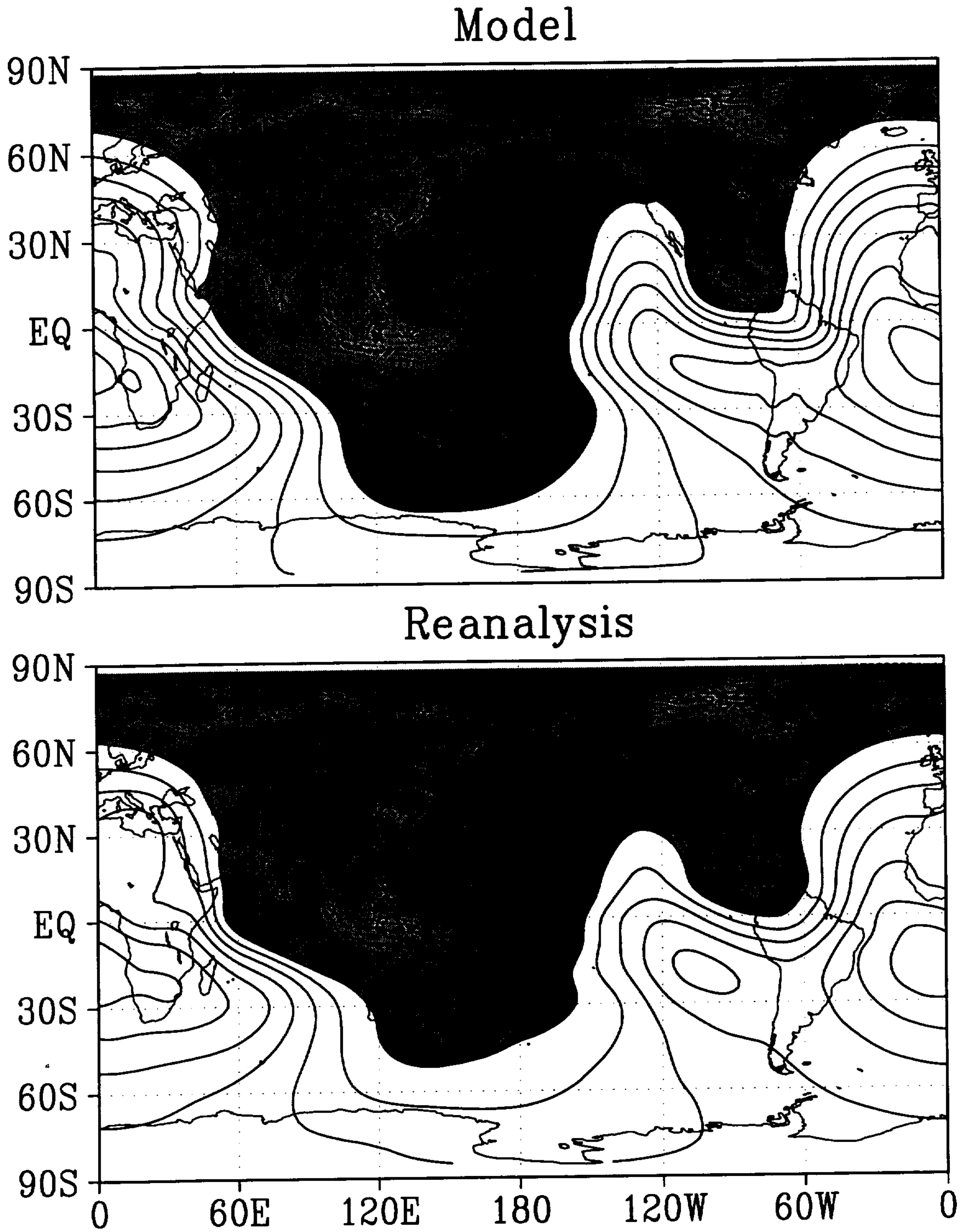

Figure 44: Velocity potential at 200 mb for JJA— Top: Model, Bottom: Reanalysis. Contour interval: 5 $\times 10^6$ m^2 s^{-1}. Shading indicates negative values.

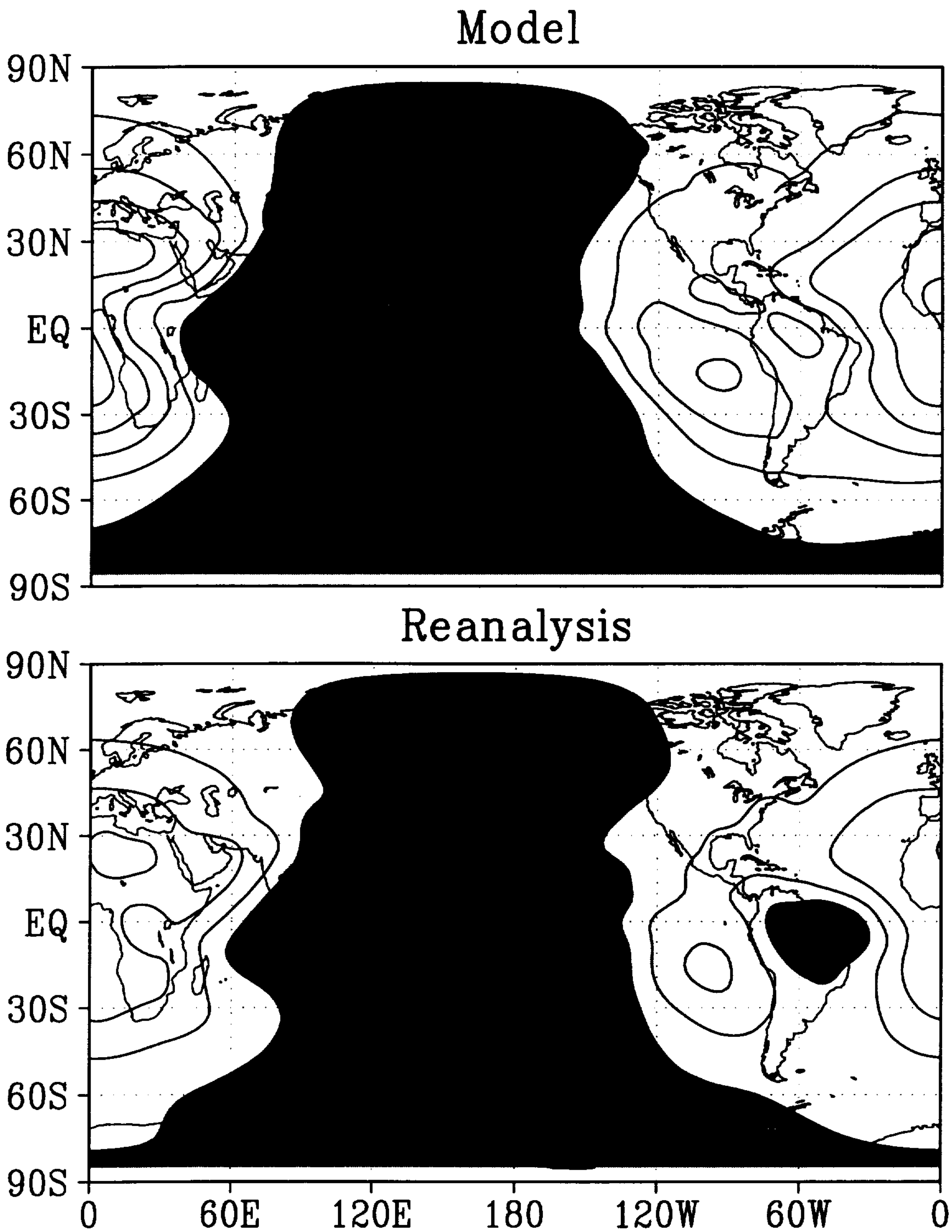

Figure 45: Velocity potential at 200 mb for MAM— Top: Model, Bottom: Reanalysis. Contour interval: 5 $\times 10^6$ m^2 s^{-1}. Shading indicates negative values.

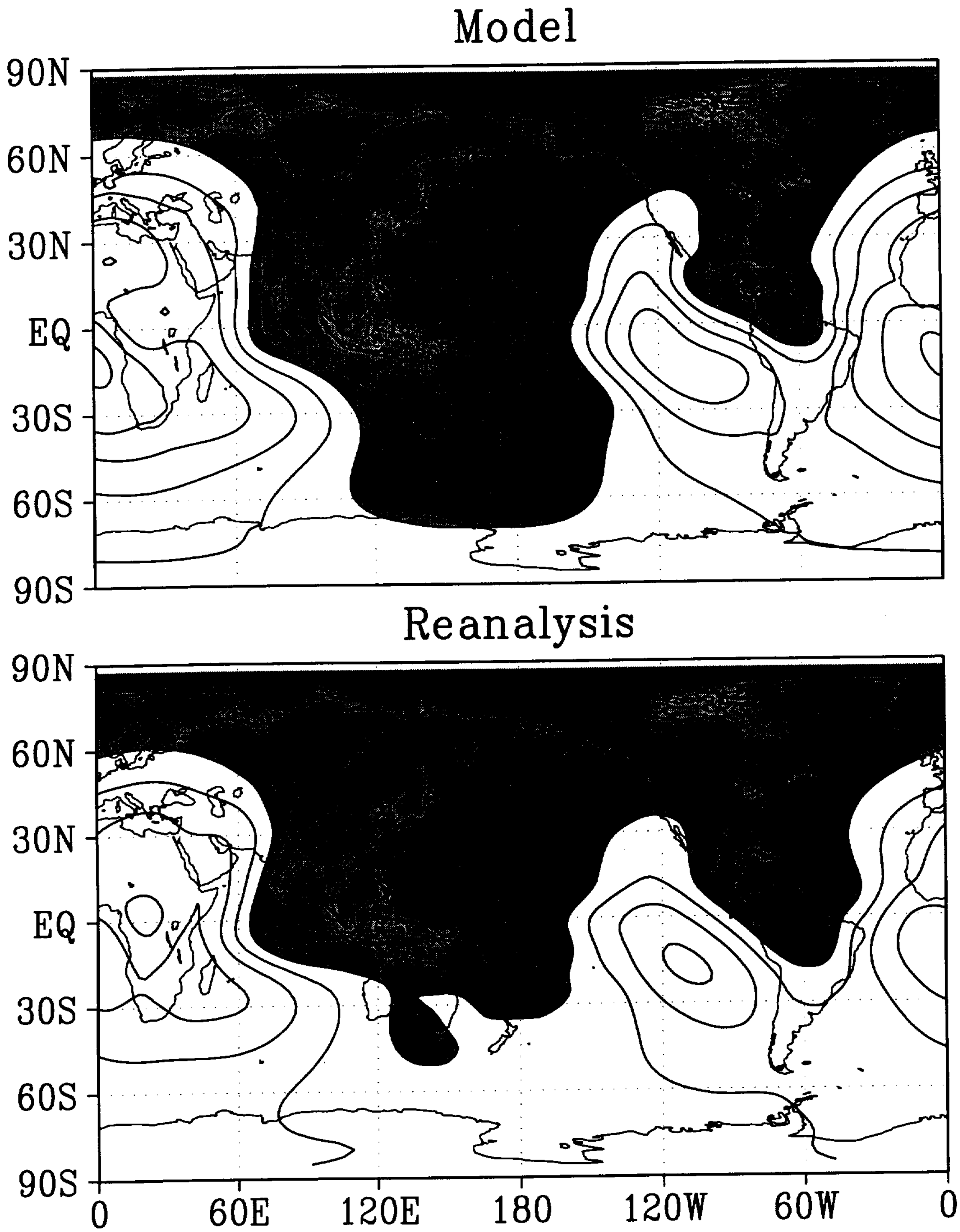

Figure 46: Velocity potential at 200 mb for SON— Top: Model, Bottom: Reanalysis. Contour interval: 5 $\times 10^6$ m^2 s^{-1}. Shading indicates negative values.

$[\overline{\mathrm{SLP}}]$

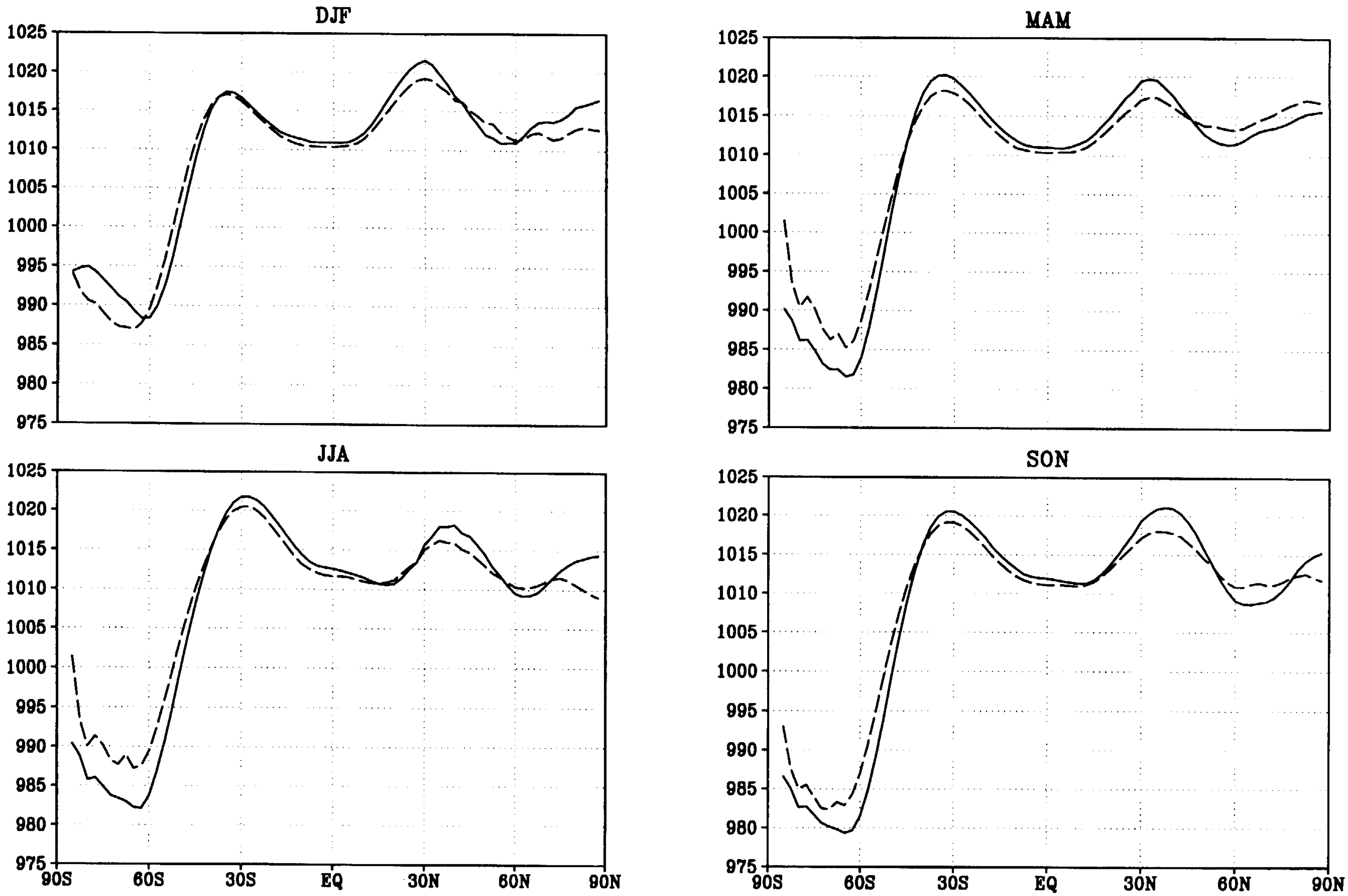

Figure 47: Zonal mean sea-level pressure (mb) Solid: Model, Dashed:Reanalysis.

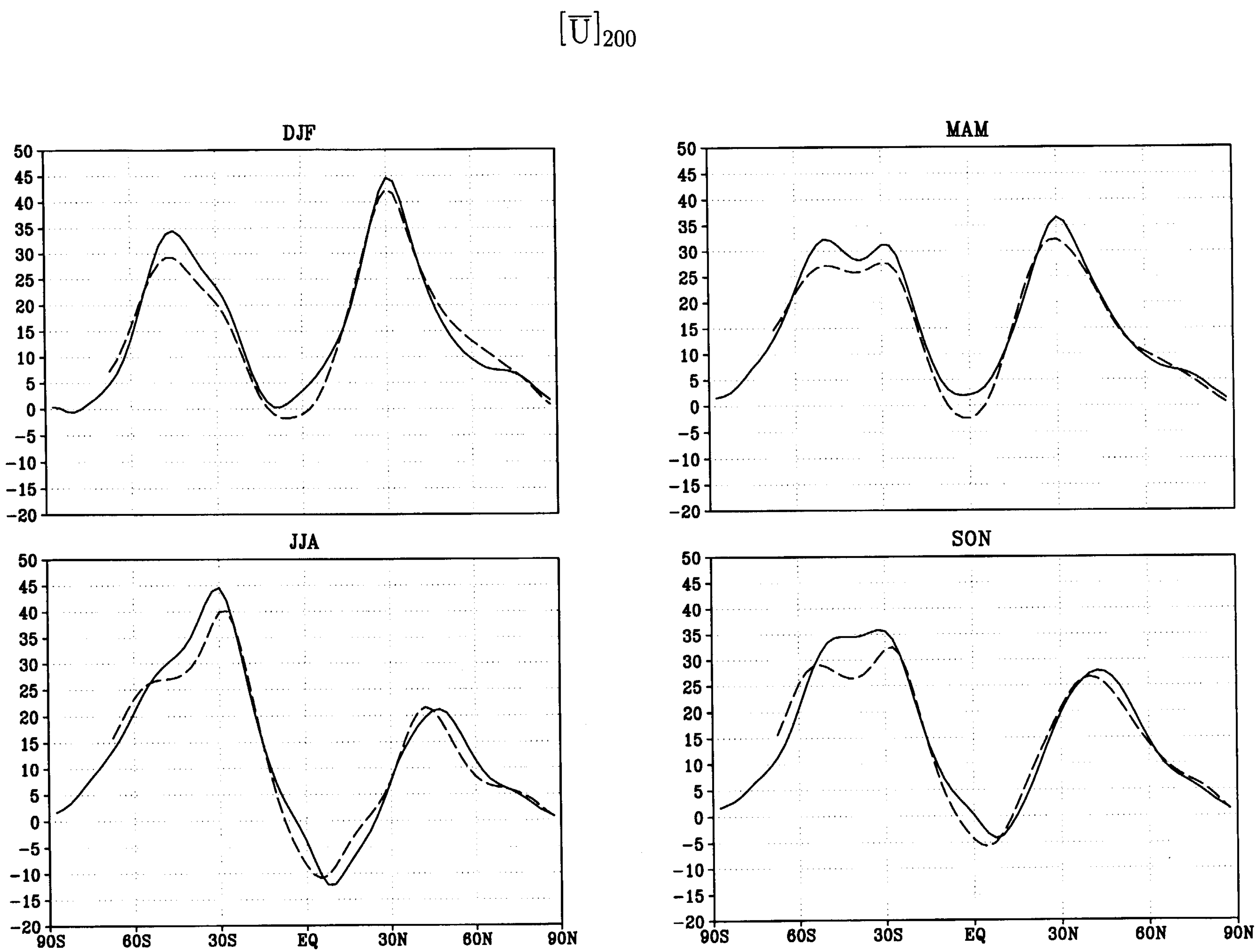

Figure 48: Zonal mean zonal wind at 200 mb (m s^{-1}) Solid: Model, Dashed:Reanalysis.

$[\overline{\mathrm{U}}]_{850}$

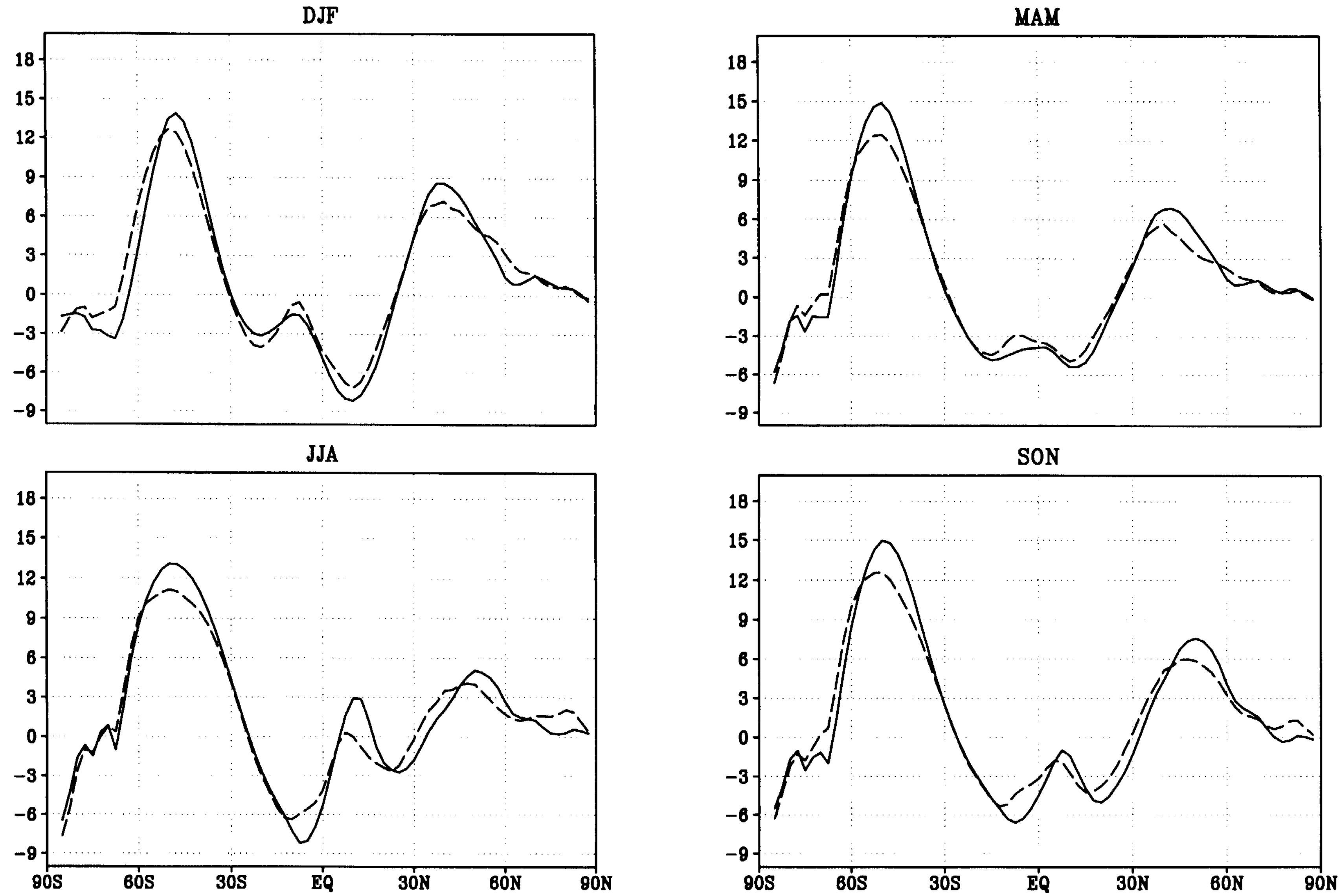

Figure 49: Zonal mean zonal wind at 850 mb (m s^{-1}) Solid: Model, Dashed:Reanalysis.

ZONAL MEAN STATISTICS

(DJF, MAM, JJA, SON)

$$\sqrt{[\overline{(u')^2}]} \quad \text{and} \quad \sqrt{[(\overline{u}^*)^2]}$$

$$\sqrt{[\overline{(v')^2}]} \quad \text{and} \quad \sqrt{[(\overline{v}^*)^2]}$$

$$\tfrac{1}{2}[\overline{(u')^2} + \overline{(v')^2}] \quad \text{and} \quad \tfrac{1}{2}[(\overline{u}^*)^2 + (\overline{v}^*)^2]$$

$$\sqrt{[\overline{(\omega')^2}]} \quad \text{and} \quad \sqrt{[(\overline{\omega}^*)^2]}$$

$$\sqrt{[\overline{(T')^2}]} \quad \text{and} \quad \sqrt{[(\overline{T}^*)^2]}$$

$$\sqrt{[\overline{(Z')^2}]} \quad \text{and} \quad \sqrt{[(\overline{Z}^*)^2]}$$

$$[\overline{u'v'}] \quad \text{and} \quad [\overline{u}^*\overline{v}^*]$$

$$[\overline{v'T'}] \quad \text{and} \quad [\overline{v}^*\overline{T}^*]$$

$$[\overline{\omega'T'}] \quad \text{and} \quad [\overline{\omega}^*\overline{T}^*]$$

$$[\overline{v'q'}] \quad \text{and} \quad [\overline{v}^*\overline{q}^*]$$

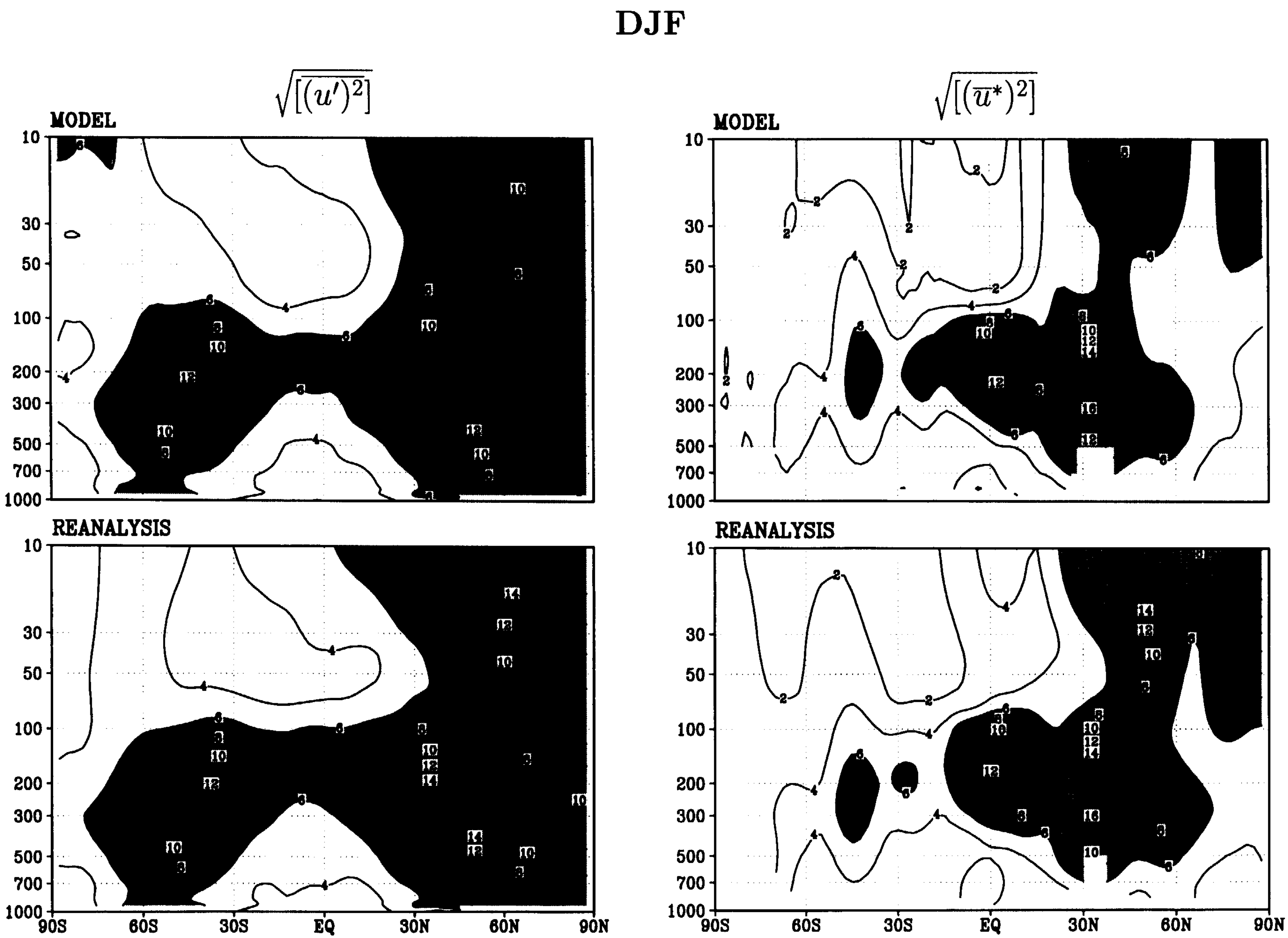

Figure 50: Zonal mean eddy standard deviation of u (m s^{-1}) for DJF— Upper panels: Model; Lower panels: Reanalysis; Left panels: Transients; Right panels: Stationary.

JJA

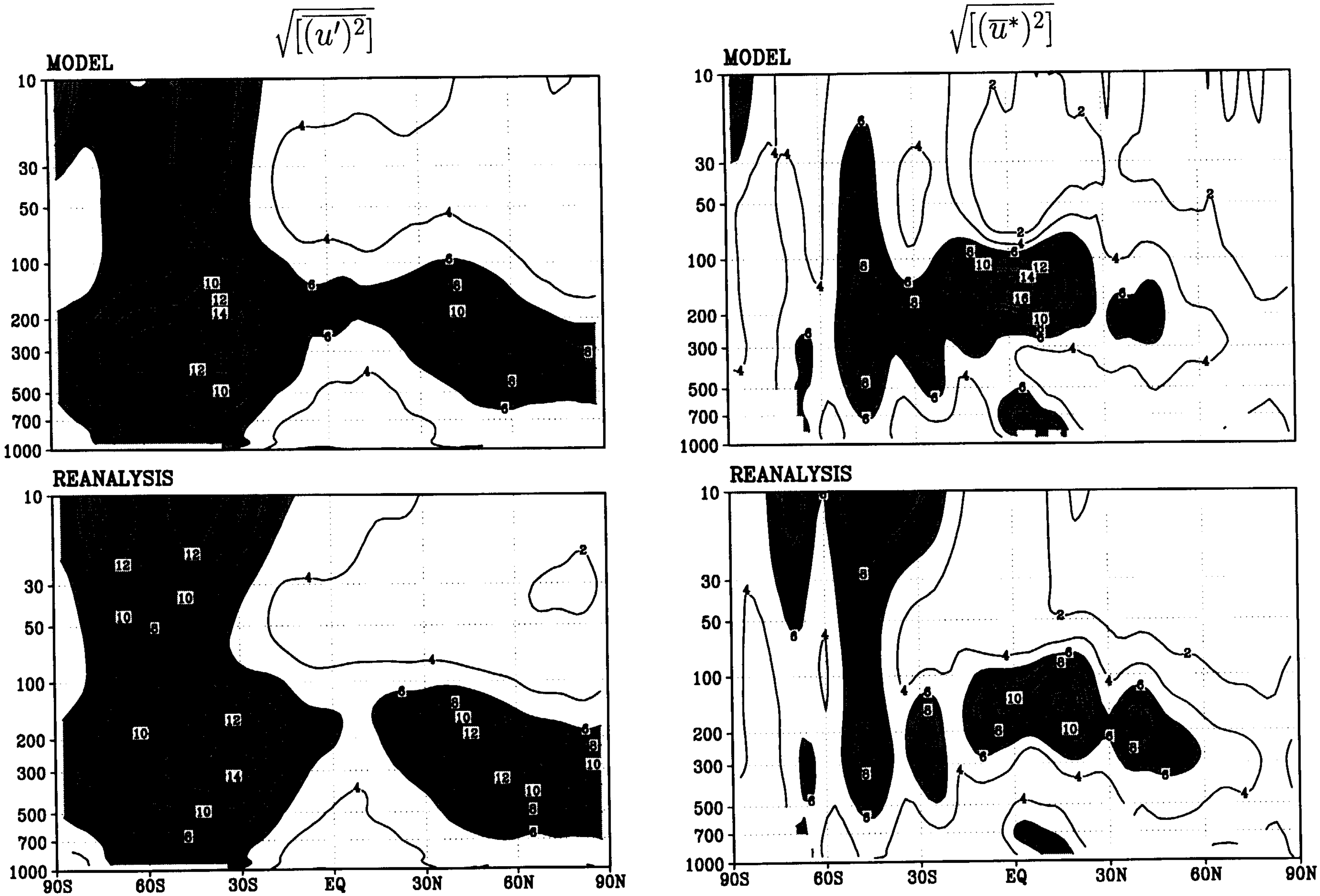

Figure 51: Zonal mean eddy standard deviation of u (m s^{-1}) for JJA— Upper panels: Model; Lower panels: Reanalysis; Left panels: Transients; Right panels: Stationary.

MAM

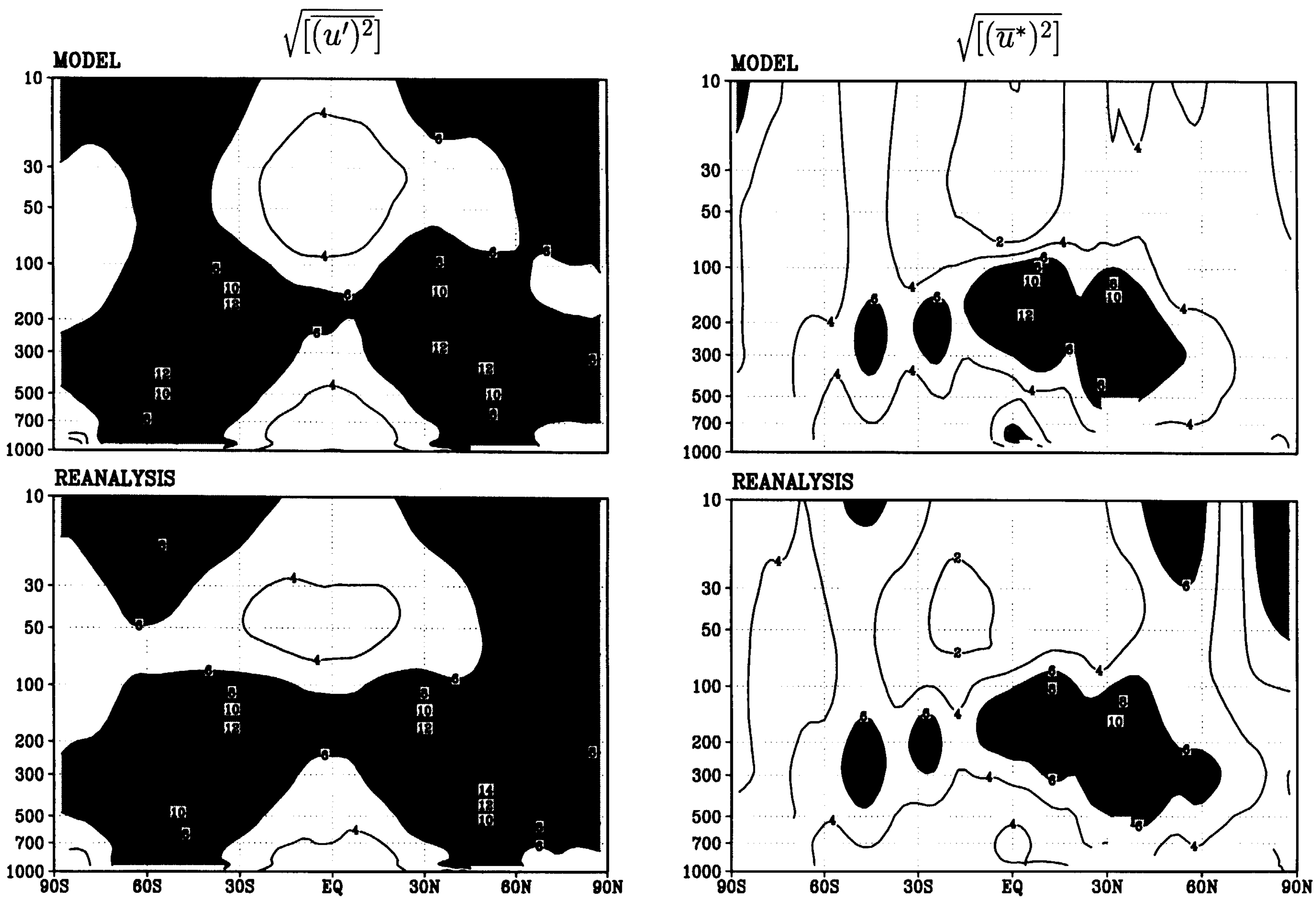

Figure 52: Zonal mean eddy standard deviation of u (m s^{-1}) for MAM— Upper panels: Model; Lower panels: Reanalysis; Left panels: Transients; Right panels: Stationary.

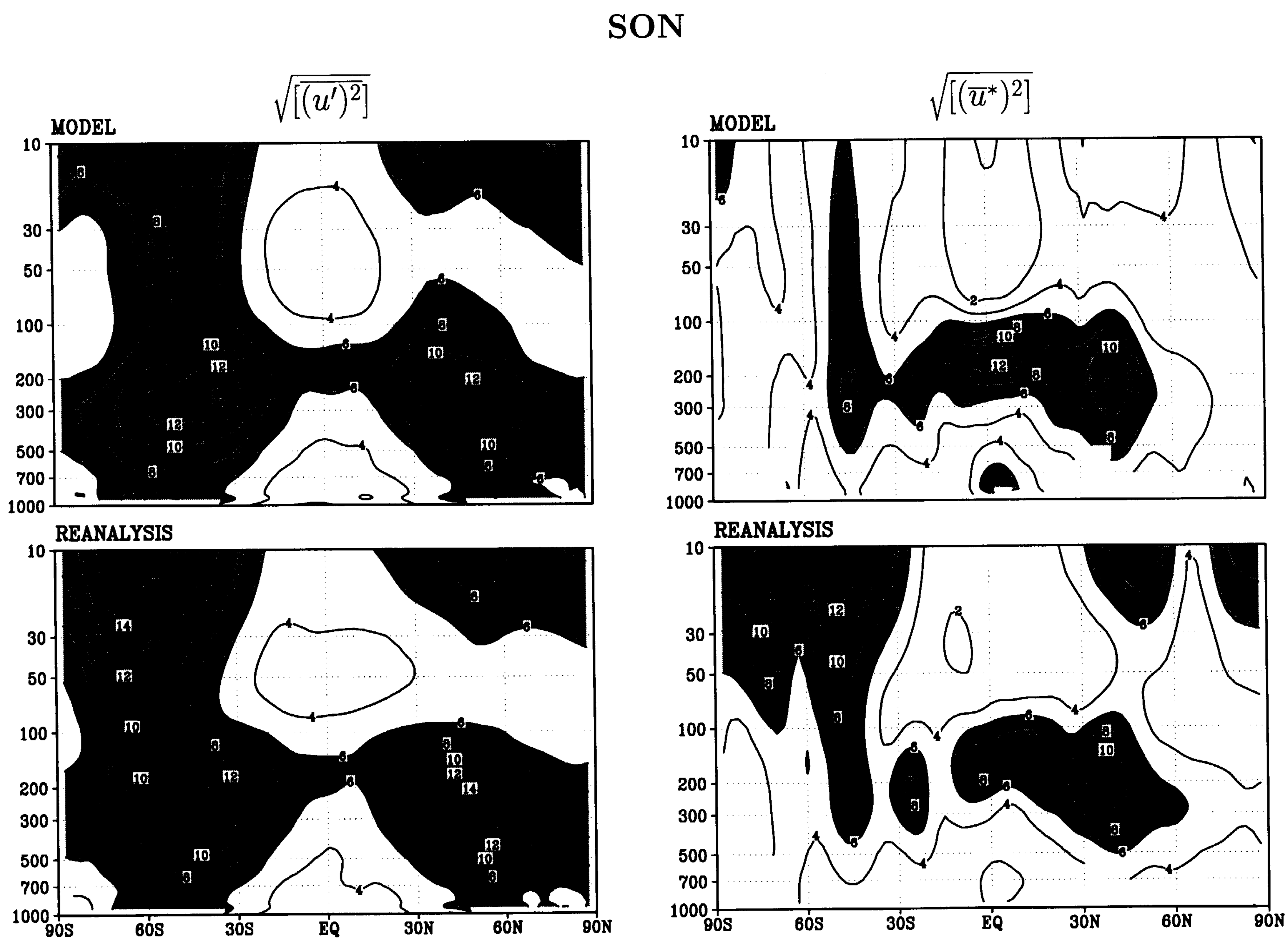

Figure 53: Zonal mean eddy standard deviation of u (m s^{-1}) for SON— Upper panels: Model; Lower panels: Reanalysis; Left panels: Transients; Right panels: Stationary.

DJF

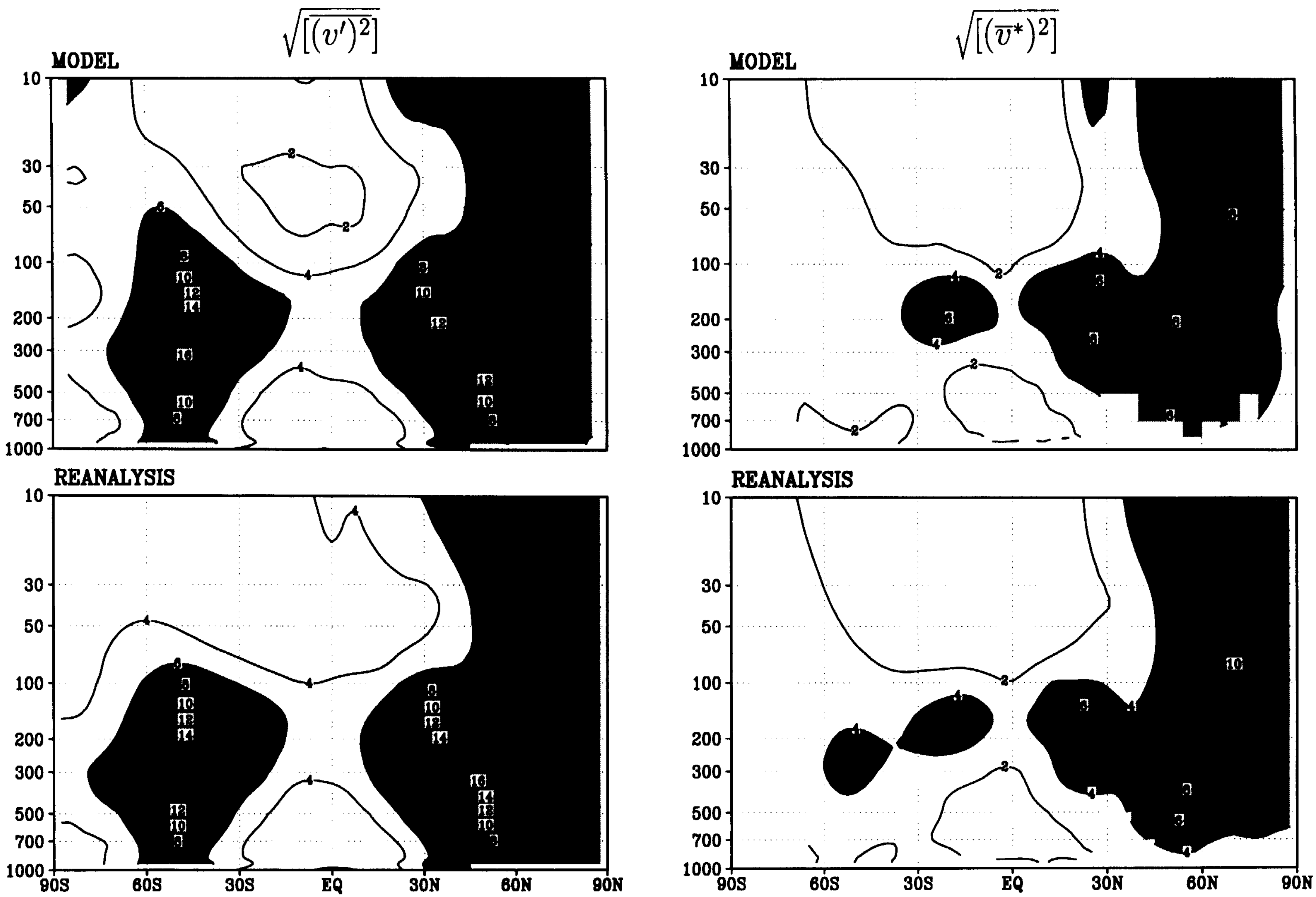

Figure 54: Zonal mean eddy standard deviation of v (m s^{-1}) for DJF— Upper panels: Model; Lower panels: Reanalysis; Left panels: Transients; Right panels: Stationary.

JJA

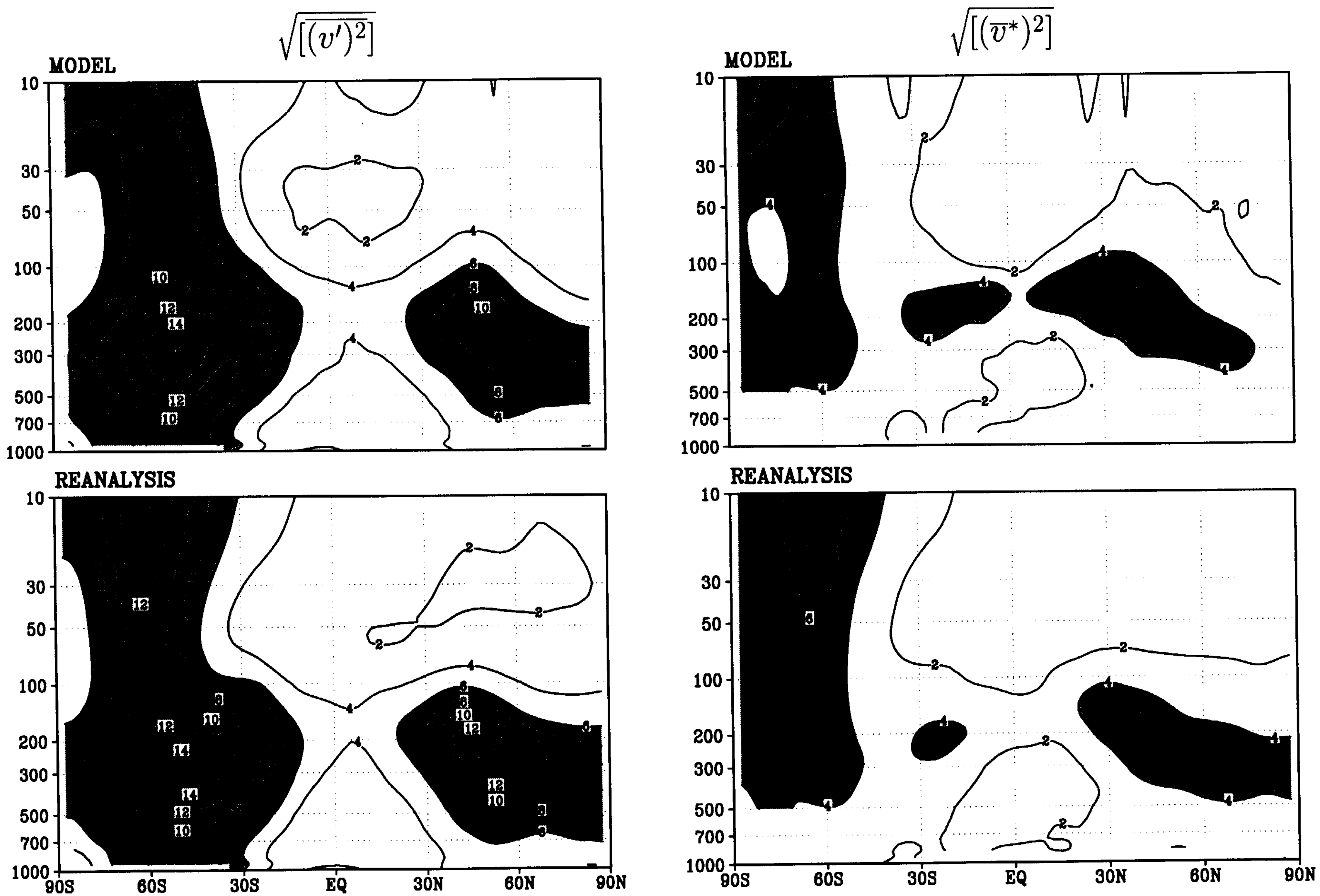

Figure 55: Zonal mean eddy standard deviation of v (m s^{-1}) for JJA— Upper panels: Model; Lower panels: Reanalysis; Left panels: Transients; Right panels: Stationary.

MAM

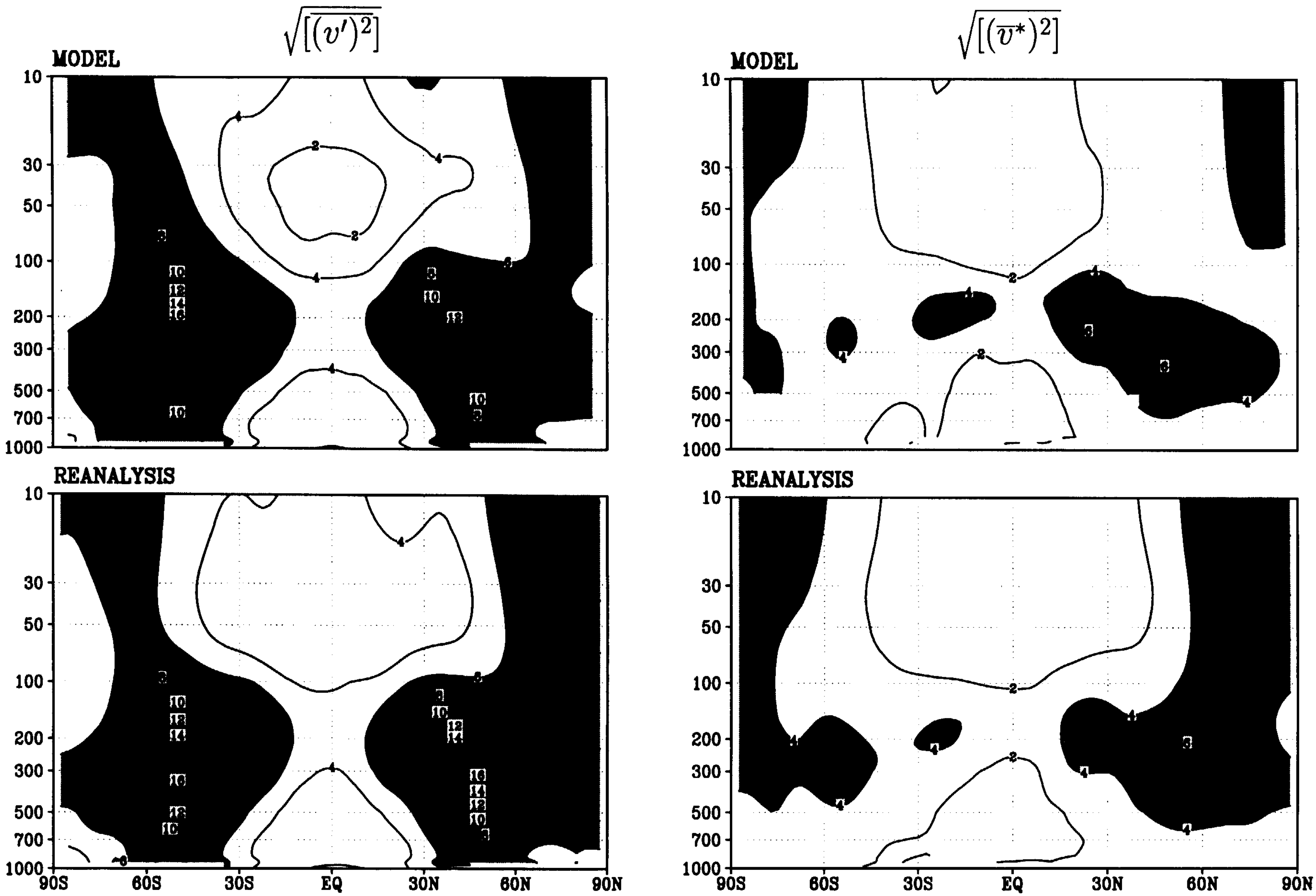

Figure 56: Zonal mean eddy standard deviation of v (m s^{-1}) for MAM— Upper panels: Model; Lower panels: Reanalysis; Left panels: Transients; Right panels: Stationary.

SON

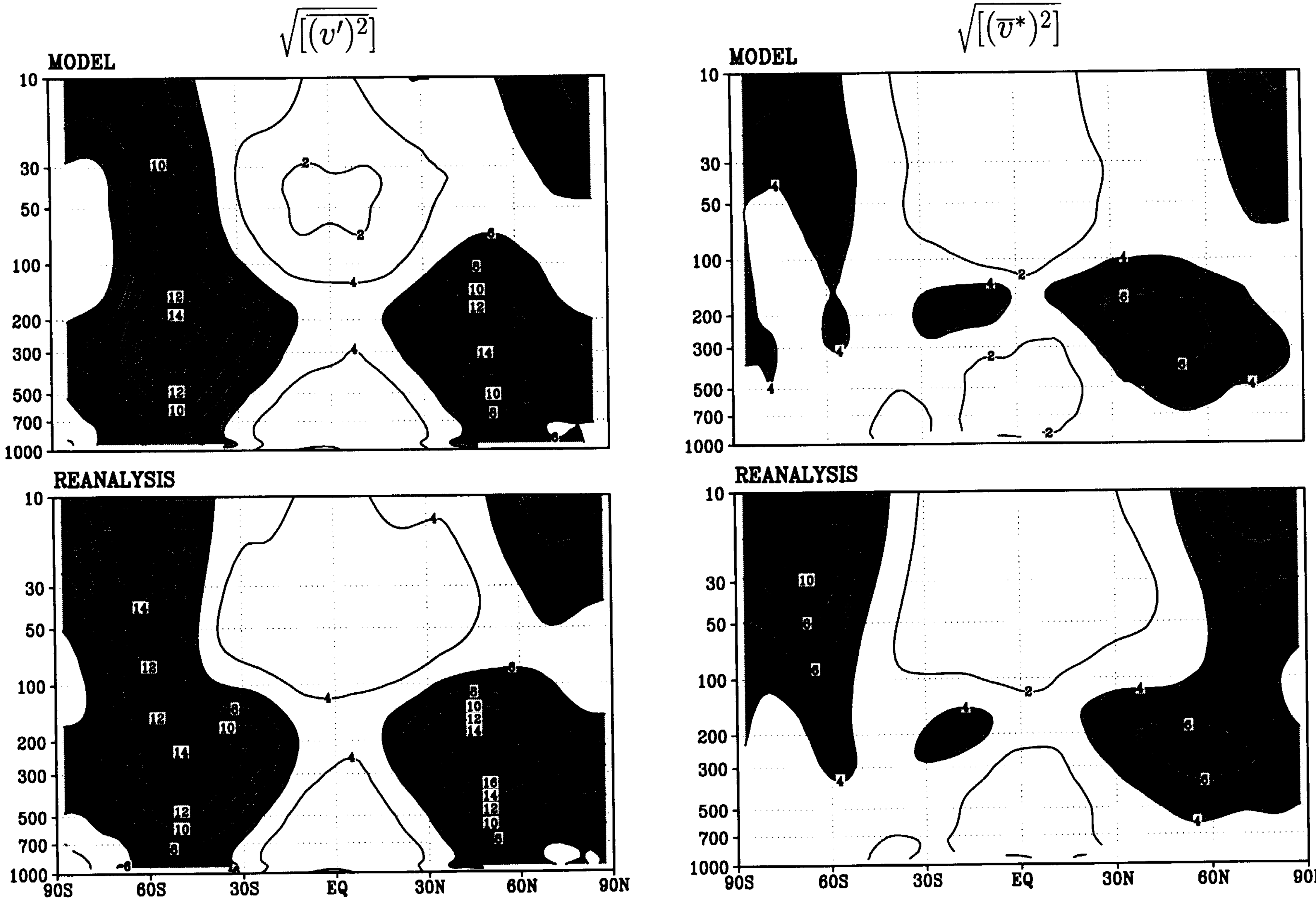

Figure 57: Zonal mean eddy standard deviation of v (m s^{-1}) for SON— Upper panels: Model; Lower panels: Reanalysis; Left panels: Transients; Right panels: Stationary.

DJF

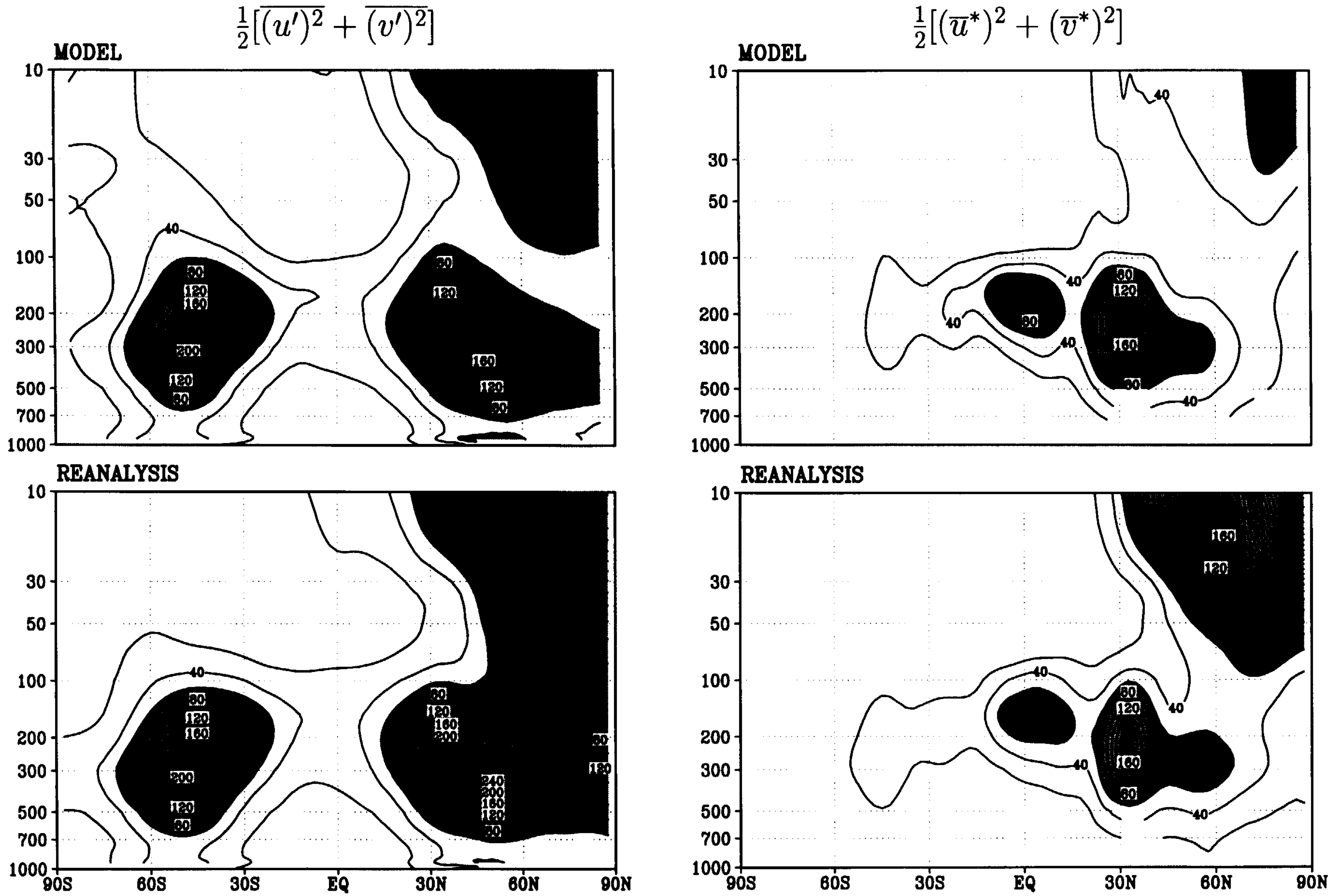

Figure 58: Zonal mean eddy kinetic energy ($m^2\ s^{-2}$) for DJF— Upper panels: Model; Lower panels: Reanalysis; Left panels: Transients; Right panels: Stationary.

JJA

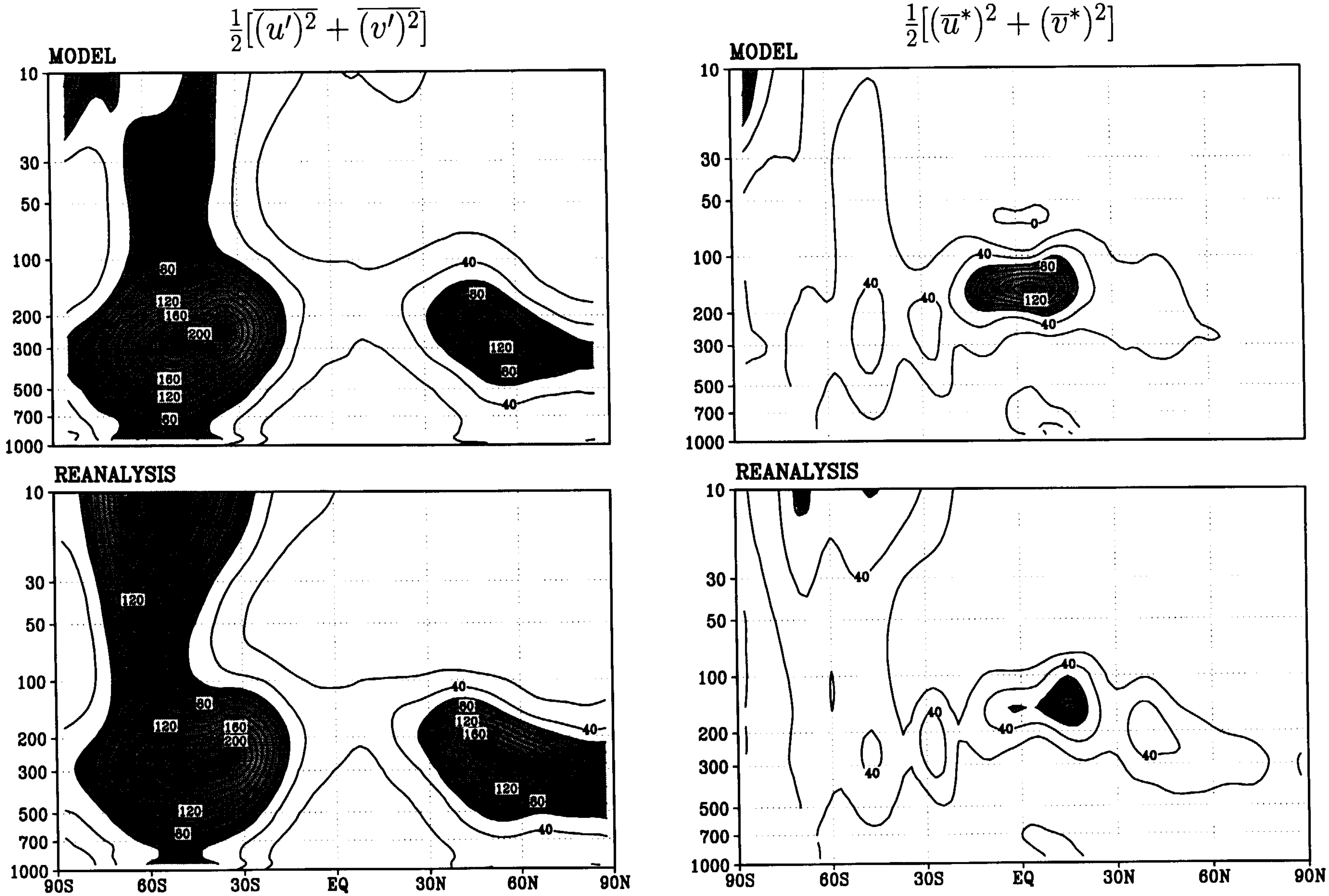

Figure 59: Zonal mean eddy kinetic energy ($m^2\ s^{-2}$) for JJA— Upper panels: Model; Lower panels: Reanalysis; Left panels: Transients; Right panels: Stationary.

MAM

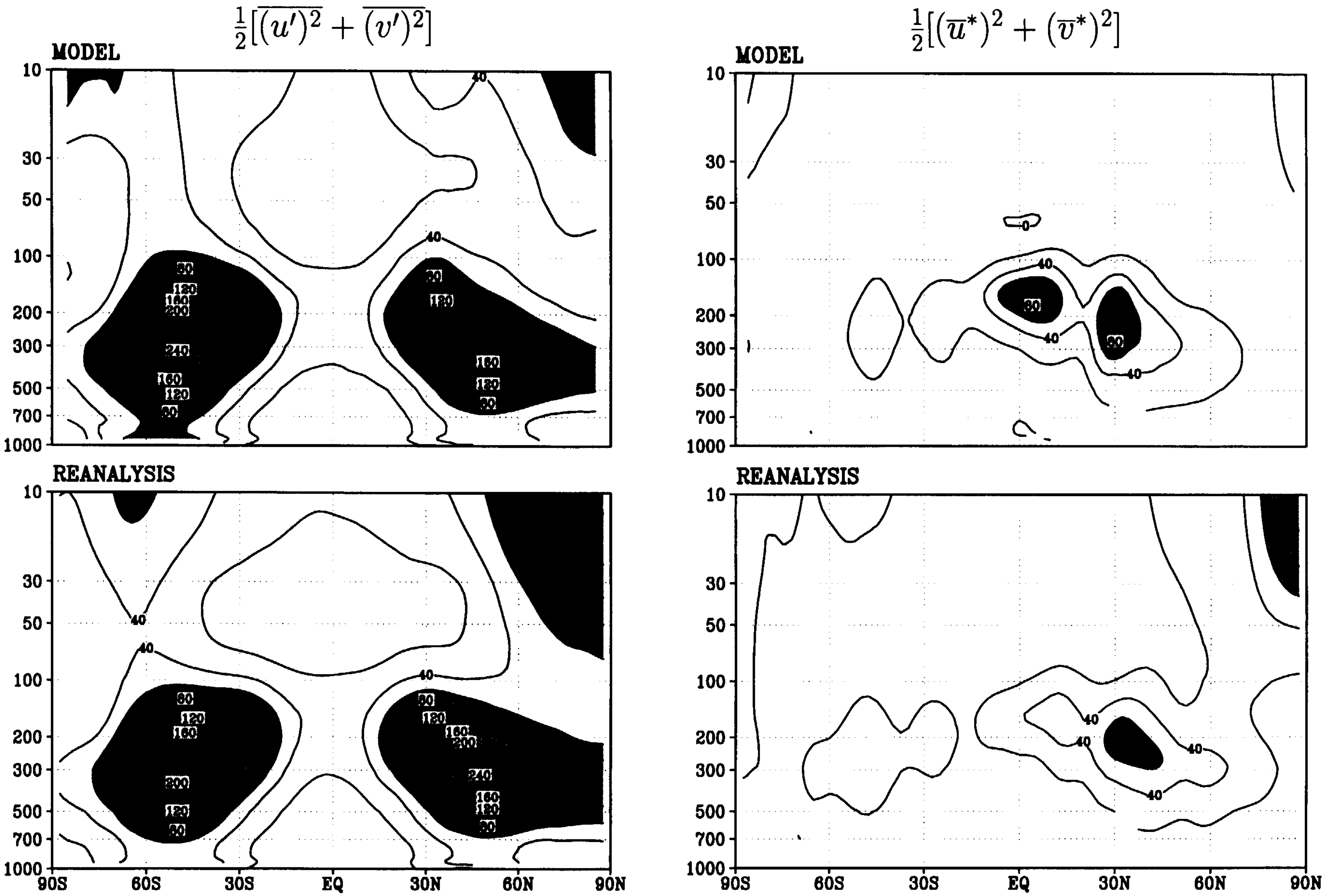

Figure 60: Zonal mean eddy kinetic energy ($m^2\ s^{-2}$) for MAM— Upper panels: Model; Lower panels: Reanalysis; Left panels: Transients; Right panels: Stationary.

SON

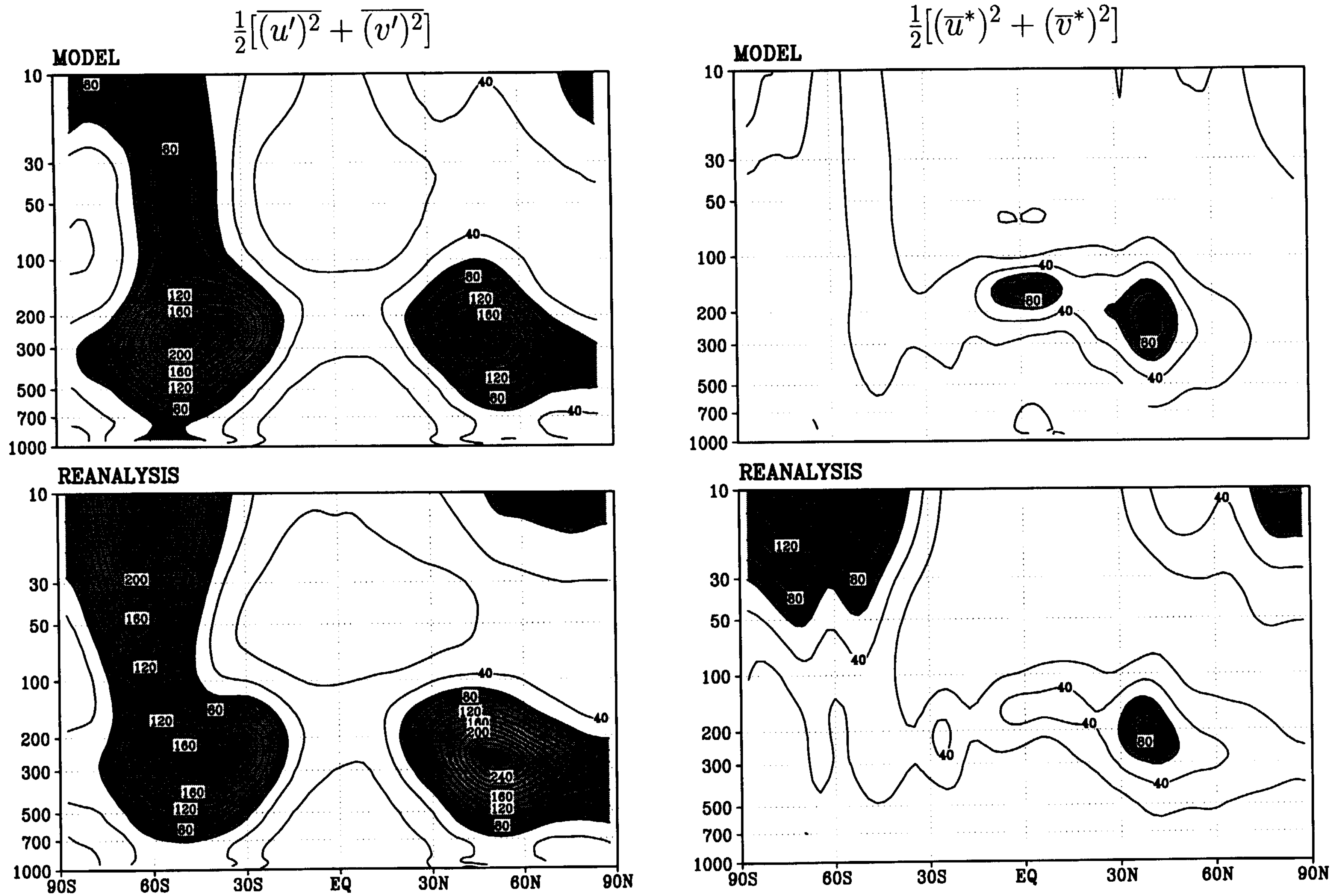

Figure 61: Zonal mean eddy kinetic energy ($m^2\ s^{-2}$) for SON— Upper panels: Model; Lower panels: Reanalysis; Left panels: Transients; Right panels: Stationary.

DJF

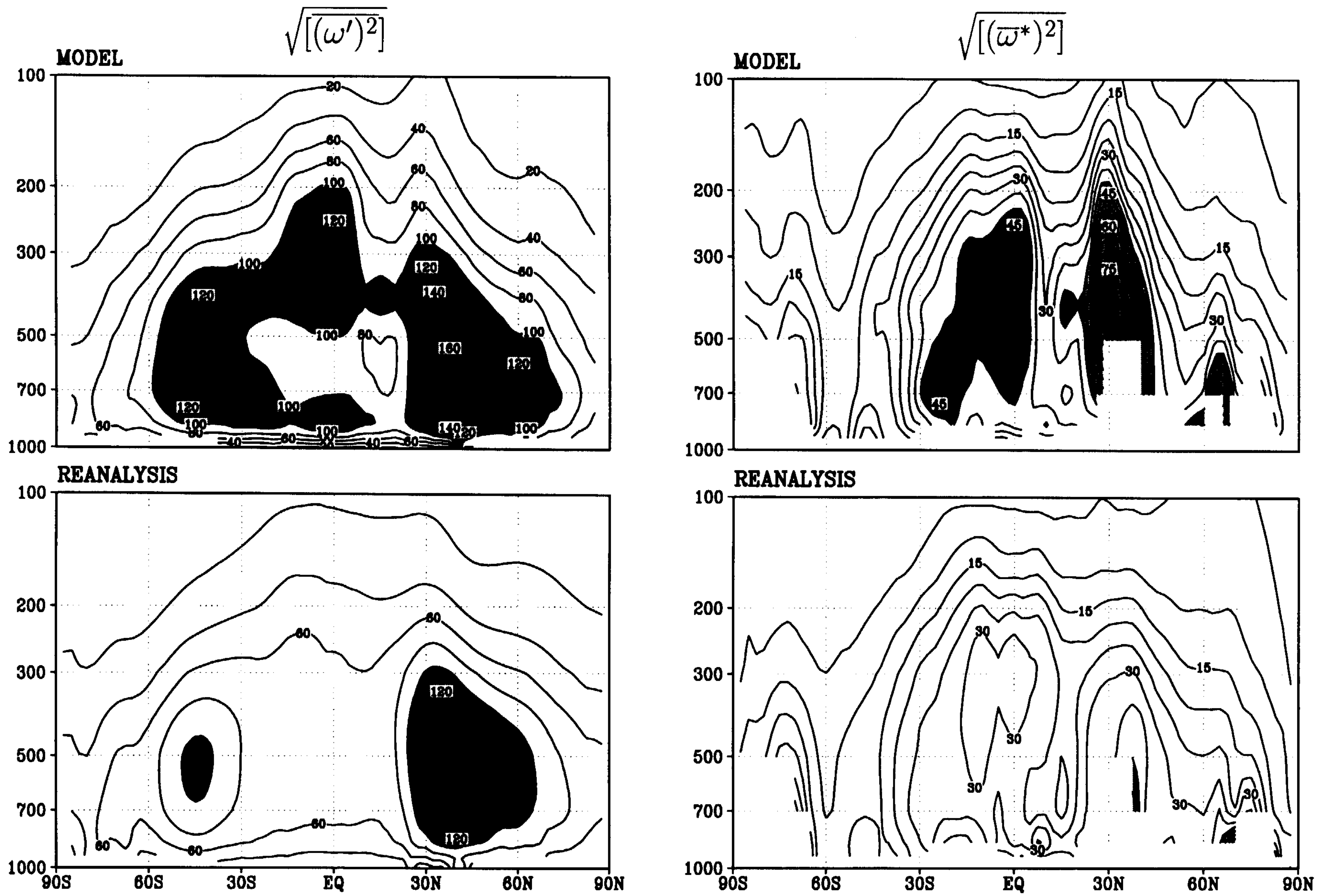

Figure 62: Zonal mean standard deviation of ω (mb d^{-1}) for DJF— Upper panels: Model; Lower panels: Reanalysis; Left panels: Transients; Right panels: Stationary.

JJA

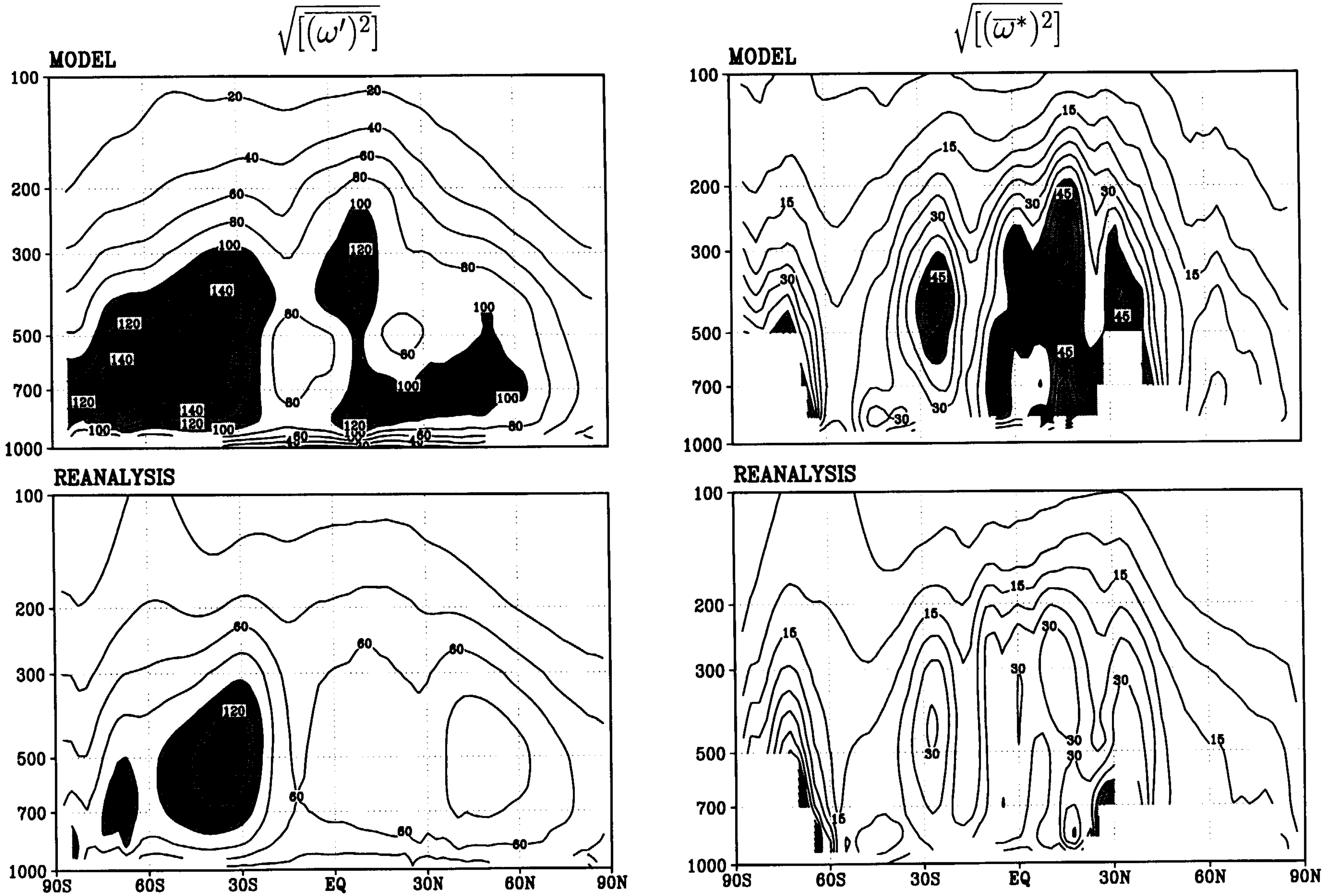

Figure 63: Zonal mean standard deviation of ω (mb d^{-1}) for JJA— Upper panels: Model; Lower panels: Reanalysis; Left panels: Transients; Right panels: Stationary.

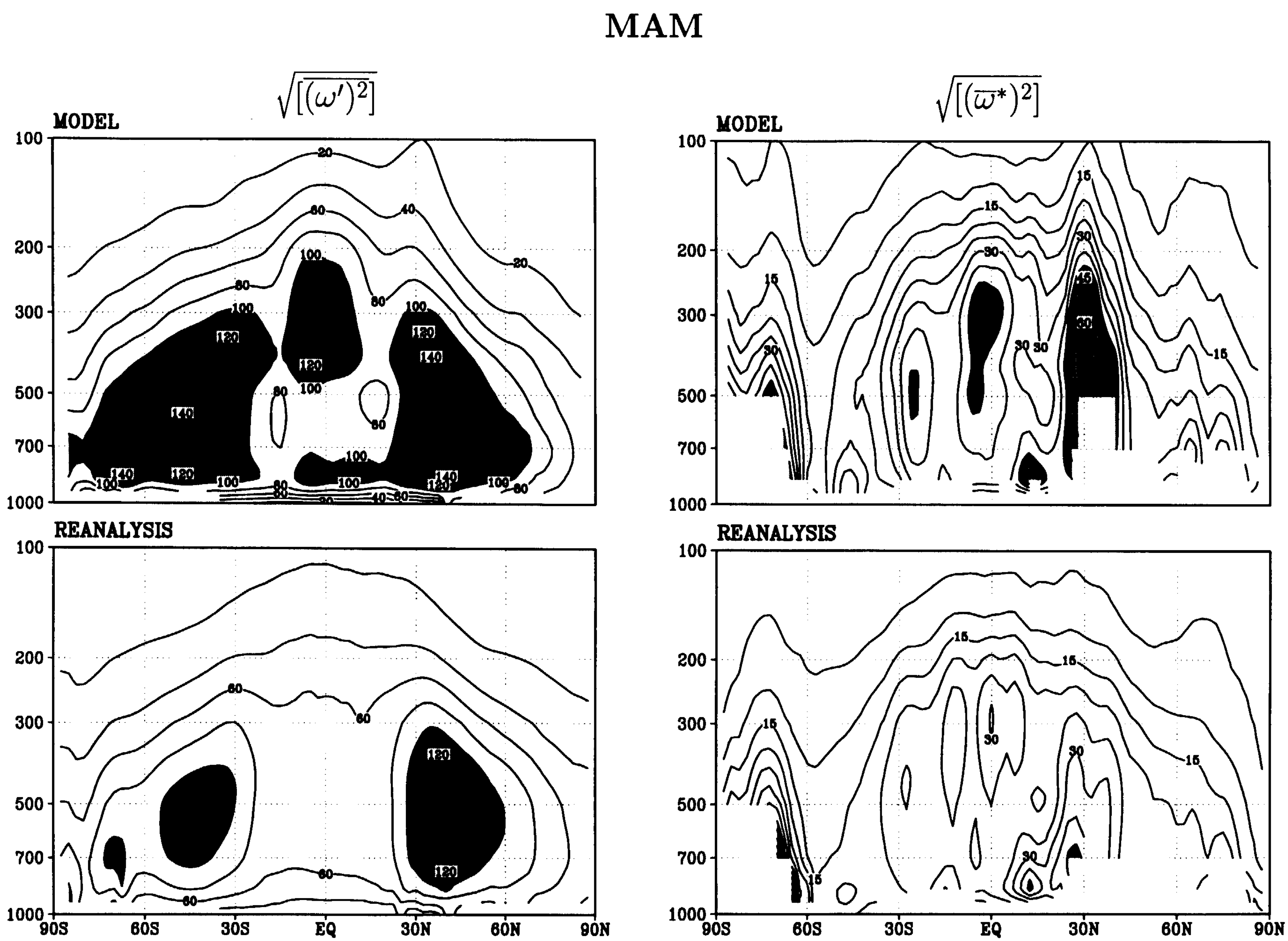

Figure 64: Zonal mean standard deviation of ω (mb d^{-1}) for MAM— Upper panels: Model; Lower panels: Reanalysis; Left panels: Transients; Right panels: Stationary.

SON

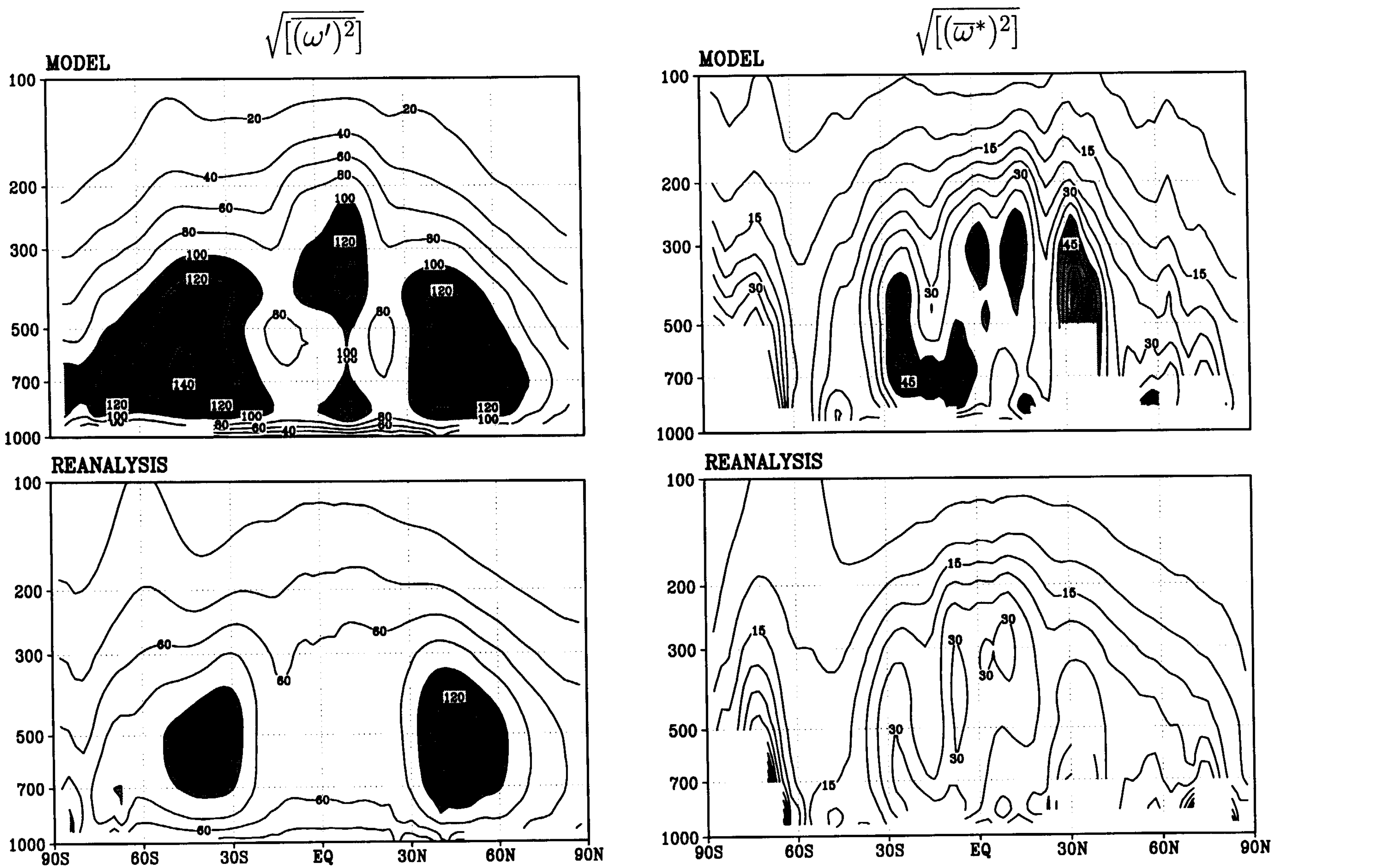

Figure 65: Zonal mean standard deviation of ω (mb d^{-1}) for SON— Upper panels: Model; Lower panels: Reanalysis; Left panels: Transients; Right panels: Stationary.

DJF

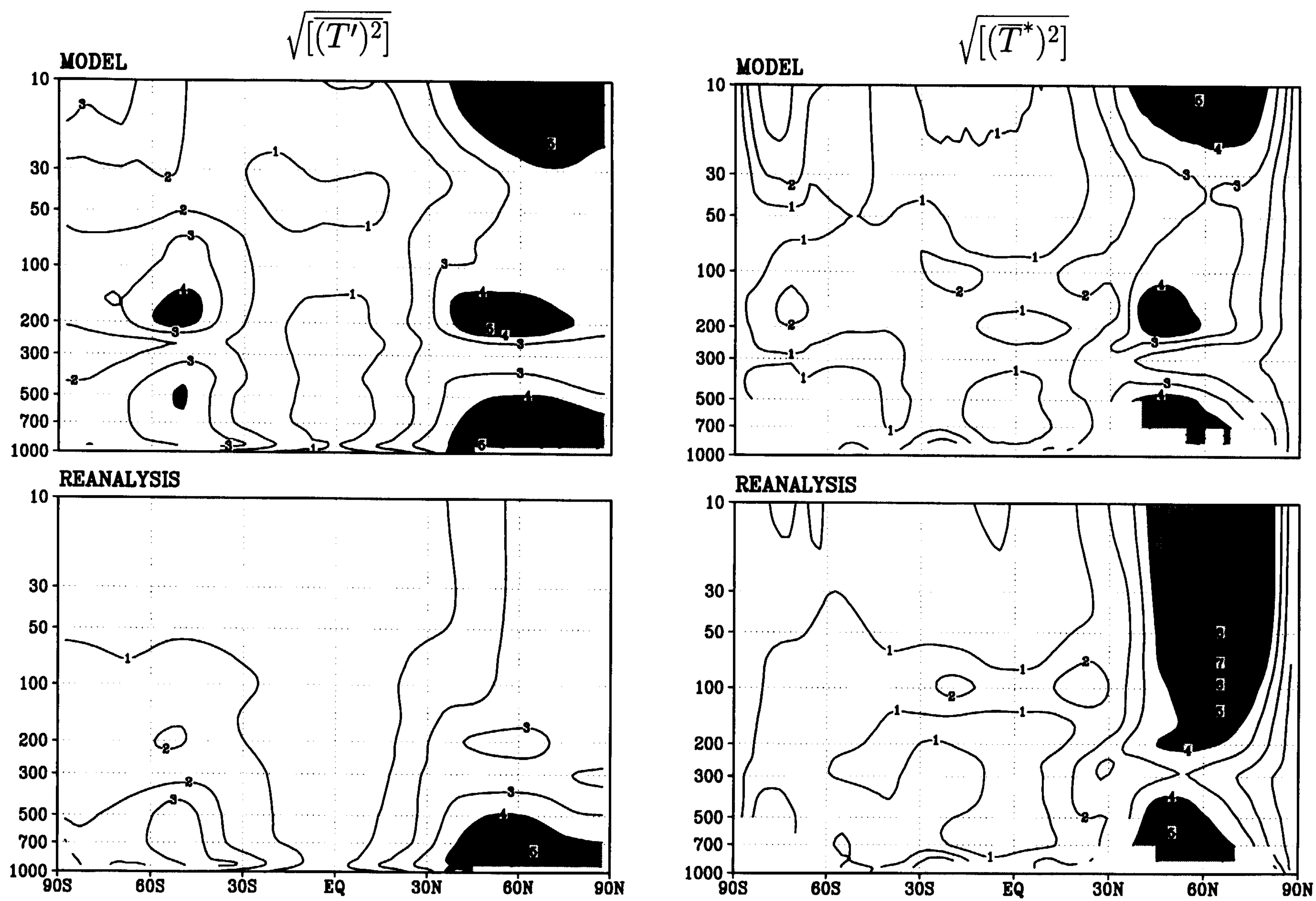

Figure 66: Zonal mean standard deviation of T (K) for DJF— Upper panels: Model; Lower panels: Reanalysis; Left panels: Transients; Right panels: Stationary.

JJA

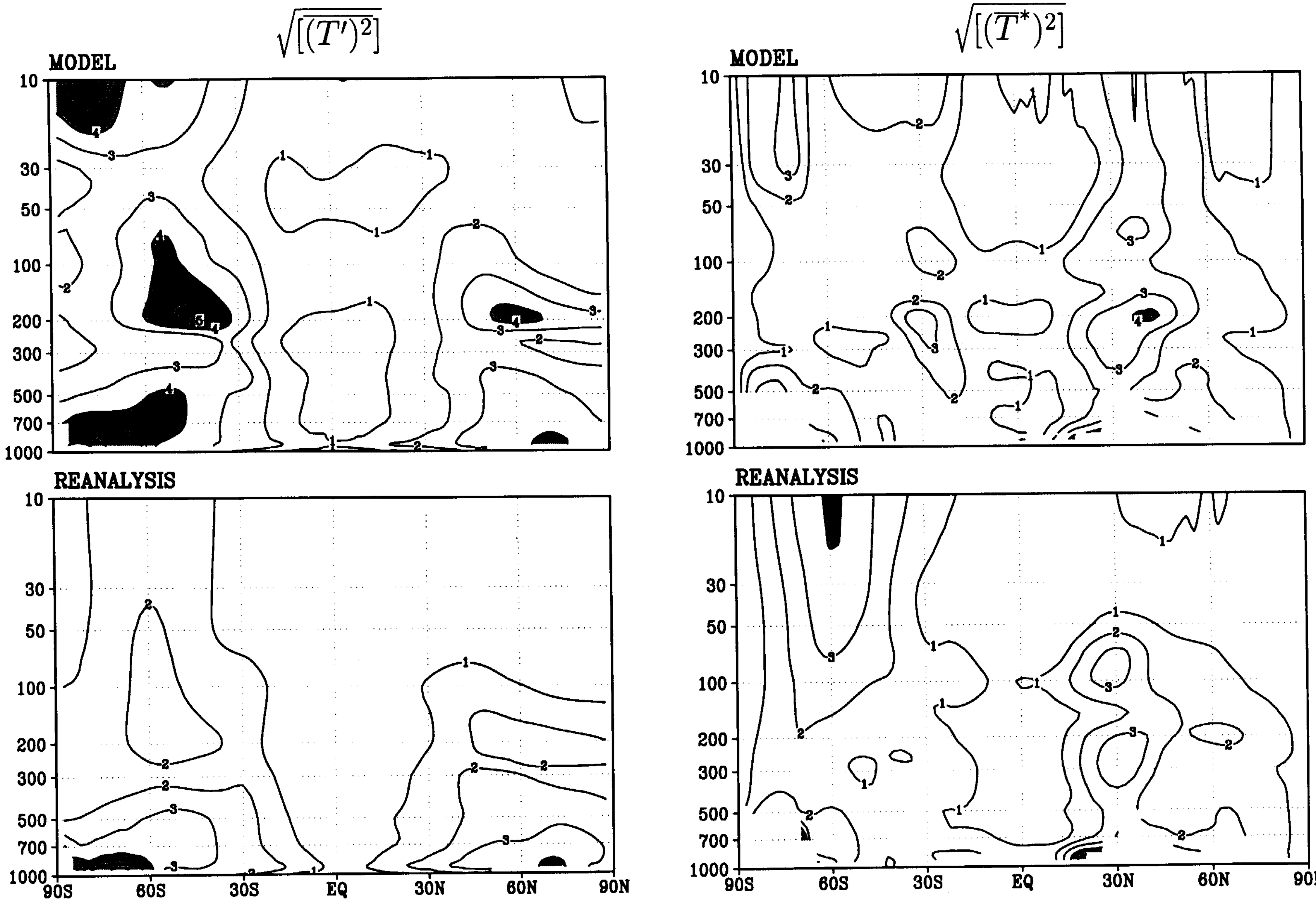

Figure 67: Zonal mean standard deviation of T (K) for JJA— Upper panels: Model; Lower panels: Reanalysis; Left panels: Transients; Right panels: Stationary.

MAM

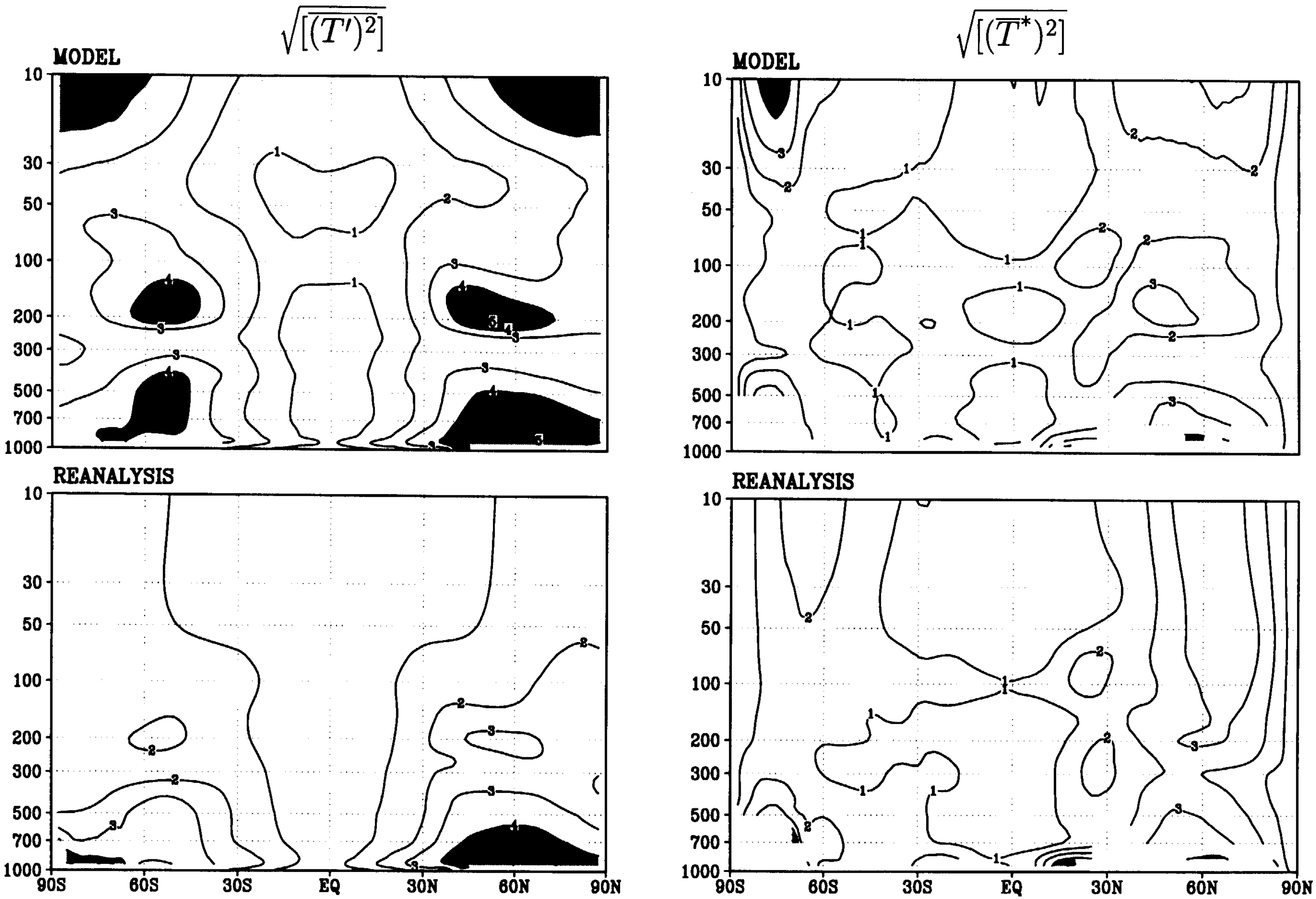

Figure 68: Zonal mean standard deviation of T (K) for MAM— Upper panels: Model; Lower panels: Reanalysis; Left panels: Transients; Right panels: Stationary.

SON

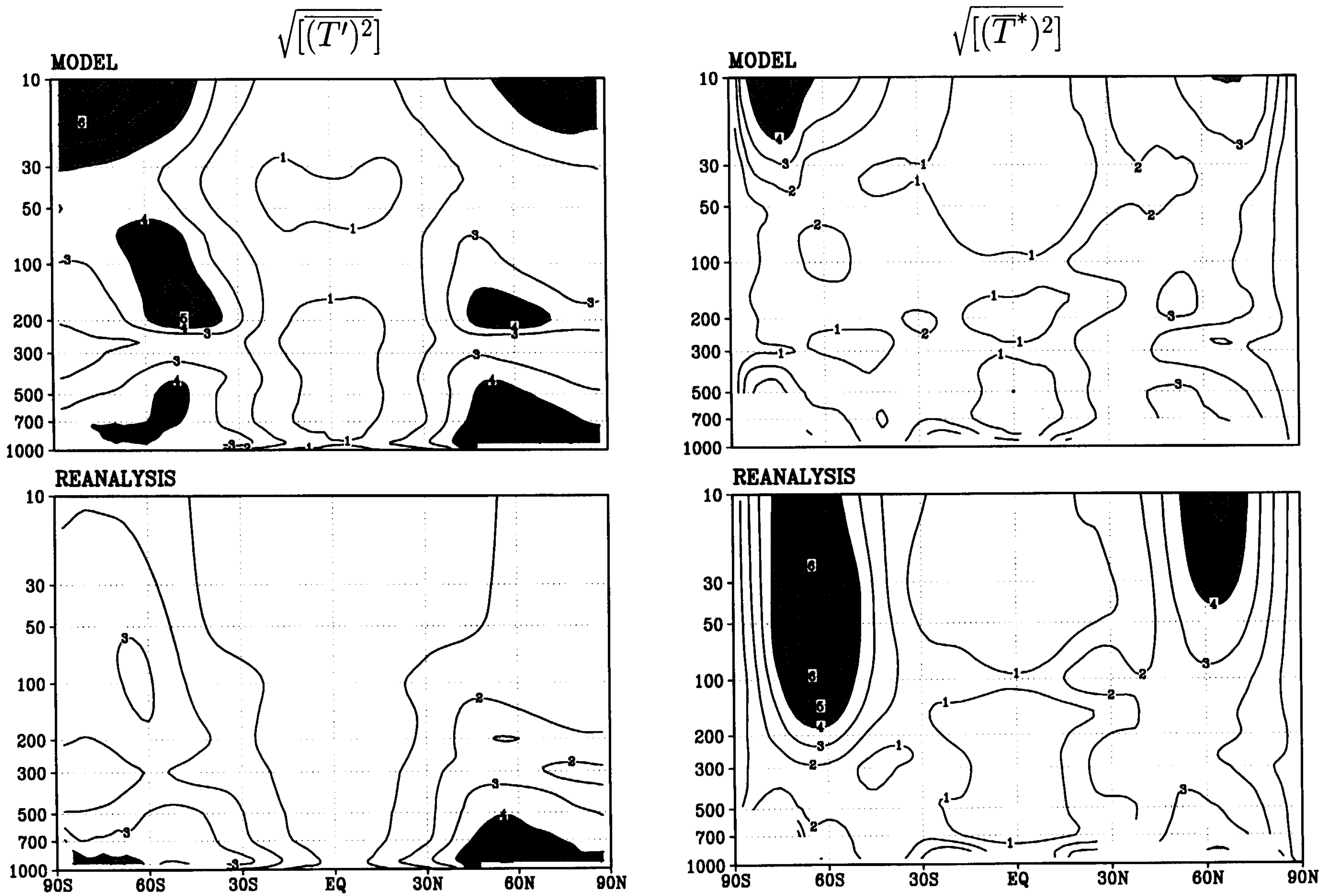

Figure 69: Zonal mean standard deviation of T (K) for SON— Upper panels: Model; Lower panels: Reanalysis; Left panels: Transients; Right panels: Stationary.

DJF

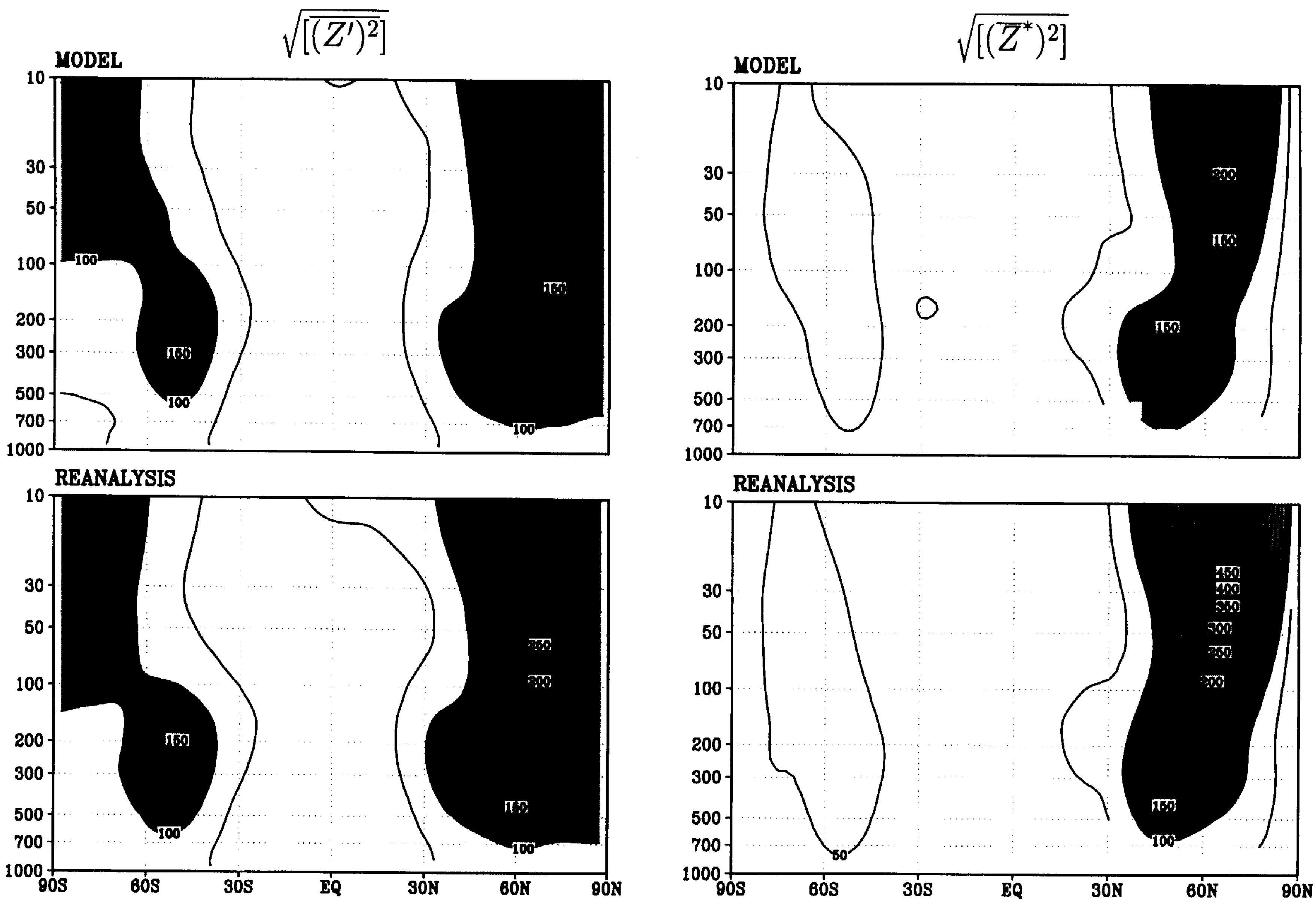

Figure 70: Zonal mean standard deviation of Z (m) for DJF— Upper panels: Model; Lower panels: Reanalysis; Left panels: Transients; Right panels: Stationary.

JJA

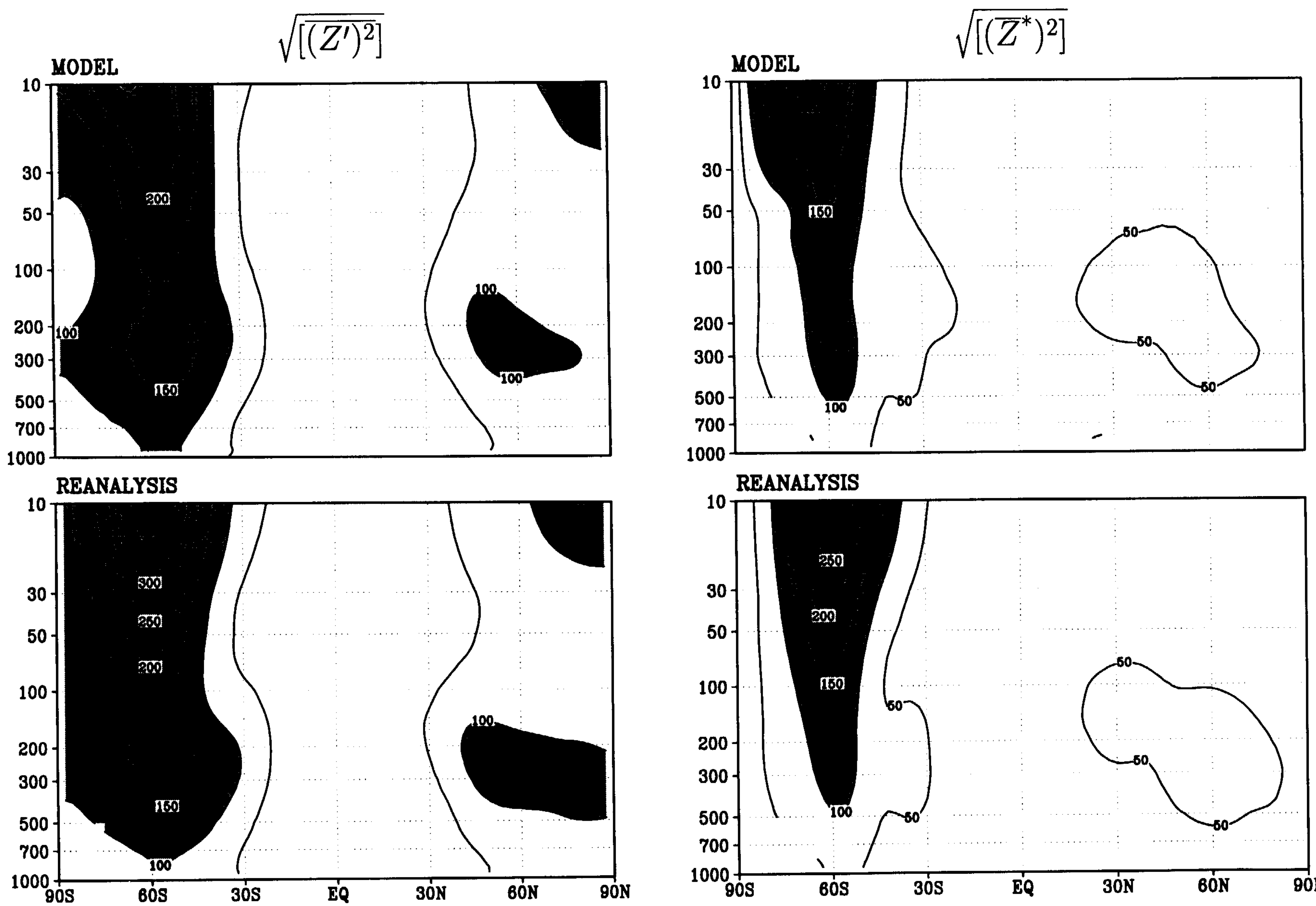

Figure 71: Zonal mean standard deviation of Z (m) for JJA— Upper panels: Model; Lower panels: Reanalysis; Left panels: Transients; Right panels: Stationary.

MAM

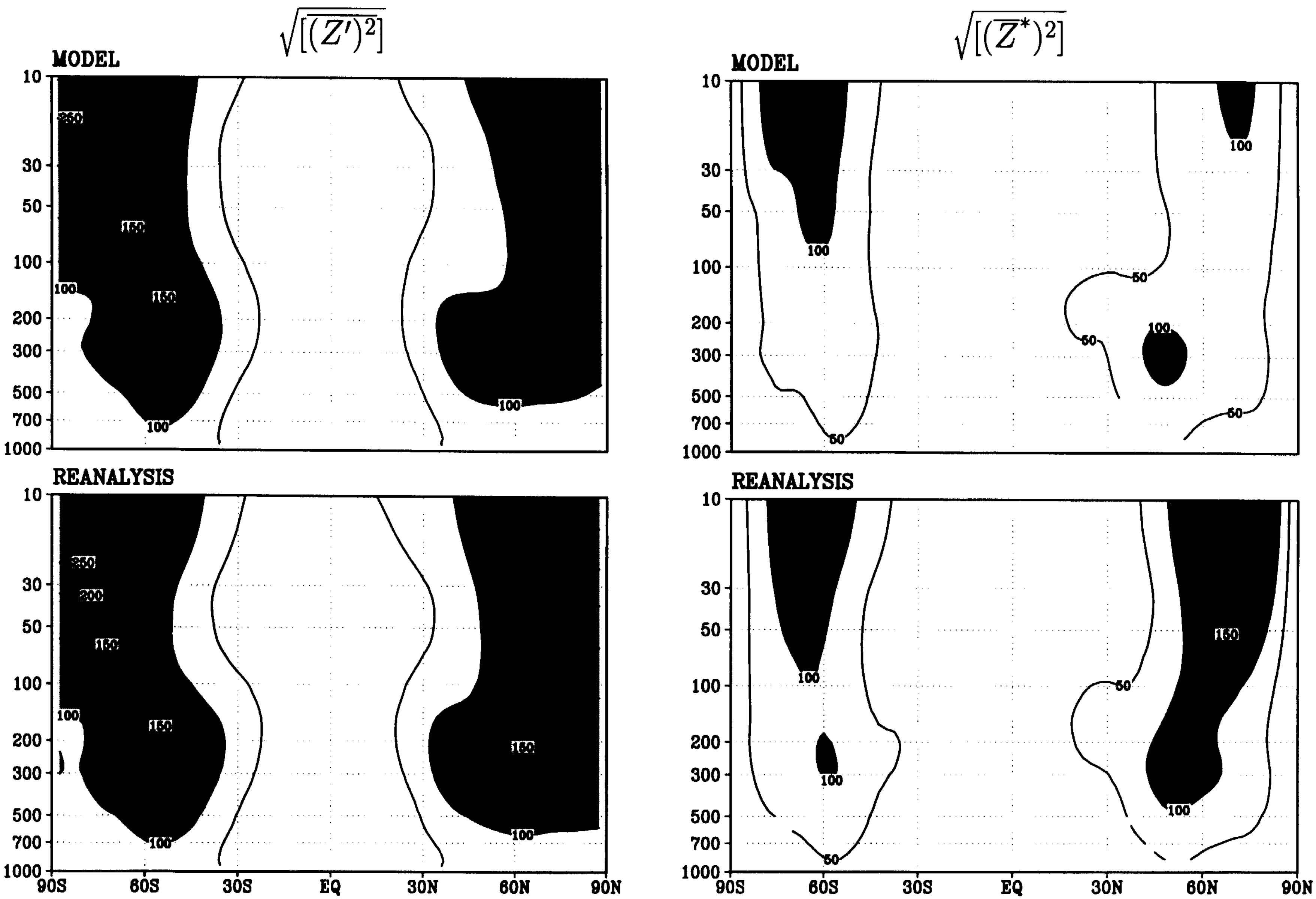

Figure 72: Zonal mean standard deviation of Z (m) for MAM— Upper panels: Model; Lower panels: Reanalysis; Left panels: Transients; Right panels: Stationary.

SON

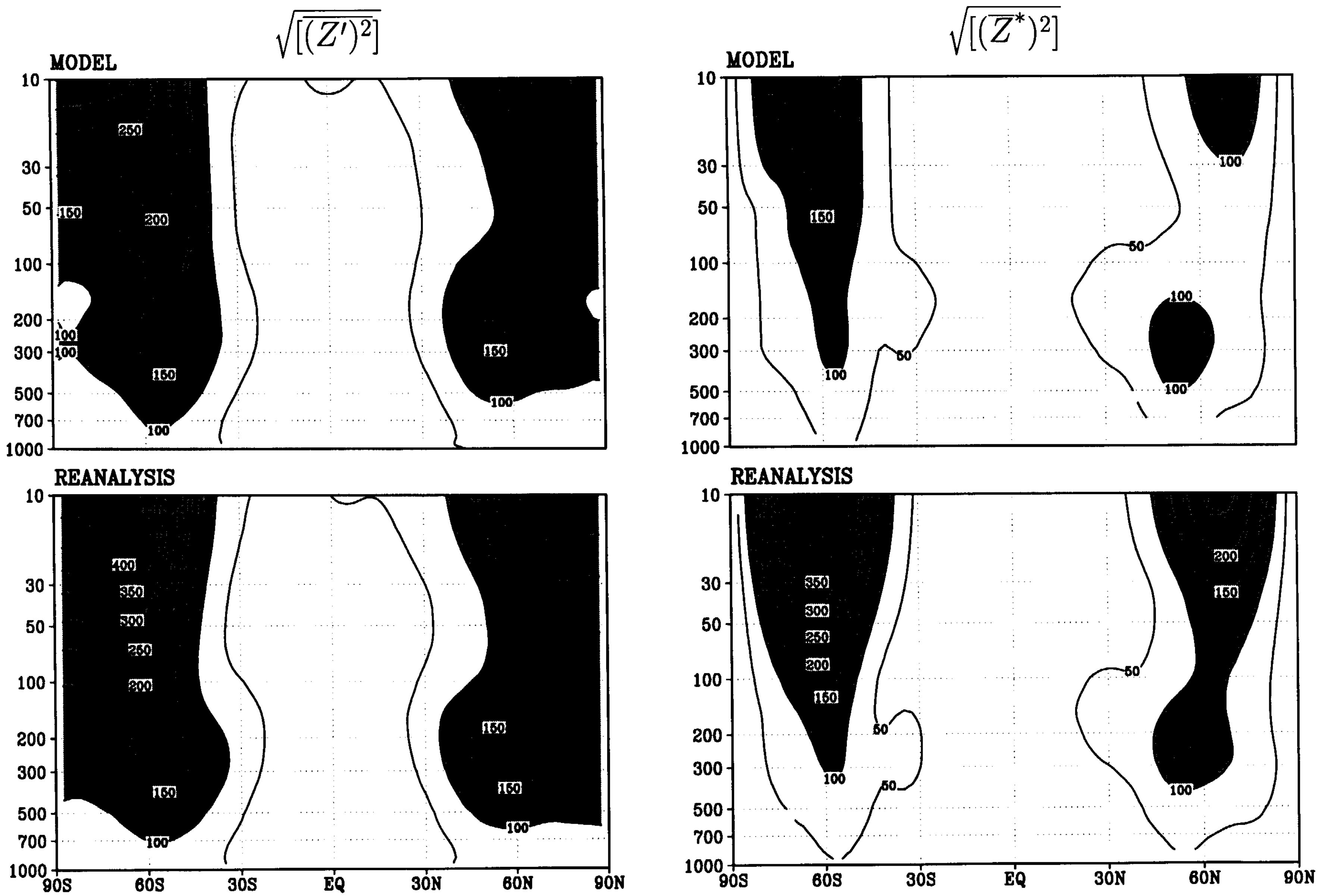

Figure 73: Zonal mean standard deviation of Z (m) for SON— Upper panels: Model; Lower panels: Reanalysis; Left panels: Transients; Right panels: Stationary.

DJF

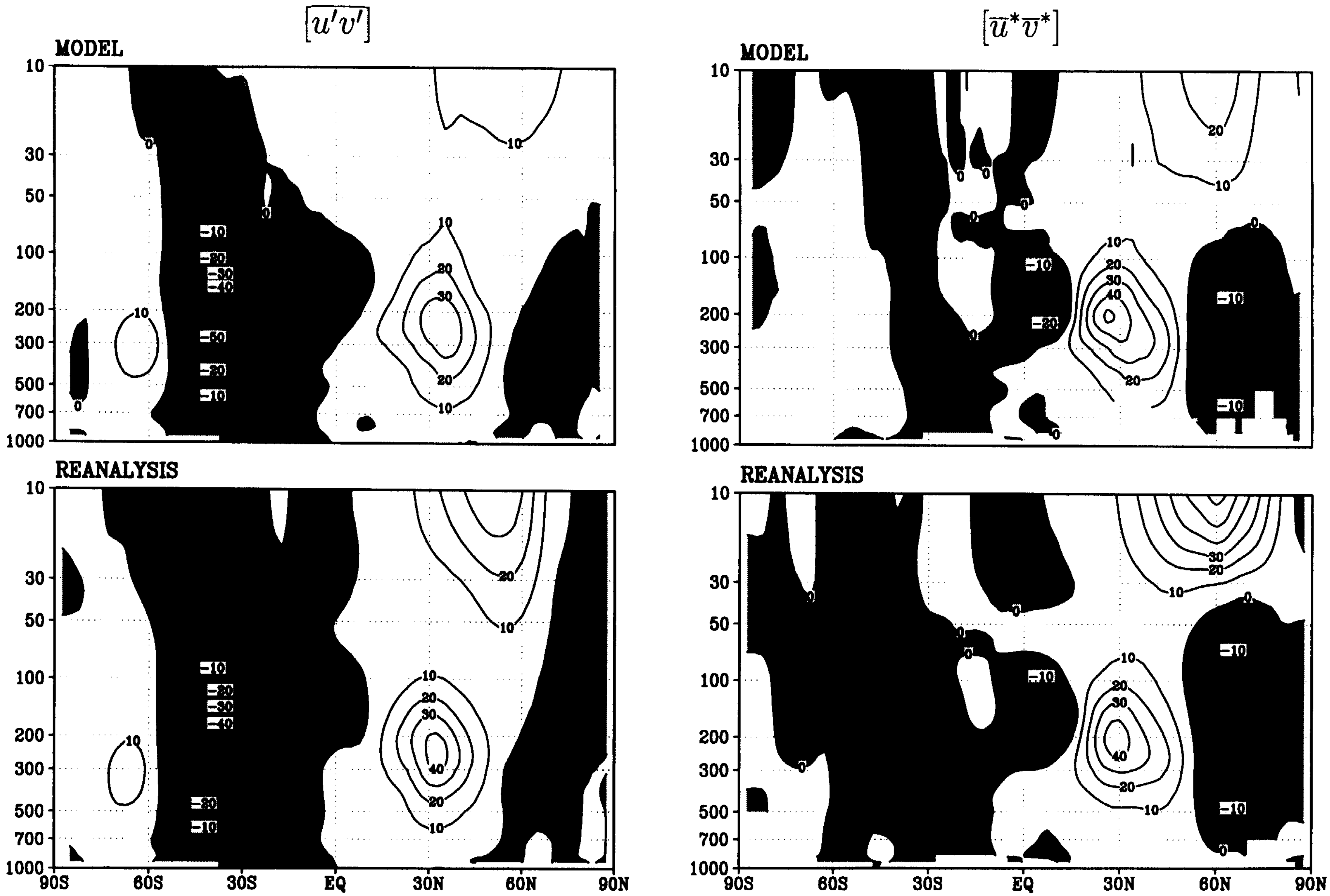

Figure 74: Zonal mean eddy momentum transports (m^2 s^{-2}) for DJF— Upper panels: Model; Lower panels: Reanalysis; Left panels: Transients; Right panels: Stationary.

JJA

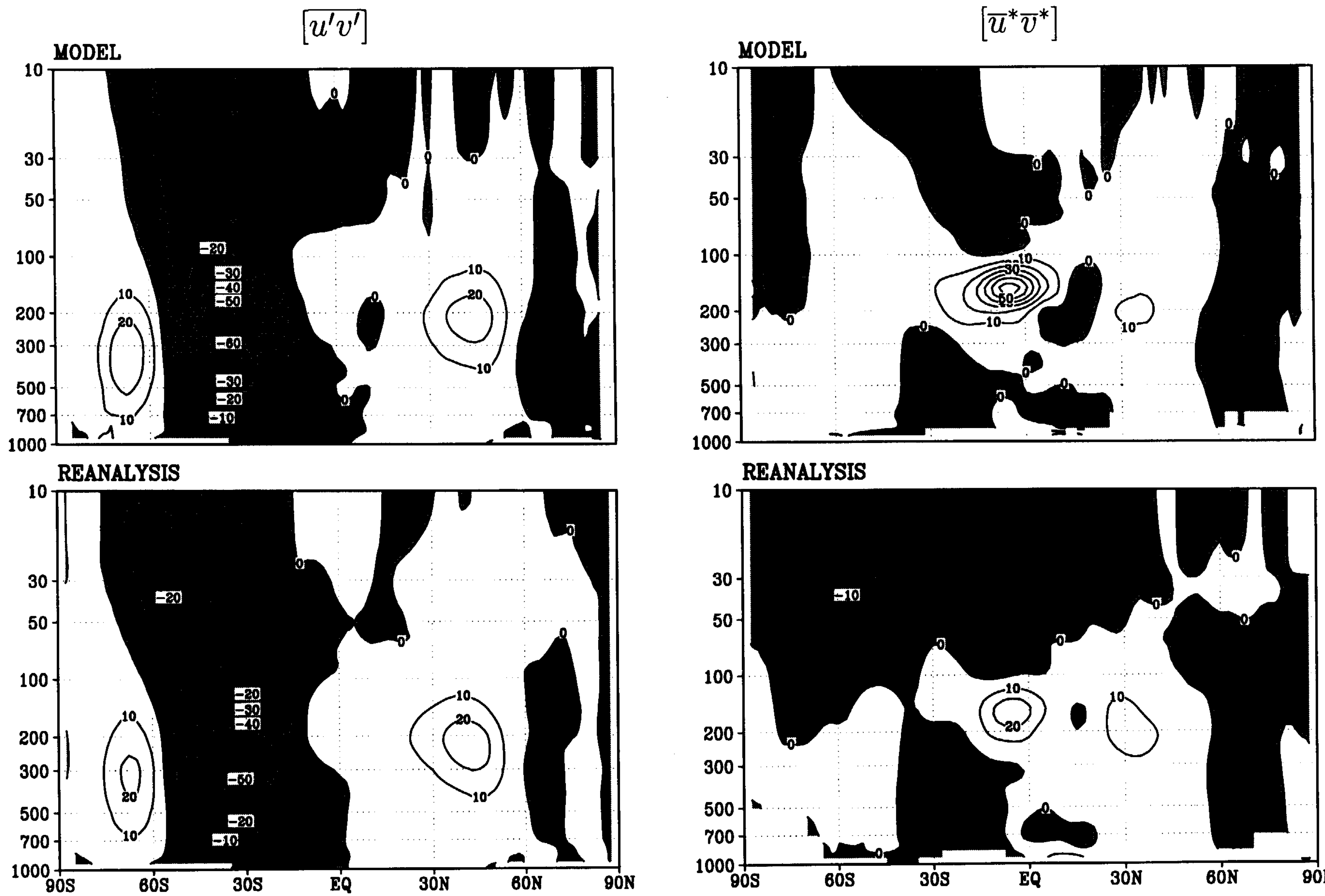

Figure 75: Zonal mean eddy momentum transports (m^2 s^{-2}) for JJA— Upper panels: Model; Lower panels: Reanalysis; Left panels: Transients; Right panels: Stationary.

MAM

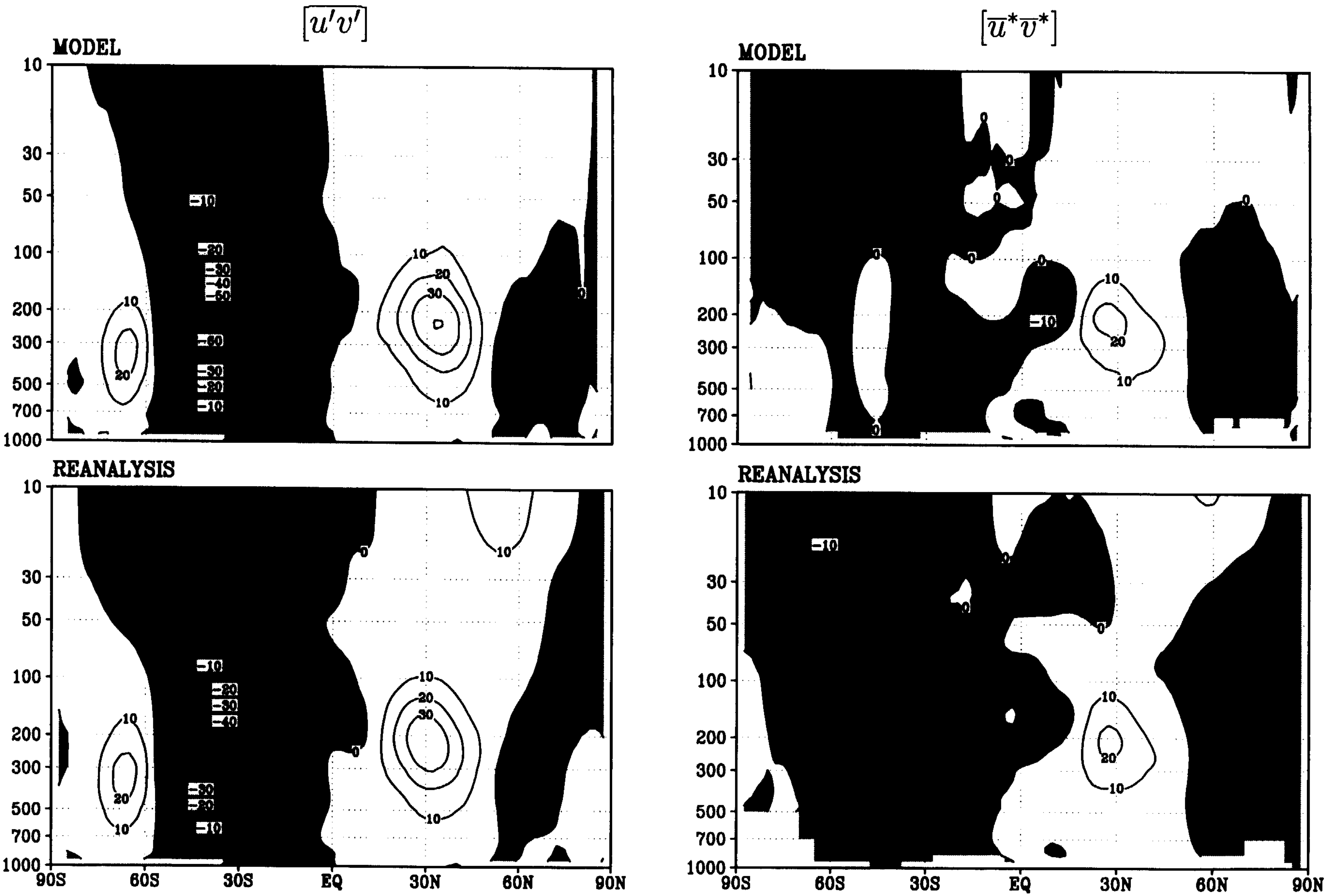

Figure 76: Zonal mean eddy momentum transports ($m^2\ s^{-2}$) for MAM— Upper panels: Model; Lower panels: Reanalysis; Left panels: Transients; Right panels: Stationary.

SON

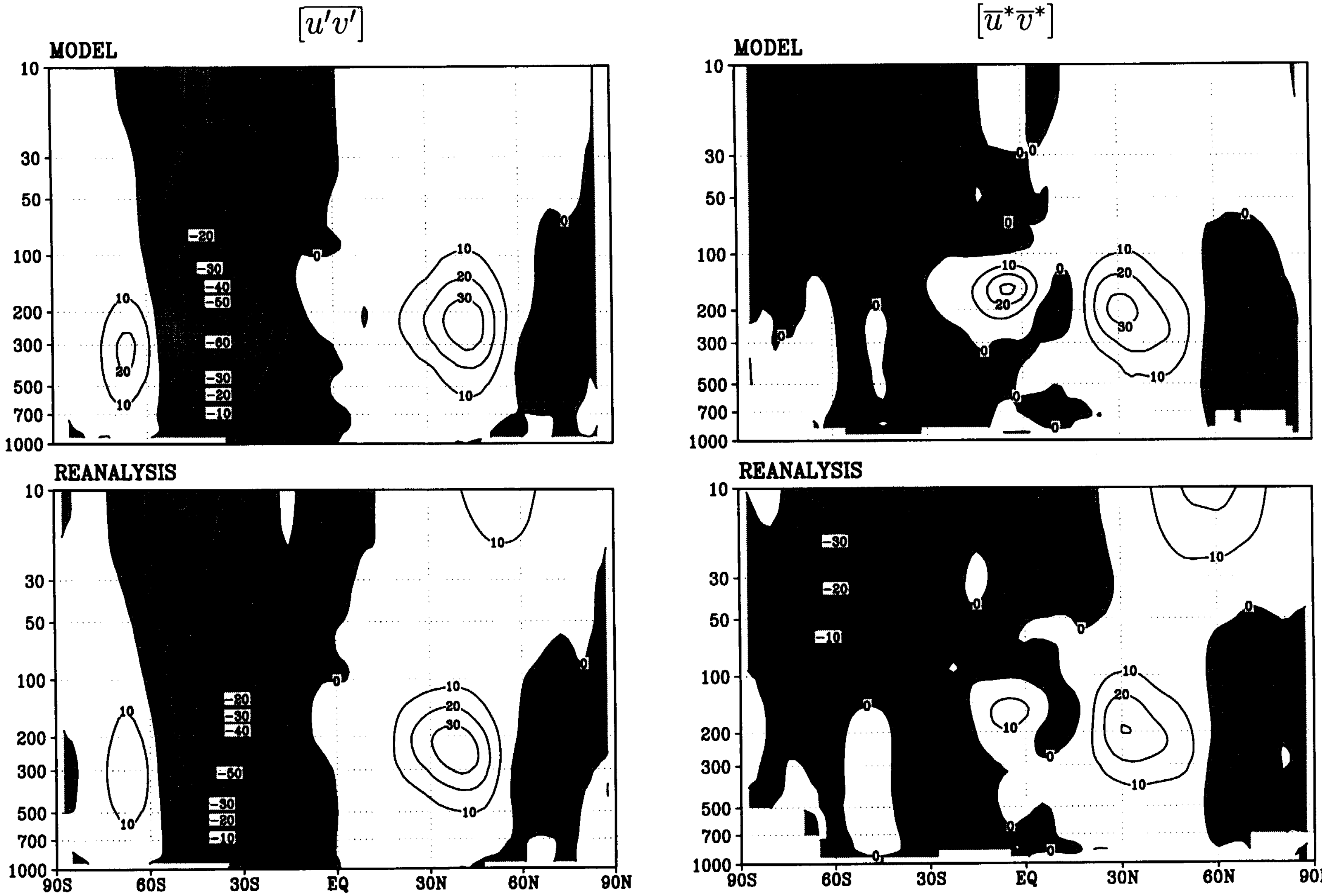

Figure 77: Zonal mean eddy momentum transports ($m^2\ s^{-2}$) for SON— Upper panels: Model; Lower panels: Reanalysis; Left panels: Transients; Right panels: Stationary.

DJF

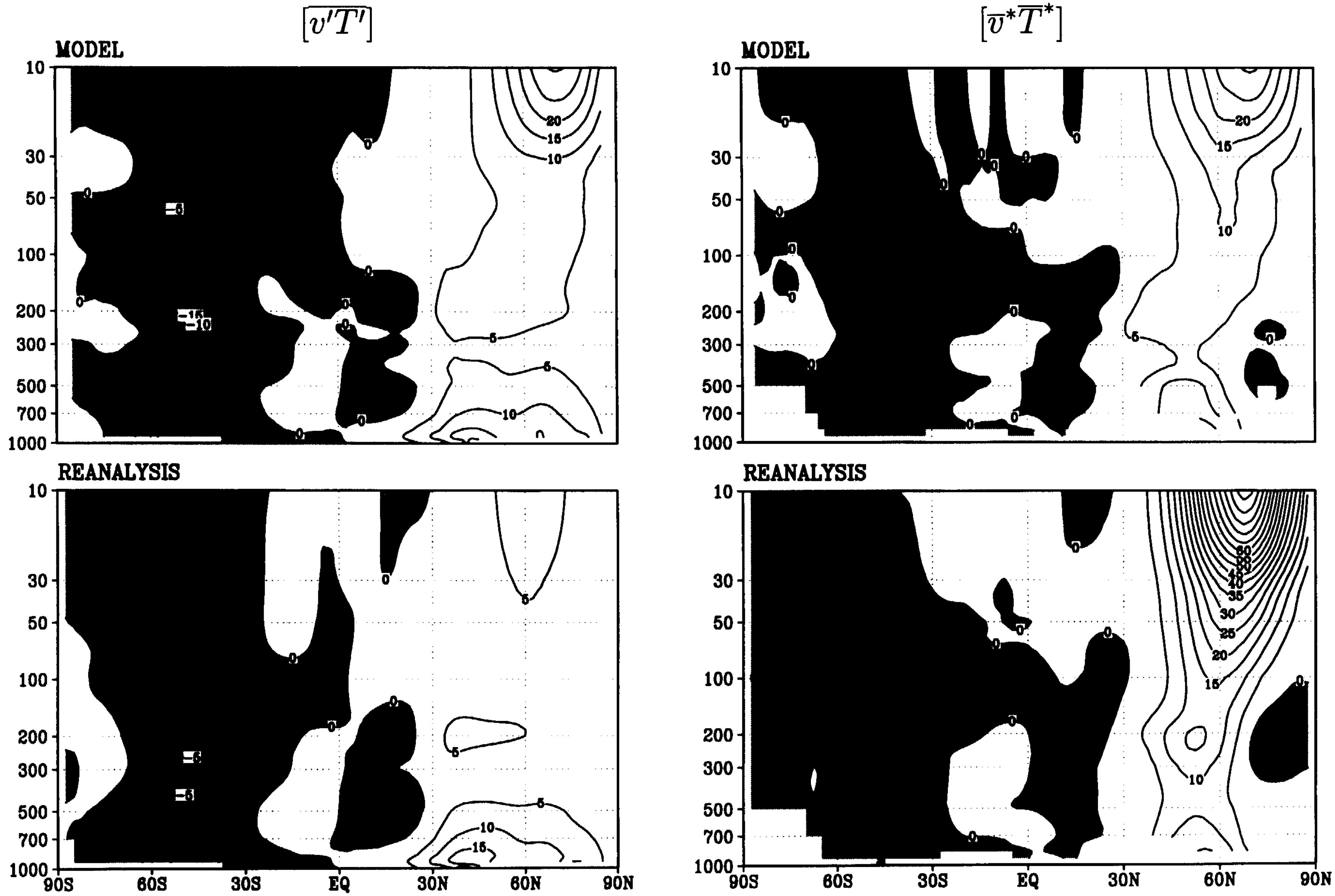

Figure 78: Zonal mean eddy meridional heat transports (m s^{-1} K) for DJF— Upper panels: Model; Lower panels: Reanalysis; Left panels: Transients; Right panels: Stationary.

JJA

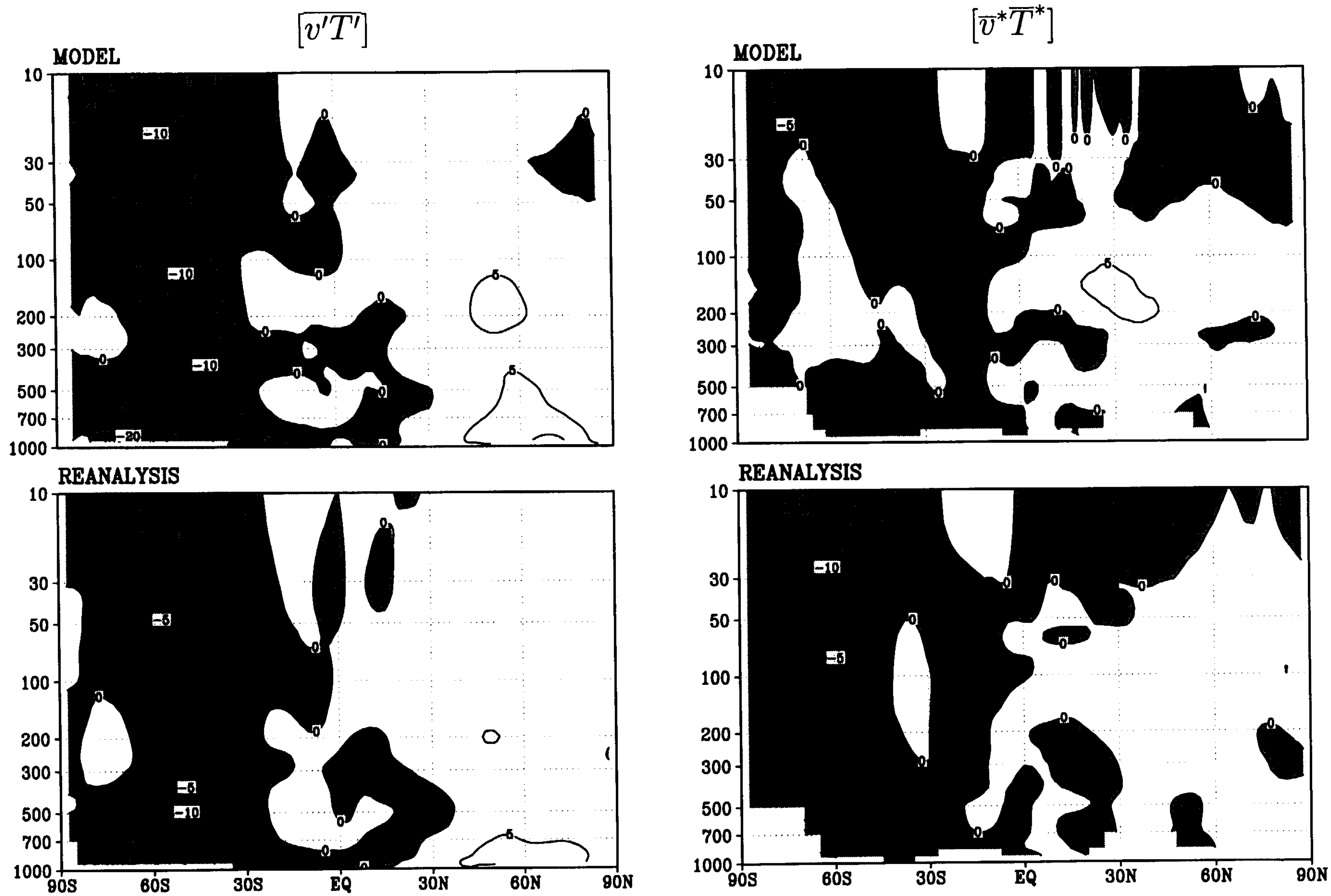

Figure 79: Zonal mean eddy meridional heat transports (m s^{-1} K) for JJA— Upper panels: Model; Lower panels: Reanalysis; Left panels: Transients; Right panels: Stationary.

MAM

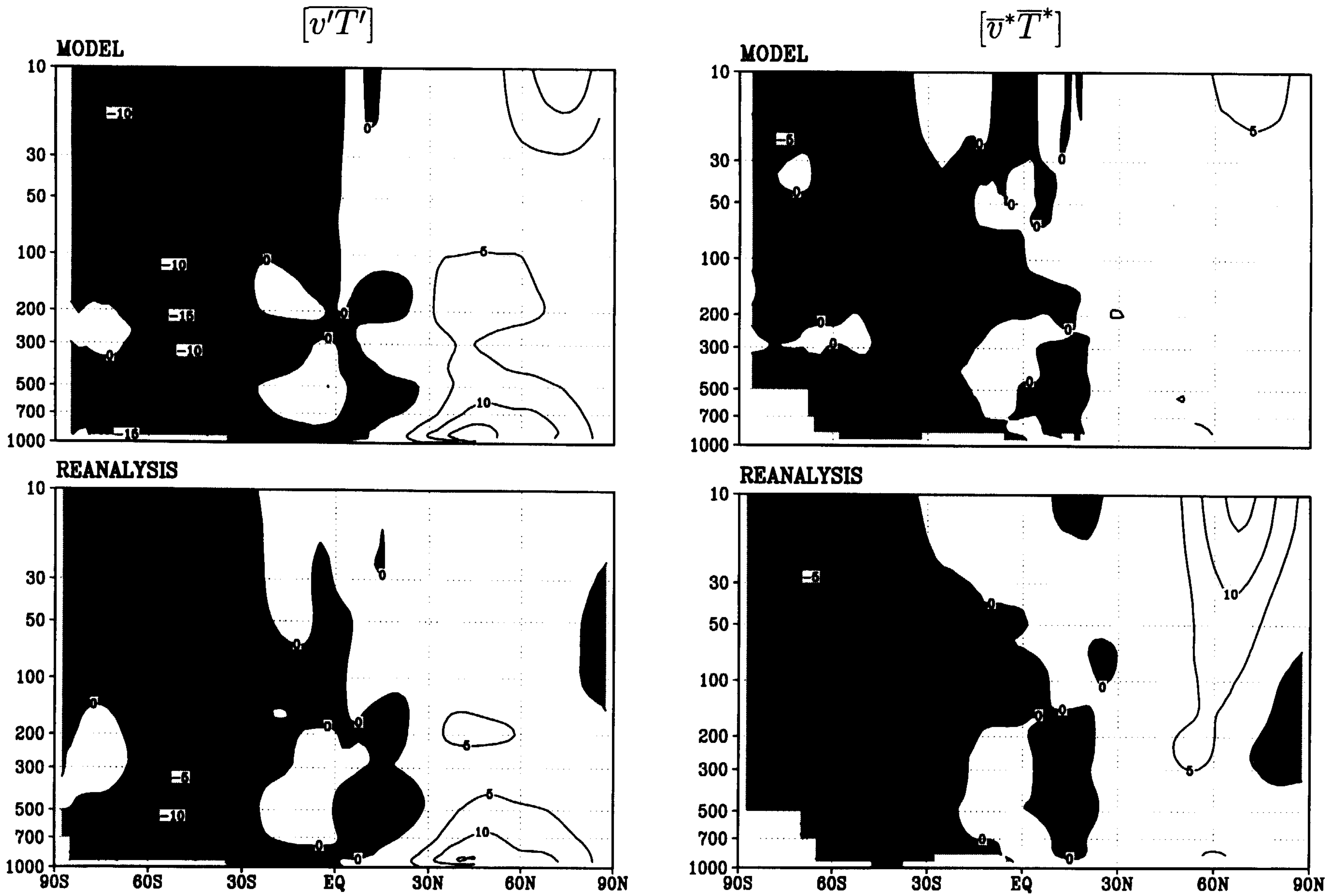

Figure 80: Zonal mean eddy meridional heat transports (m s^{-1} K) for MAM— Upper panels: Model; Lower panels: Reanalysis; Left panels: Transients; Right panels: Stationary.

SON

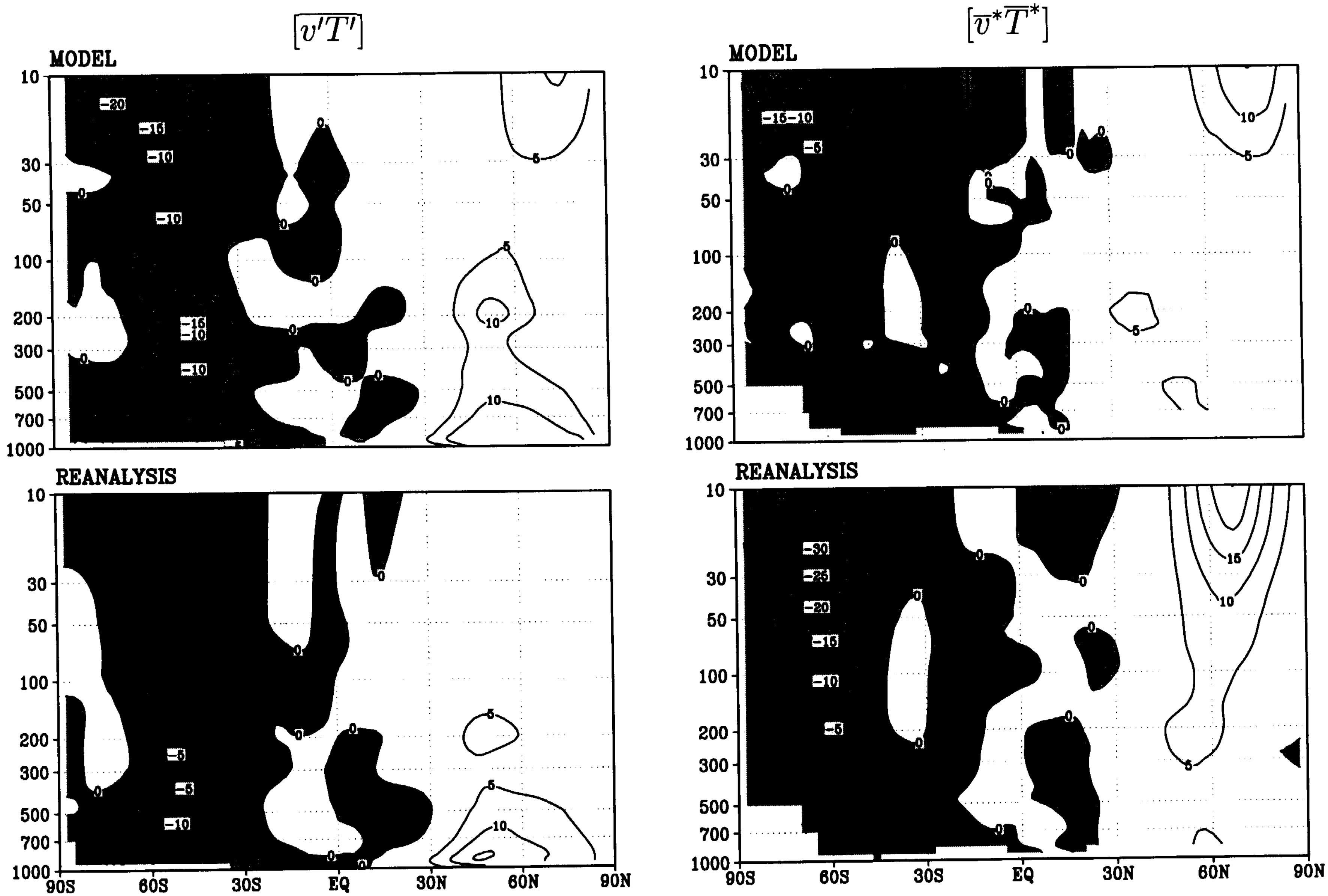

Figure 81: Zonal mean eddy meridional heat transports (m s^{-1} K) for SON— Upper panels: Model; Lower panels: Reanalysis; Left panels: Transients; Right panels: Stationary.

DJF

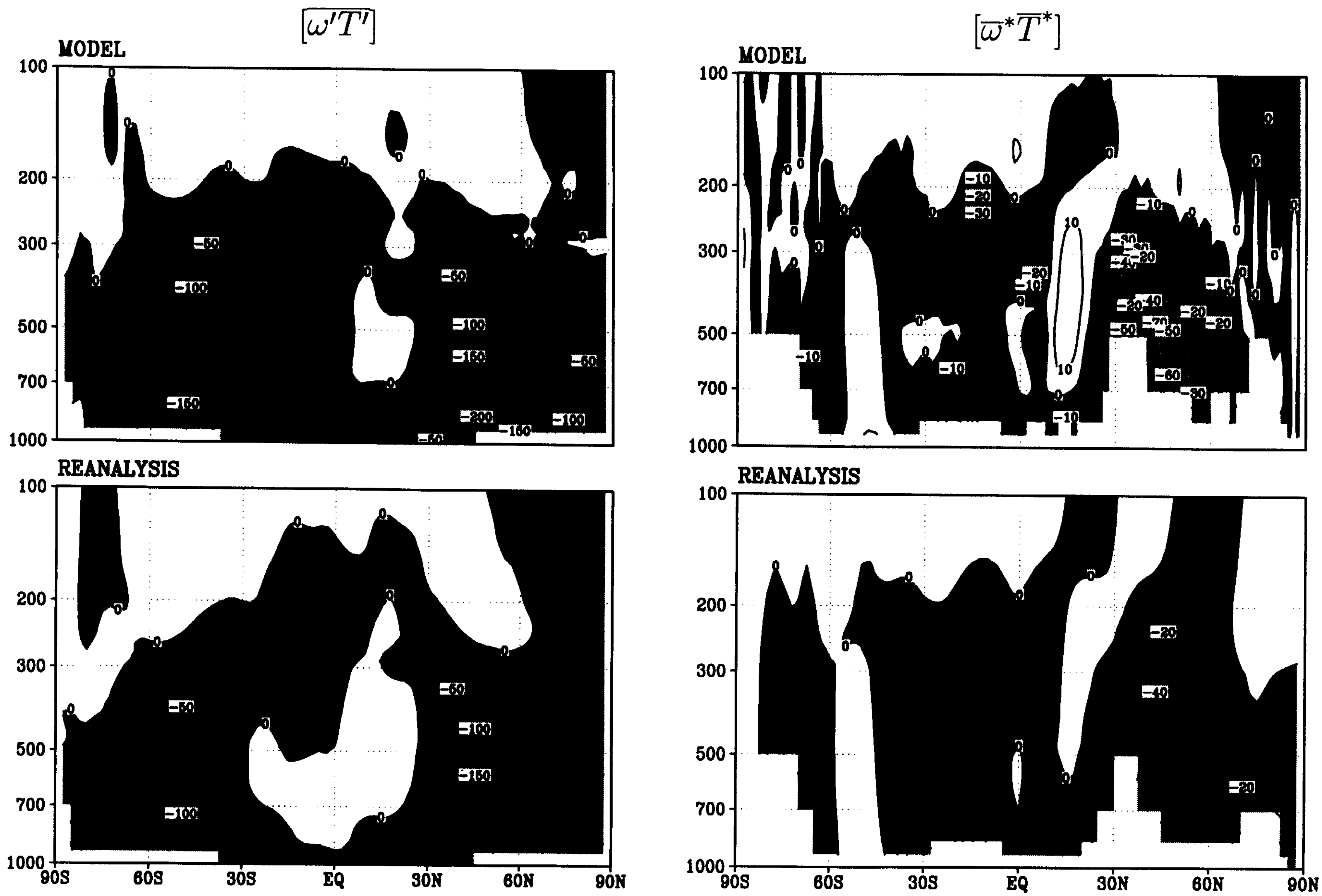

Figure 82: Zonal mean eddy vertical heat transports (mb d^{-1} K). for DJF— Upper panels: Model; Lower panels: Reanalysis; Left panels: Transients; Right panels: Stationary.

JJA

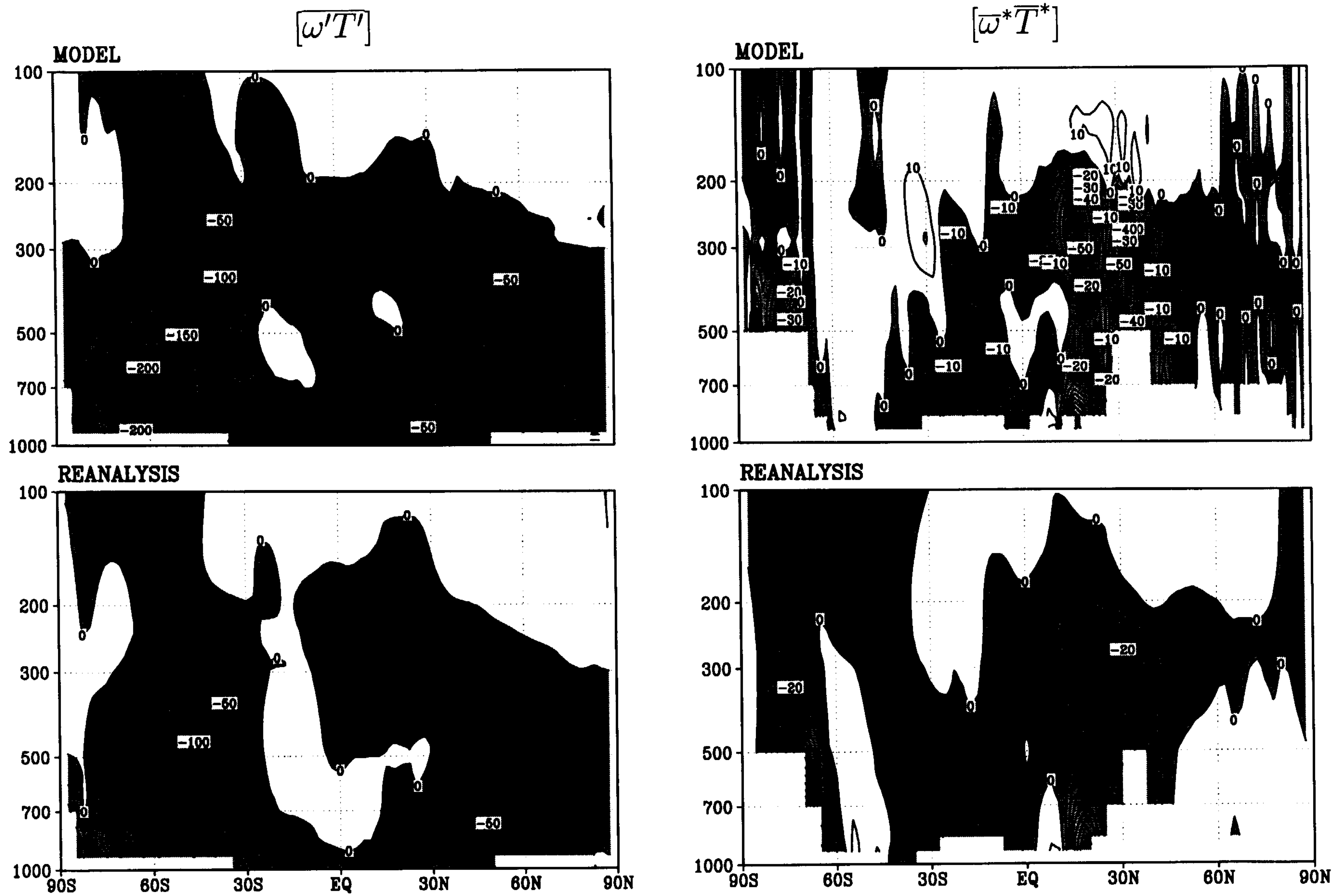

Figure 83: Zonal mean eddy vertical heat transports (mb d^{-1} K). for JJA— Upper panels: Model; Lower panels: Reanalysis; Left panels: Transients; Right panels: Stationary.

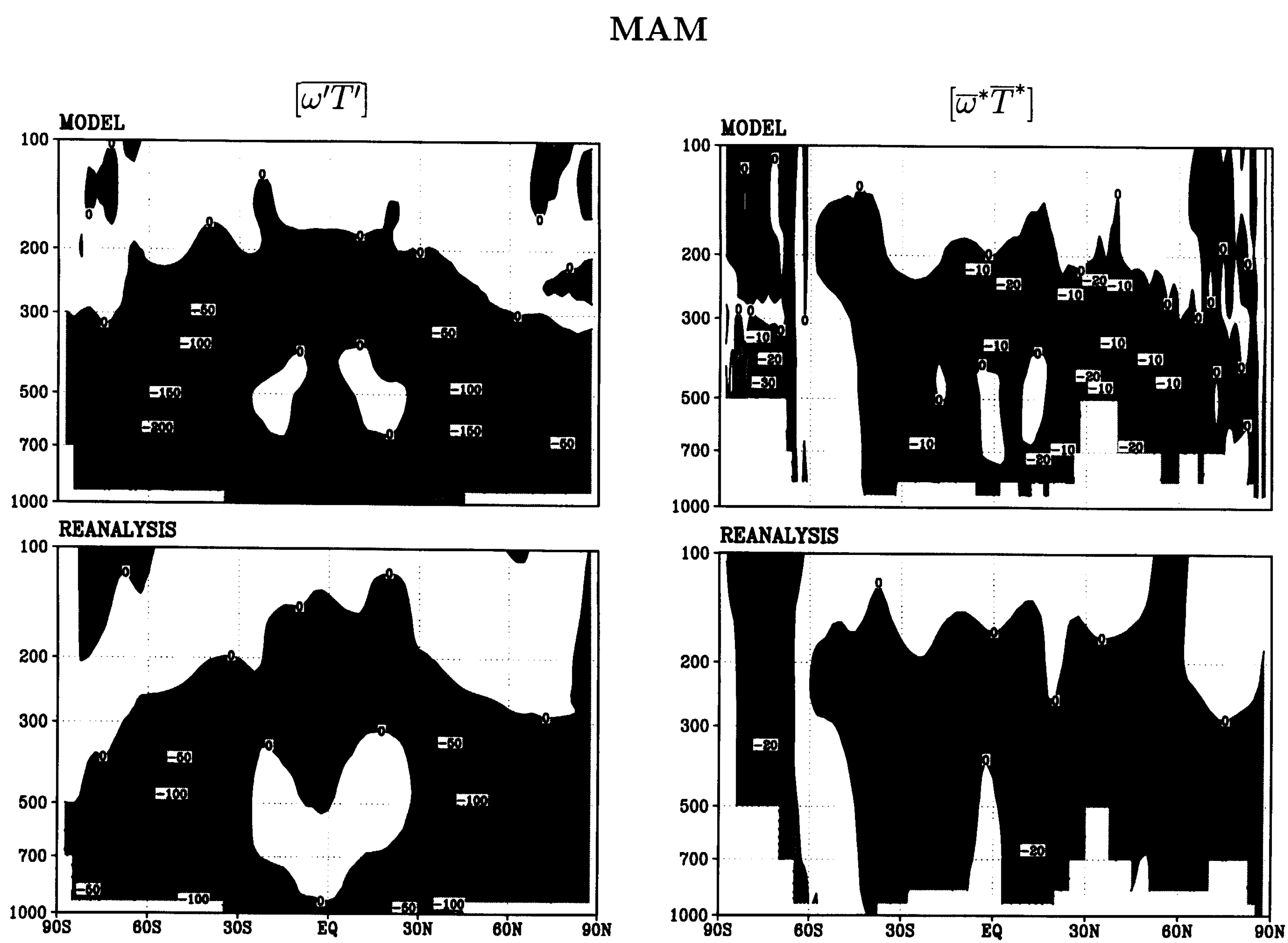

Figure 84: Zonal mean eddy vertical heat transports (mb d^{-1} K). for MAM— Upper panels: Model; Lower panels: Reanalysis; Left panels: Transients; Right panels: Stationary.

SON

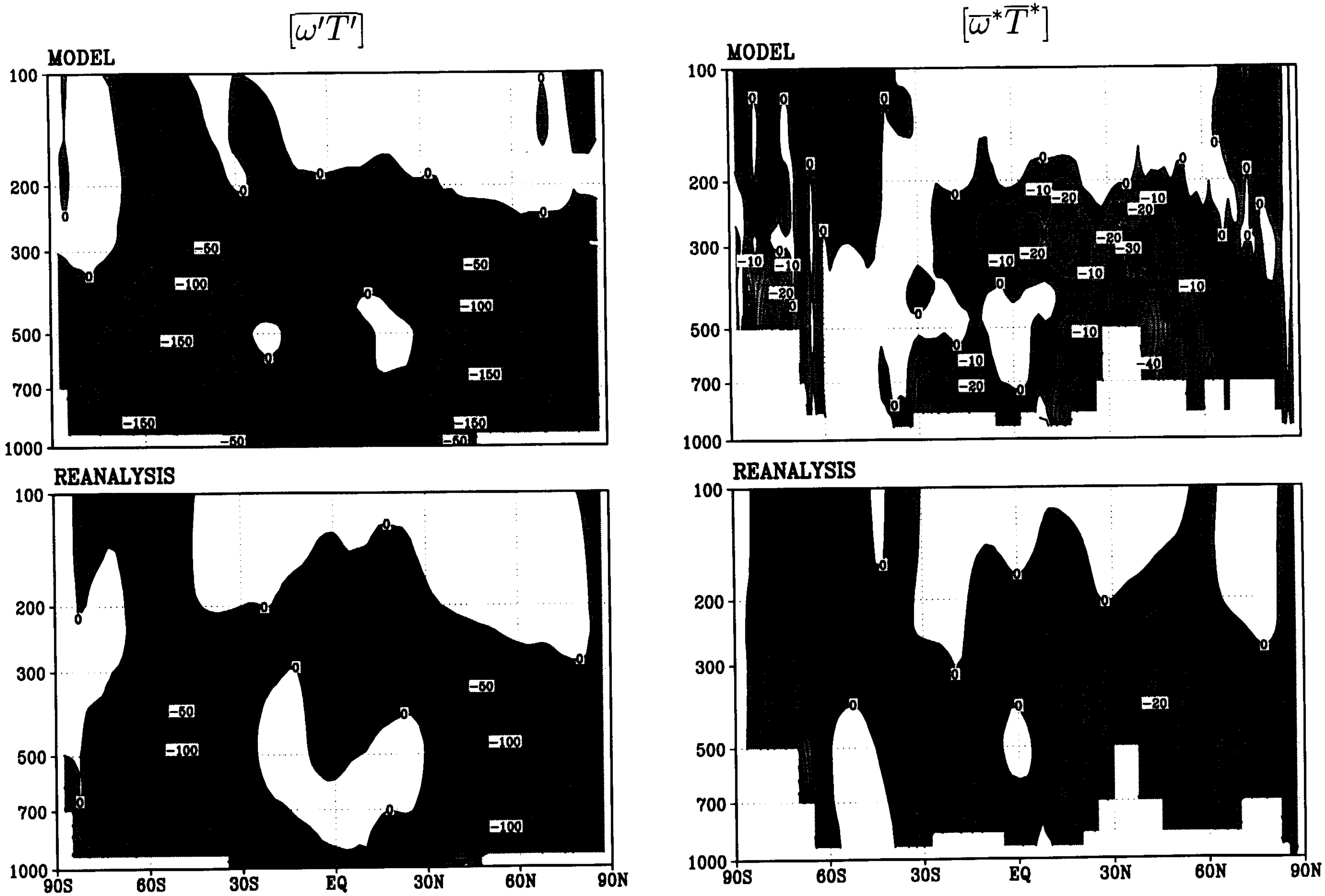

Figure 85: Zonal mean eddy vertical heat transports (mb d^{-1} K). for SON— Upper panels: Model; Lower panels: Reanalysis; Left panels: Transients; Right panels: Stationary.

DJF

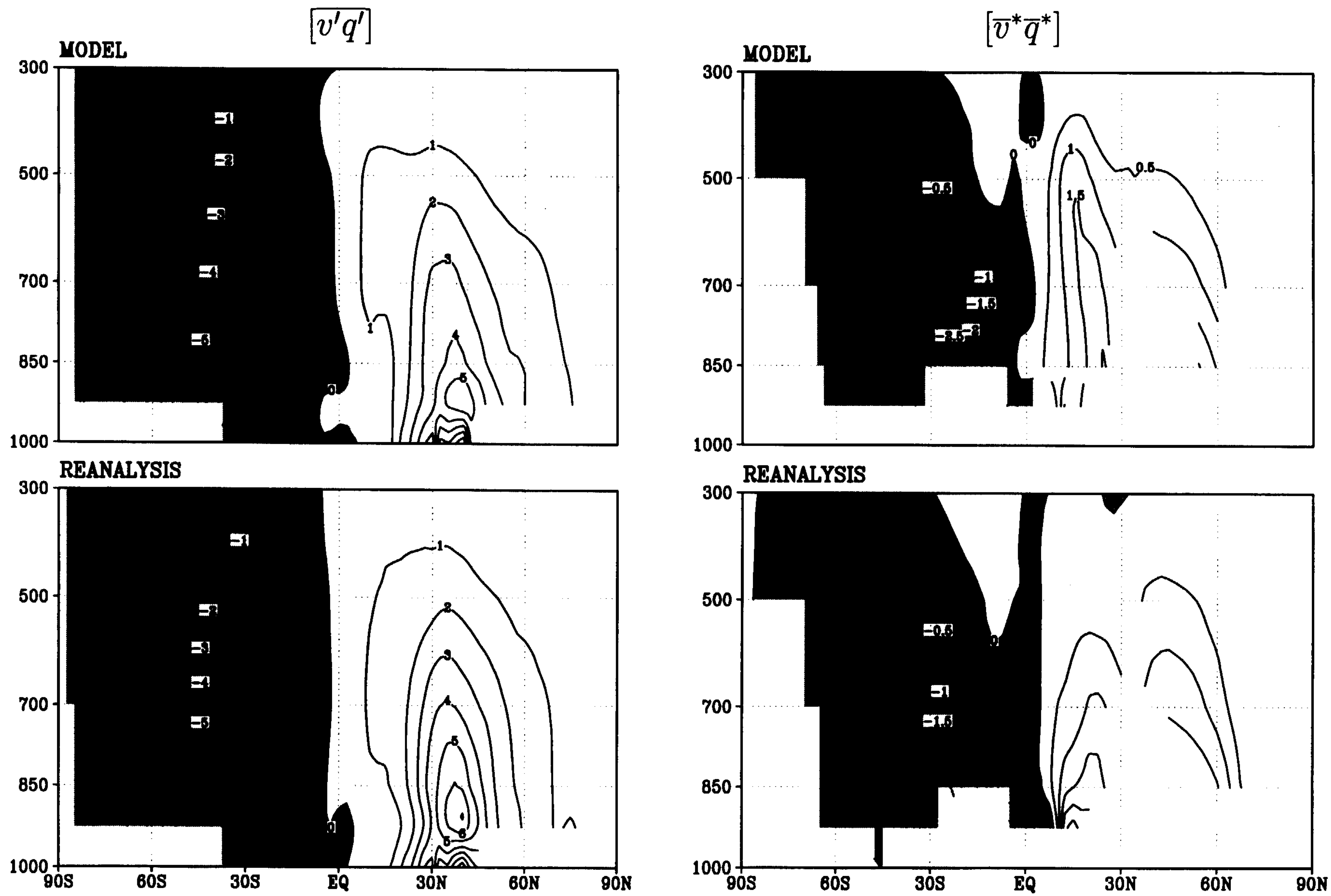

Figure 86: Zonal mean eddy meridional moisture transports (m s^{-1} g kg^{-1}) for DJF— Upper panels: Model; Lower panels: Reanalysis; Left panels: Transients; Right panels: Stationary.

JJA

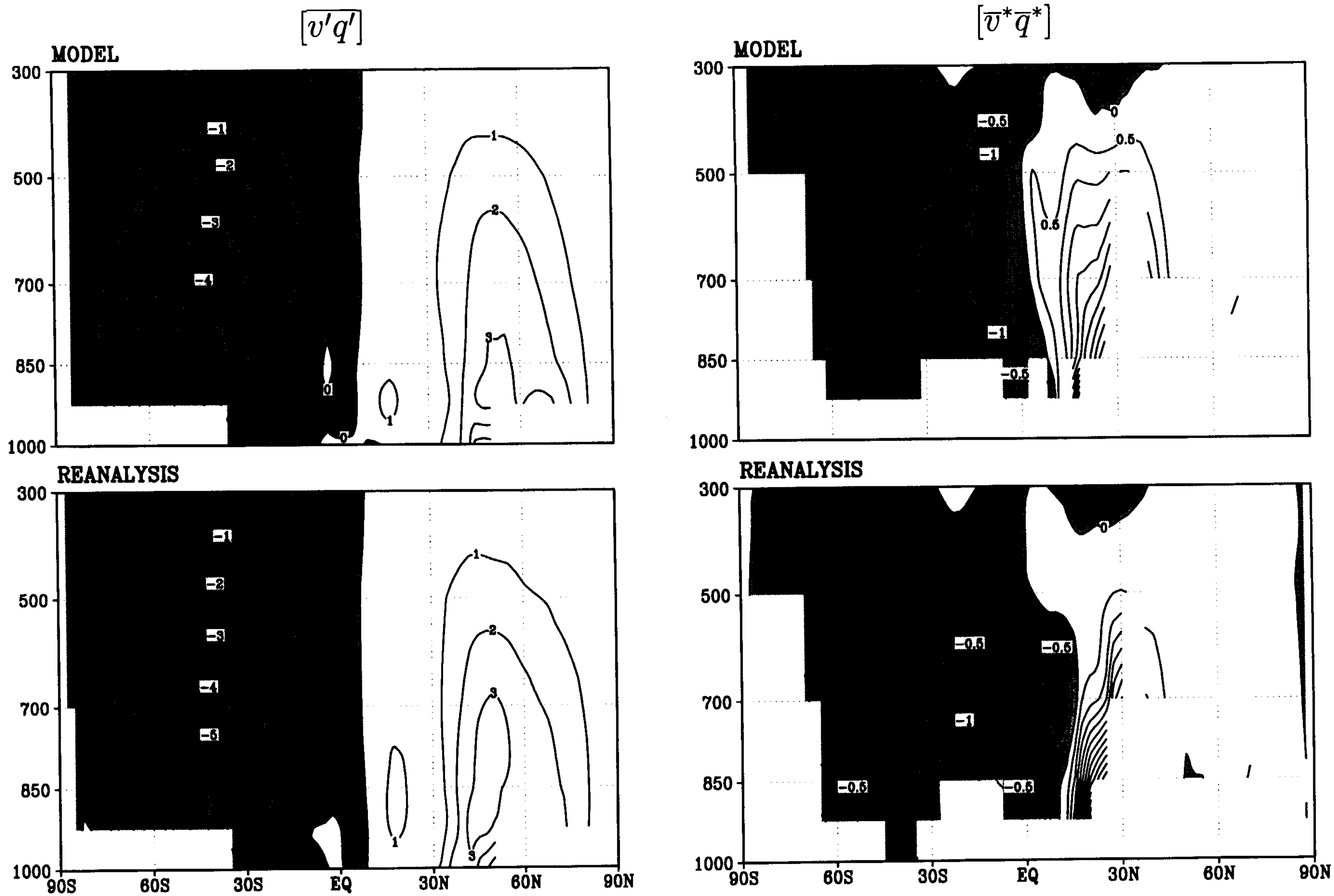

Figure 87: Zonal mean eddy meridional moisture transports (m s^{-1} g kg^{-1}) for JJA— Upper panels: Model; Lower panels: Reanalysis; Left panels: Transients; Right panels: Stationary.

MAM

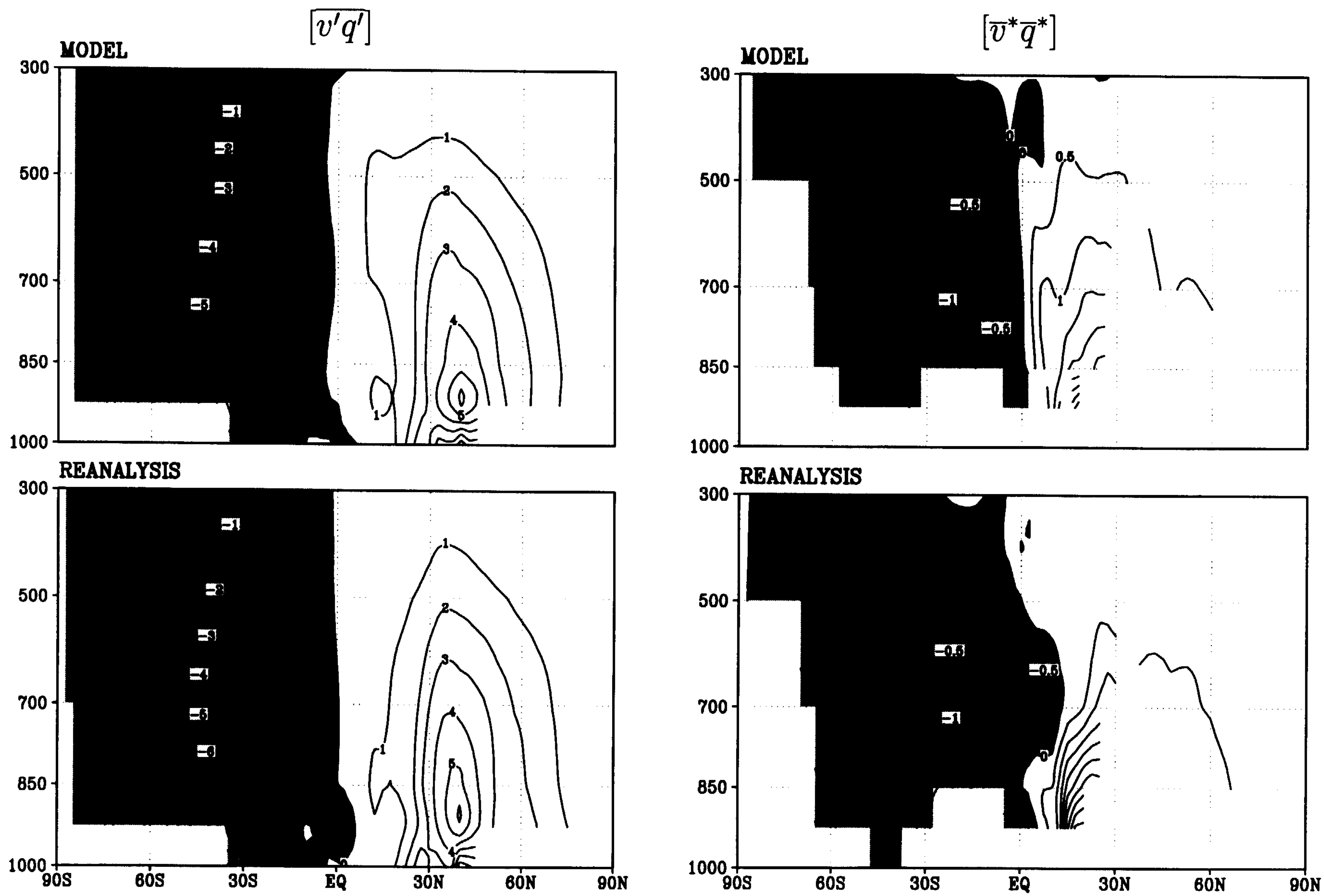

Figure 88: Zonal mean eddy meridional moisture transports (m s^{-1} g kg^{-1}) for MAM— Upper panels: Model; Lower panels: Reanalysis; Left panels: Transients; Right panels: Stationary.

SON

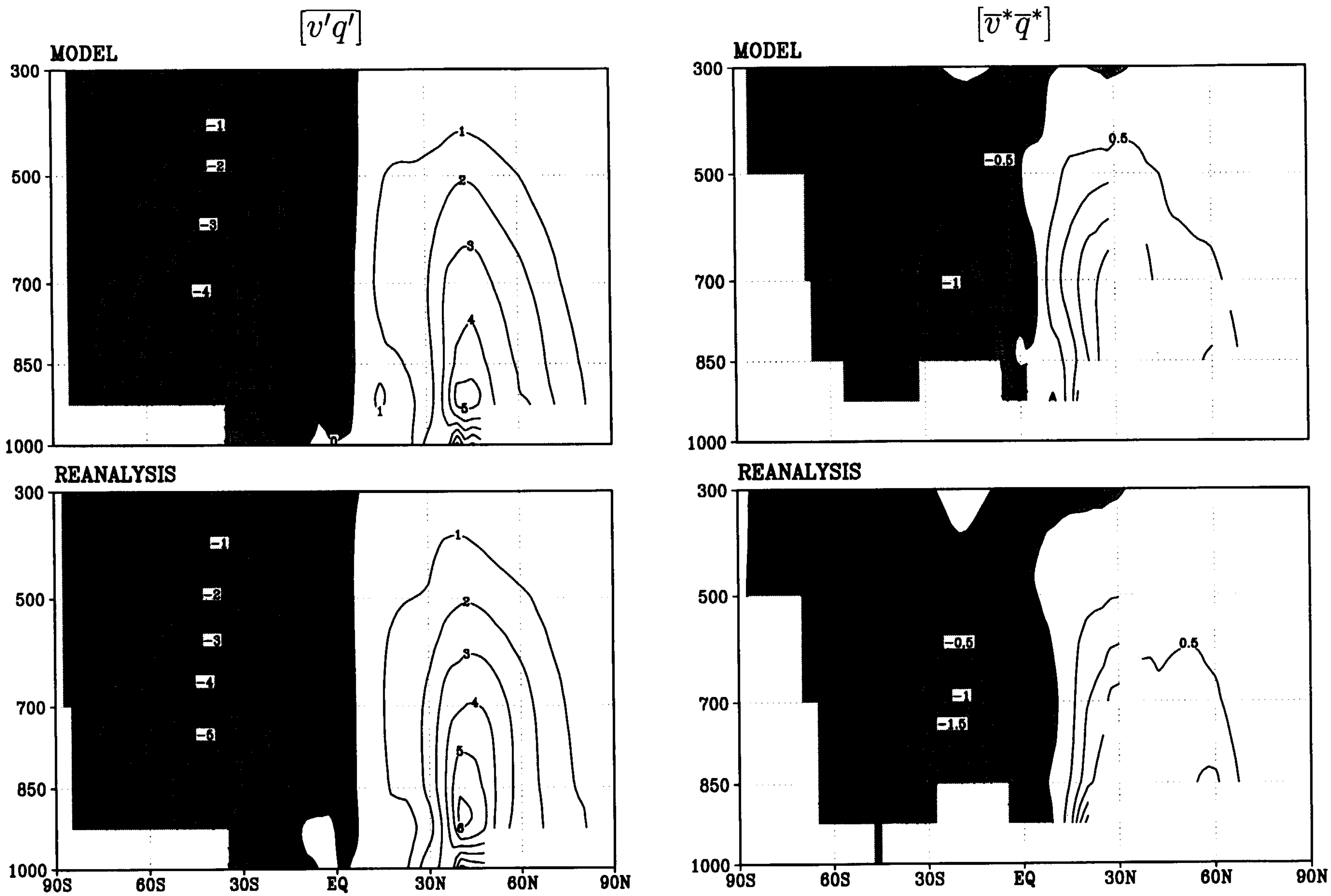

Figure 89: Zonal mean eddy meridional moisture transports (m s^{-1} g kg^{-1}) for SON— Upper panels: Model; Lower panels: Reanalysis; Left panels: Transients; Right panels: Stationary.

$$\frac{1}{2}[\overline{(u')^2} + \overline{(v')^2}]$$

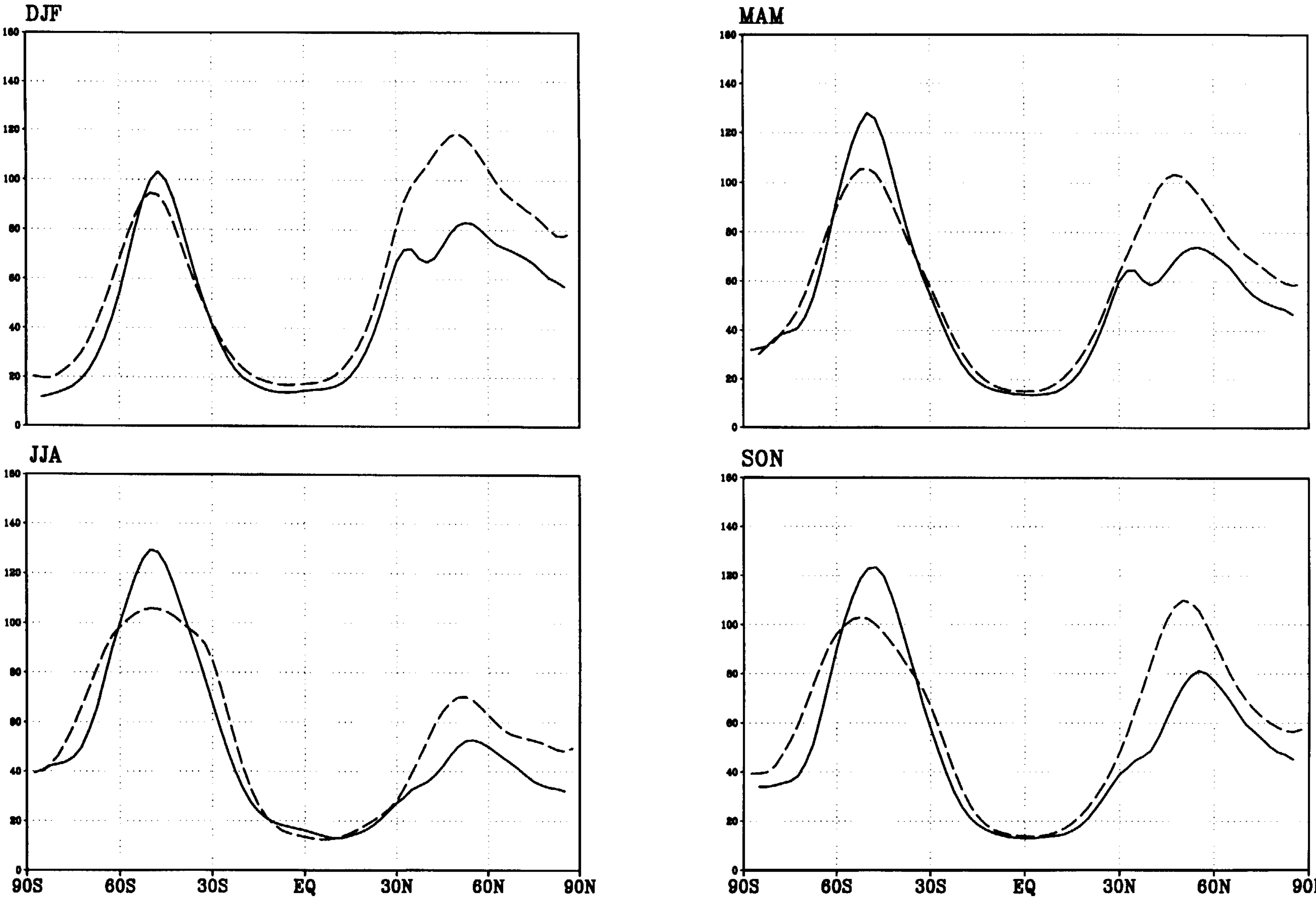

Figure 90: Vertical mean transient eddy kinetic energy (m^2 s^{-2}). Solid: Model, Dashed:Reanalysis.

$[\overline{(\omega')^2}]$

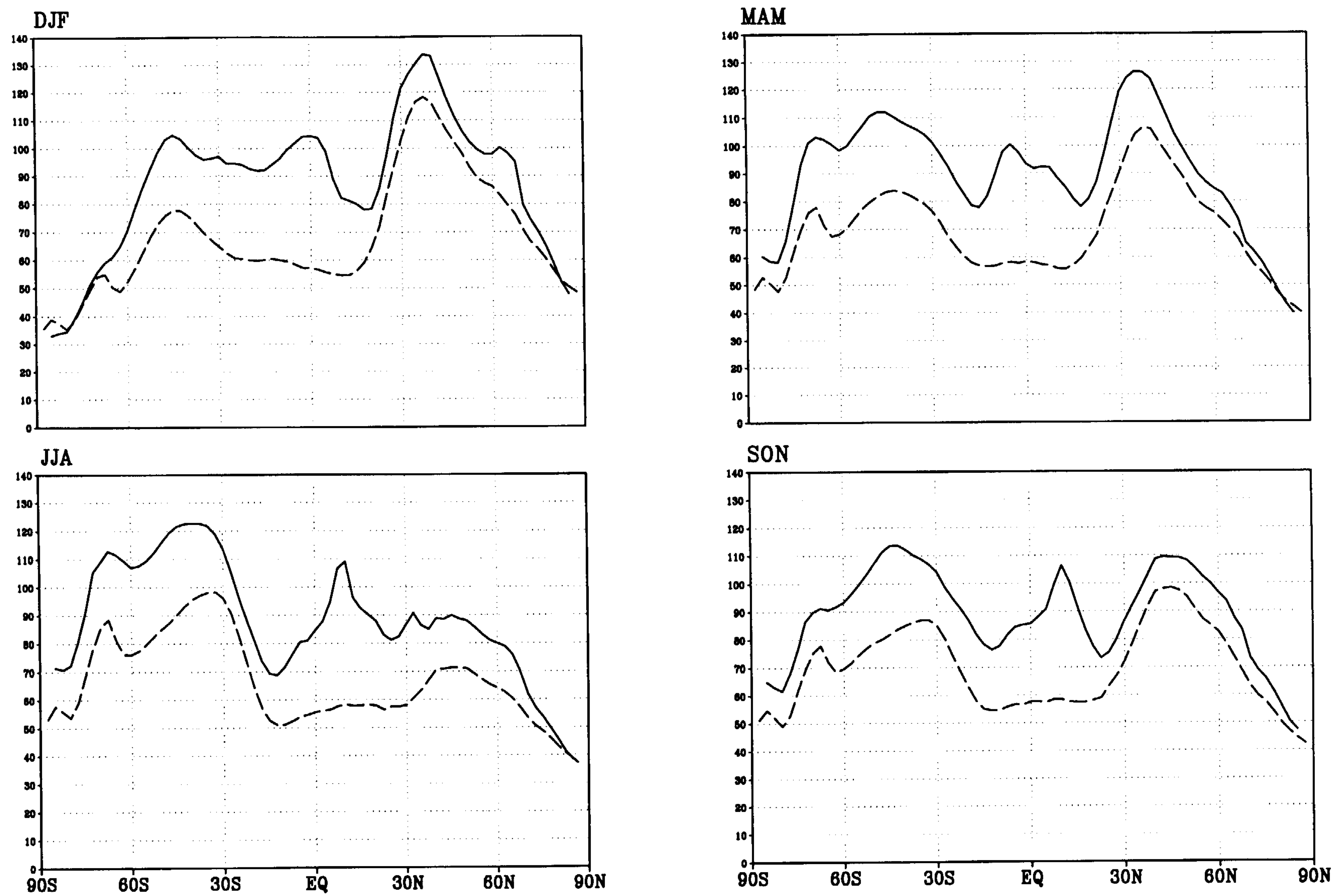

Figure 91: Square root of the vertical mean $[\overline{(\omega')^2}]$ (mb d^{-1}) Solid: Model, Dashed:Reanalysis.

$$[\overline{(T')^2}]$$

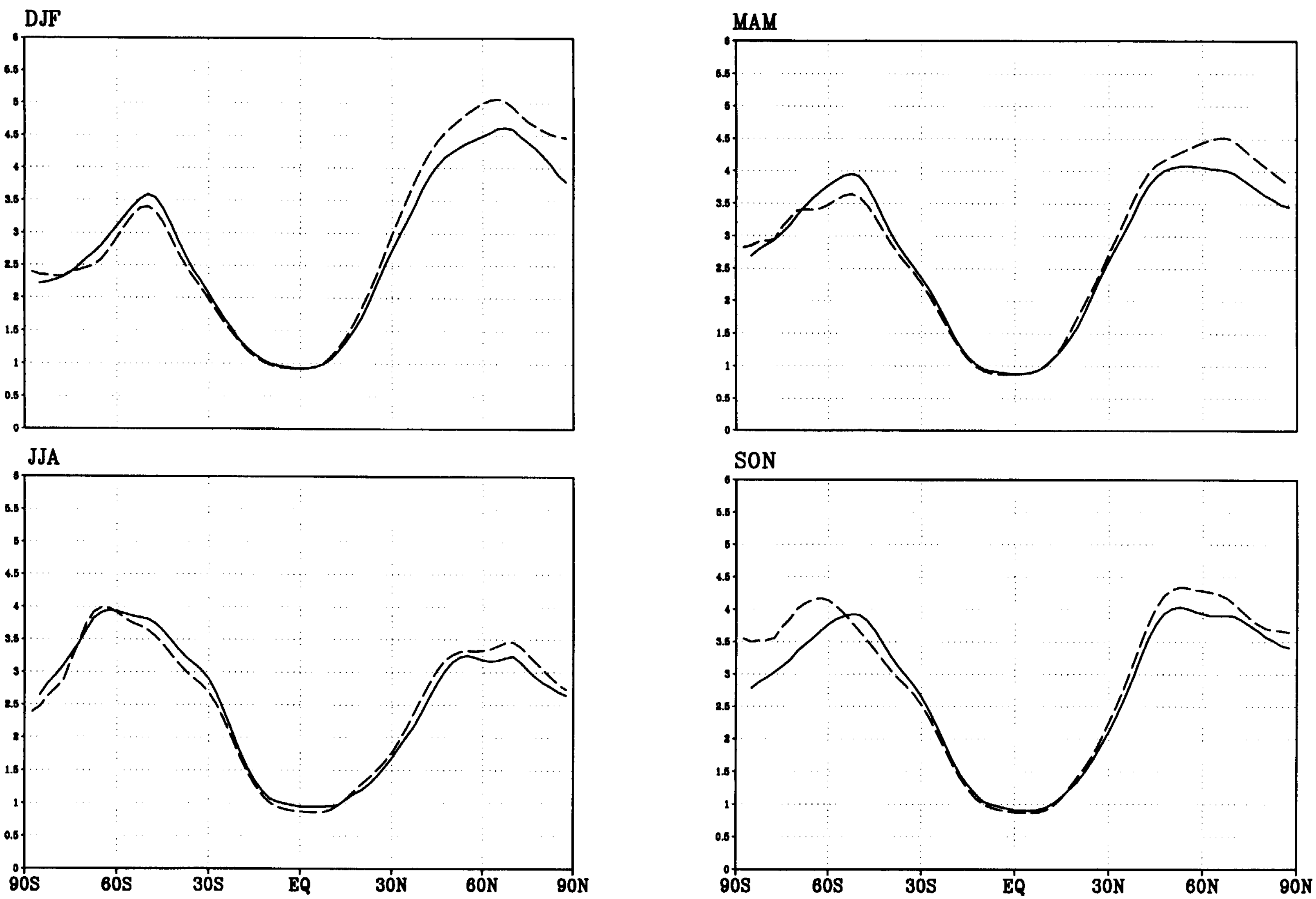

Figure 92: Square root of the vertical mean $[\overline{(T')^2}]$ (K) Solid: Model, Dashed:Reanalysis.

$$[\overline{(Z')^2}]$$

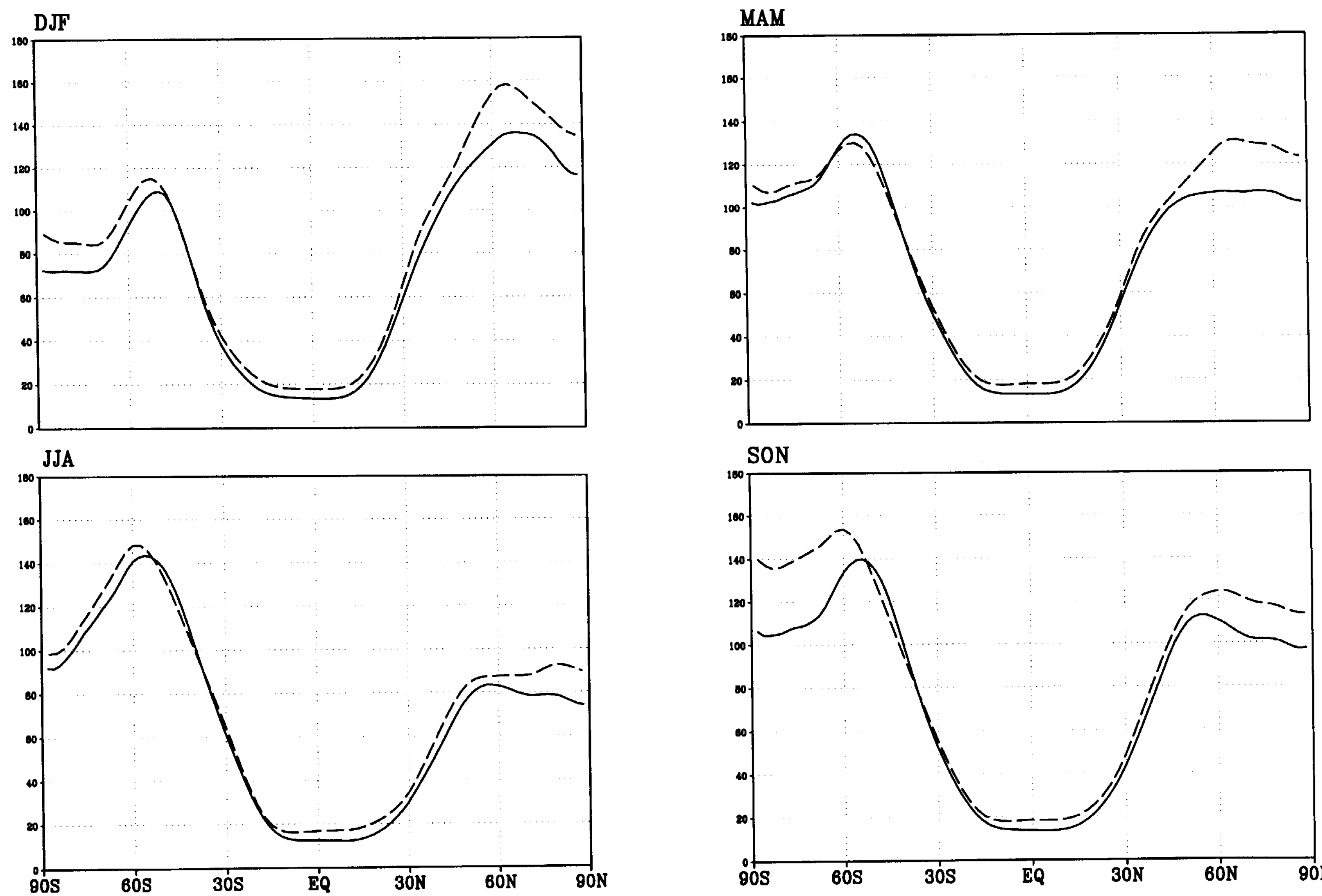

Figure 93: Square root of the vertical mean $[\overline{(Z')^2}]$ (m) Solid: Model, Dashed:Reanalysis.

$[u'v']$

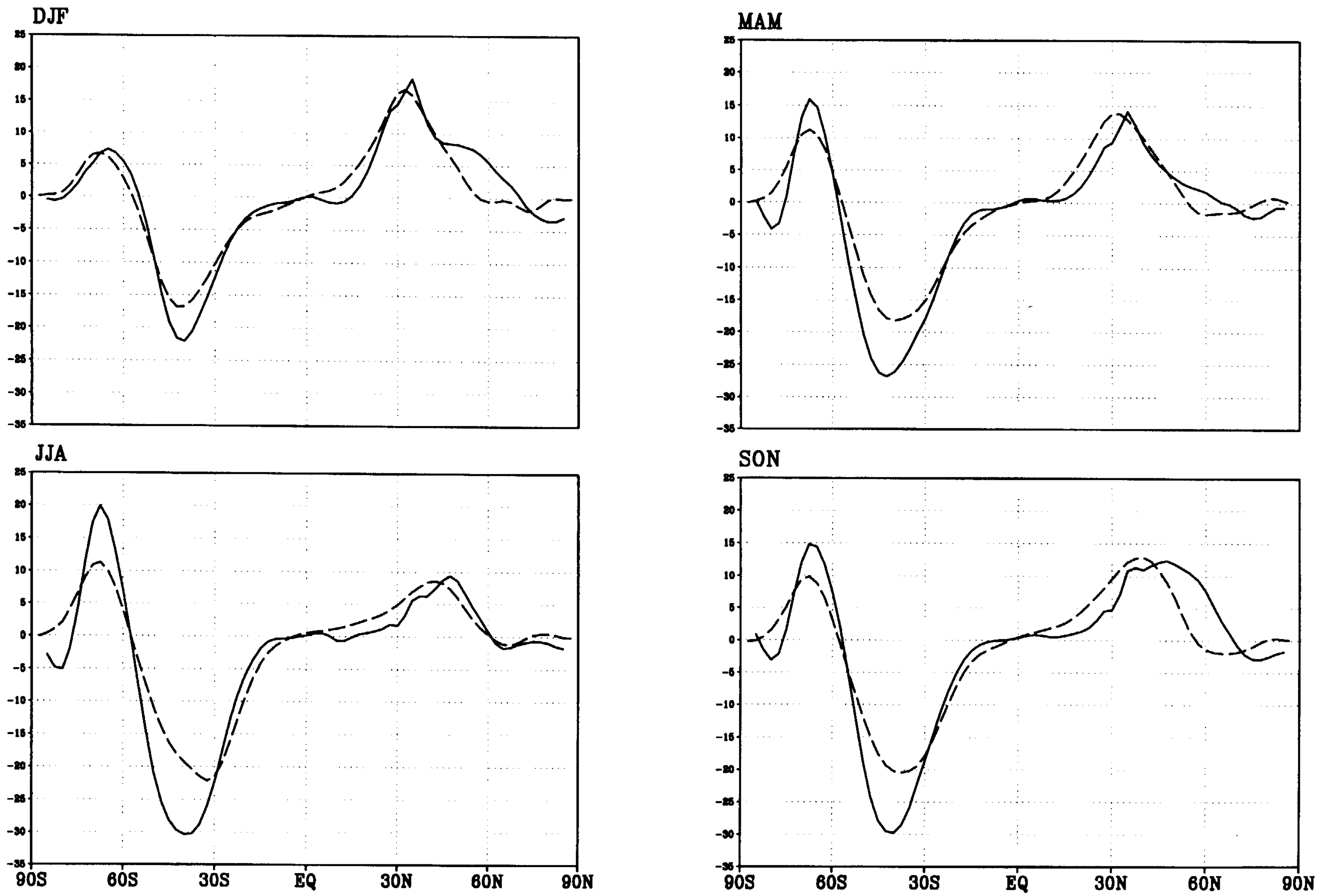

Figure 94: Vertical mean $[\overline{u'v'}]$ (m^2 s^{-2}) Solid: Model, Dashed:Reanalysis.

$[\overline{v'T'}]$

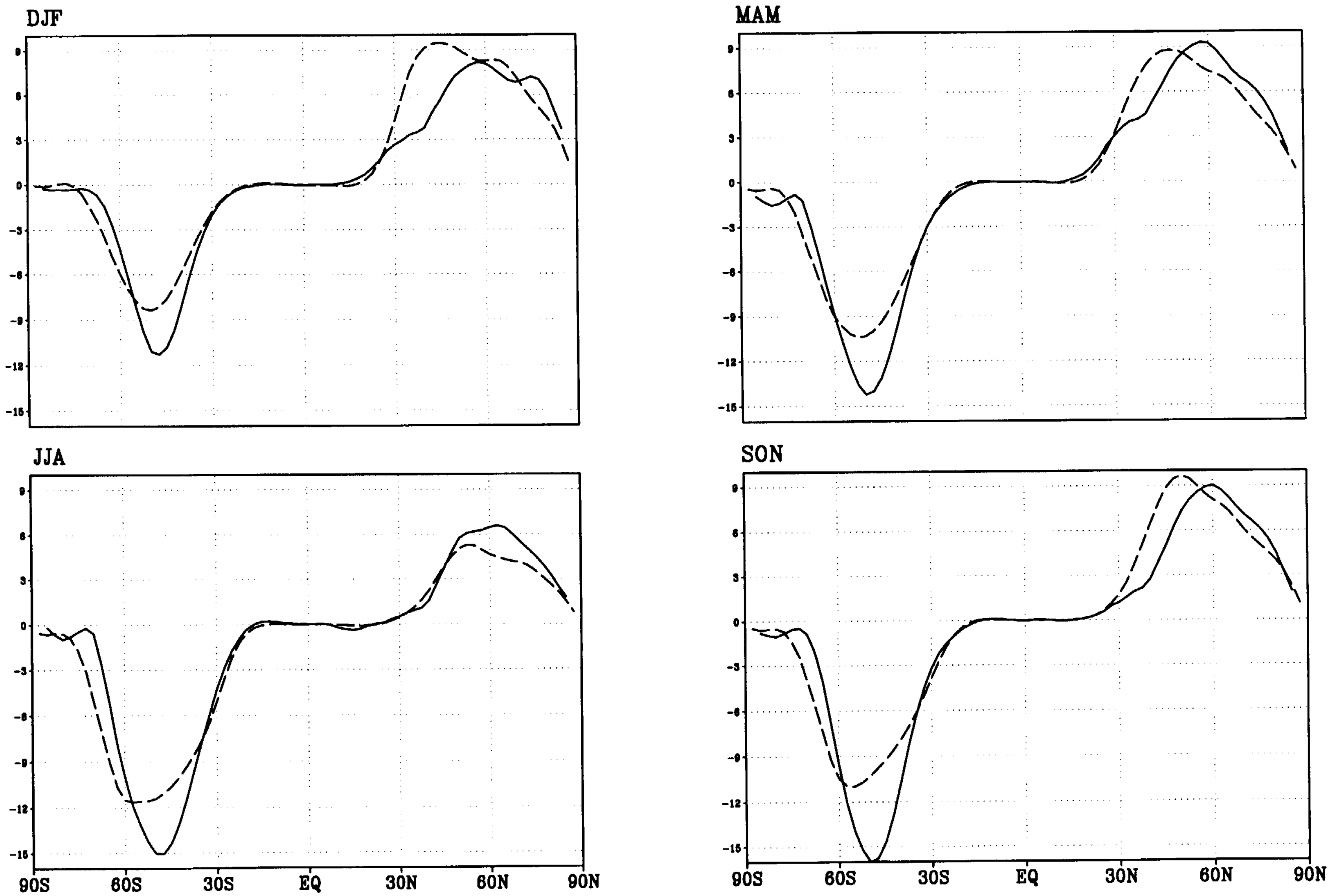

Figure 95: Vertical mean $[\overline{v'T'}]$ (m s^{-1} K) Solid: Model, Dashed:Reanalysis.

$\overline{[\omega' T']}$

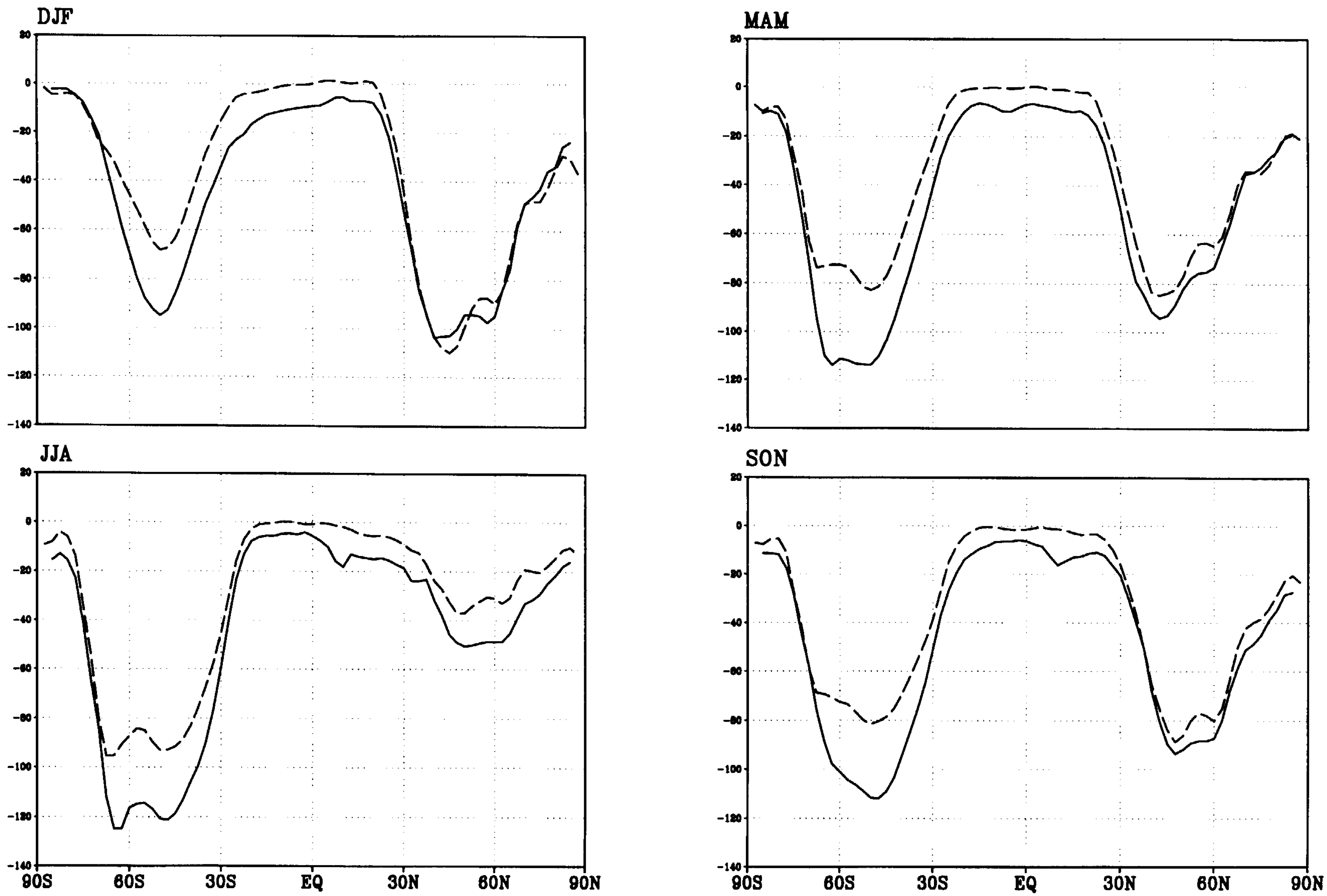

Figure 96: Vertical mean $\overline{[\omega' T']}$ (mb d^{-1} K) Solid: Model, Dashed:Reanalysis.

$\left[\overline{v'q'}\right]$

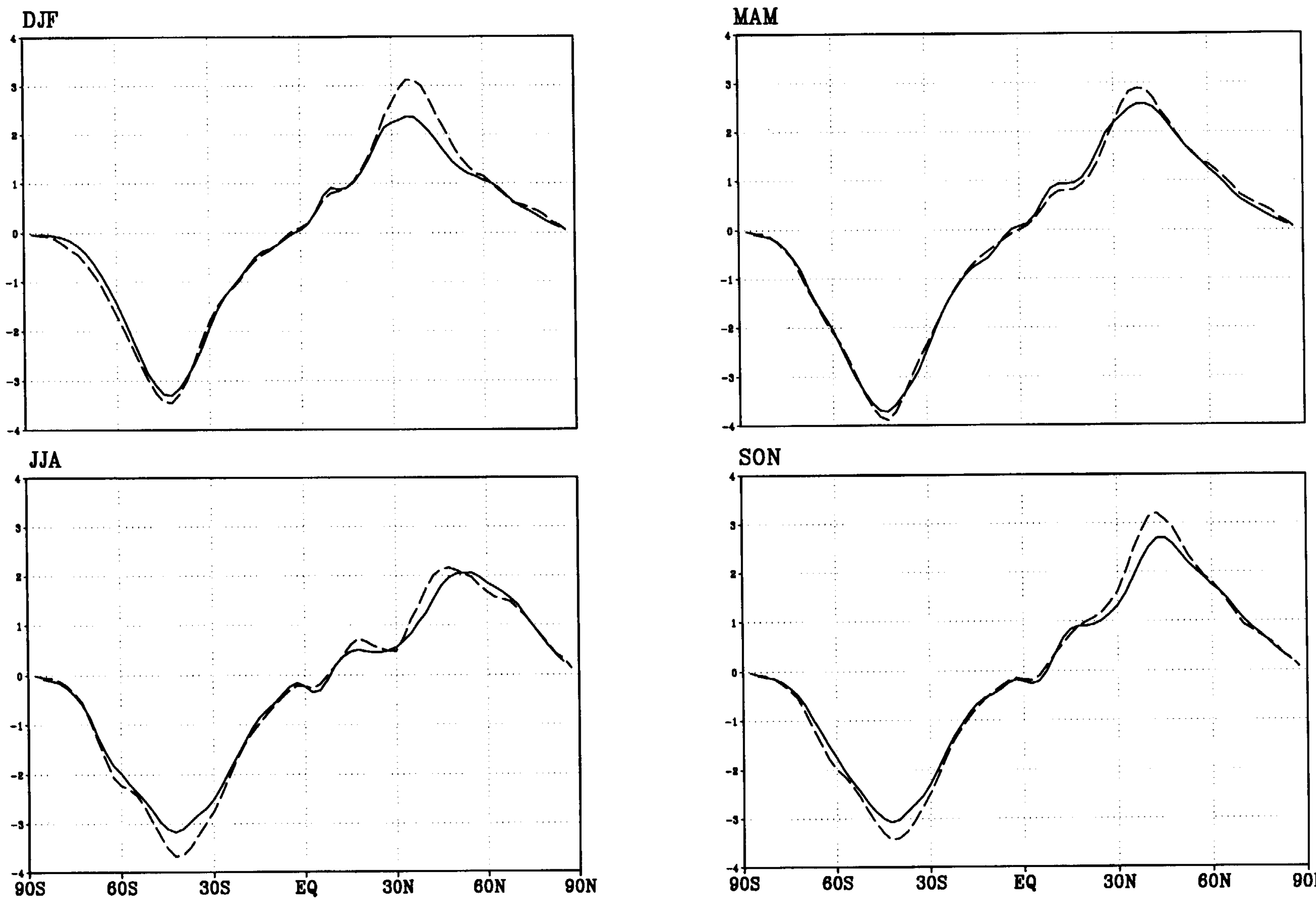

Figure 97: Vertical mean $\left[\overline{v'q'}\right]$ (m s^{-1} g kg^{-1}) Solid: Model, Dashed:Reanalysis.

GLOBAL MAPS OF SELECTED STATISTICS

(DJF, MAM, JJA, SON)

$\sqrt{[\overline{(u')^2}]}$ 200 mb

$\sqrt{[\overline{(v')^2}]}$ 200 mb

$\frac{1}{2}[\overline{(u')^2} + \overline{(v')^2}]$ 200 mb

$\sqrt{[\overline{(\omega')^2}]}$ 500 mb

$\sqrt{[\overline{(T')^2}]}$ 850 mb

$\sqrt{[\overline{(Z')^2}]}$ 200 mb

$\sqrt{[\overline{(\chi')^2}]}$ 200 mb

$[\overline{u'v'}]$ 200 mb

$[\overline{v'T'}]$ 850 mb

-$[\overline{\omega'T'}]$ 850 mb

$[\overline{v'q'}]$ 850 mb

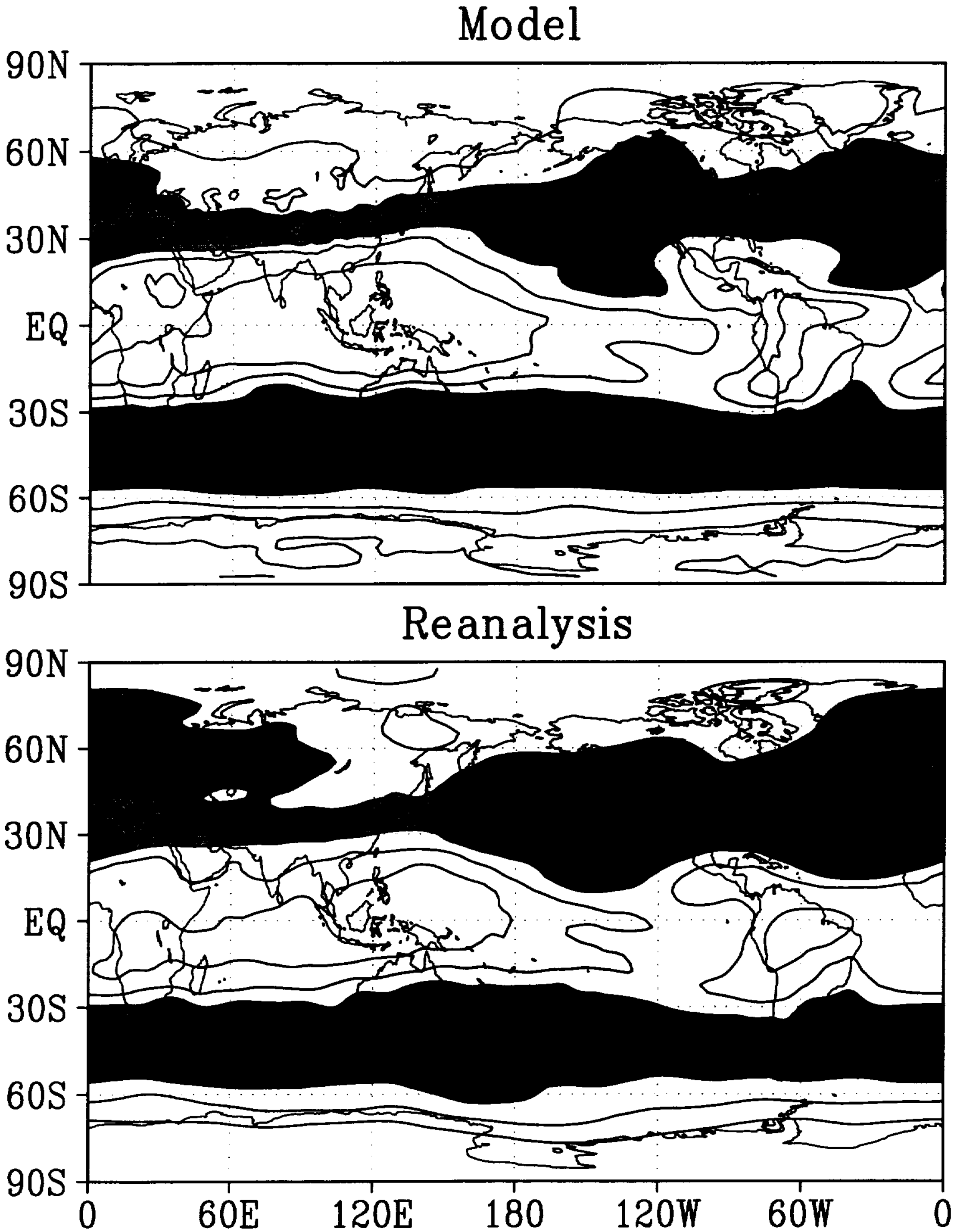

Figure 98: $\sqrt{[\overline{(u')^2}]}$ at 200mb for DJF— Top: Model, Bottom: Reanalysis. Contour interval: 2 m s^{-1}. Shading indicates values exceeding 6 m s^{-1}.

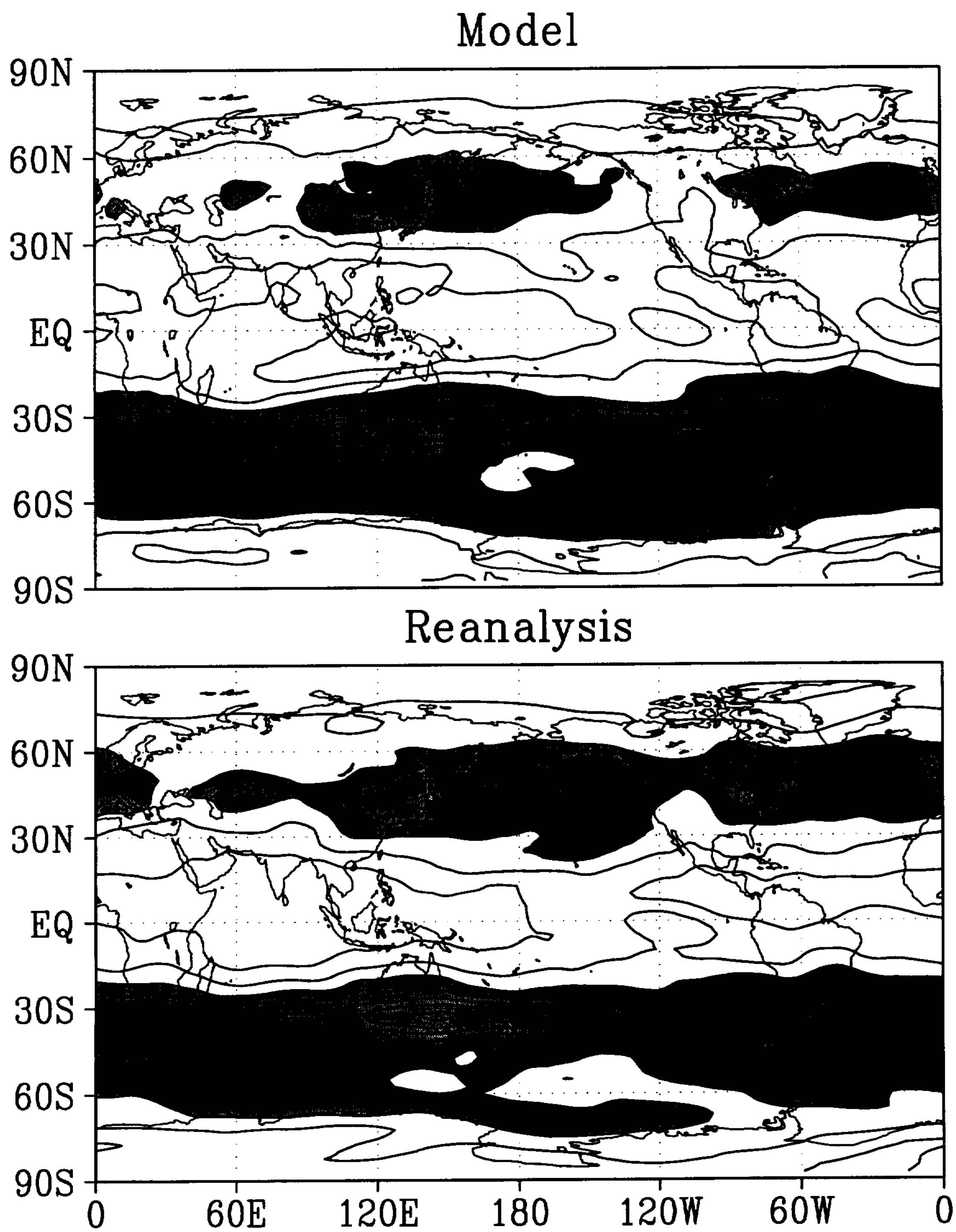

Figure 99: $\sqrt{[\overline{(u')^2}]}$ at 200mb for JJA— Top: Model, Bottom: Reanalysis. Contour interval: 2 m s^{-1}. Shading indicates values exceeding 6 m s^{-1}.

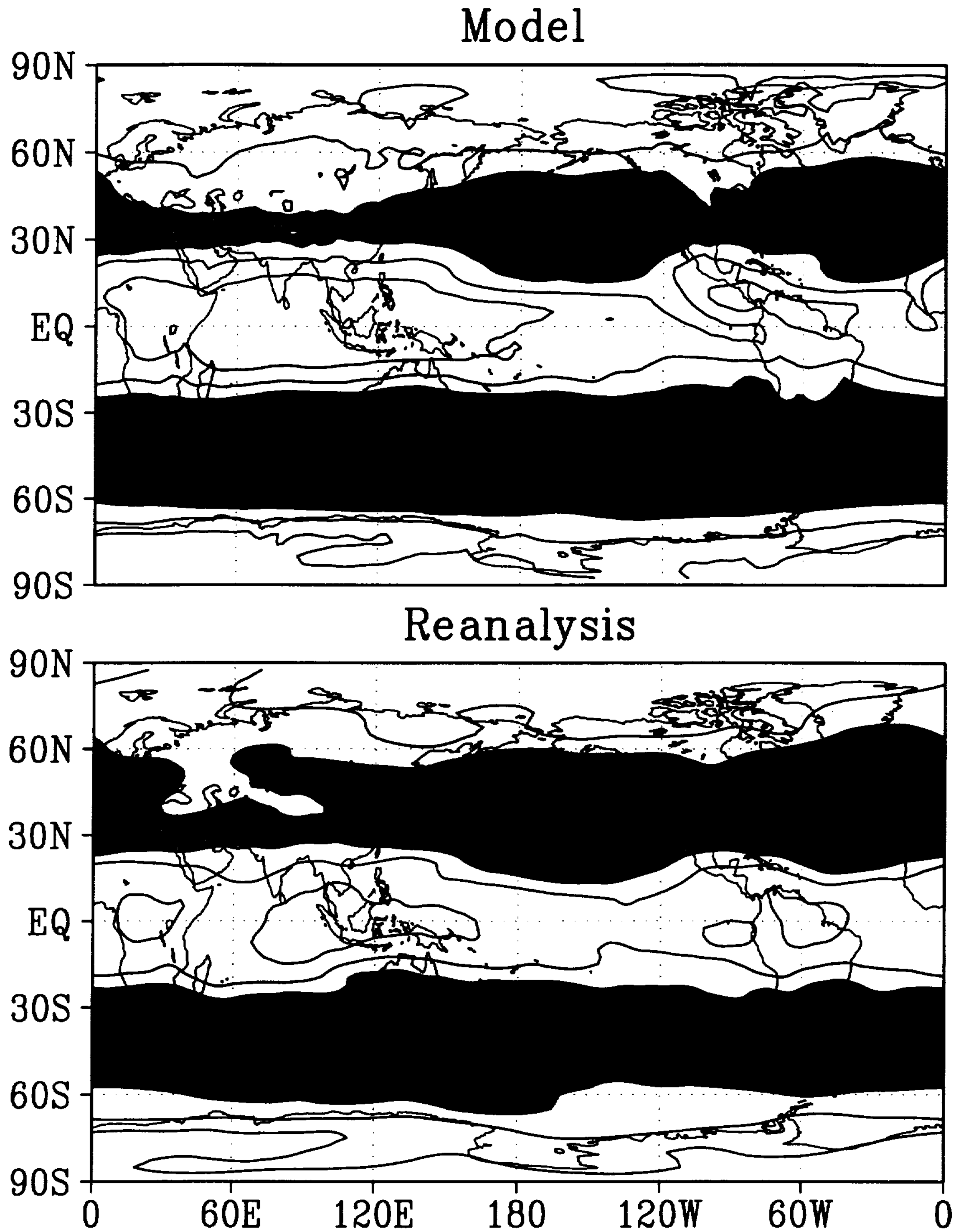

Figure 100: $\sqrt{[\overline{(u')^2}]}$ at 200mb for MAM— Top: Model, Bottom: Reanalysis. Contour interval: 2 m s^{-1}. Shading indicates values exceeding 6 m s^{-1}.

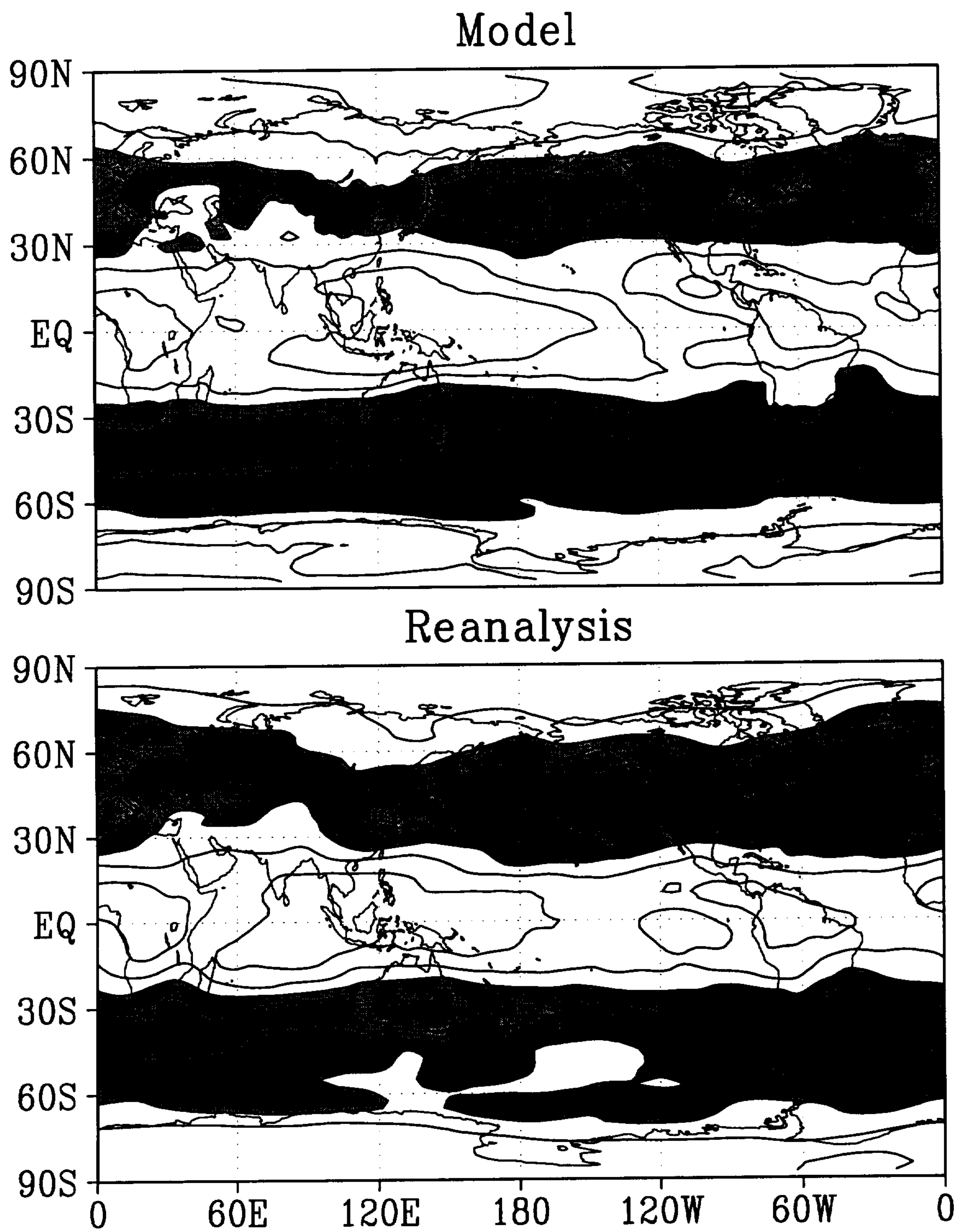

Figure 101: $\sqrt{[\overline{(u')^2}]}$ at 200mb for SON— Top: Model, Bottom: Reanalysis. Contour interval: 2 m s^{-1}. Shading indicates values exceeding 6 m s^{-1}.

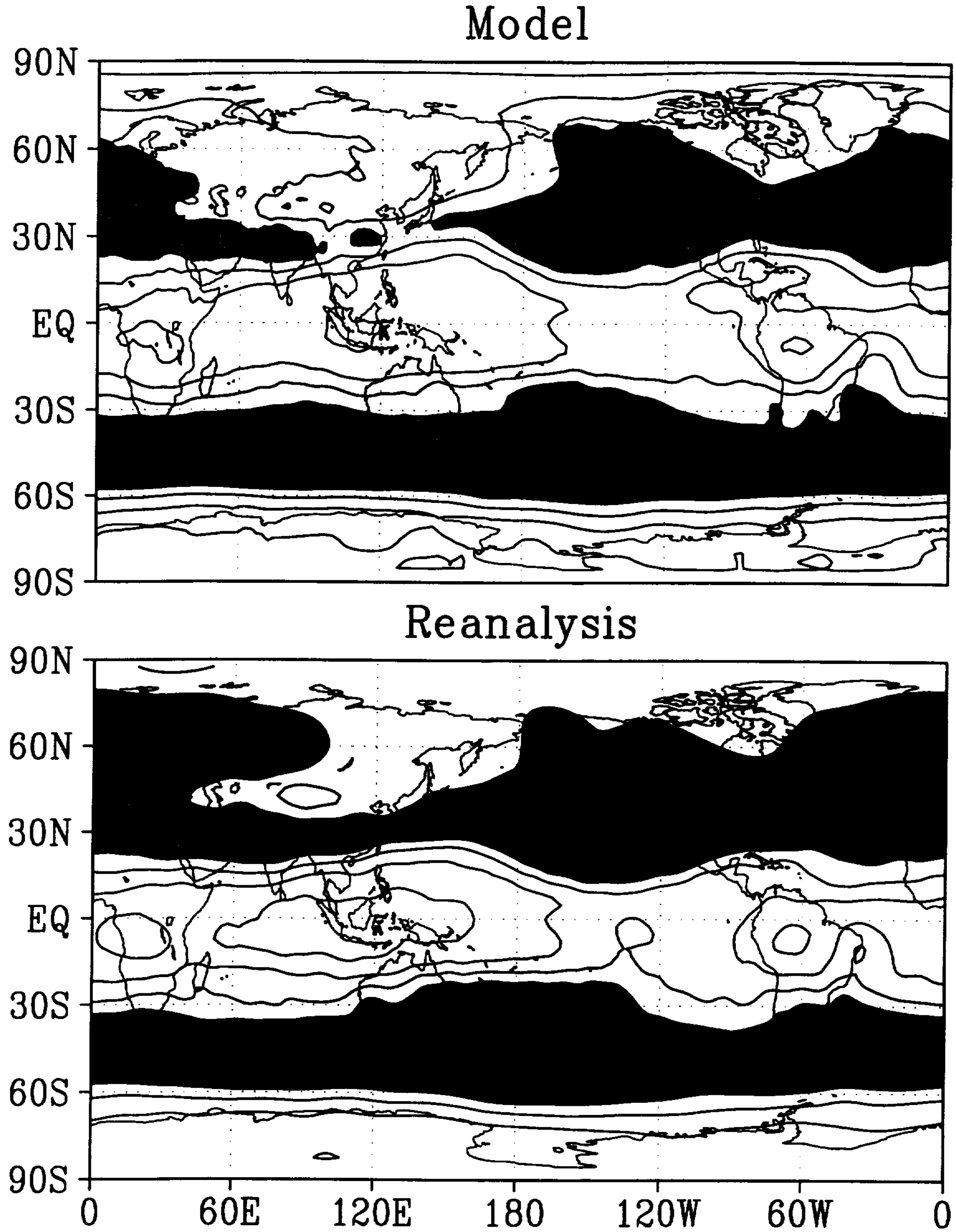

Figure 102: $\sqrt{[\overline{(v')^2}]}$ at 200mb for DJF— Top: Model, Bottom: Reanalysis. Contour interval: 2 m s^{-1}. Shading indicates values exceeding 6 m s^{-1}.

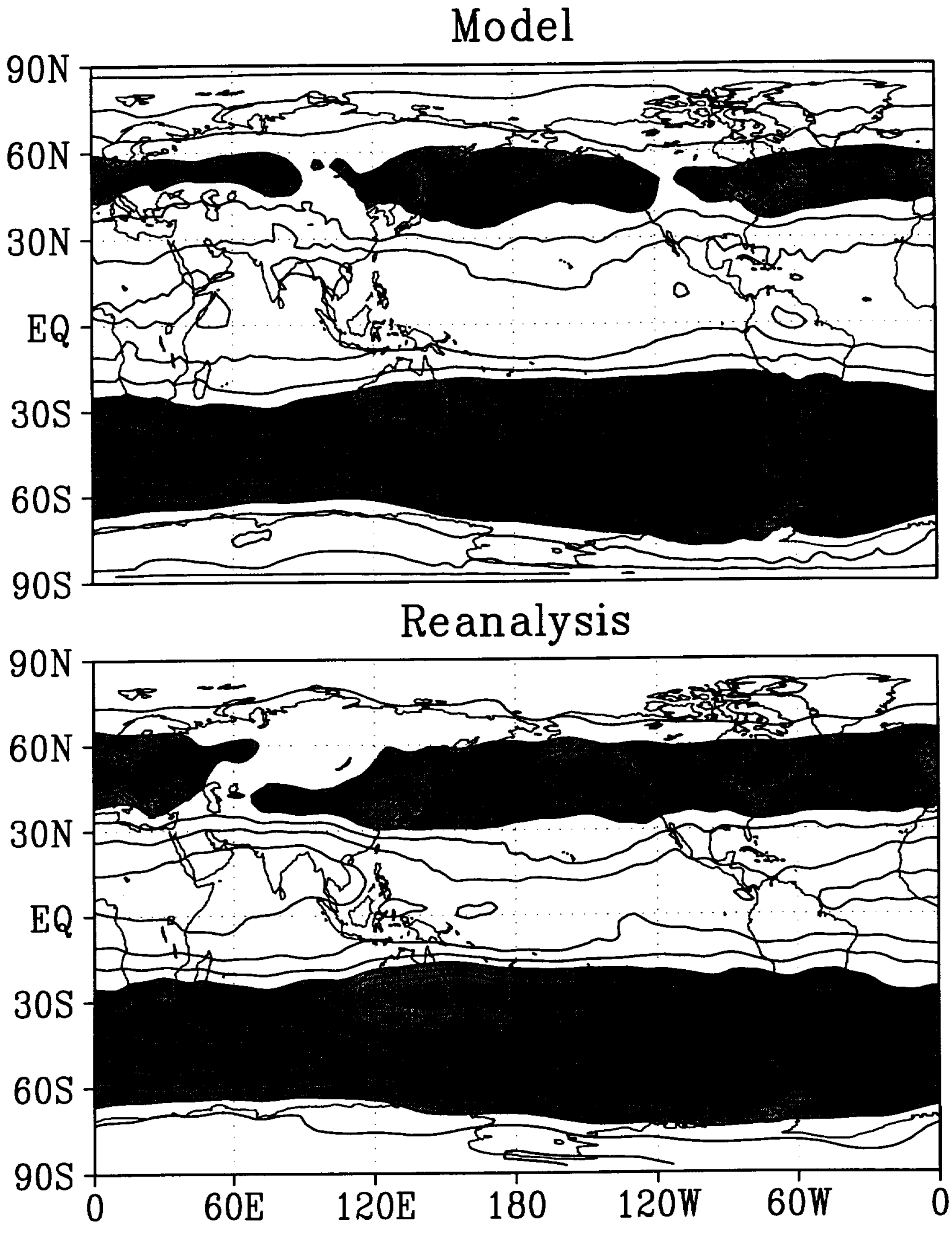

Figure 103: $\sqrt{[\overline{(v')^2}]}$ at 200mb for JJA— Top: Model, Bottom: Reanalysis. Contour interval: 2 m s^{-1}. Shading indicates values exceeding 6 m s^{-1}.

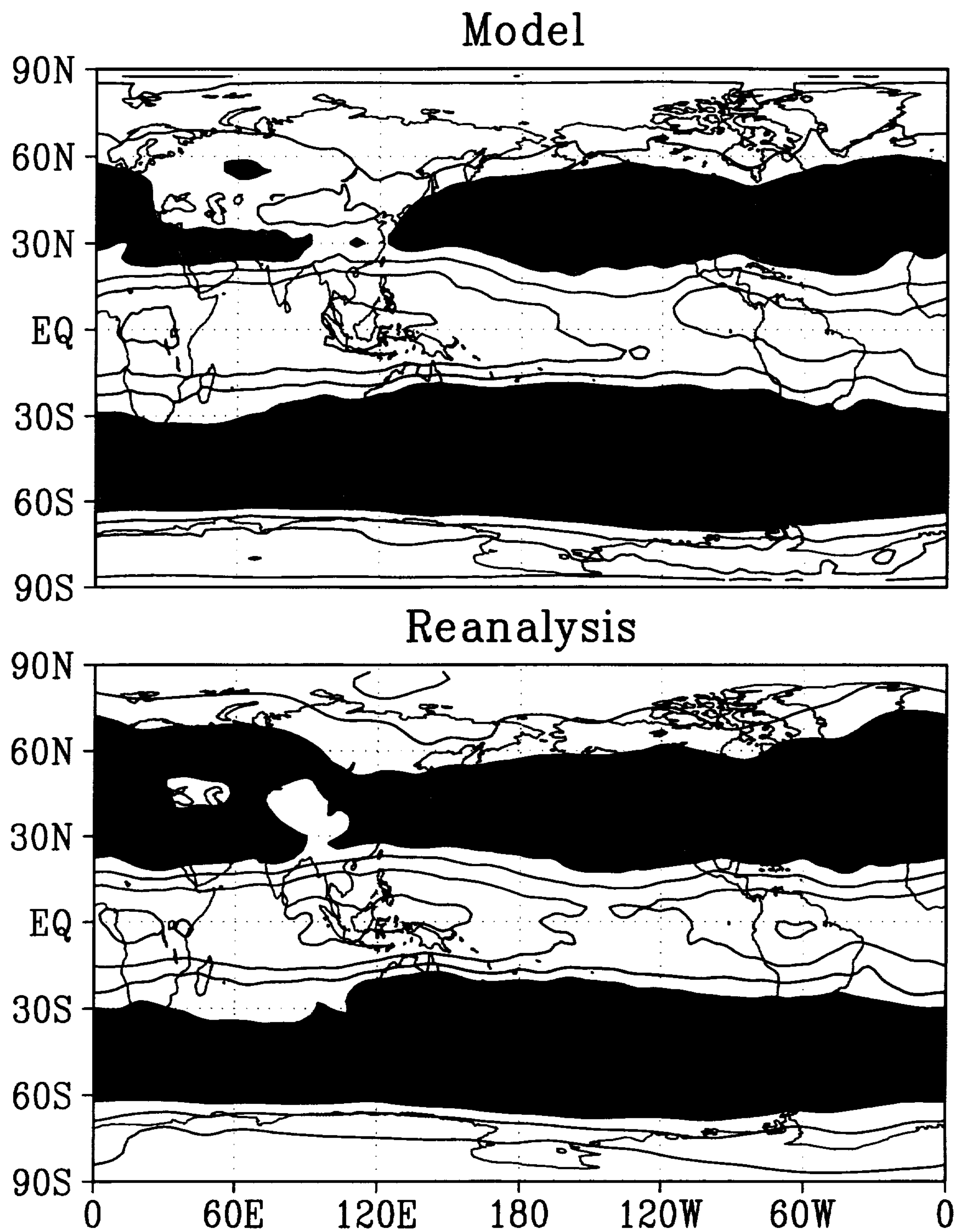

Figure 104: $\sqrt{[(v')^2]}$ at 200mb for MAM— Top: Model, Bottom: Reanalysis. Contour interval: 2 m s^{-1}. Shading indicates values exceeding 6 m s^{-1}.

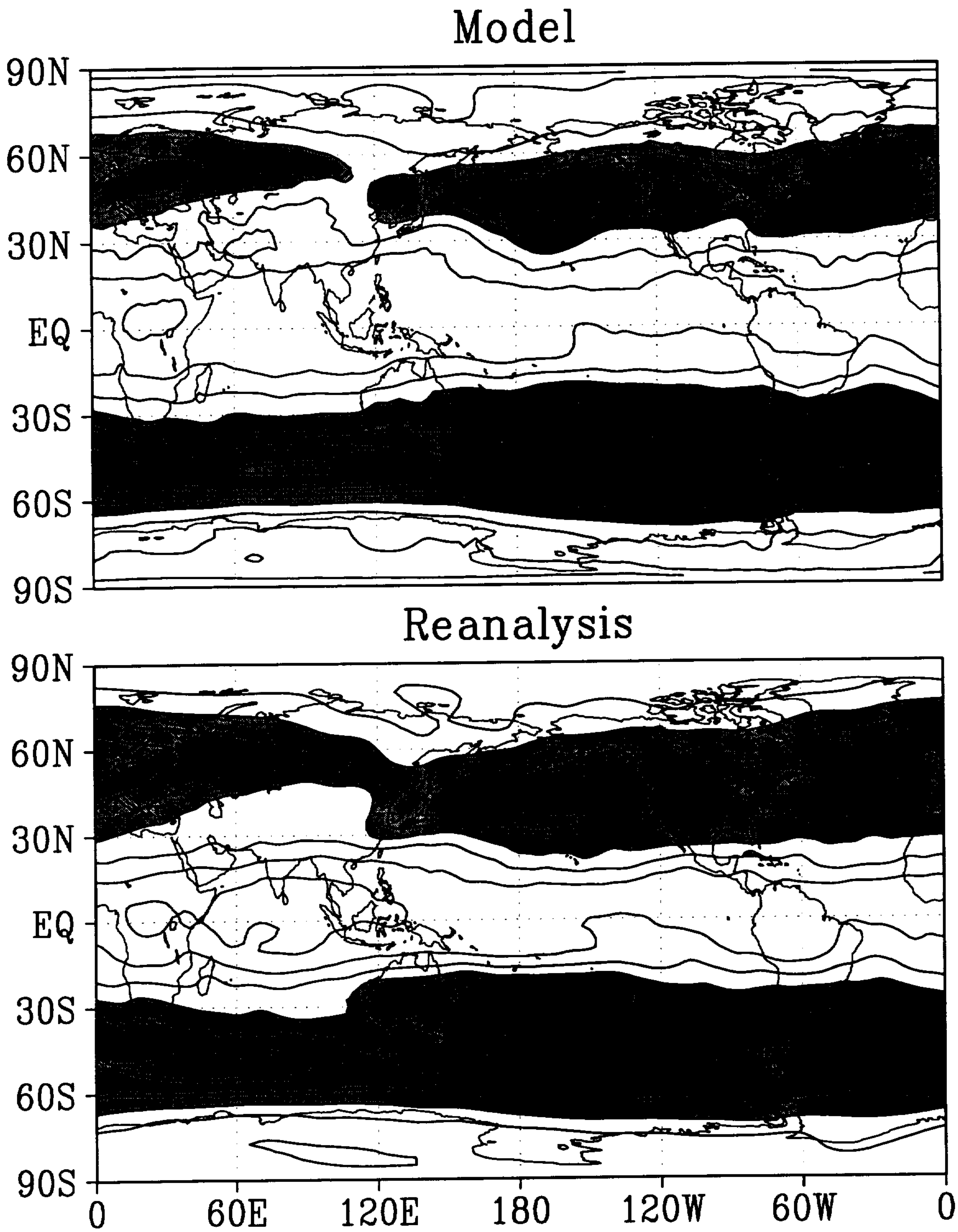

Figure 105: $\sqrt{\overline{[(v')^2]}}$ at 200mb for SON— Top: Model, Bottom: Reanalysis. Contour interval: 2 m s^{-1}. Shading indicates values exceeding 6 m s^{-1}.

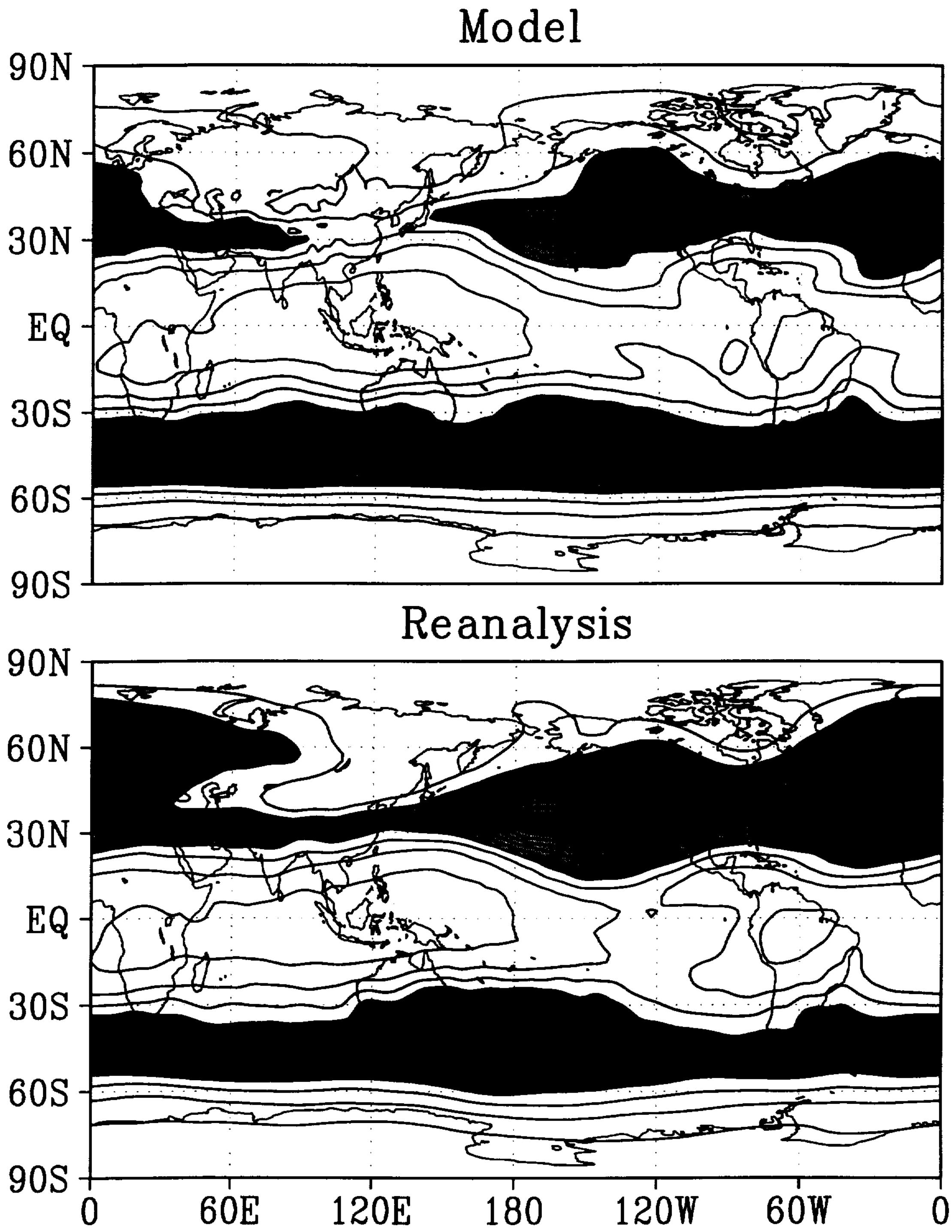

Figure 106: $\frac{1}{2}[\overline{(u')^2} + \overline{(v')^2}]$ at 200mb for DJF— Top: Model, Bottom: Reanalysis. Contour interval: 30 m^2 s^{-2}. Shading indicates values exceeding 120 m^2 s^{-2}.

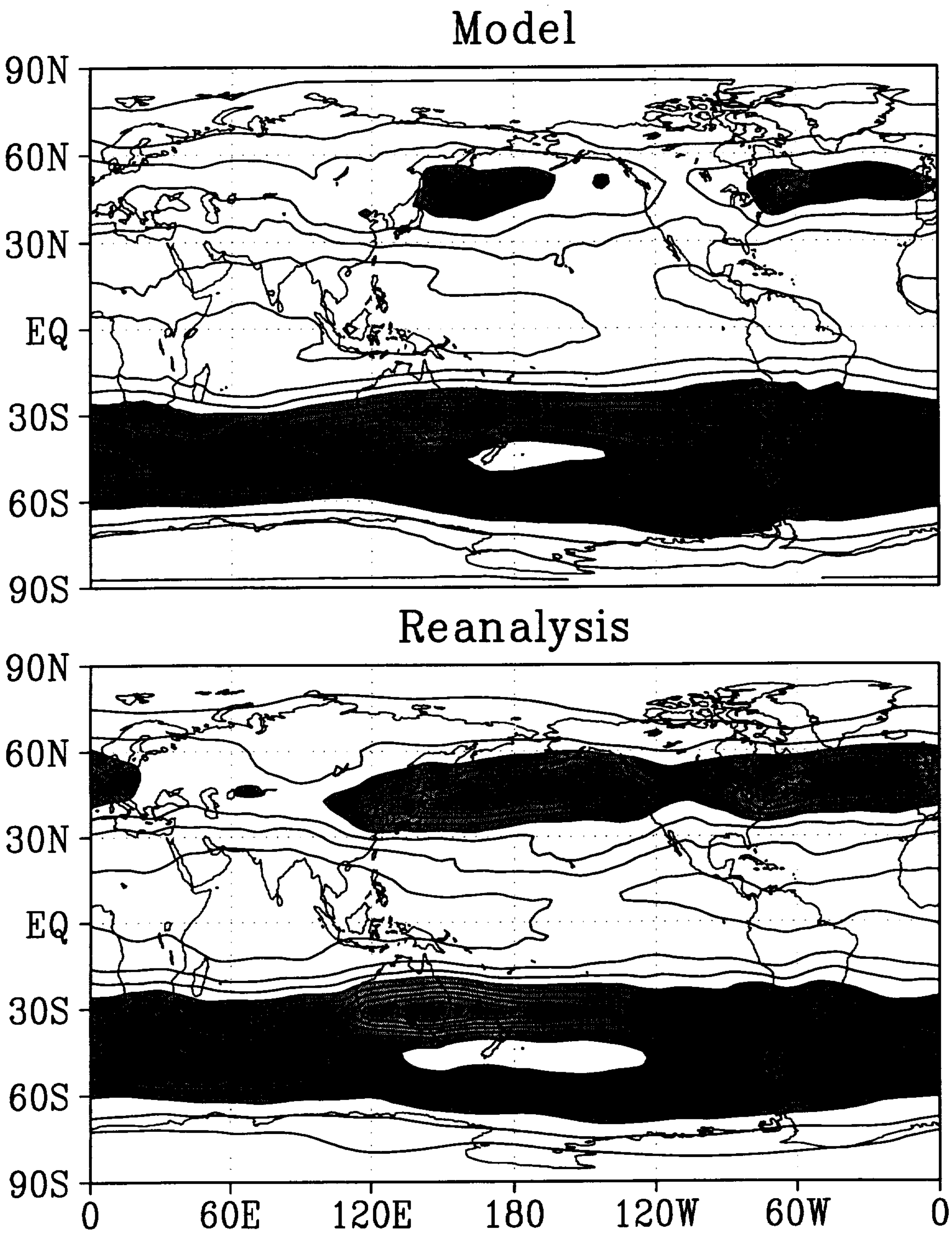

Figure 107: $\frac{1}{2}[\overline{(u')^2} + \overline{(v')^2}]$ at 200mb for JJA— Top: Model, Bottom: Reanalysis. Contour interval: 30 m^2 s^{-2}. Shading indicates values exceeding 120 m^2 s^{-2}.

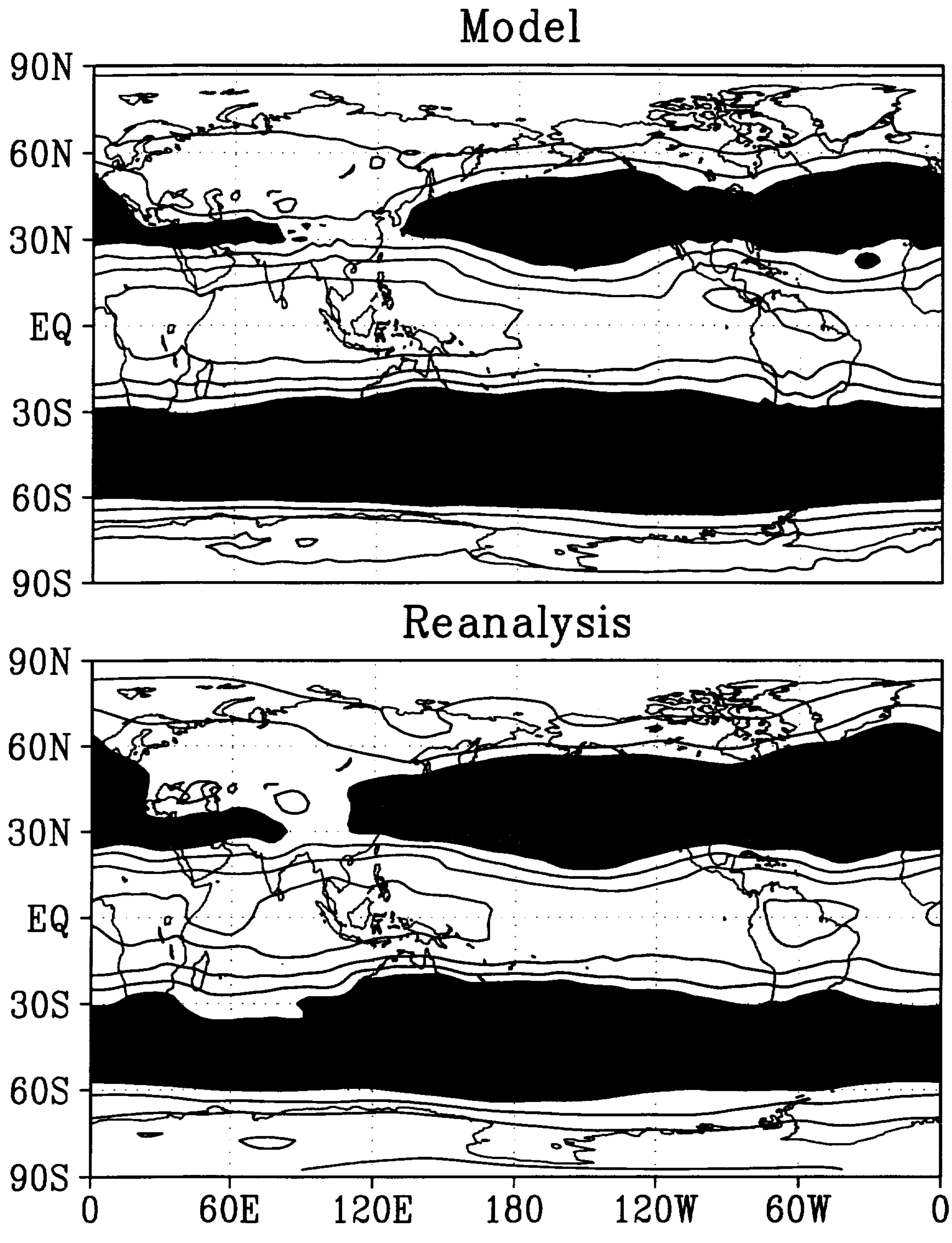

Figure 108: $\frac{1}{2}[\overline{(u')^2}+\overline{(v')^2}]$ at 200mb for MAM— Top: Model, Bottom: Reanalysis. Contour interval: 30 m^2 s^{-2}. Shading indicates values exceeding 120 m^2 s^{-2}.

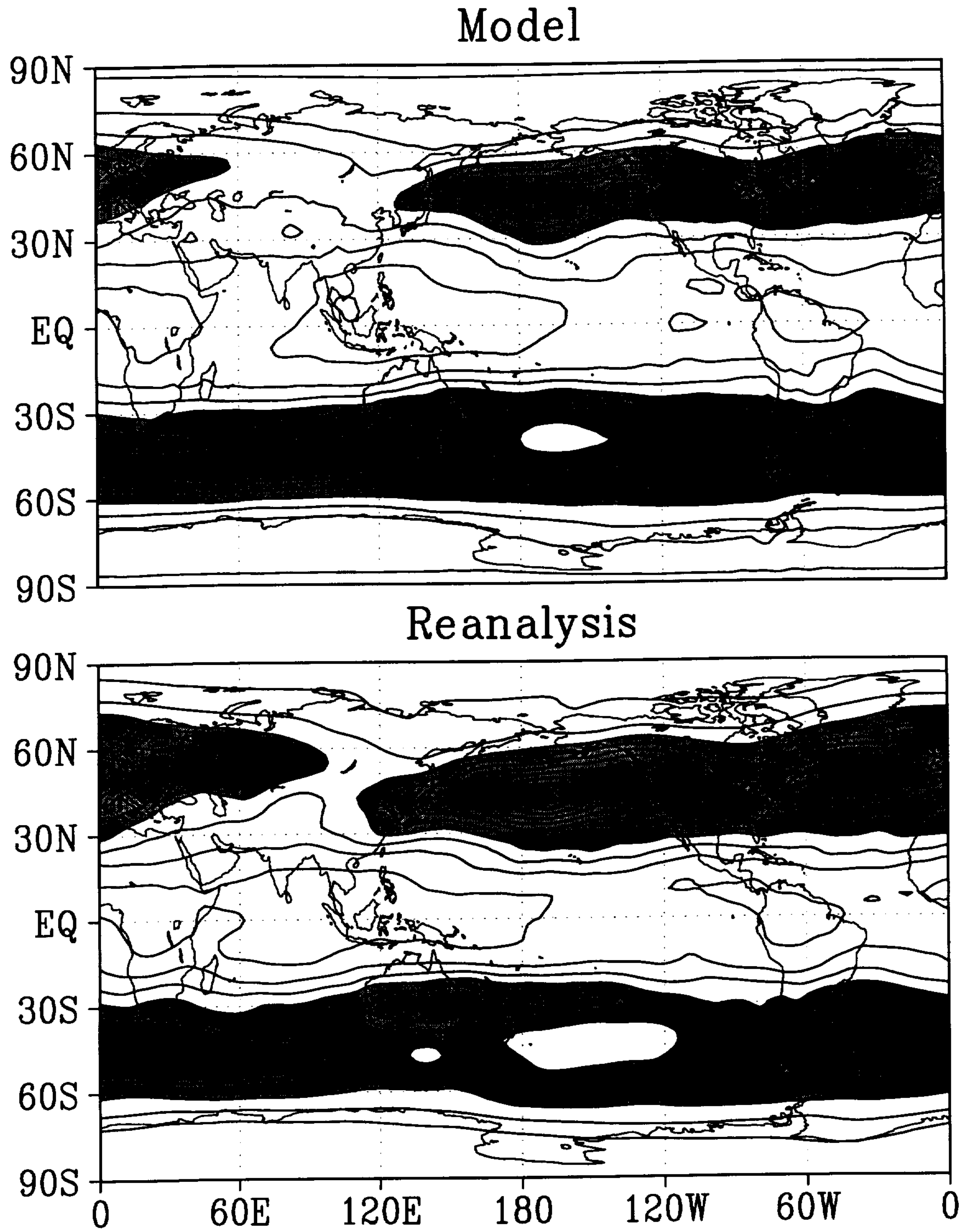

Figure 109: $\frac{1}{2}[\overline{(u')^2} + \overline{(v')^2}]$ at 200mb for SON— Top: Model, Bottom: Reanalysis. Contour interval: 30 m^2 s^{-2}. Shading indicates values exceeding 120 m^2 s^{-2}.

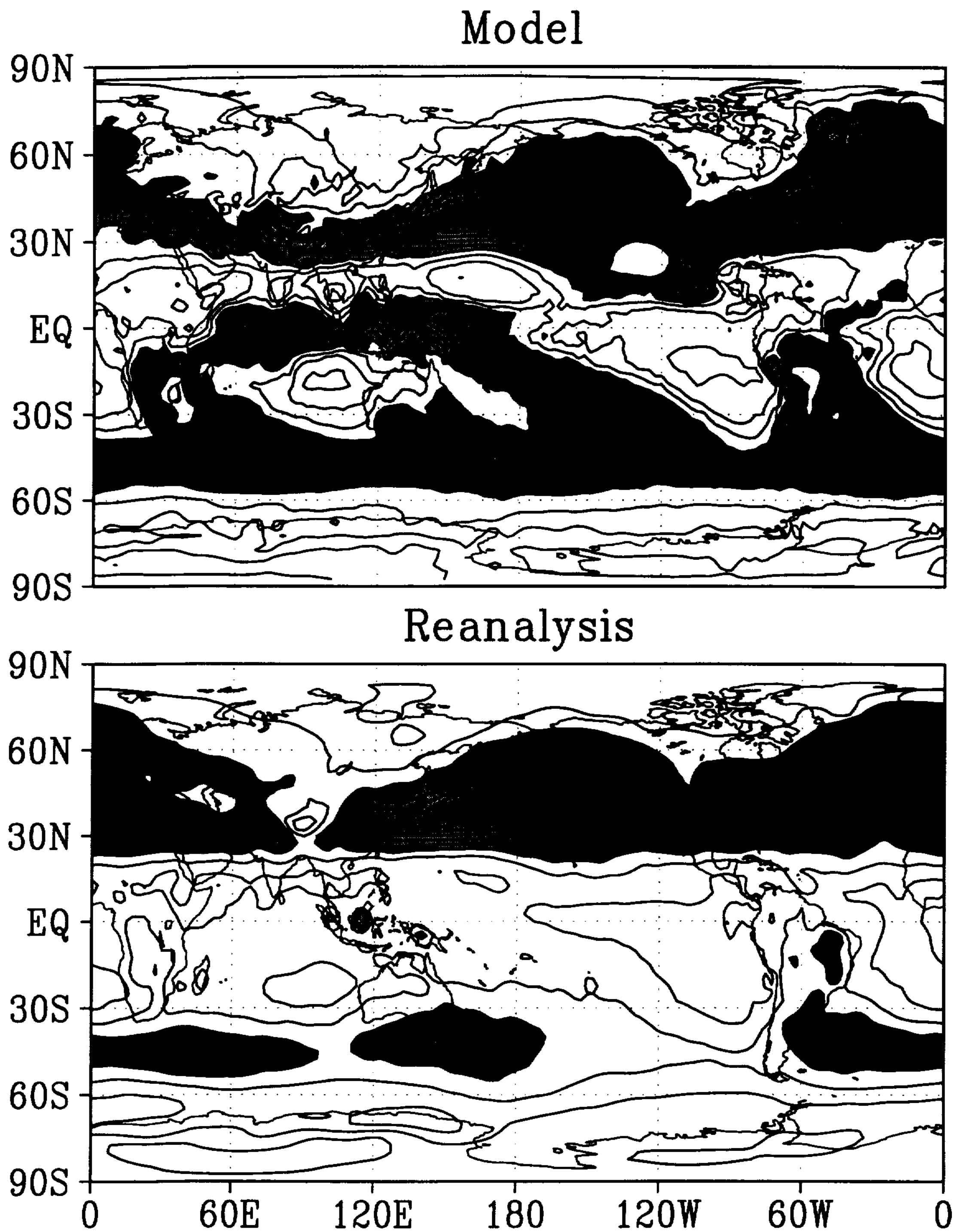

Figure 110: $\sqrt{[\overline{(\omega')^2}]}$ at 500mb for DJF— Top: Model, Bottom: Reanalysis. Contour interval: 20 mb d^{-1}. Shading indicates values exceeding 120 mb d^{-1}.

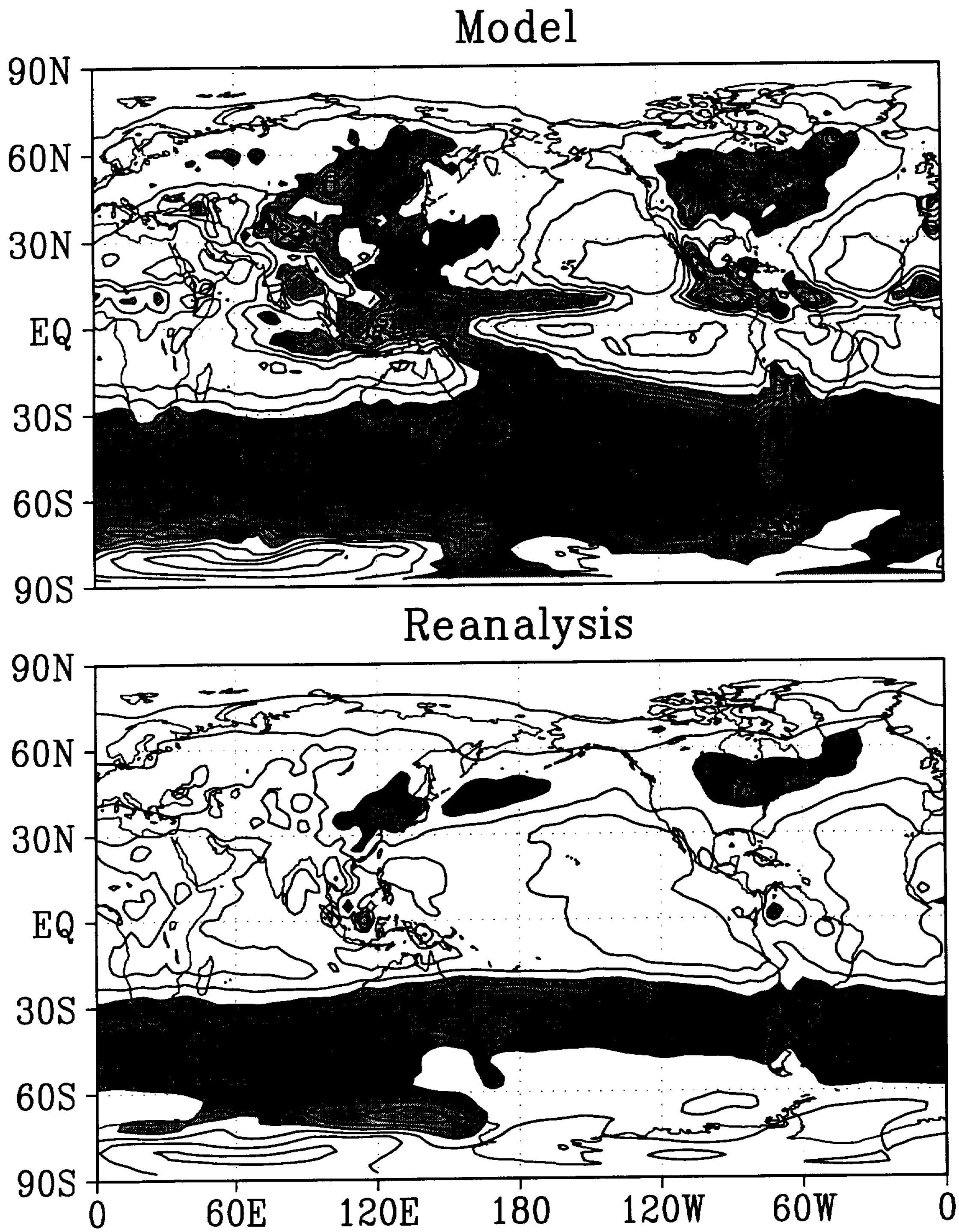

Figure 111: $\sqrt{[\overline{(\omega')^2}]}$ at 500mb for JJA— Top: Model, Bottom: Reanalysis. Contour interval: 20 mb d^{-1}. Shading indicates values exceeding 120 mb d^{-1}.

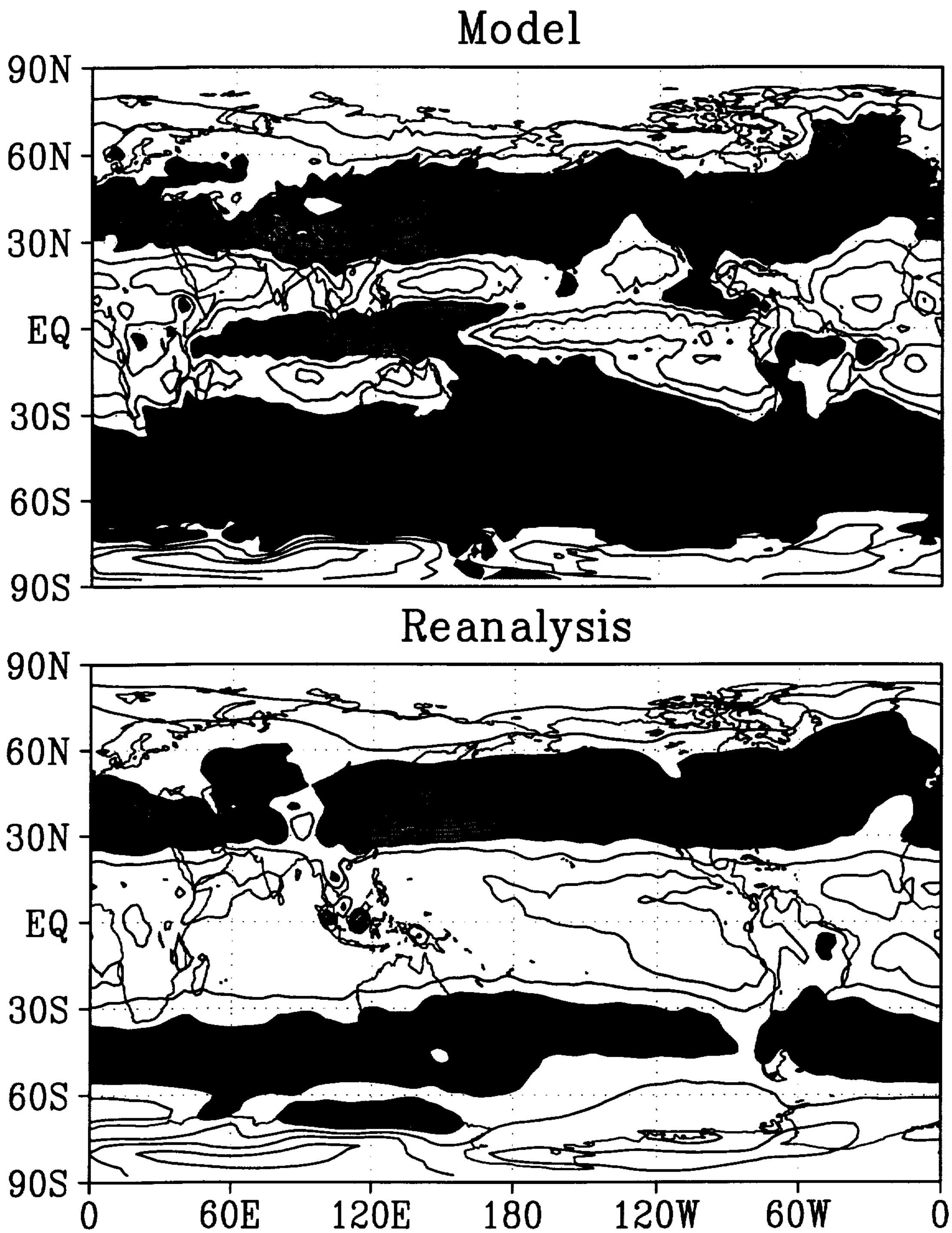

Figure 112: $\sqrt{[\overline{(\omega')^2}]}$ at 500mb for MAM— Top: Model, Bottom: Reanalysis. Contour interval: 20 mb d^{-1}. Shading indicates values exceeding 120 mb d^{-1}.

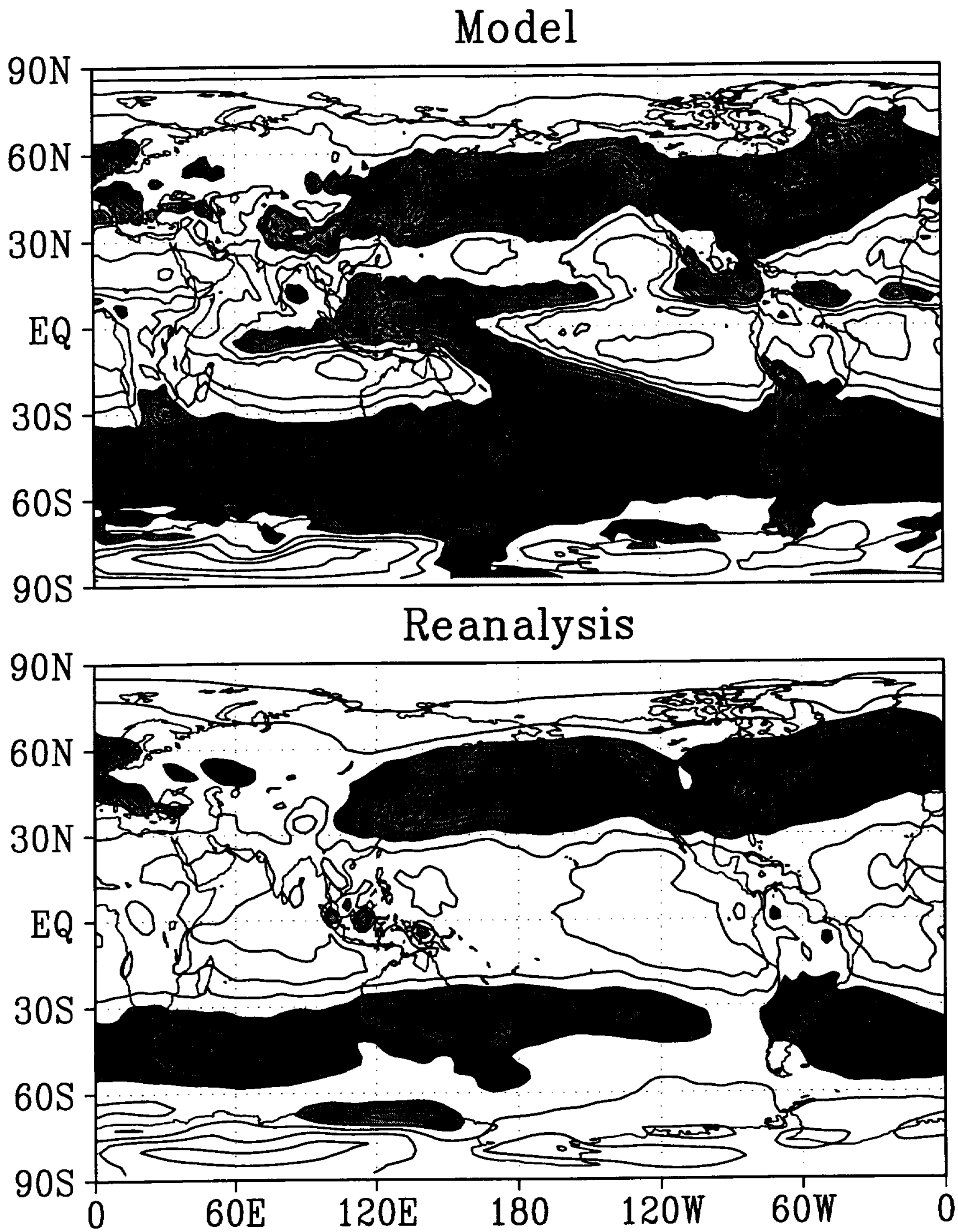

Figure 113: $\sqrt{[\overline{(\omega')^2}]}$ at 500mb for SON— Top: Model, Bottom: Reanalysis. Contour interval: 20 mb d^{-1}. Shading indicates values exceeding 120 mb d^{-1}.

DJF $\sqrt{[\overline{(T')^2}]}$ 850

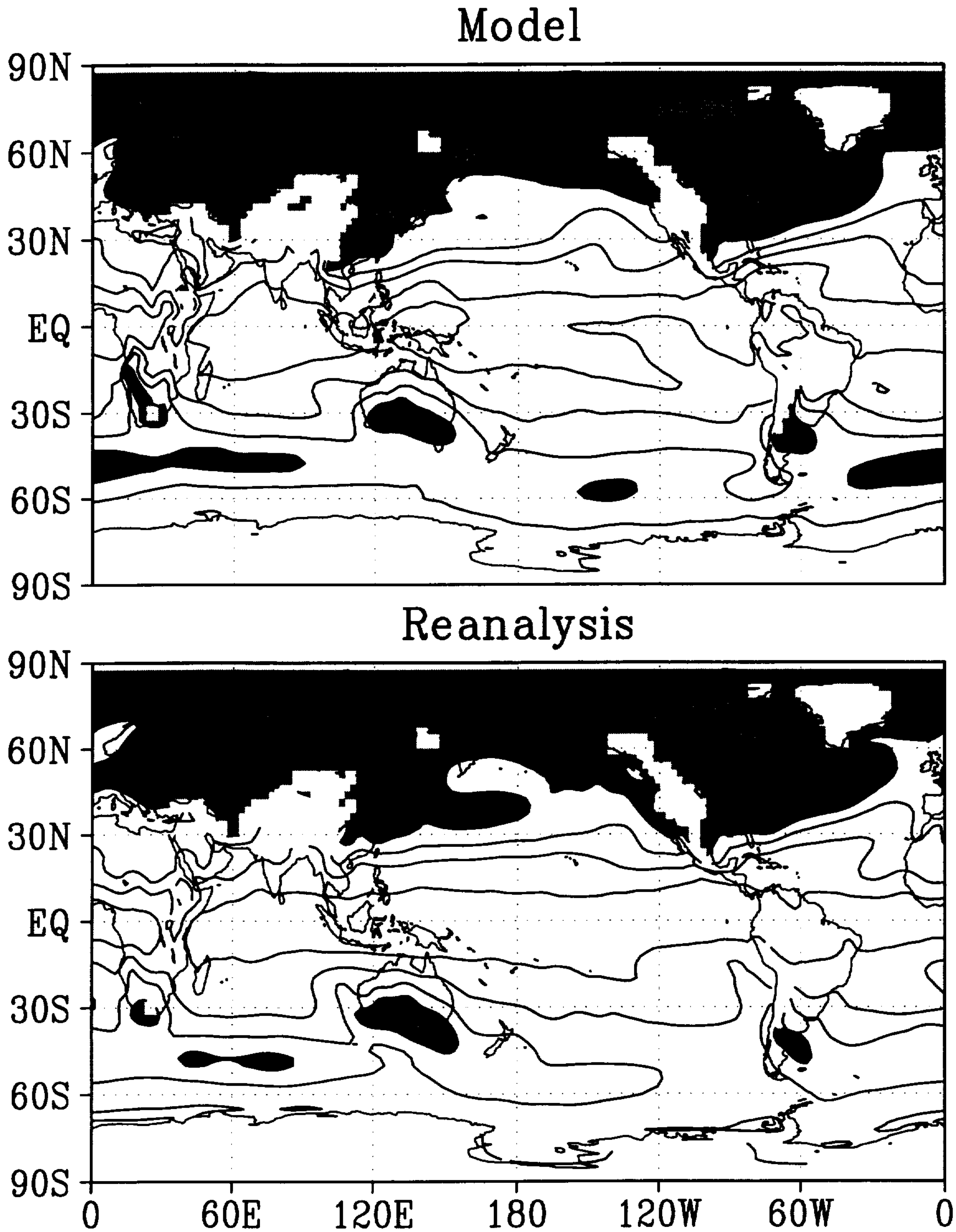

Figure 114: $\sqrt{[\overline{(T')^2}]}$ at 850mp (K) for DJF— Top: Model, Bottom: Reanalysis. Contour interval: 1 K. Shading indicates values exceeding 4 K.

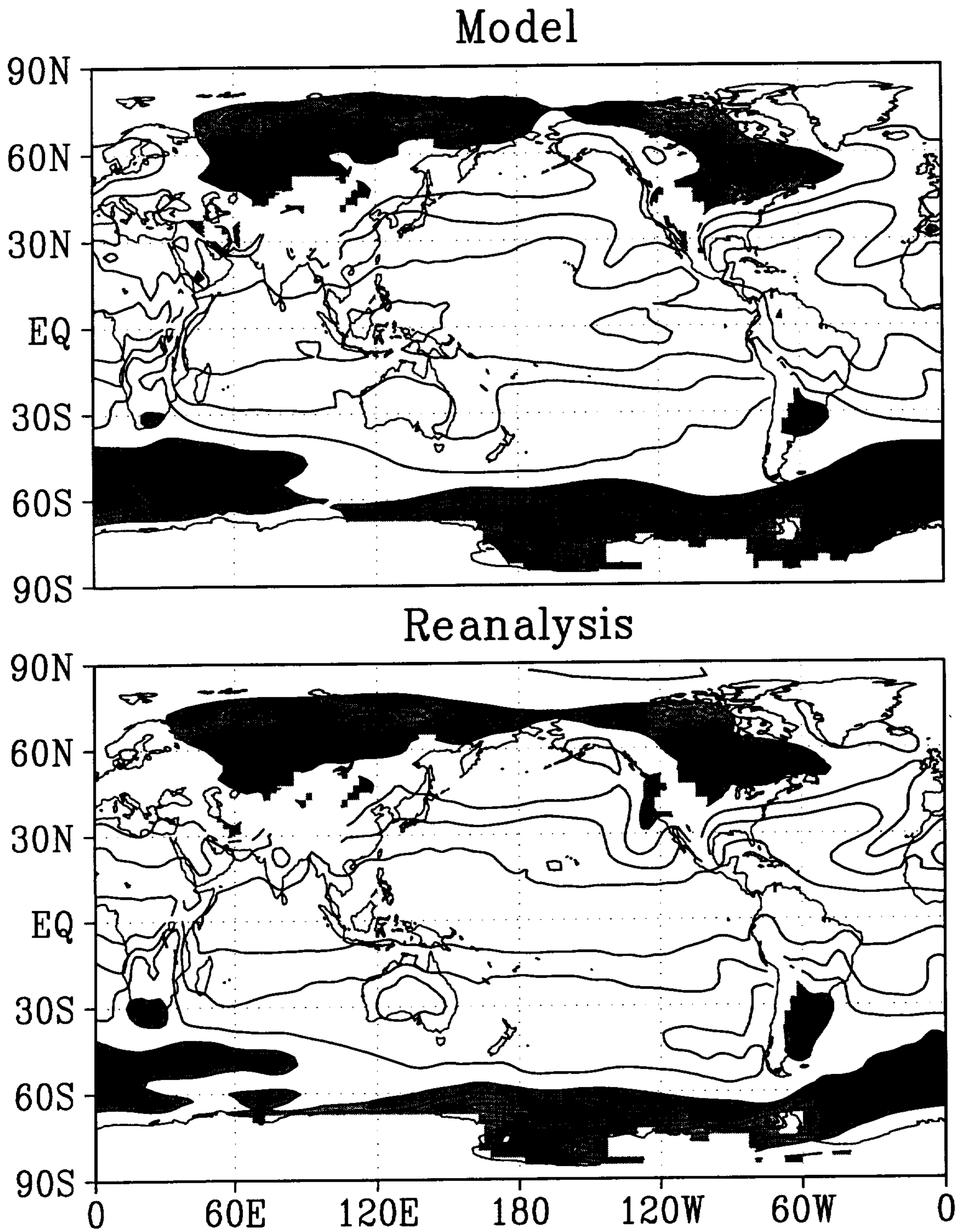

Figure 115: $\sqrt{\overline{[(T')^2]}}$ at 850mp (K) for JJA— Top: Model, Bottom: Reanalysis. Contour interval: 1 K. Shading indicates values exceeding 4 K.

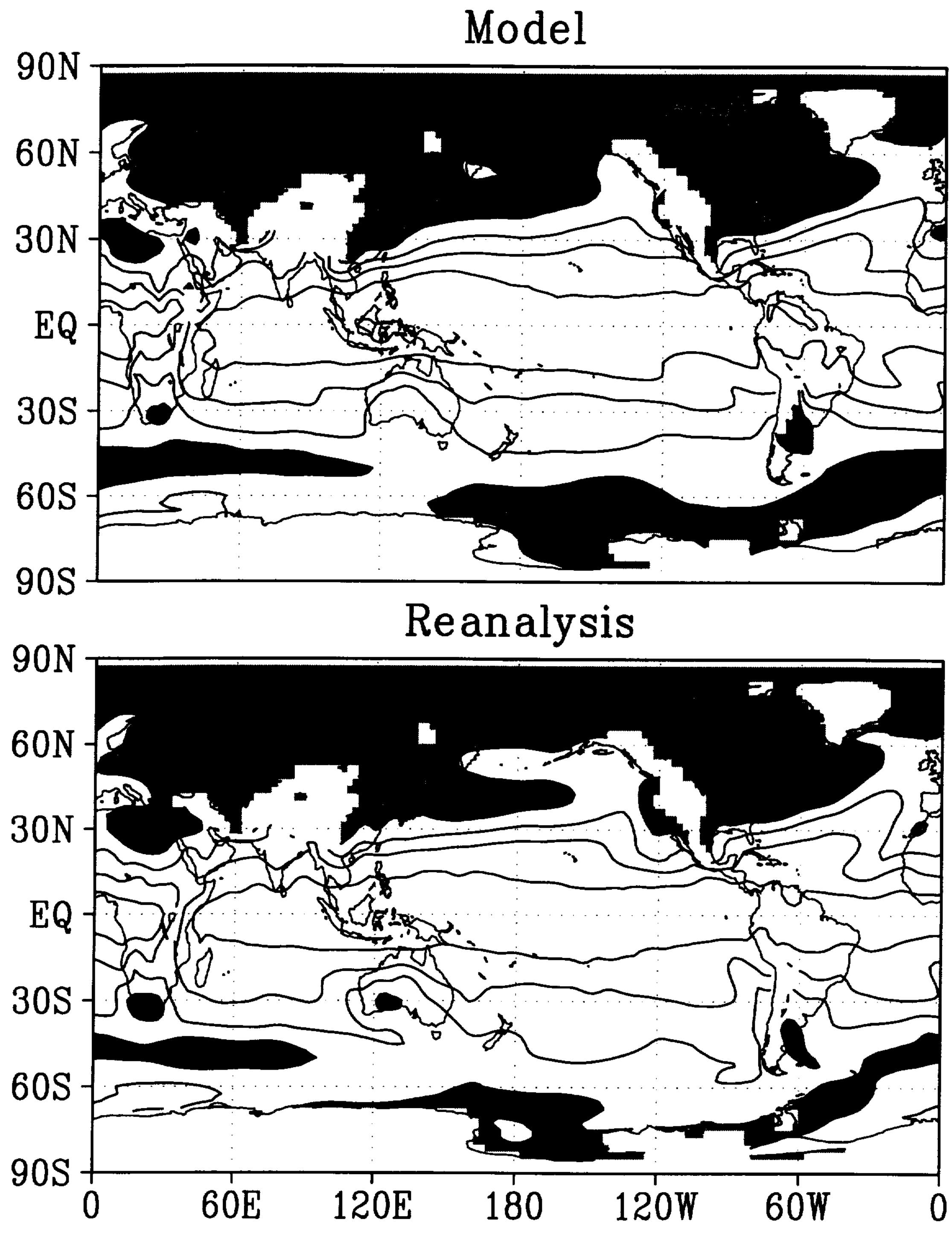

Figure 116: $\sqrt{[(T')^2]}$ at 850mp (K) for MAM— Top: Model, Bottom: Reanalysis. Contour interval: 1 K. Shading indicates values exceeding 4 K.

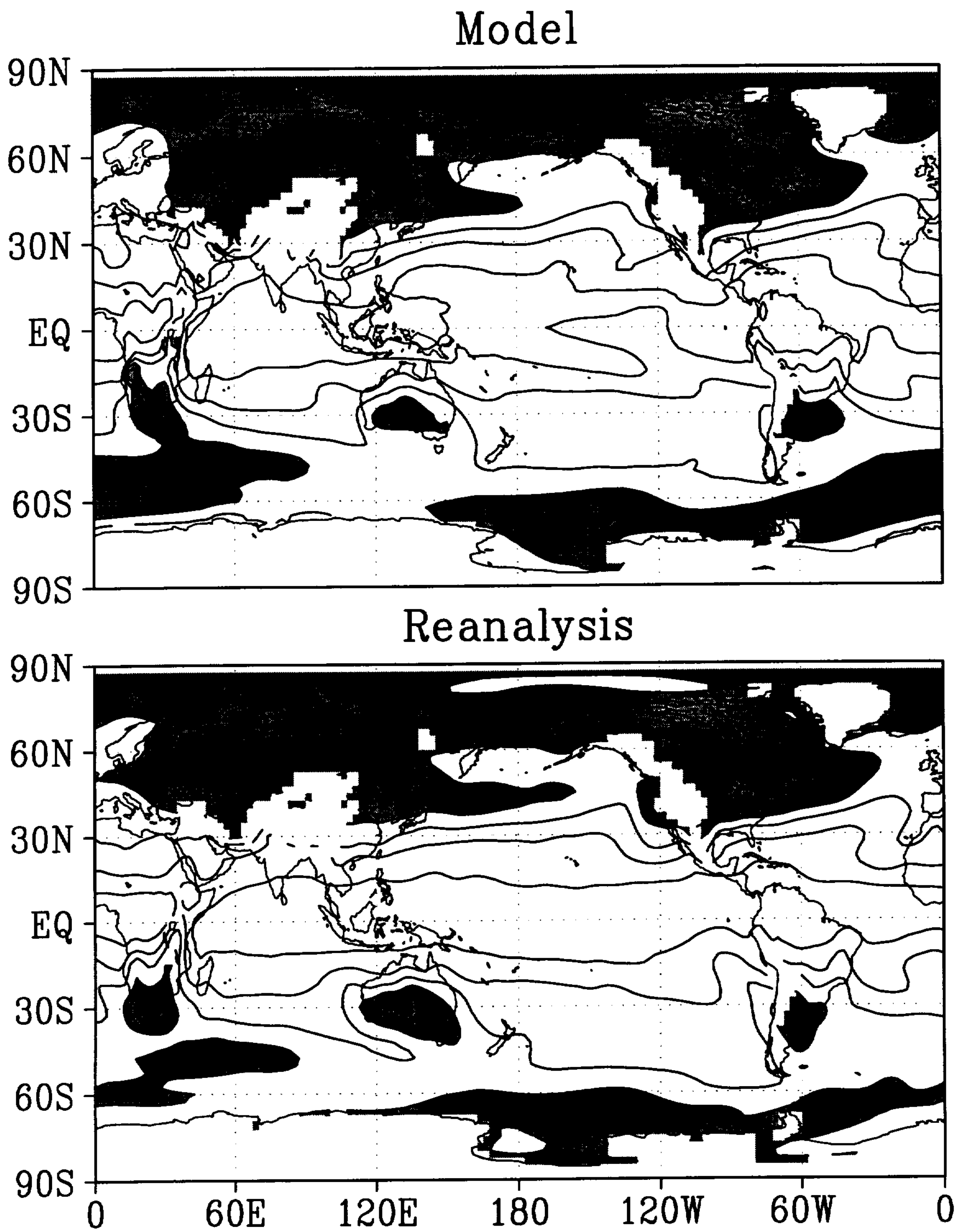

Figure 117: $\sqrt{[\overline{(T')^2}]}$ at 850mp (K) for SON— Top: Model, Bottom: Reanalysis. Contour interval: 1 K. Shading indicates values exceeding 4 K.

DJF $\sqrt{[\overline{(Z')^2}]}$ 200

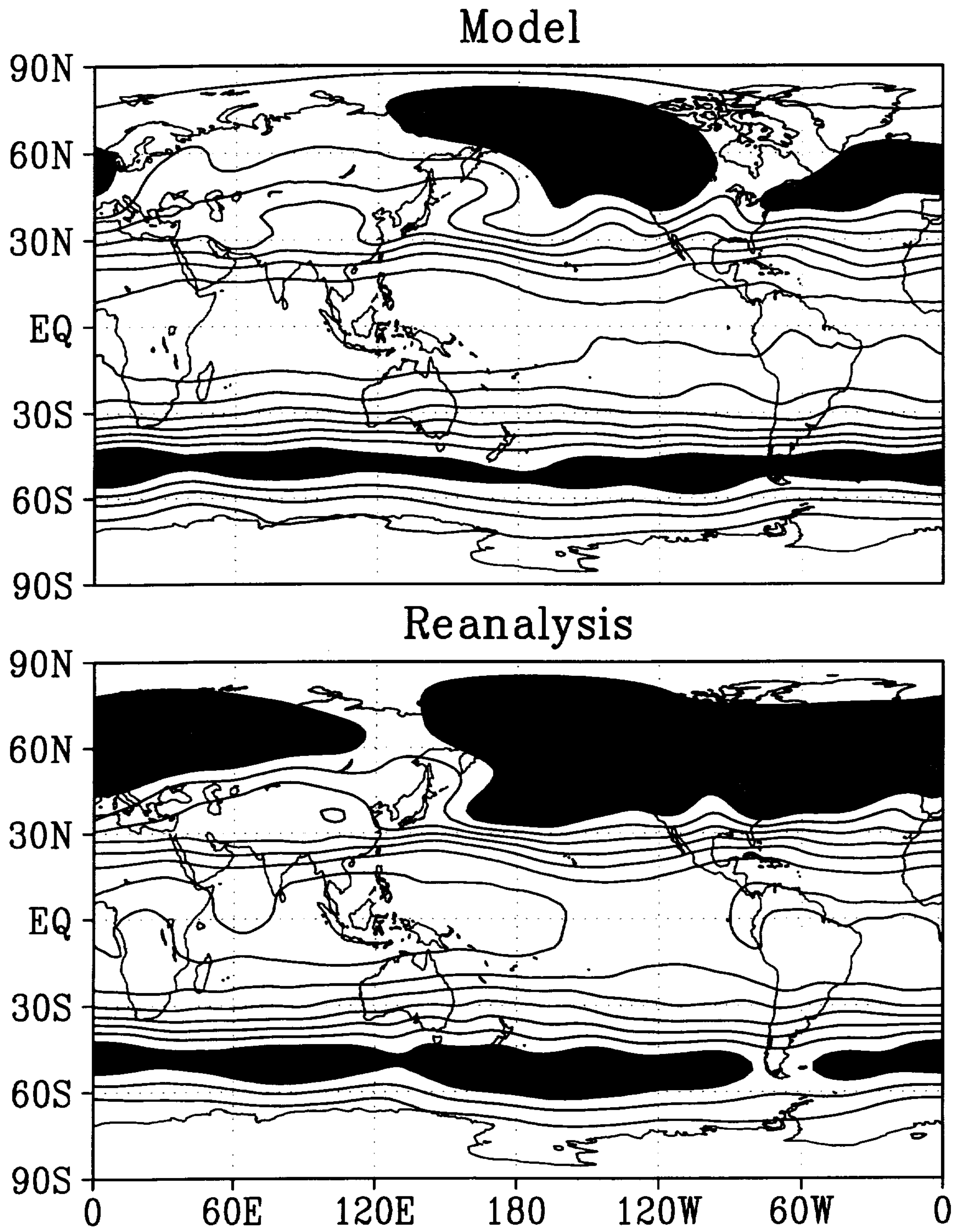

Figure 118: $\sqrt{[\overline{(Z')^2}]}$ at 200 mb (m) for DJF— Top: Model, Bottom: Reanalysis. Contour interval: 20 m. Shading indicates values exceeding 100 m.

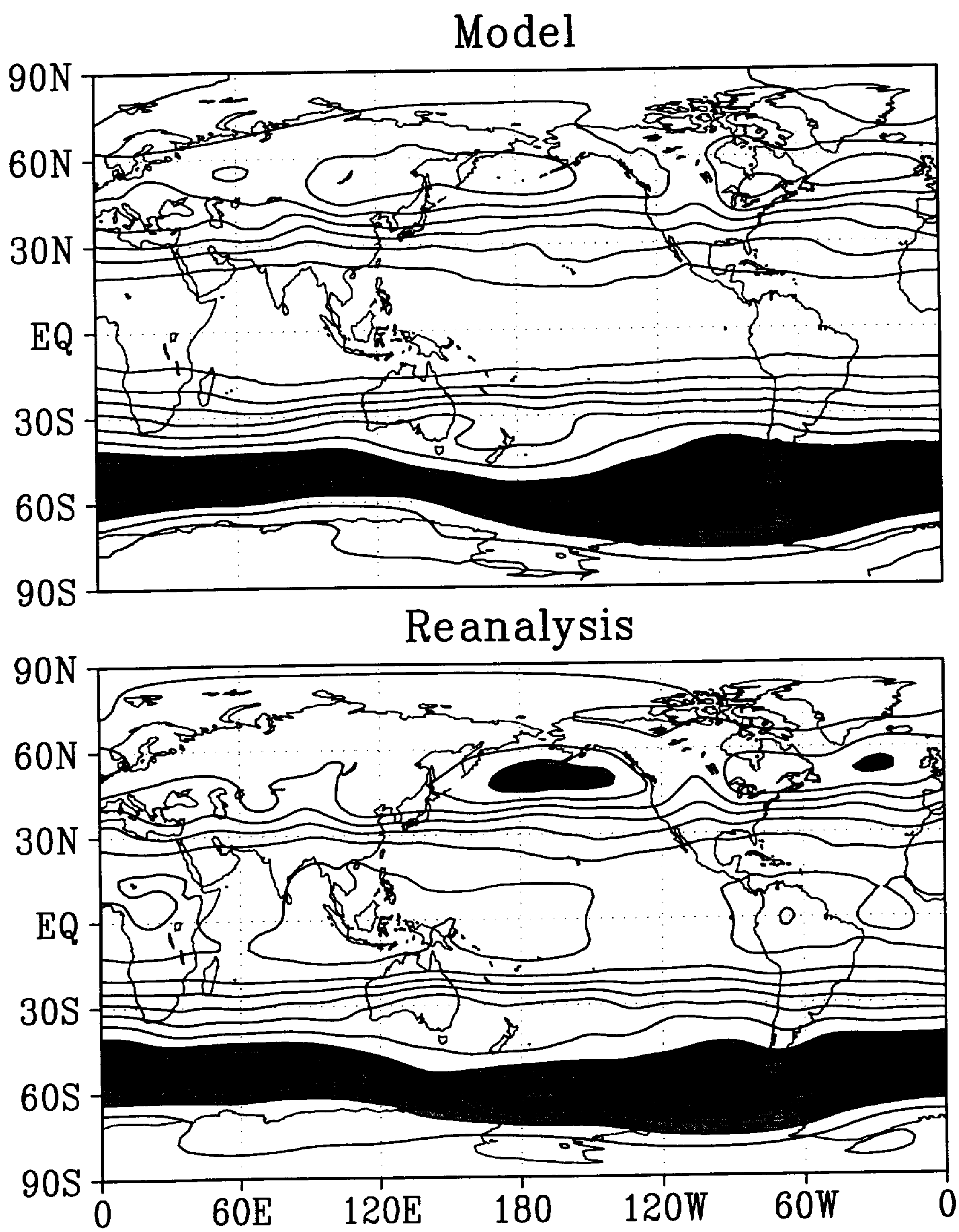

Figure 119: $\sqrt{[\overline{(Z')^2}]}$ at 200 mb (m) for JJA— Top: Model, Bottom: Reanalysis. Contour interval: 20 m. Shading indicates values exceeding 100 m.

MAM $\sqrt{[\overline{(Z')^2}]}$ 200

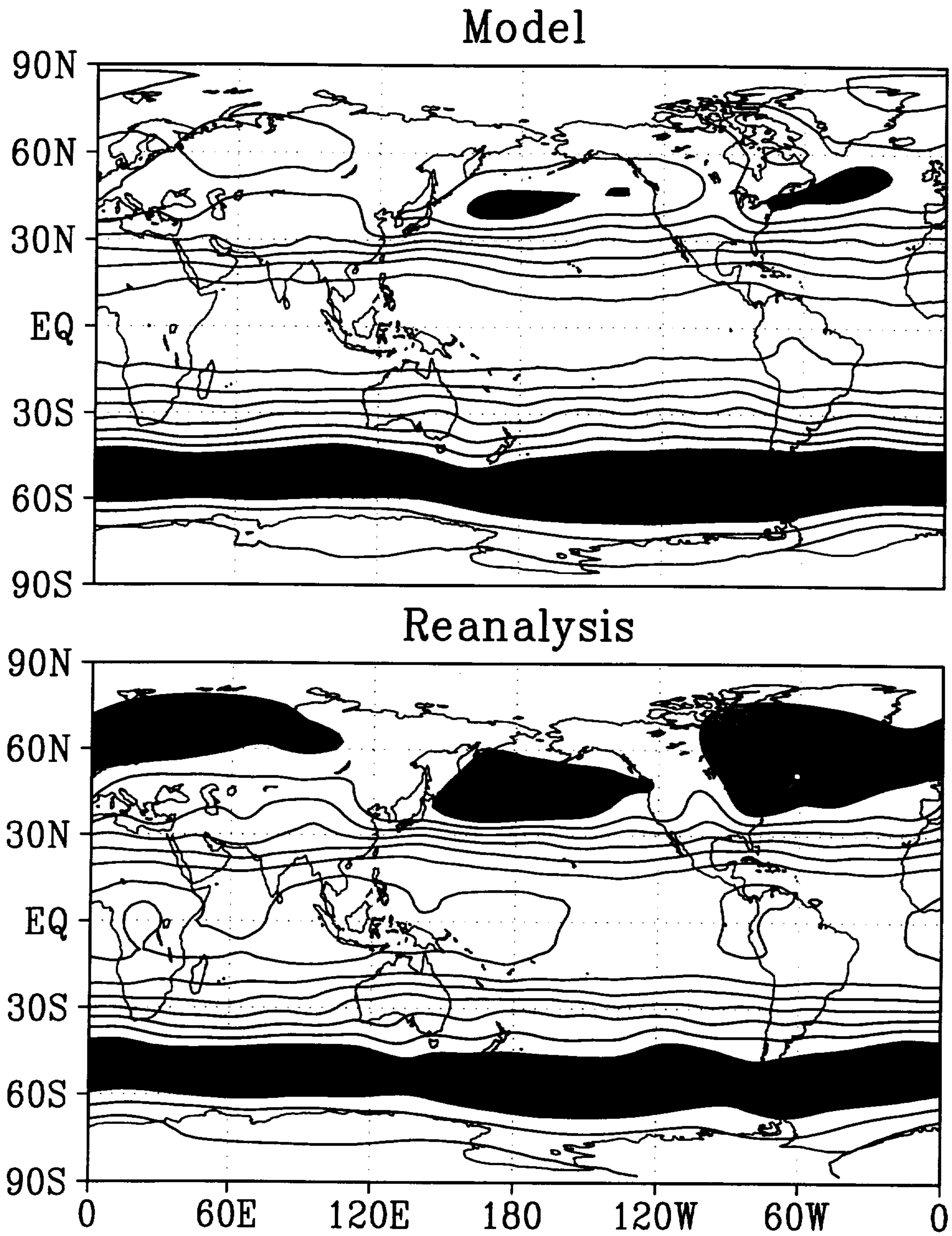

Figure 120: $\sqrt{[\overline{(Z')^2}]}$ at 200 mb (m) for MAM— Top: Model, Bottom: Reanalysis. Contour interval: 20 m. Shading indicates values exceeding 100 m.

SON $\sqrt{[\overline{(Z')^2}]}$ 200

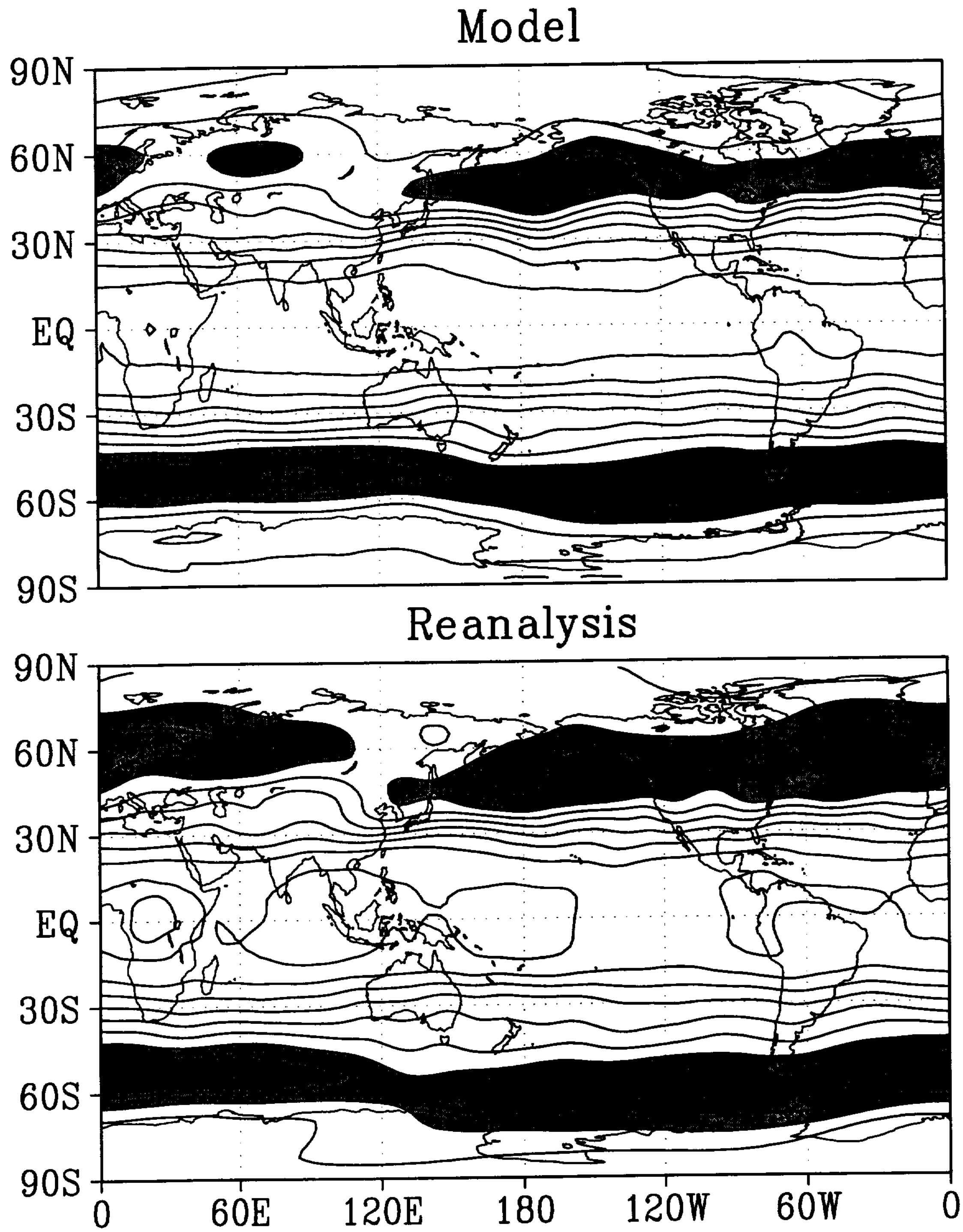

Figure 121: $\sqrt{[\overline{(Z')^2}]}$ at 200 mb (m) for SON— Top: Model, Bottom: Reanalysis. Contour interval: 20 m. Shading indicates values exceeding 100 m.

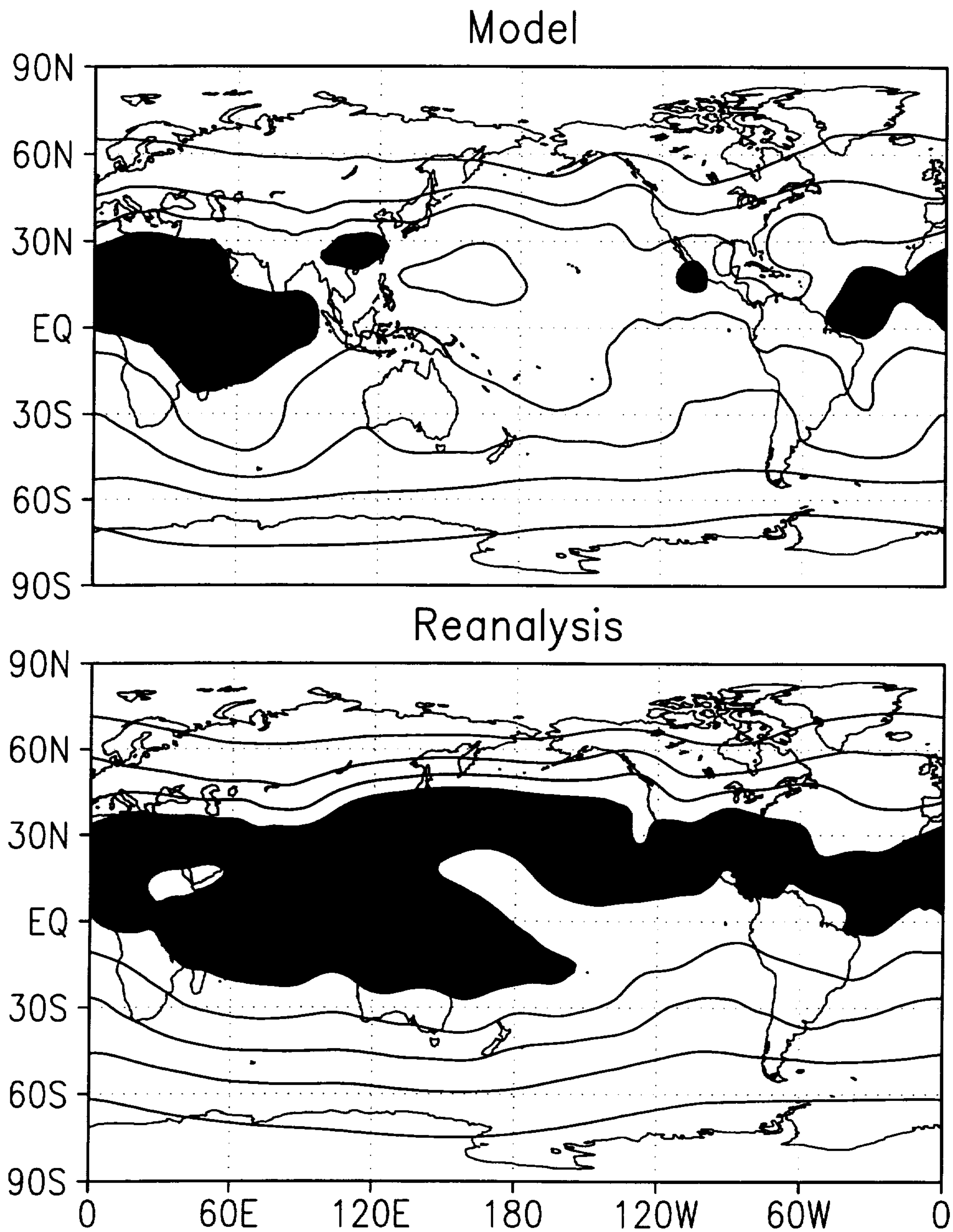

Figure 122: $\sqrt{[\overline{(\chi')^2}]}$ at 200mb for DJF— Top: Model, Bottom: Reanalysis. Contour interval: 2 $\times 10^6$ m^2 s^{-1}. Shading indicates values exceeding 8 $\times 10^6$ m^2 s^{-1}.

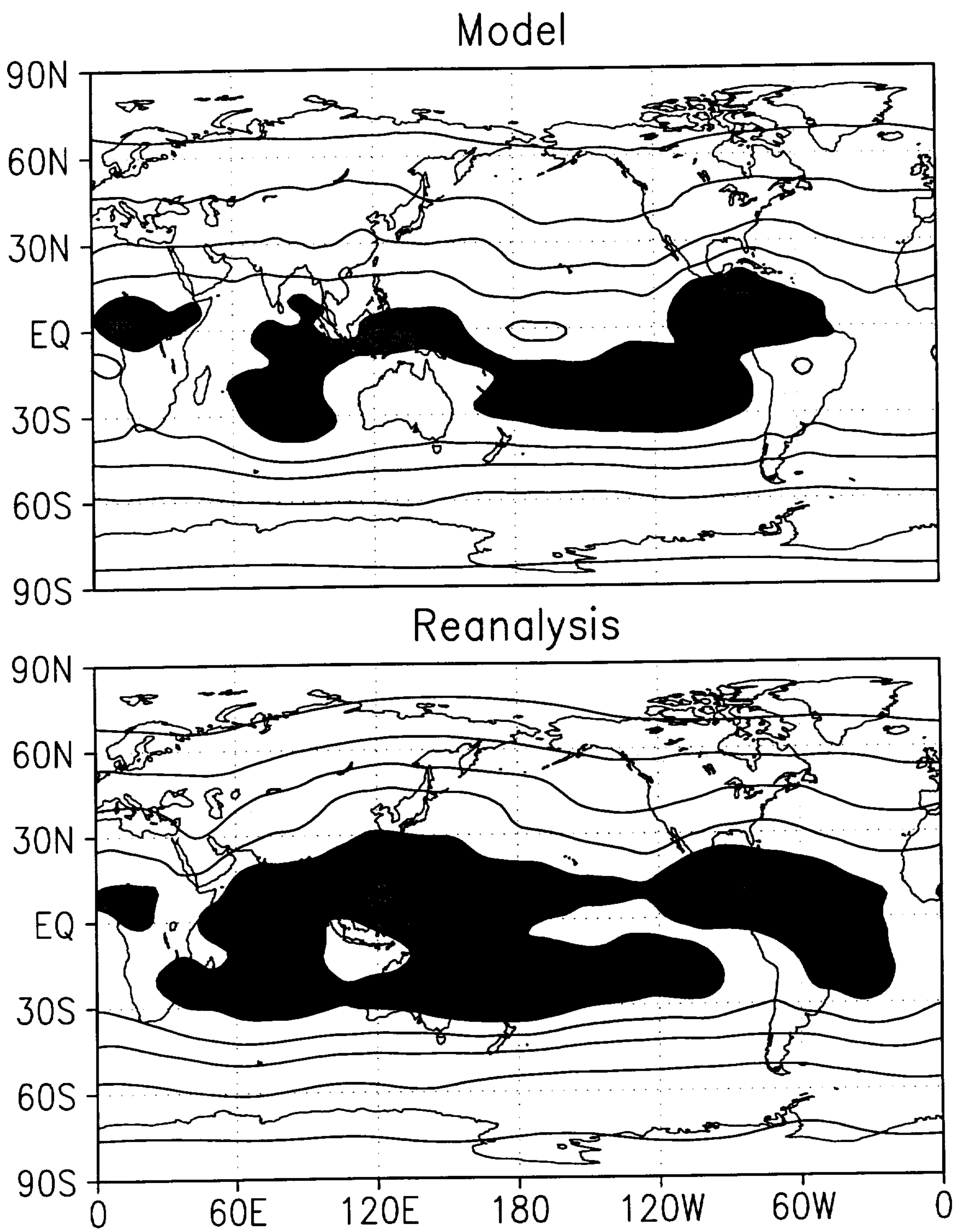

Figure 123: $\sqrt{[\overline{(\chi')^2}]}$ at 200mb for JJA— Top: Model, Bottom: Reanalysis. Contour interval: 2 $\times 10^6$ m^2 s^{-1}. Shading indicates values exceeding 8 $\times 10^6$ m^2 s^{-1}.

MAM $\sqrt{[\overline{(\chi')^2}]}$ 200

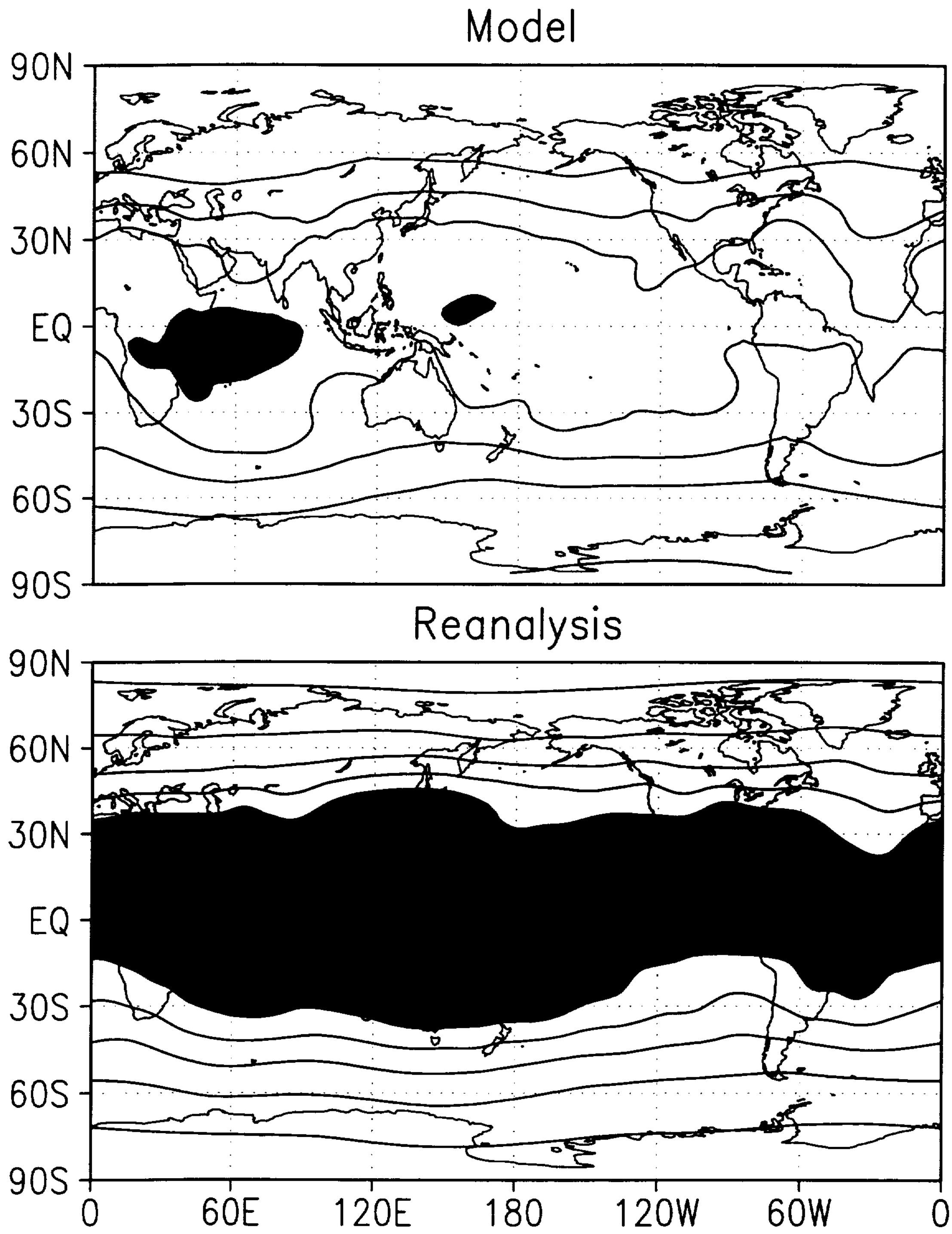

Figure 124: $\sqrt{[\overline{(\chi')^2}]}$ at 200mb for MAM— Top: Model, Bottom: Reanalysis. Contour interval: 2 $\times 10^6$ m^2 s^{-1}. Shading indicates values exceeding 8 $\times 10^6$ m^2 s^{-1}.

SON $\sqrt{[\overline{(\chi')^2}]}$ 200

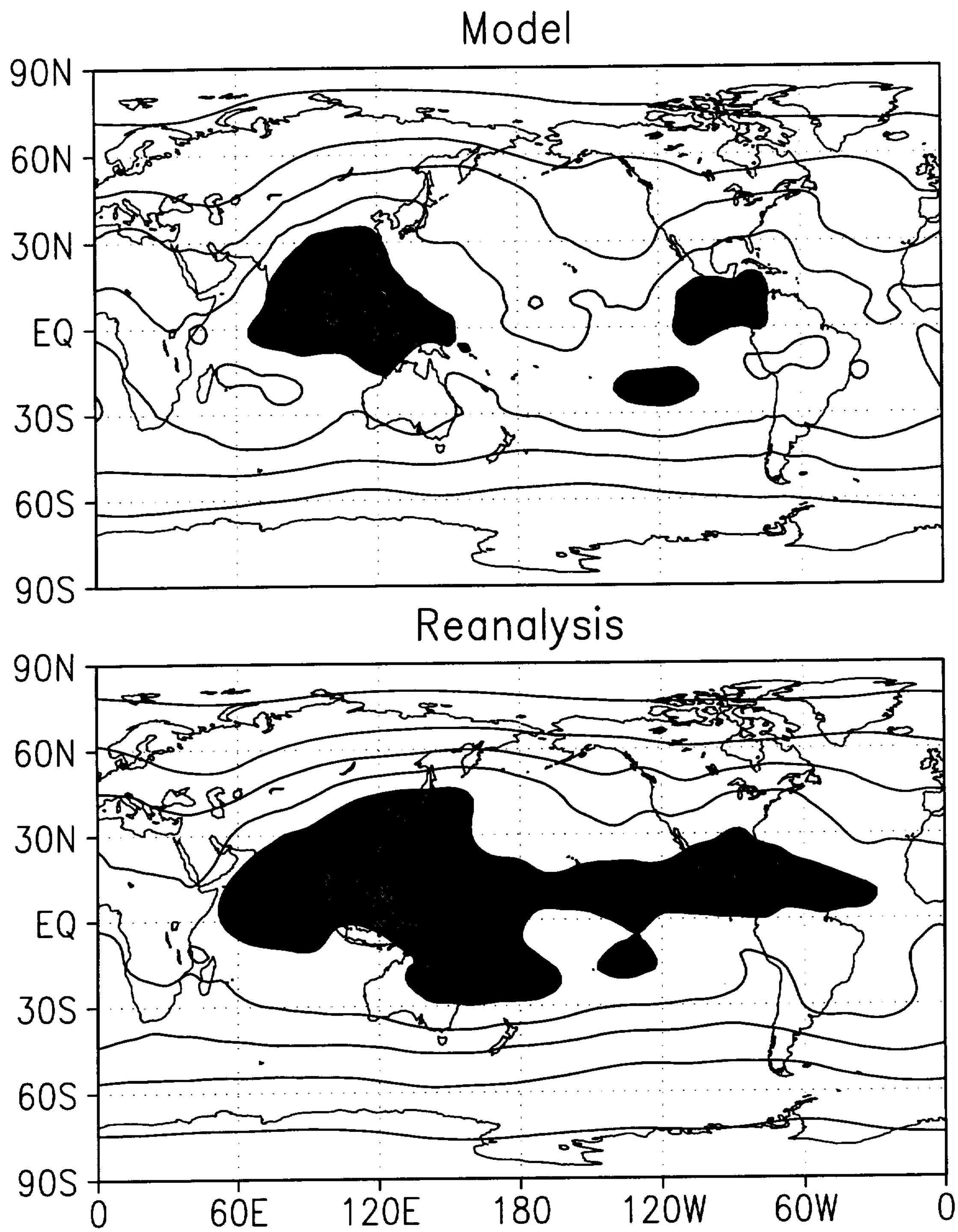

Figure 125: $\sqrt{[\overline{(\chi')^2}]}$ at 200mb for SON— Top: Model, Bottom: Reanalysis. Contour interval: 2×10^6 m^2 s^{-1}. Shading indicates values exceeding 8×10^6 m^2 s^{-1}.

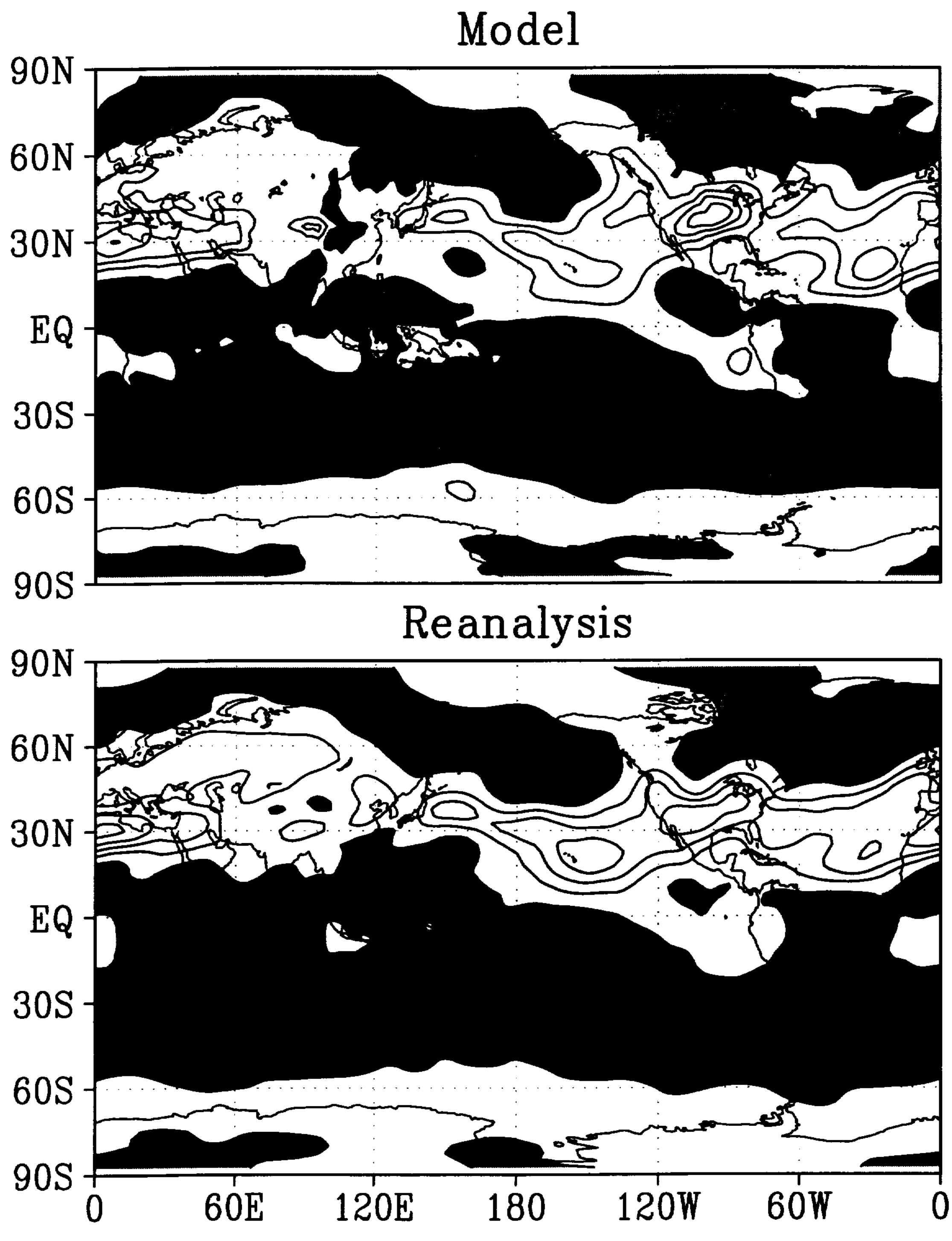

Figure 126: $[\overline{u'v'}]$ at 200 mb for DJF— Top: Model, Bottom: Reanalysis. Contour interval: 20 m^2 s^{-2}. Shading indicates negative values

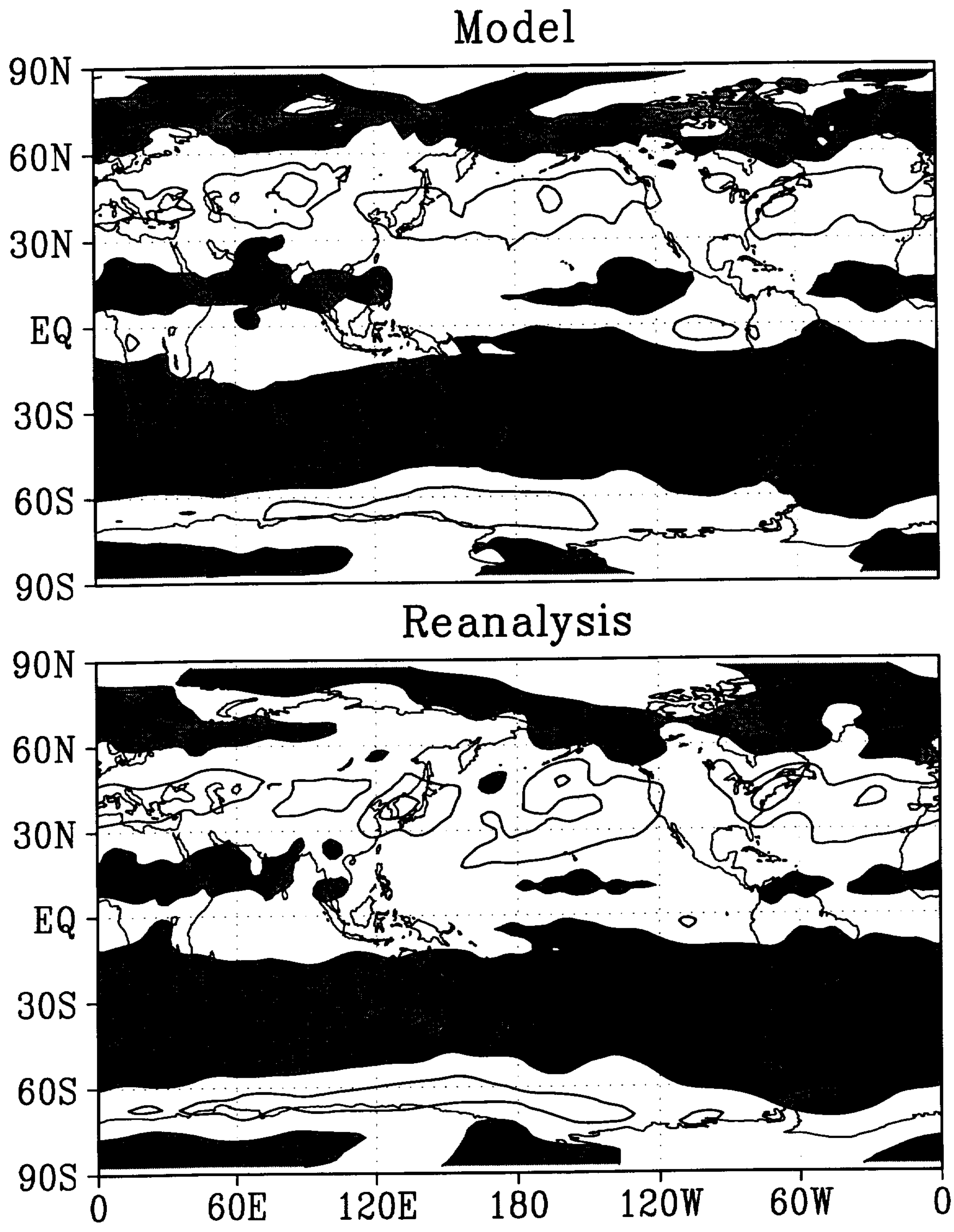

Figure 127: $[\overline{u'v'}]$ at 200 mb for JJA— Top: Model, Bottom: Reanalysis. Contour interval: 20 m^2 s^{-2}. Shading indicates negative values

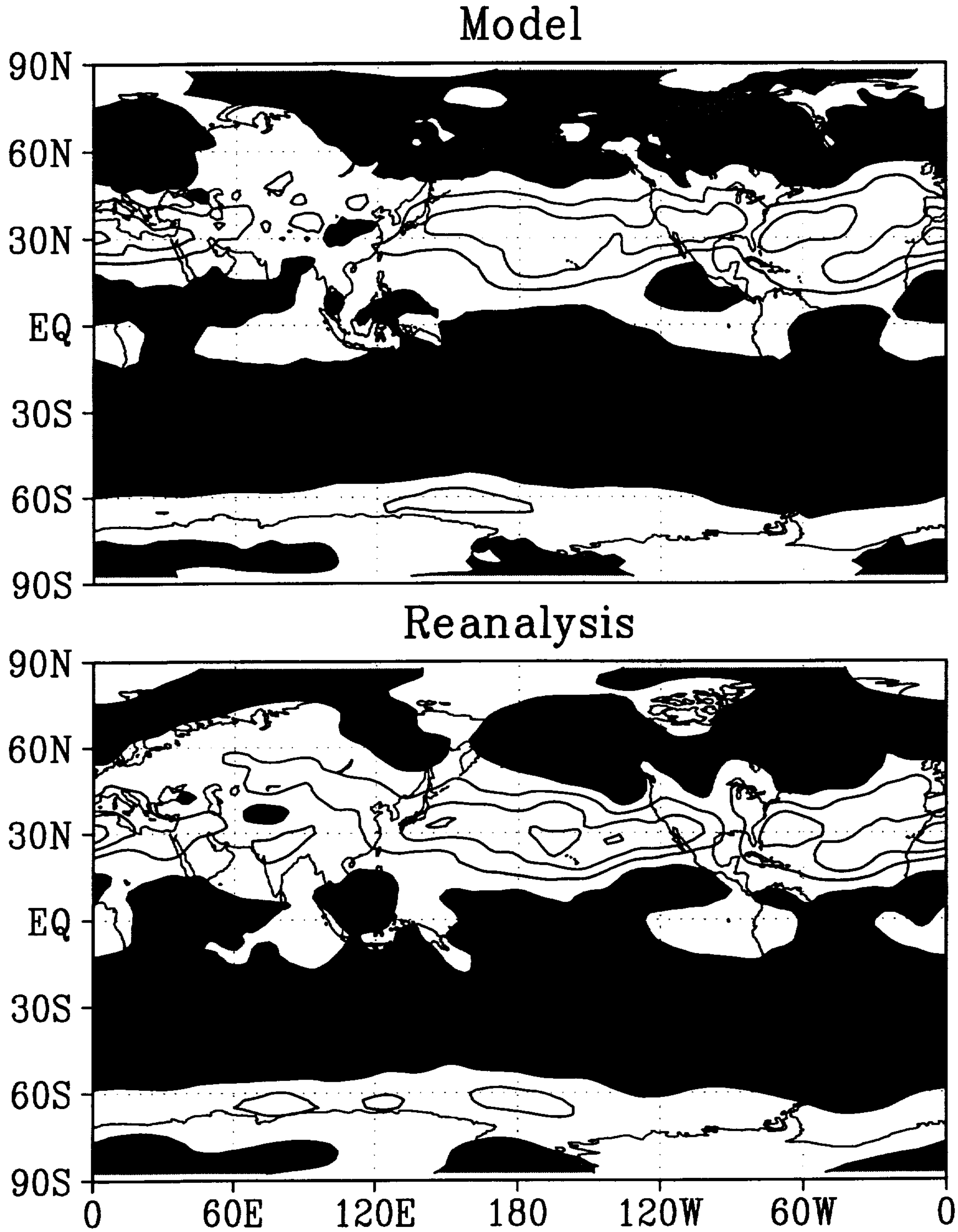

Figure 128: $[\overline{u'v'}]$ at 200 mb for MAM— Top: Model, Bottom: Reanalysis. Contour interval: 20 m^2 s^{-2}. Shading indicates negative values

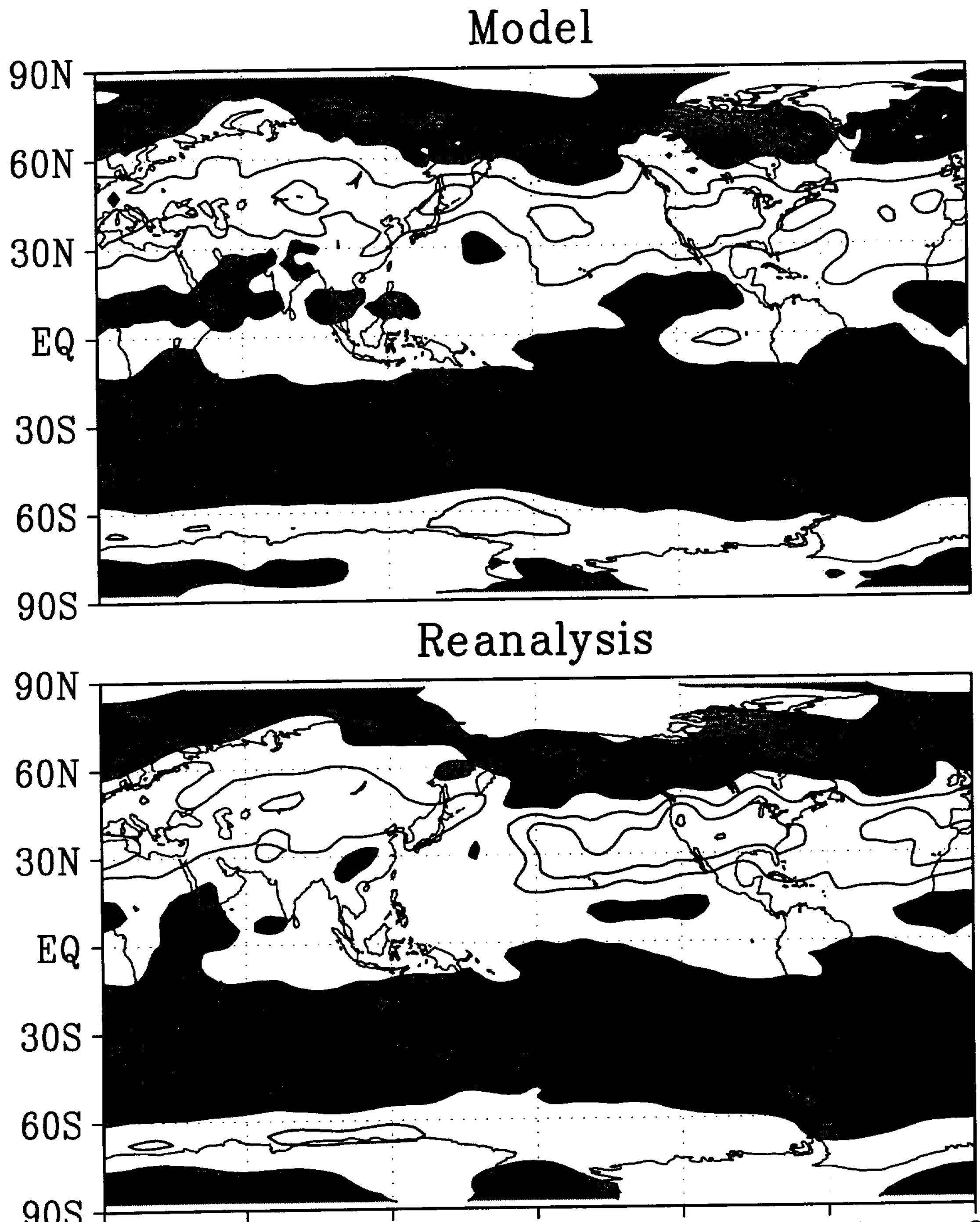

Figure 129: $[\overline{u'v'}]$ at 200 mb for SON— Top: Model, Bottom: Reanalysis. Contour interval: 20 m^2 s^{-2}. Shading indicates negative values

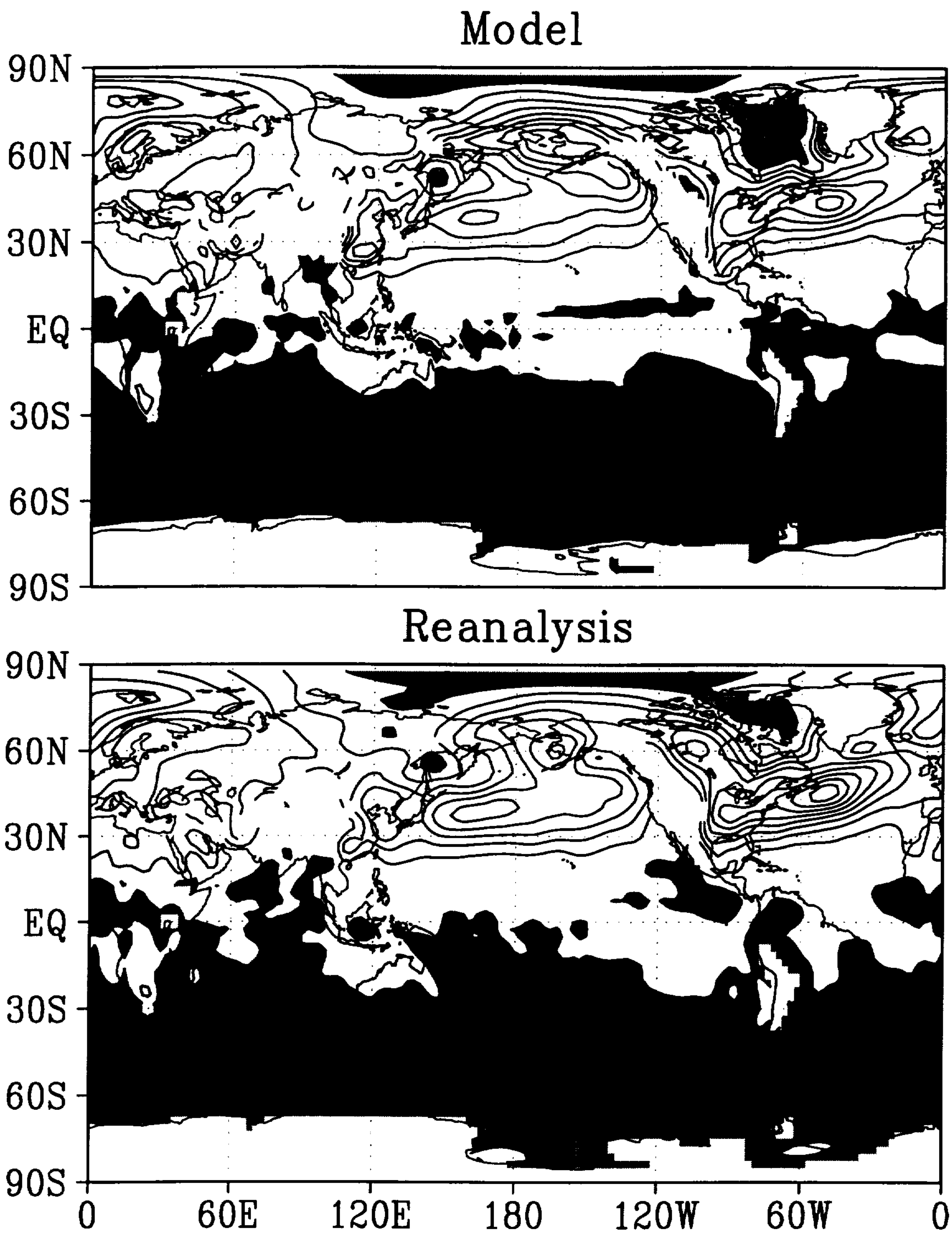

Figure 130: $\overline{[v'T']}$ at 850 mb for DJF— Top: Model, Bottom: Reanalysis. Contour interval: 5 m s^{-1} K. Shading indicates negative values

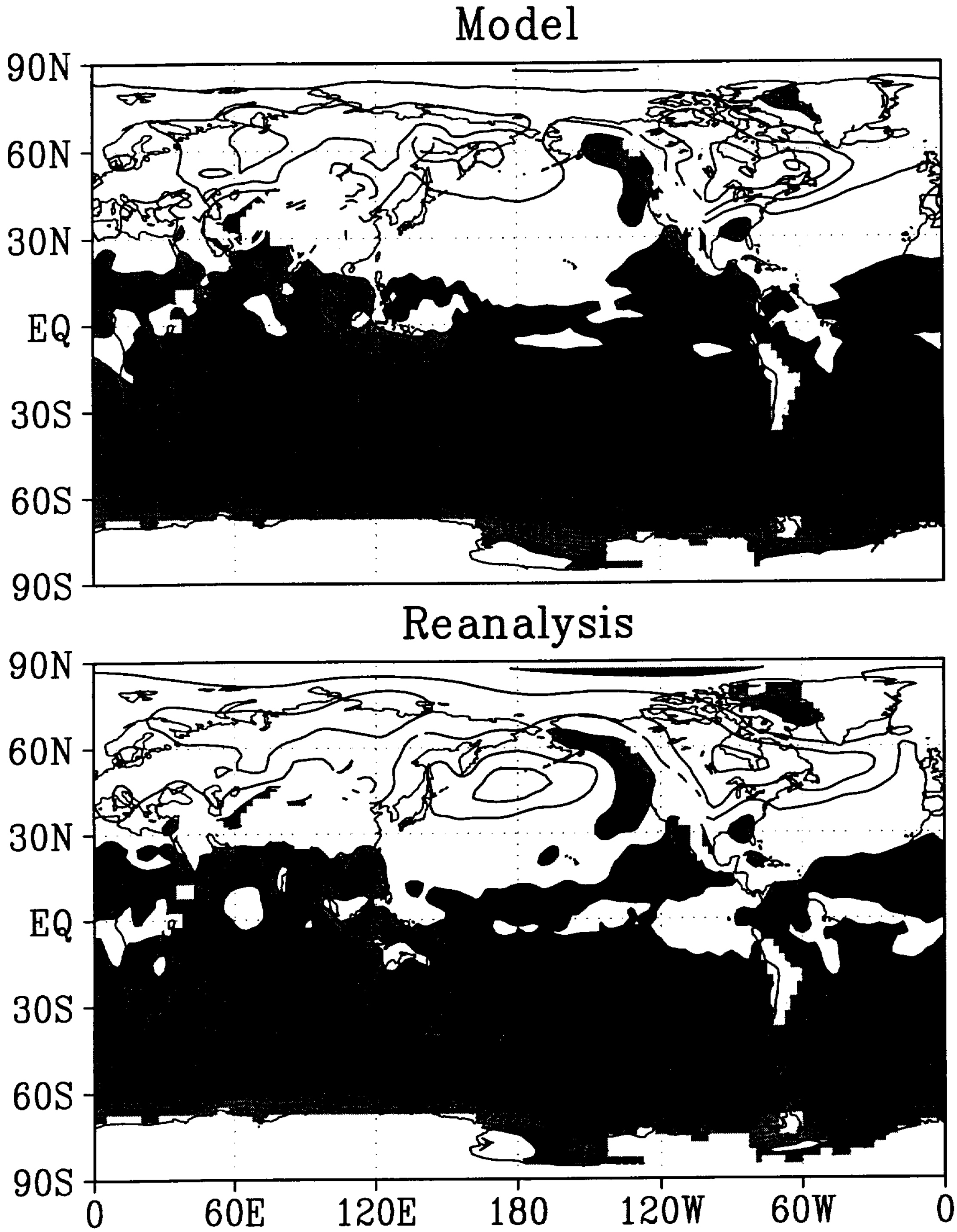

Figure 131: $[\overline{v'T'}]$ at 850 mb for JJA— Top: Model, Bottom: Reanalysis. Contour interval: 5 m s^{-1} K. Shading indicates negative values

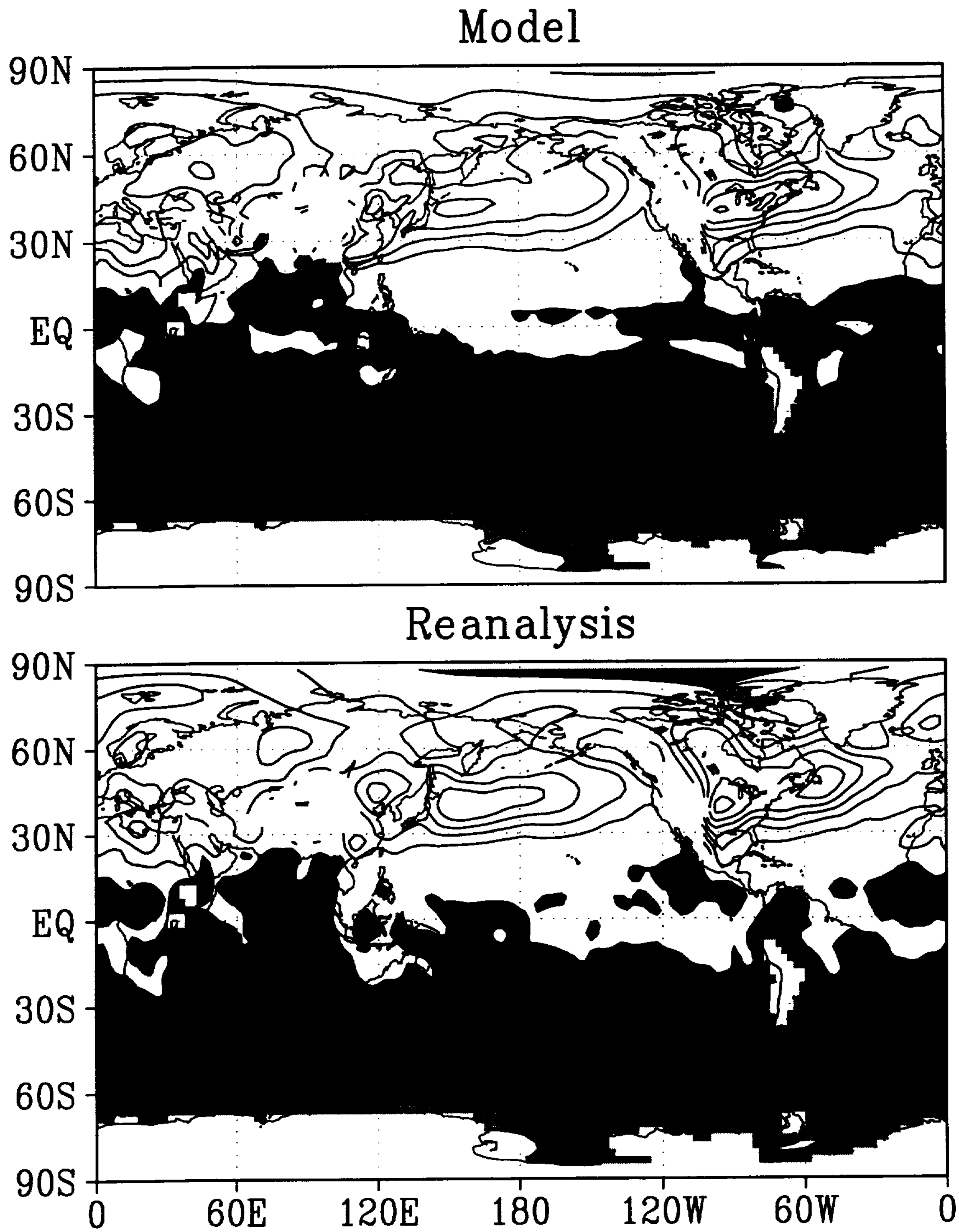

Figure 132: $[\overline{v'T'}]$ at 850 mb for MAM— Top: Model, Bottom: Reanalysis. Contour interval: 5 m s^{-1} K. Shading indicates negative values

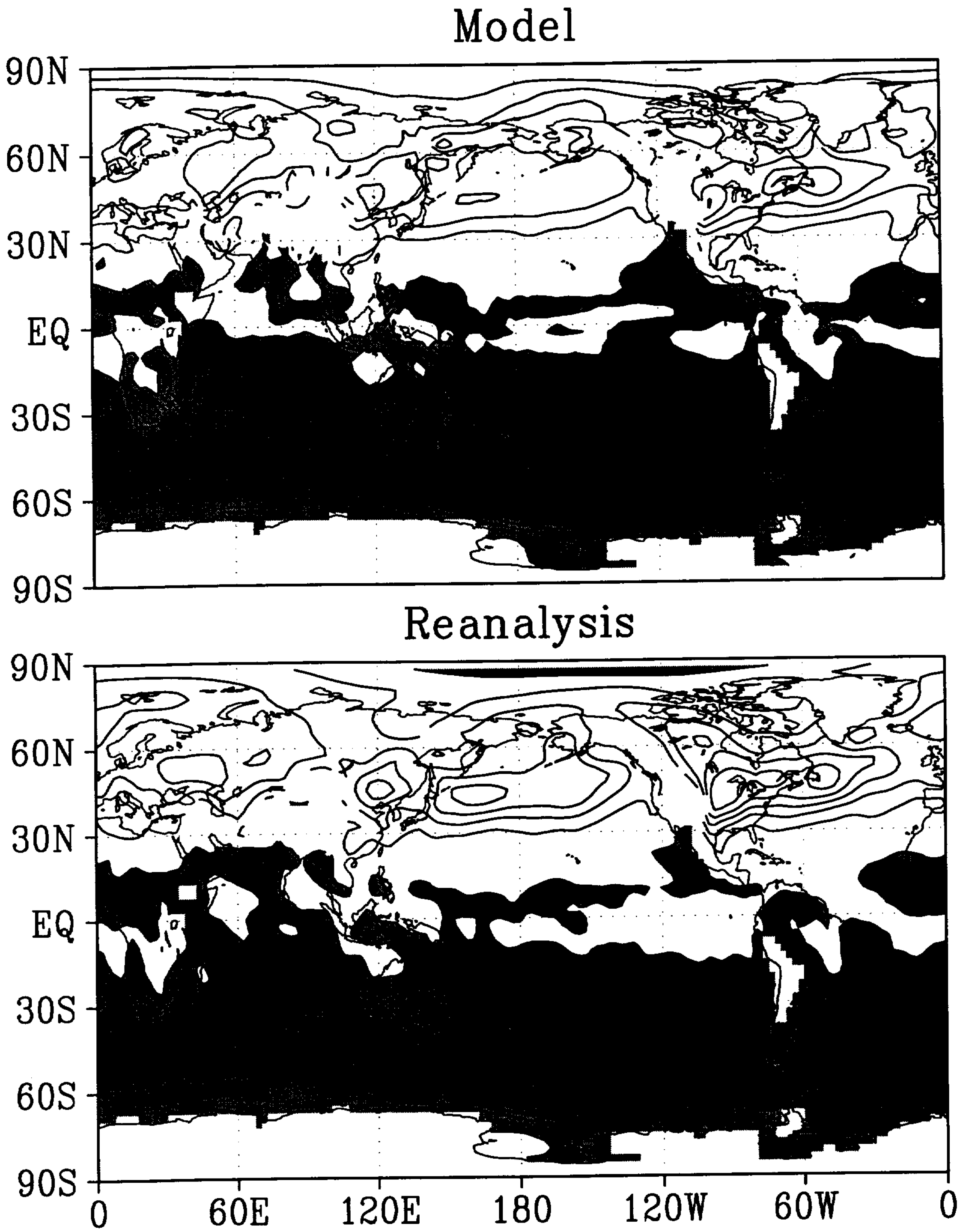

Figure 133: $[\overline{v'T'}]$ at 850 mb for SON— Top: Model, Bottom: Reanalysis. Contour interval: 5 m s^{-1} K. Shading indicates negative values

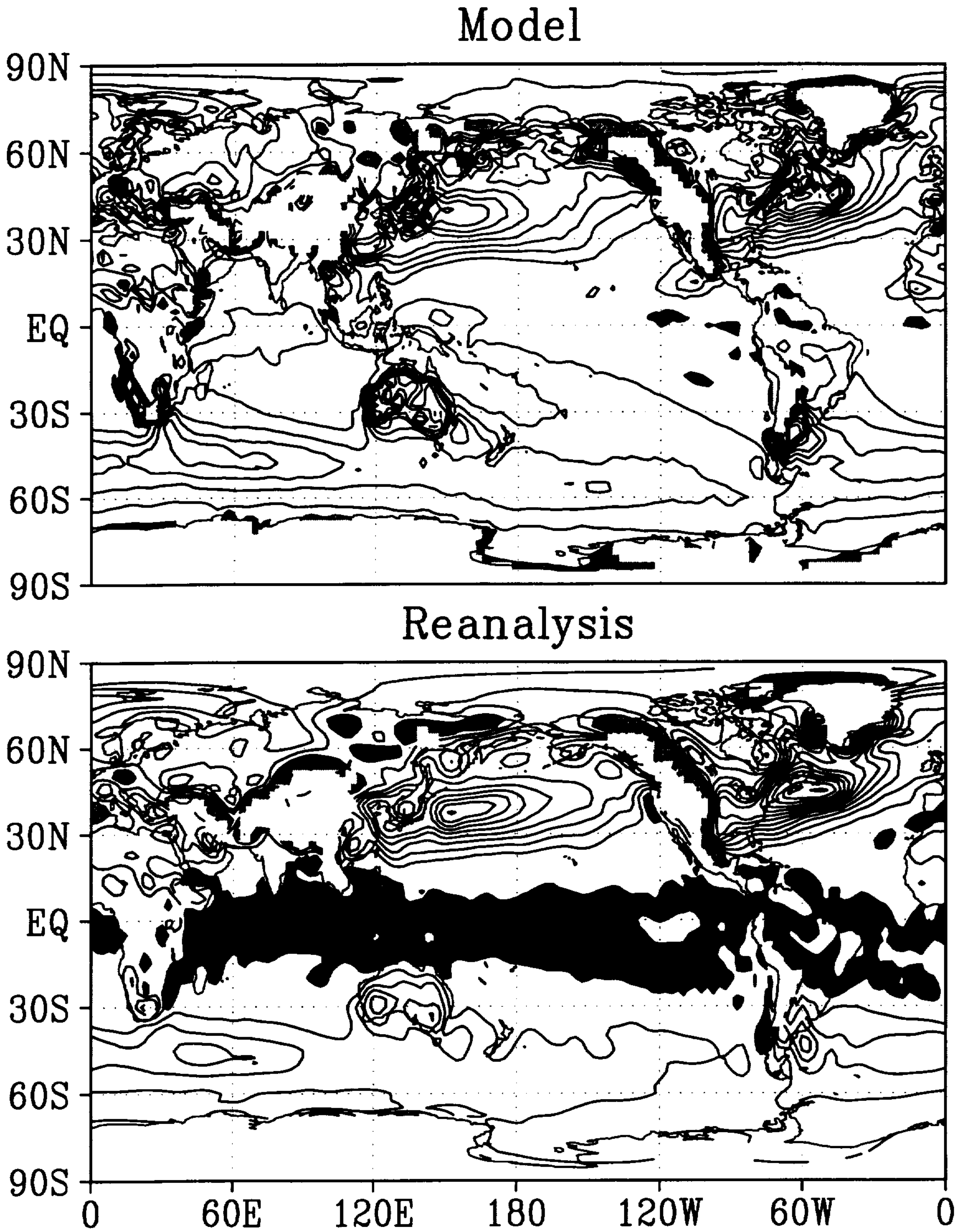

Figure 134: $-[\overline{\omega' T'}]$ at 850 mb for DJF— Top: Model, Bottom: Reanalysis. Contour interval: 50 mb d^{-1} K. Shading indicates downward heat transport

JJA $-[\overline{\omega' T'}]$ 850

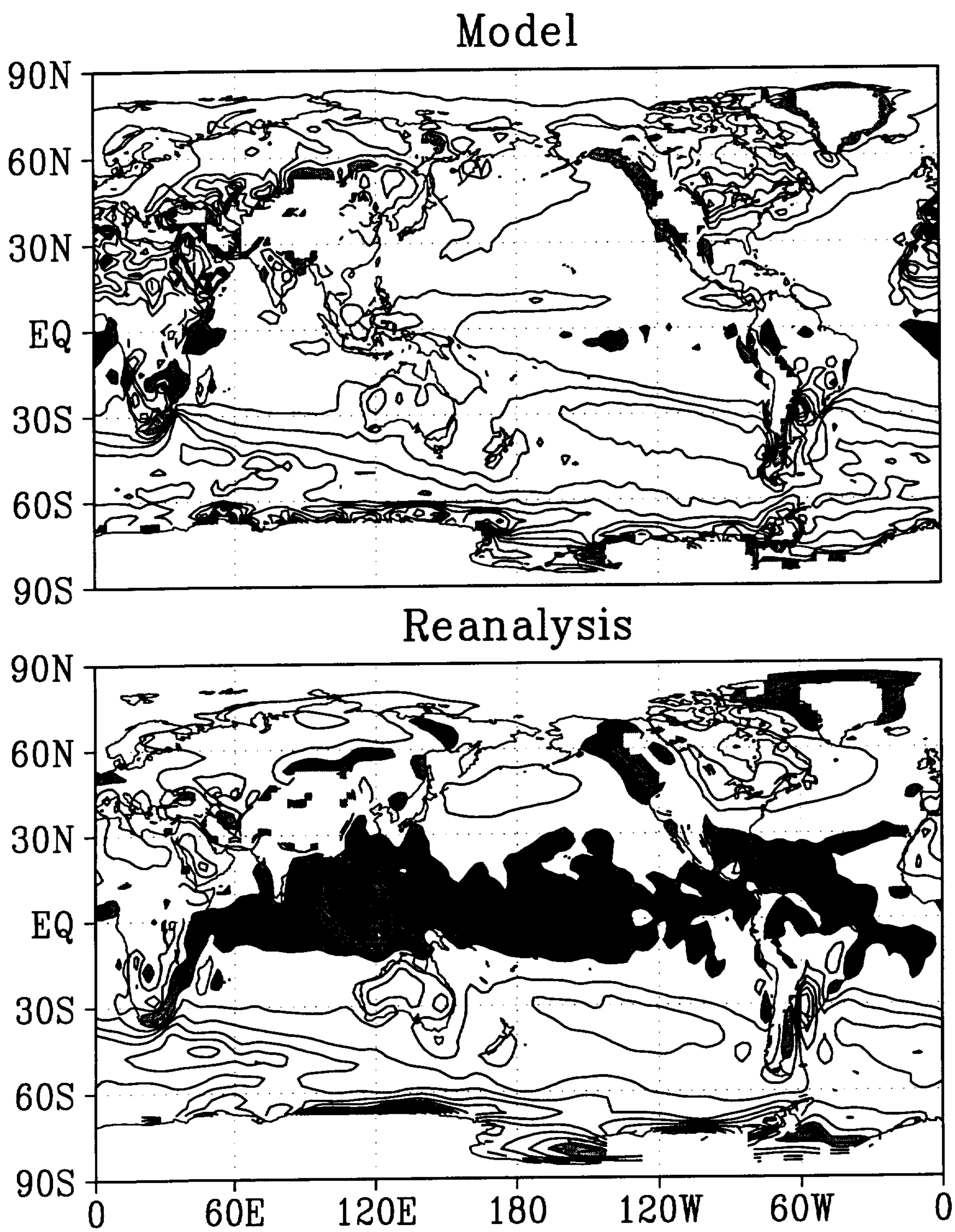

Figure 135: $-[\overline{\omega' T'}]$ at 850 mb for JJA— Top: Model, Bottom: Reanalysis. Contour interval: 50 mb d^{-1} K. Shading indicates downward heat transport

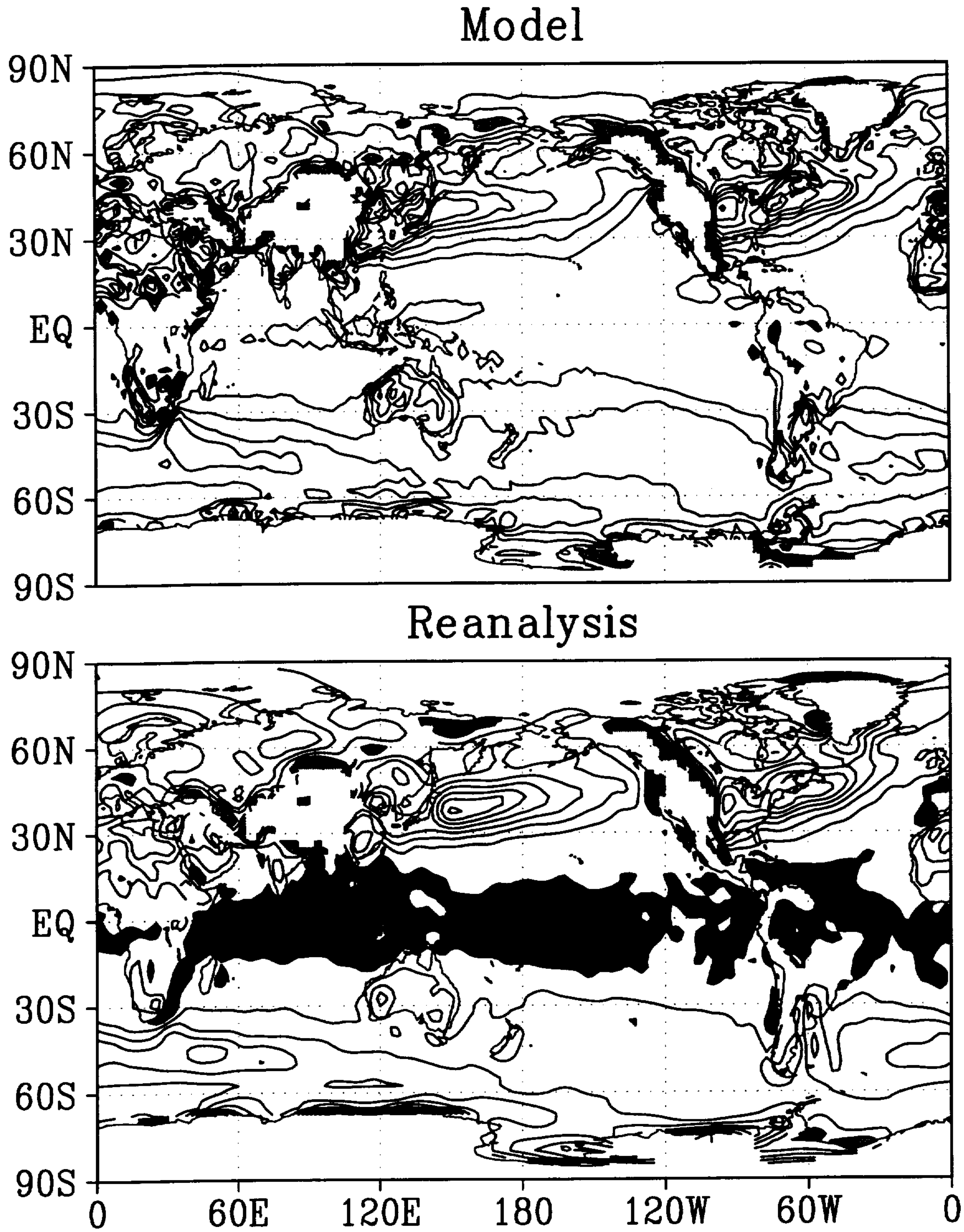

Figure 136: $-[\overline{\omega' T'}]$ at 850 mb for MAM— Top: Model, Bottom: Reanalysis. Contour interval: 50 mb d^{-1} K. Shading indicates downward heat transport

SON $-[\overline{\omega' T'}]$ 850

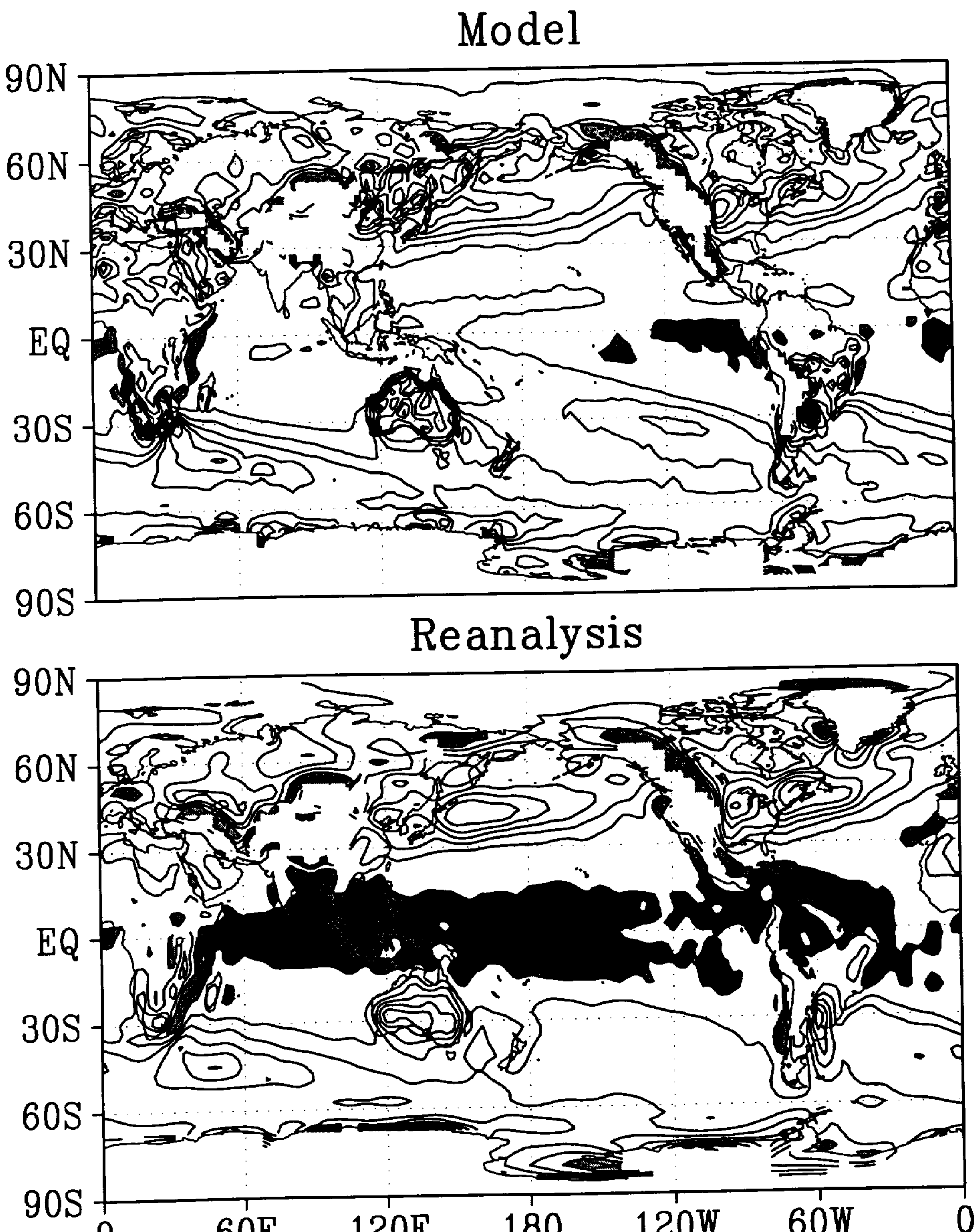

Figure 137: $-[\overline{\omega' T'}]$ at 850 mb for SON— Top: Model, Bottom: Reanalysis. Contour interval: 50 mb d^{-1} K. Shading indicates downward heat transport

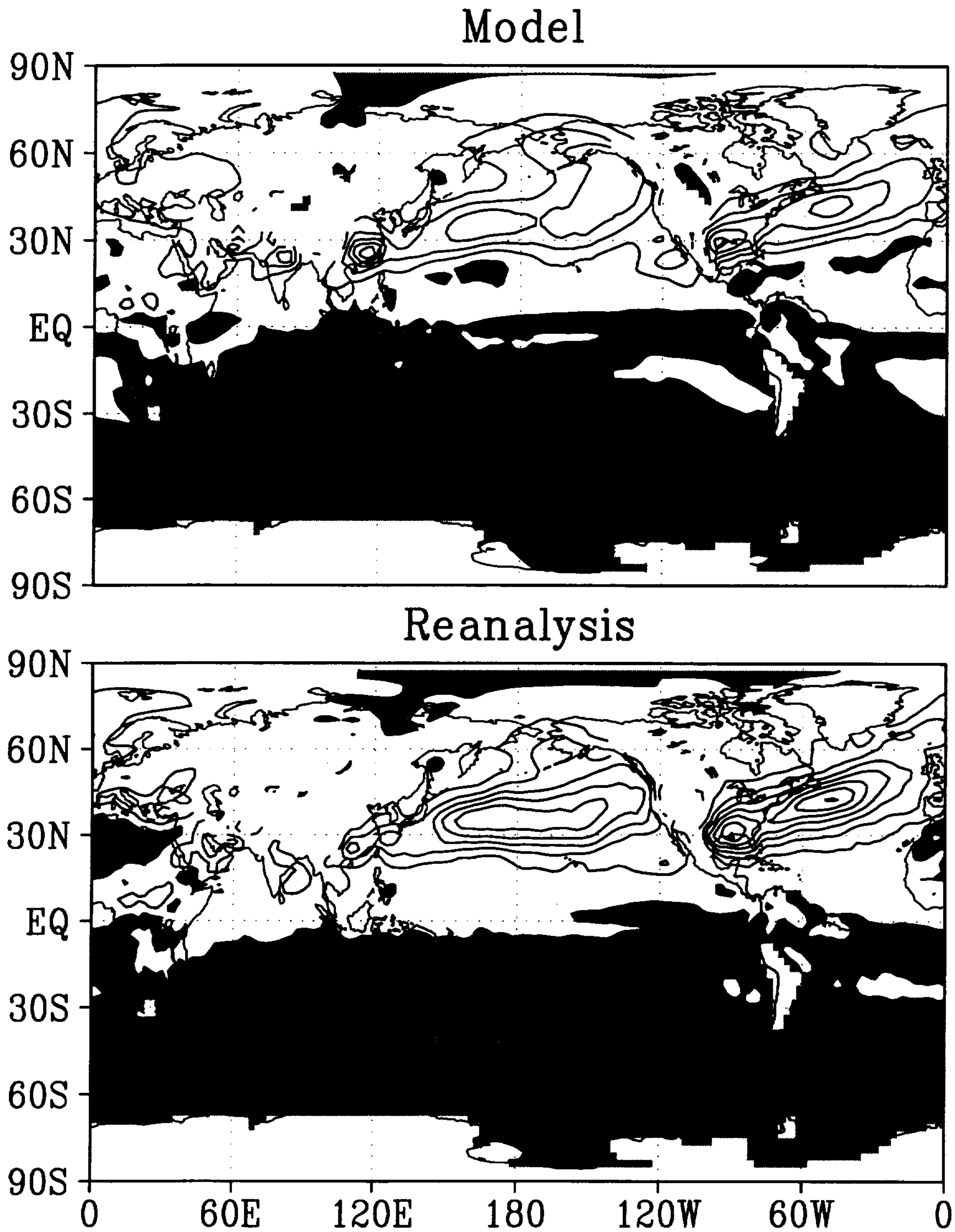

Figure 138: $\overline{[v'q']}$ at 850 mb (m s^{-1} g kg^{-1}) for DJF— Top: Model, Bottom: Reanalysis. Contour interval: 2 m s^{-1} g kg^{-1}. Shading indicates negative values

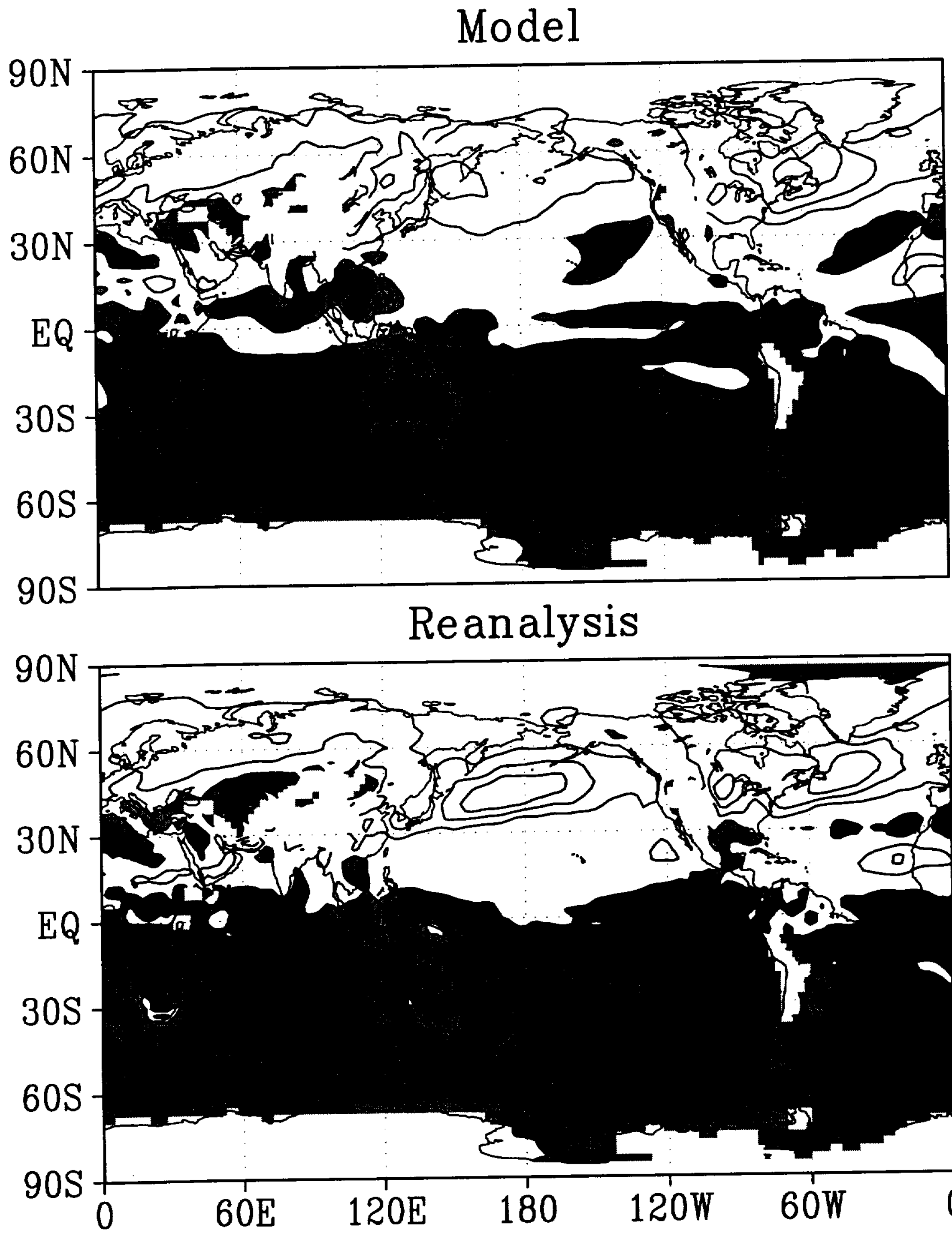

Figure 139: $[\overline{v'q'}]$ at 850 mb (m s^{-1} g kg^{-1}) for JJA— Top: Model, Bottom: Reanalysis. Contour interval: 2 m s^{-1} g kg^{-1}. Shading indicates negative values

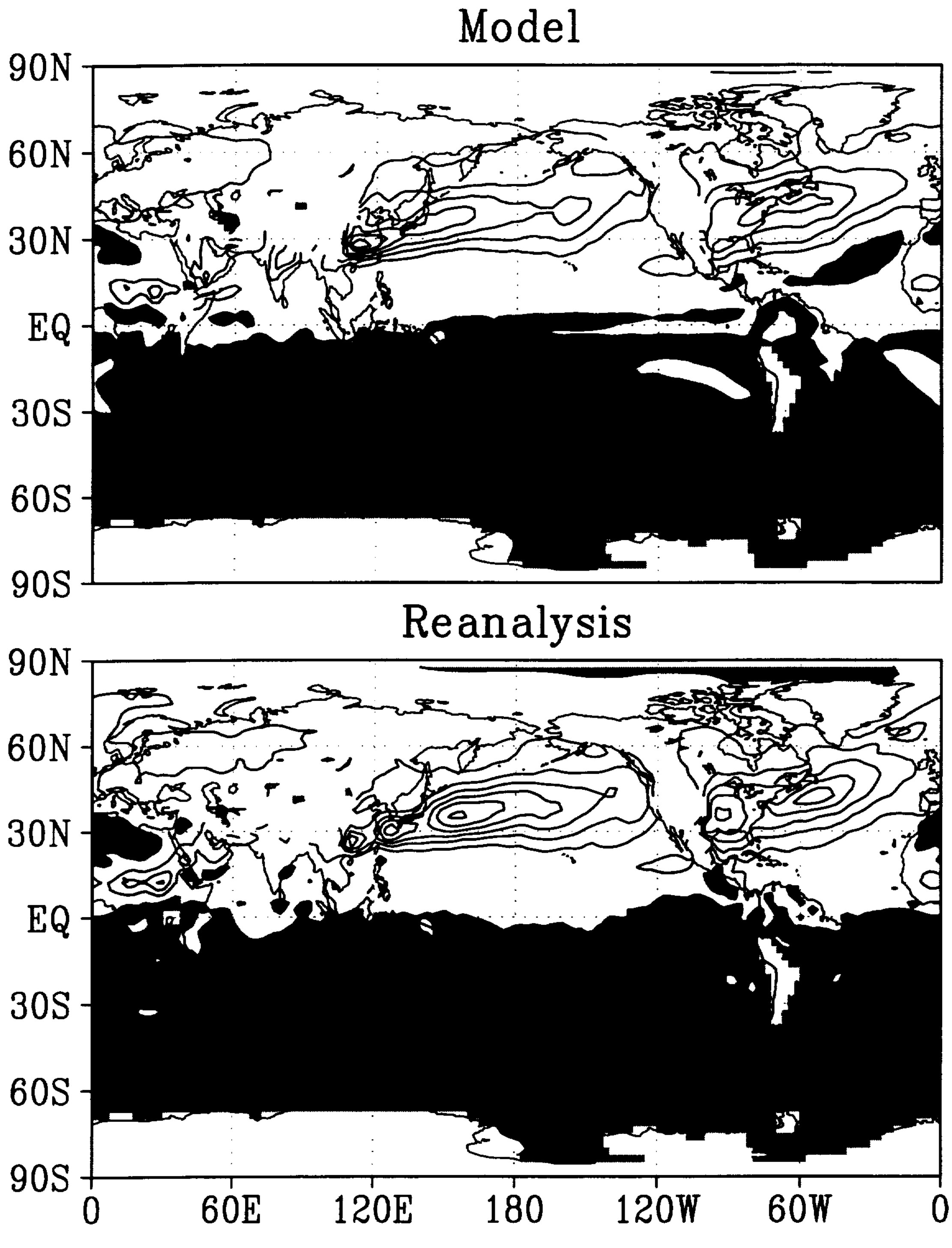

Figure 140: $[\overline{v'q'}]$ at 850 mb (m s^{-1} g kg^{-1}) for MAM— Top: Model, Bottom: Reanalysis. Contour interval: 2 m s^{-1} g kg^{-1}. Shading indicates negative values

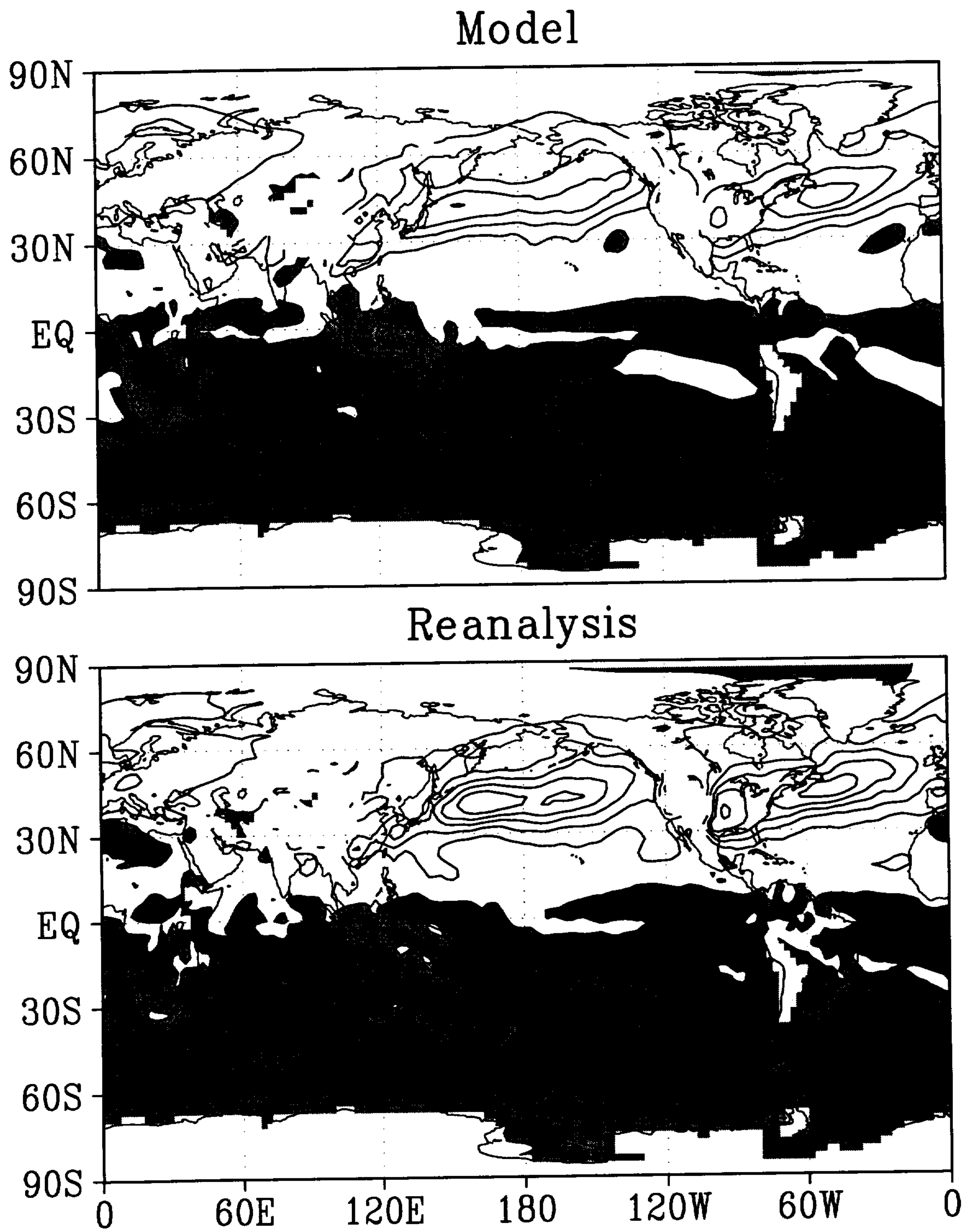

Figure 141: $\overline{[v'q']}$ at 850 mb (m s^{-1} g kg^{-1}) for SON— Top: Model, Bottom: Reanalysis. Contour interval: 2 m s^{-1} g kg^{-1}. Shading indicates negative values

GLOBAL MAPS OF PHYSICS DIAGNOSTICS

(DJF, MAM, JJA, SON)

Precipitation

Total Precipitable Water

Outgoing Longwave Radiation

Longwave Cloud Radiative Forcing

Absorbed Solar Radiation

Solar Cloud Radiative Forcing

Net Radiation at the Top of the Atmosphere

Net Cloud Radiative Forcing

Zonal Surface Stress (τ_x)

Meridional Surface Stress (τ_y)

Curl of the Surface Wind Stress

Surface Sensible Heat Flux

Surface Latent Heat Flux

Total Precipitation

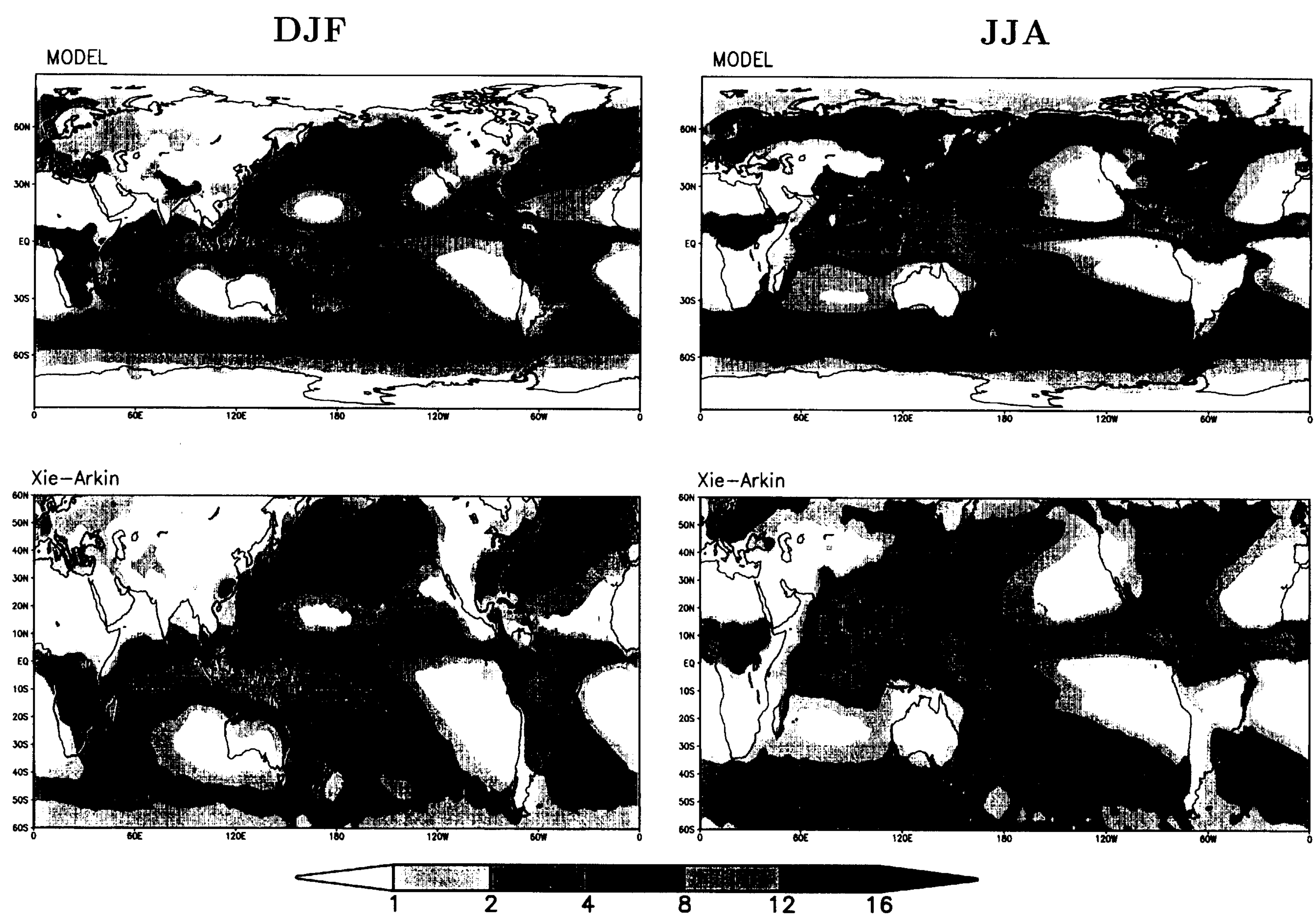

Figure 142: Total precipitation (mm d^{-1}). The comparison is for the entire 20-year period of the run. — Upper panels: Model; Lower panels: Reanalysis; Left panels: DJF; Right panels: JJA.

Total Precipitation

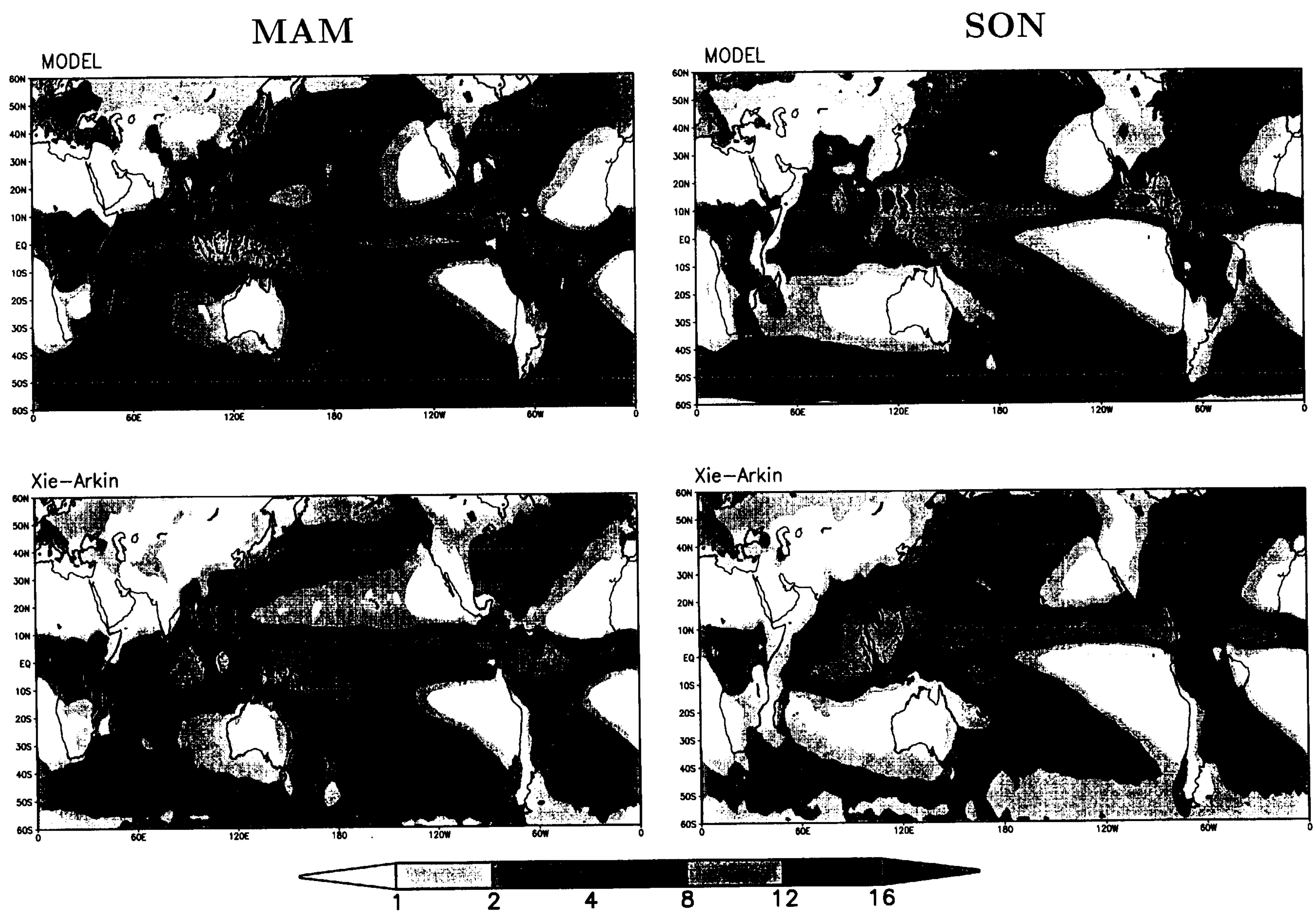

Figure 143: Total precipitation (mm d^{-1}). The comparison is for the entire 20-year period of the run. — Upper panels: Model; Lower panels: Reanalysis; Left panels: MAM; Right panels: SON.

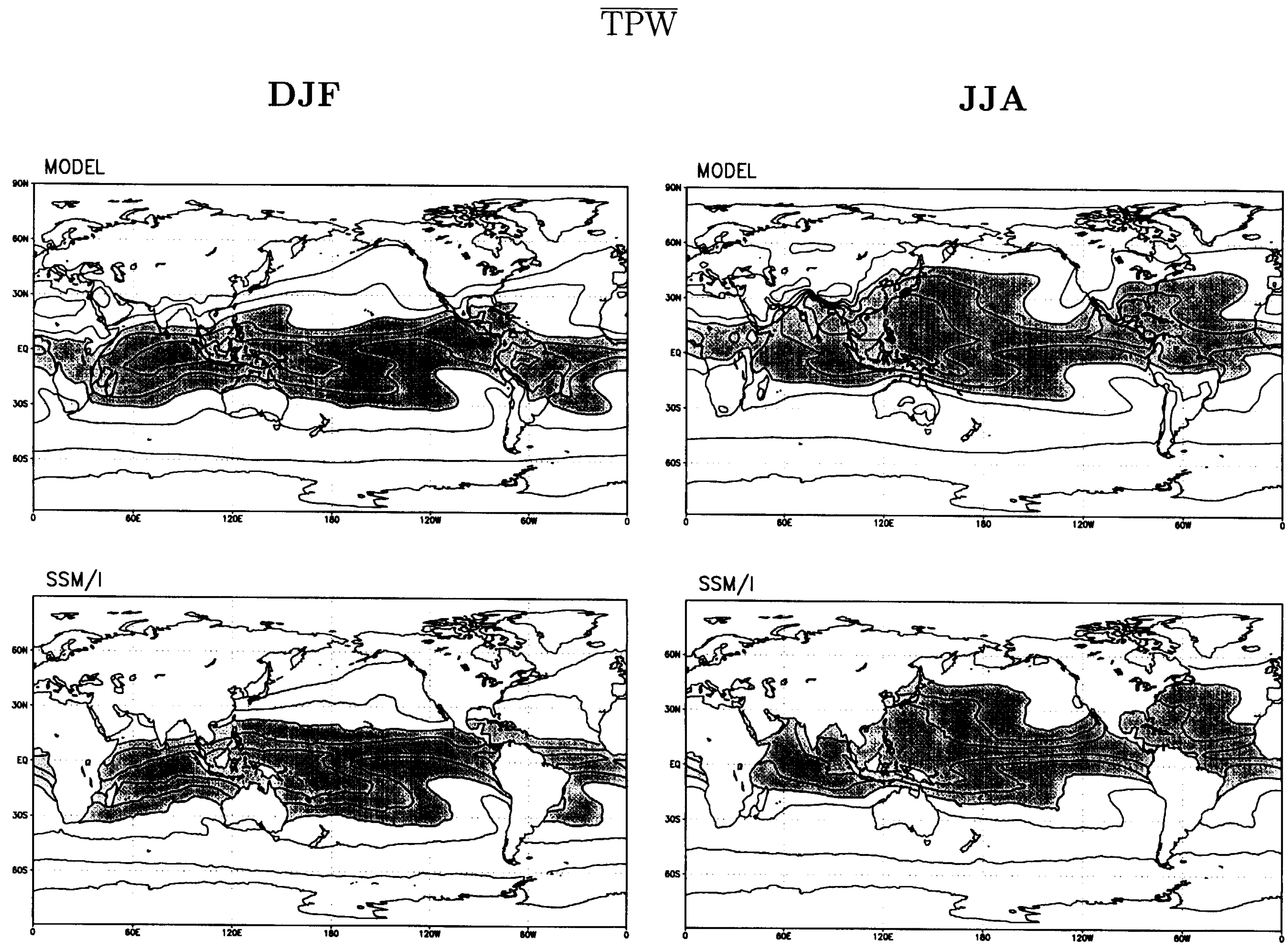

Figure 144: Total precipitable water (kg m^{-2}). The comparison is for the period July 1987 to February 1992. — Upper panels: Model; Lower panels: Reanalysis; Left panels: DJF; Right panels: JJA. Contour interval: 10 kg m^{-2}. Shading indicates values in excess of 30 kg m^{-2}.

$\overline{\text{TPW}}$

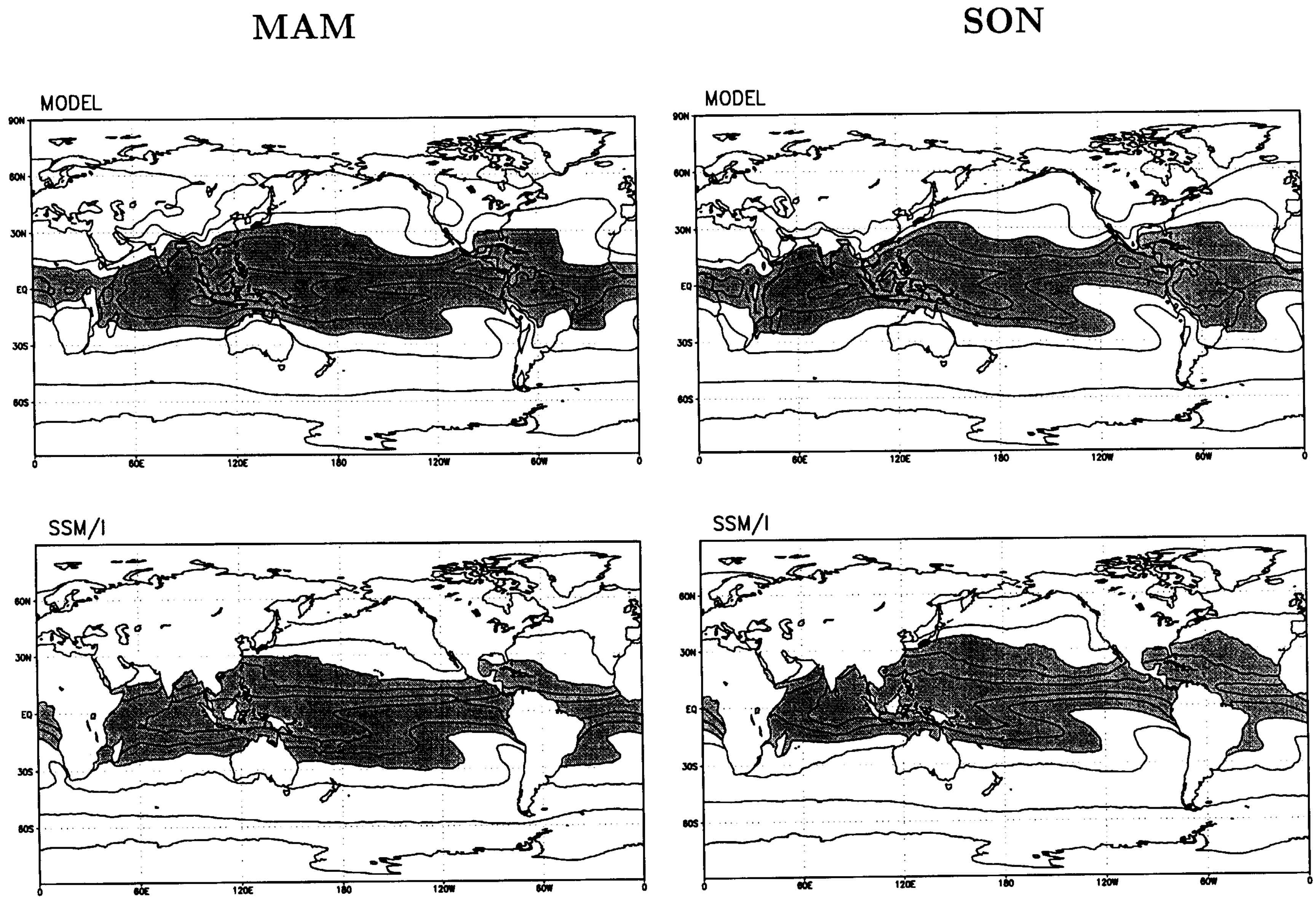

Figure 145: Total precipitable water (kg m^{-2}). The comparison is for the period July 1987 to February 1992. — Upper panels: Model; Lower panels: Reanalysis; Left panels: MAM; Right panels: SON. Contour interval: 10 kg m^{-2}. Shading indicates values in excess of 30 kg m^{-2}.

$[OLR]$

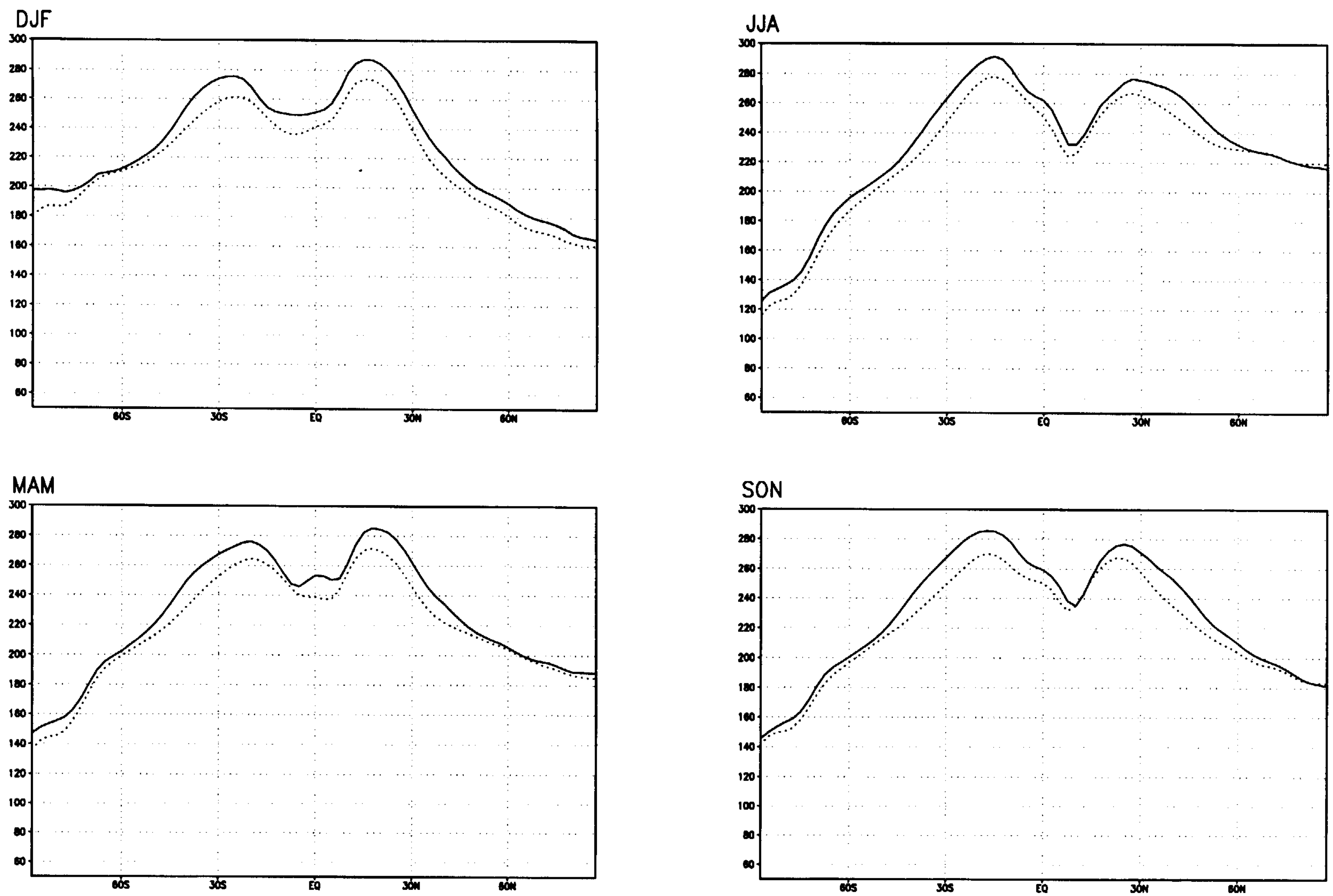

Figure 146: Outgoing longwave radiation at the top of the atmosphere (W m^{-2}). The comparison is for the ERBE period: January 1985 to December 1989. . Solid: Model, Dashed: ERBE.

$[NSR]$

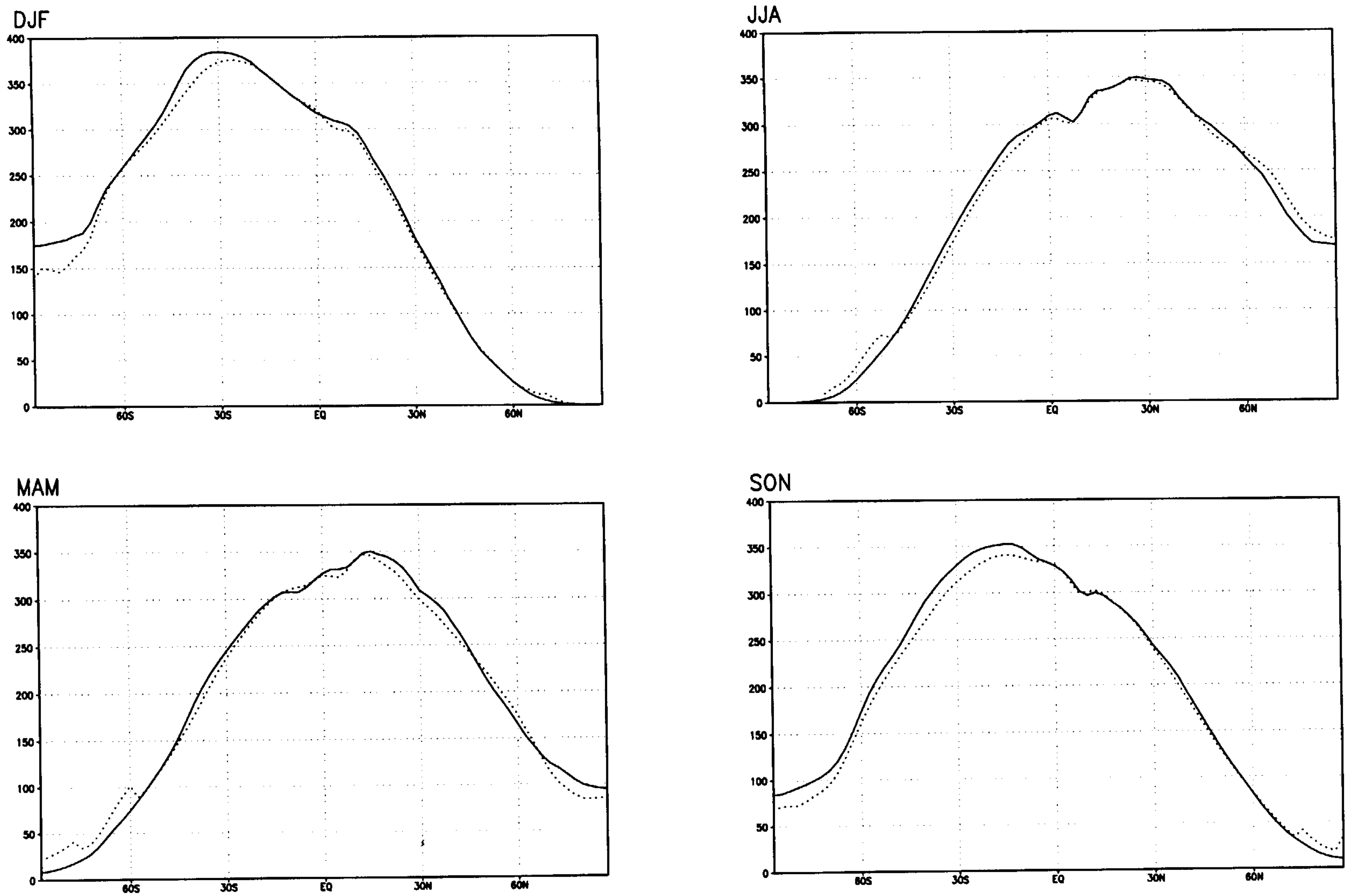

Figure 147: Net downward shortwave radiation at the top of the atmosphere (W m^{-2}). The comparison is for the ERBE period: January 1985 to December 1989. . Solid: Model, Dashed: ERBE.

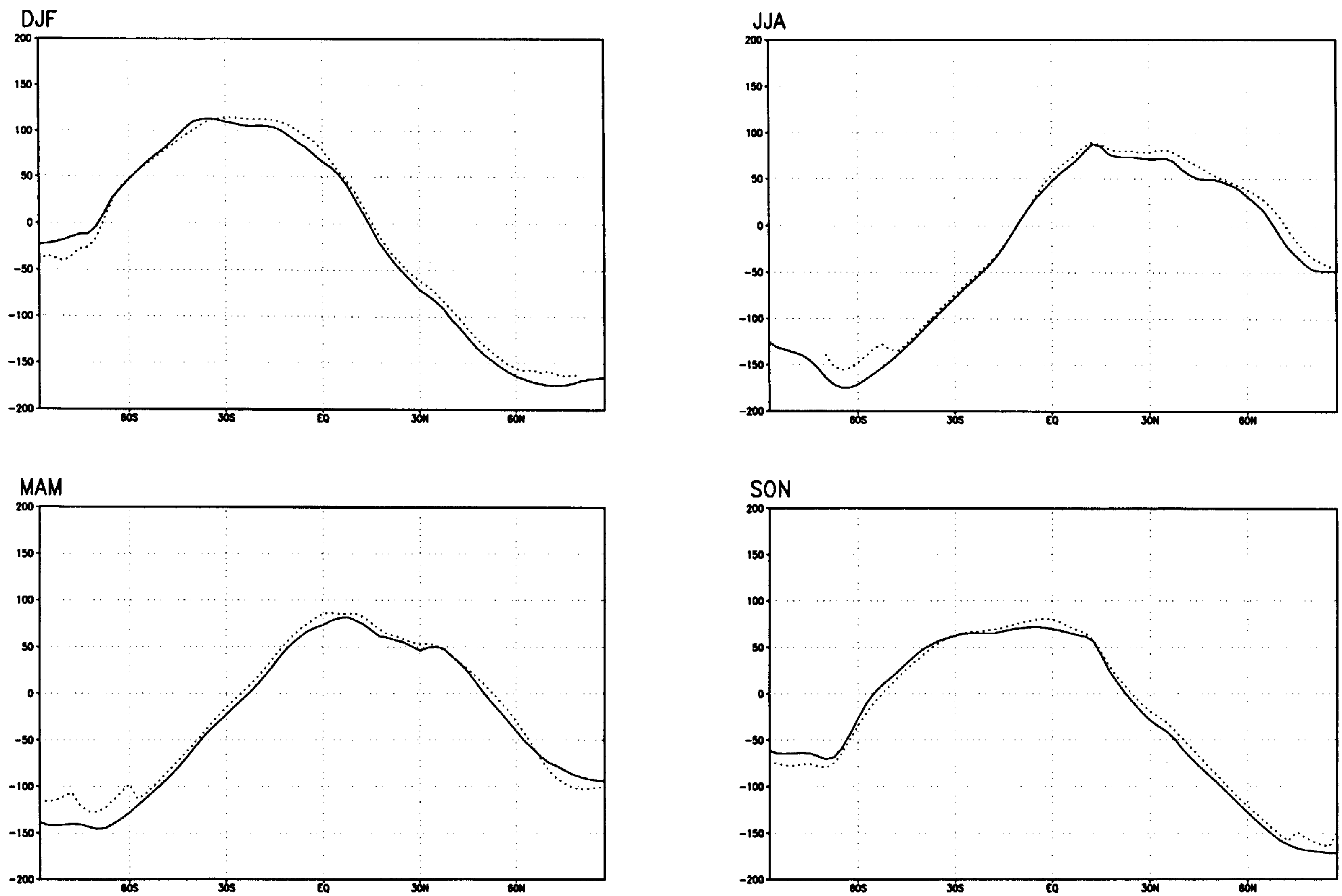

Figure 148: Net downward radiation at the top of the atmosphere at the top of the atmosphere (W m^{-2}). The comparison is for the ERBE period: January 1985 to December 1989. . Solid: Model, Dashed: ERBE.

$\boxed{OLR\_CRF}$

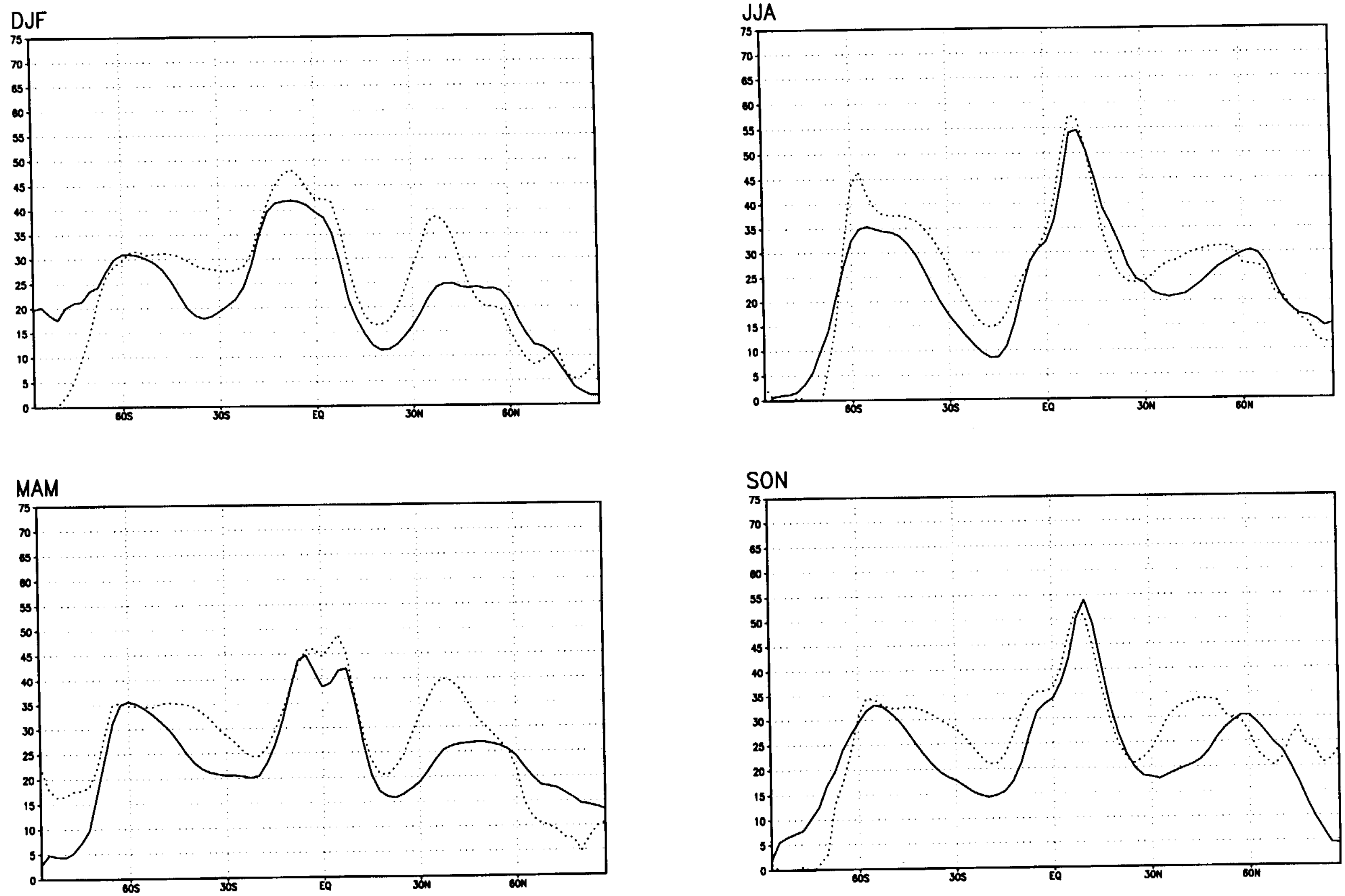

Figure 149: Longwave cloud radiative forcing (W m^{-2}). . Solid: Model, Dashed: ERBE.

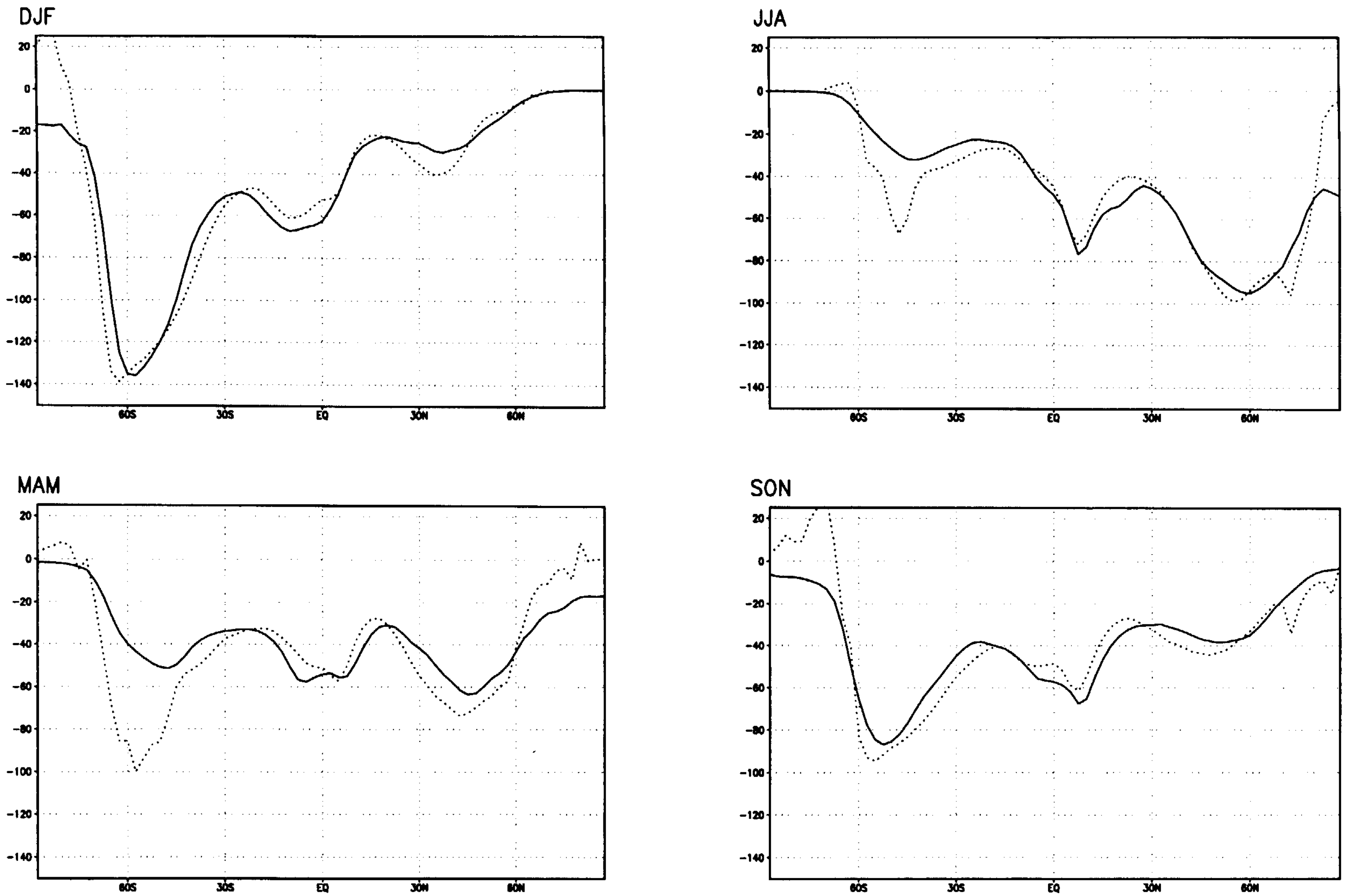

Figure 150: Shortwave cloud radiative forcing (W m^{-2}). The comparison is for the ERBE period: January 1985 to December 1989. . Solid: Model, Dashed: ERBE.

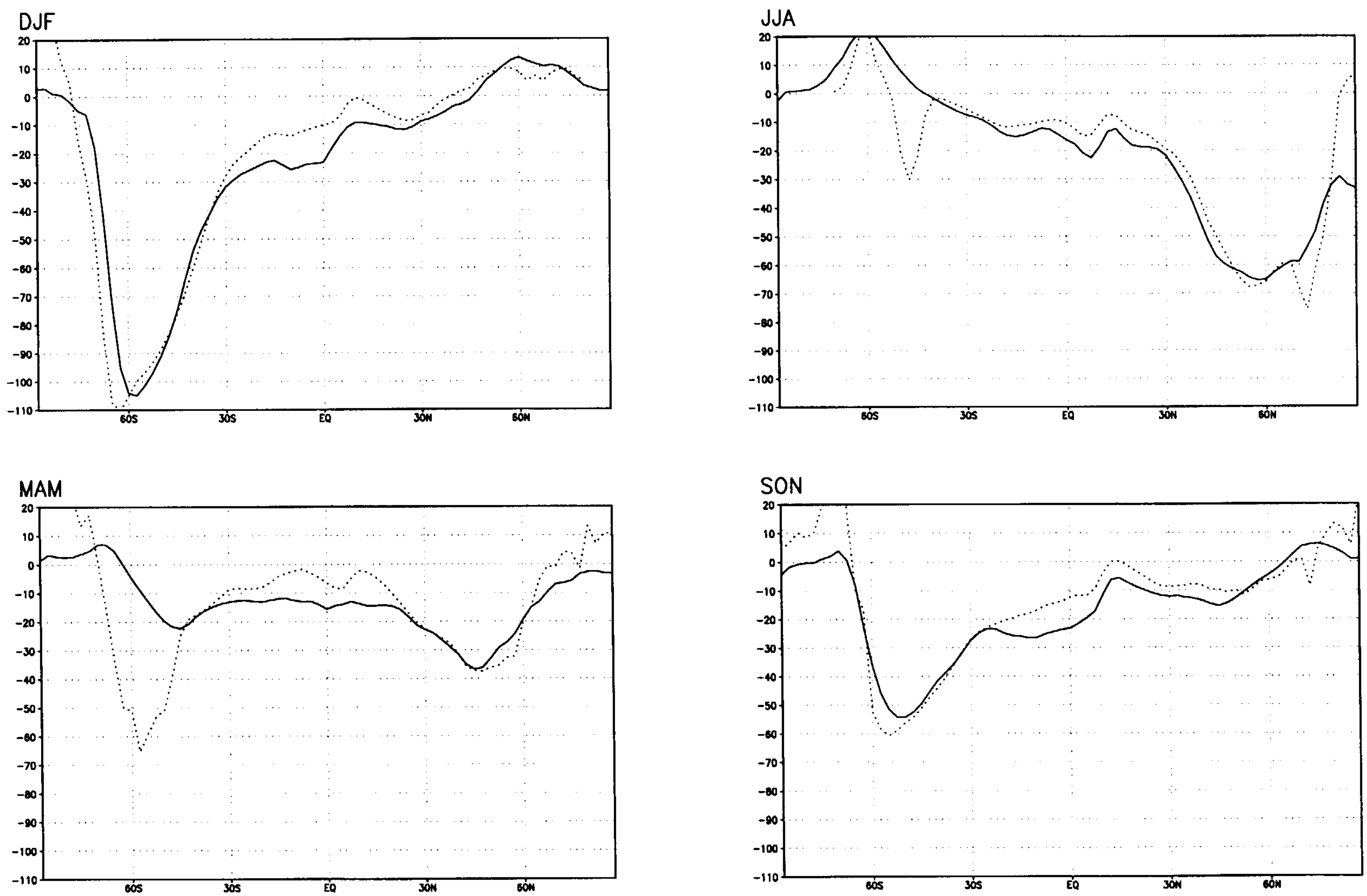

Figure 151: Net cloud radiative forcing (W m^{-2}). The comparison is for the ERBE period: January 1985 to December 1989. . Solid: Model, Dashed: ERBE.

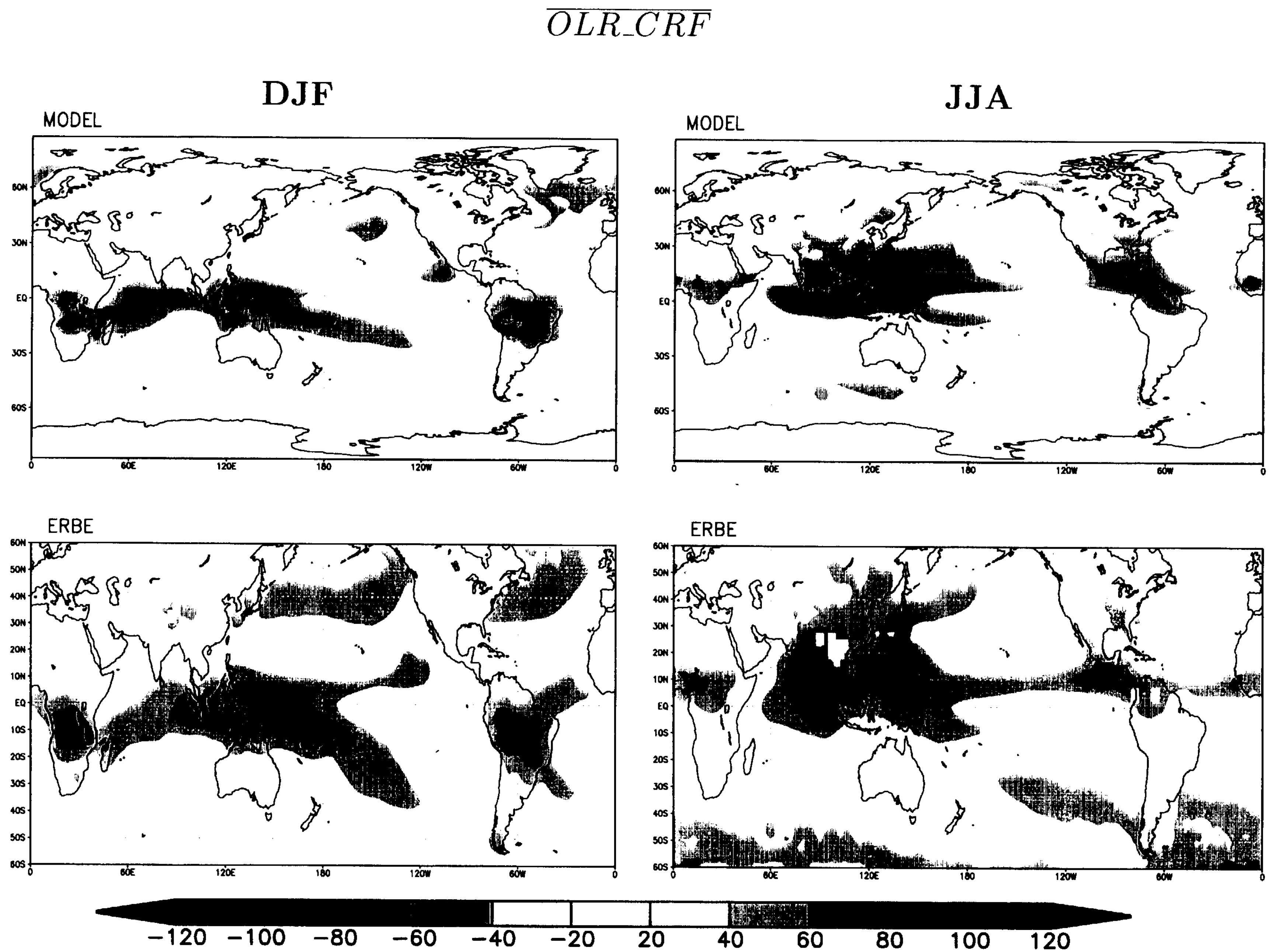

Figure 152: Longwave cloud radiative forcing (W m^{-2}). The comparison is for the ERBE period: January 1985 to December 1989.— Upper panels: Model; Lower panels: Reanalysis; Left panels: DJF; Right panels: JJA.

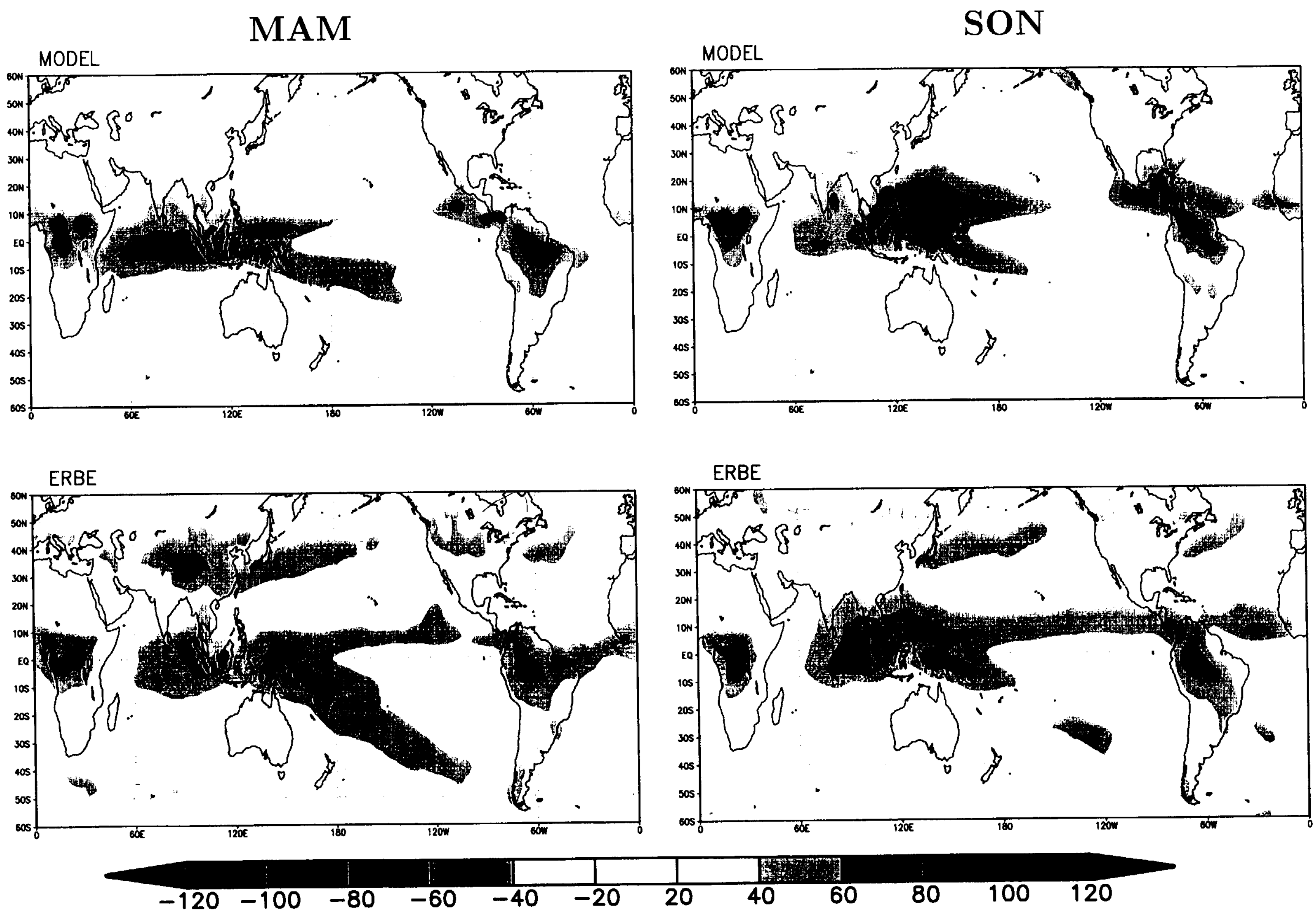

Figure 153: Longwave cloud radiative forcing (W m^{-2}). The comparison is for the ERBE period: January 1985 to December 1989.— Upper panels: Model; Lower panels: Reanalysis; Left panels: MAM; Right panels: SON.

$\overline{NSR\_CRF}$

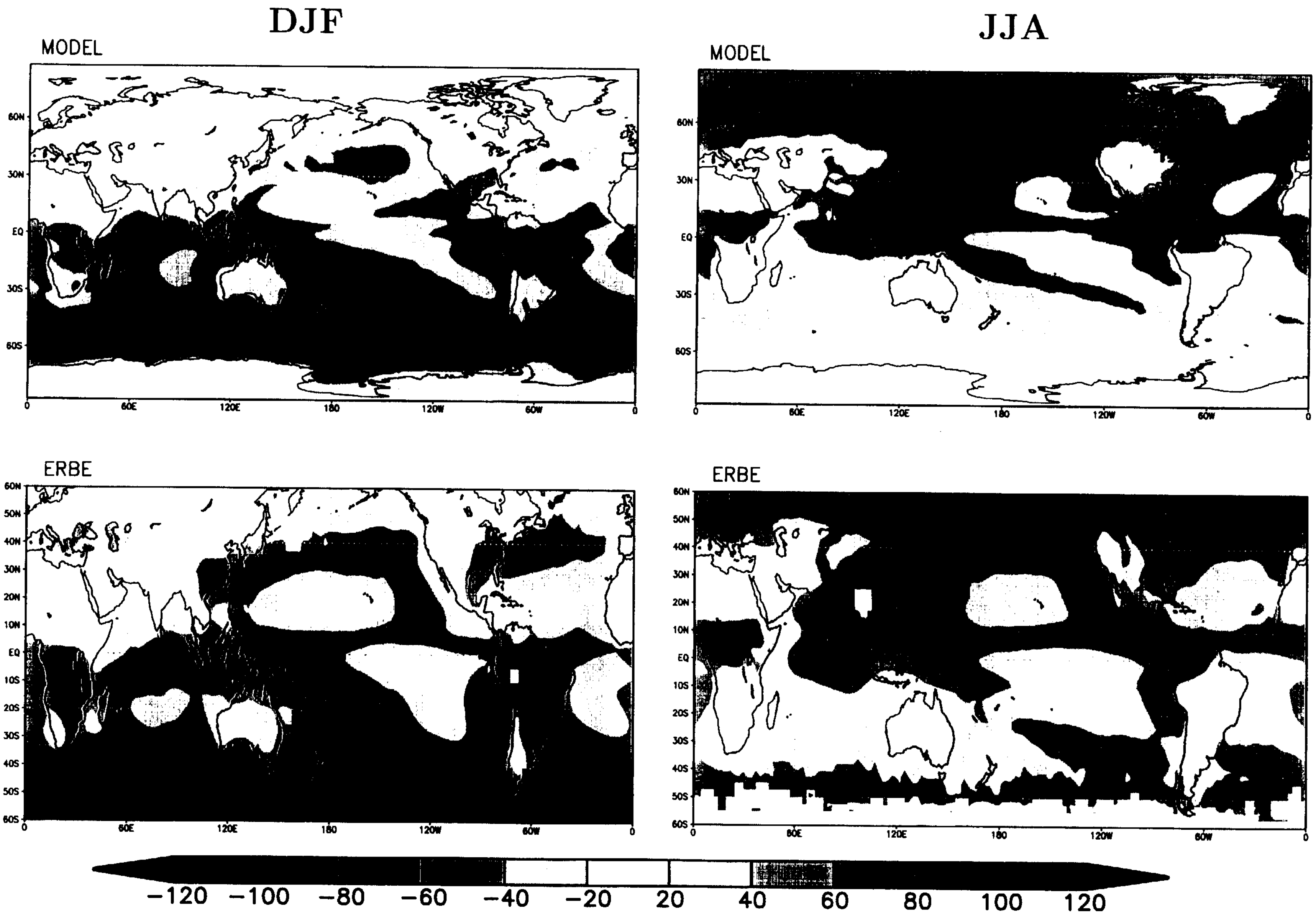

Figure 154: Shortwave cloud radiative forcing (W m^{-2}). The comparison is for the ERBE period: January 1985 to December 1989.—Upper panels: Model; Lower panels: Reanalysis; Left panels: DJF; Right panels: JJA.

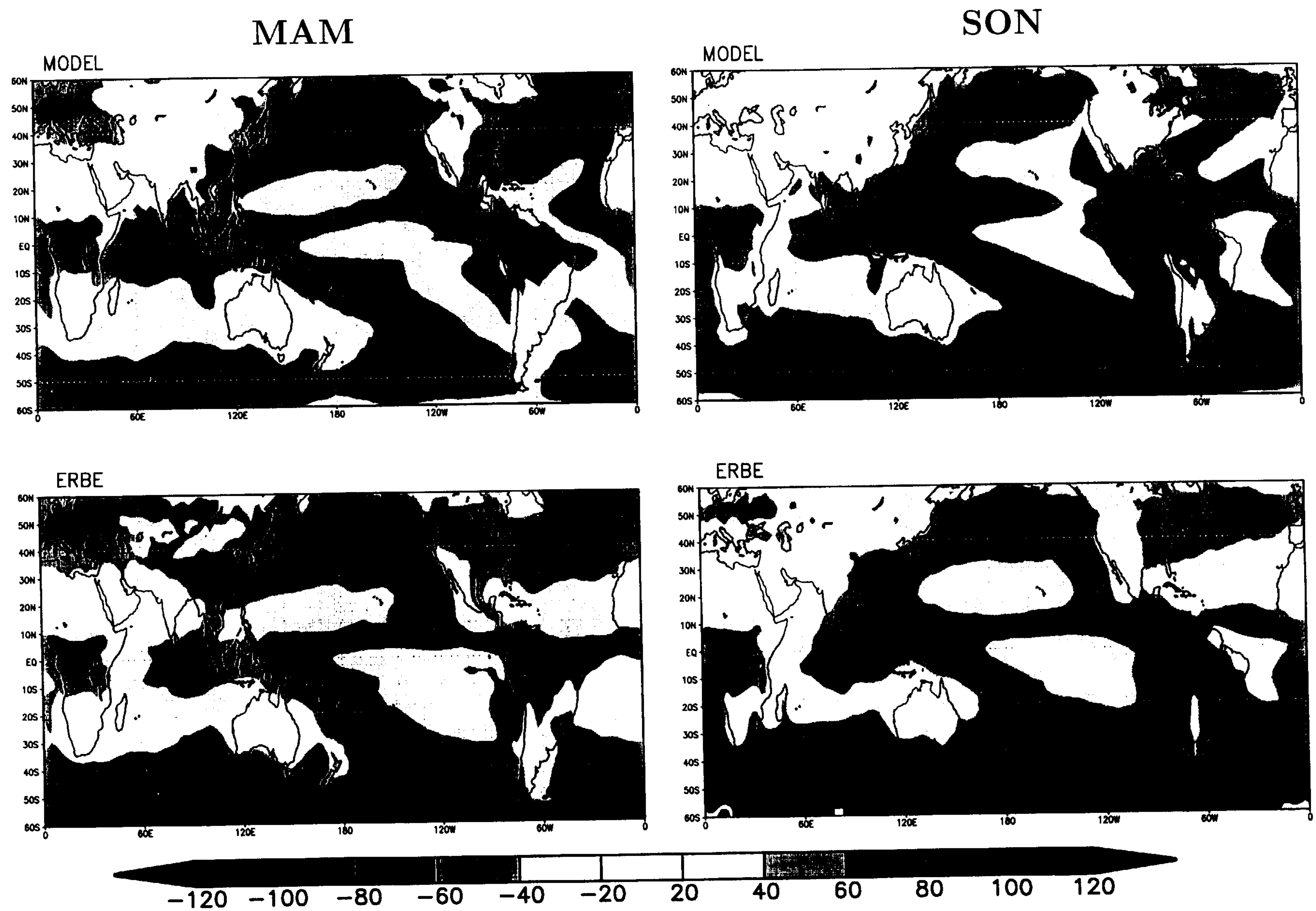

Figure 155: Shortwave cloud radiative forcing (W m^{-2}). The comparison is for the ERBE period: January 1985 to December 1989.— Upper panels: Model; Lower panels: Reanalysis; Left panels: MAM; Right panels: SON.

NET_CRF

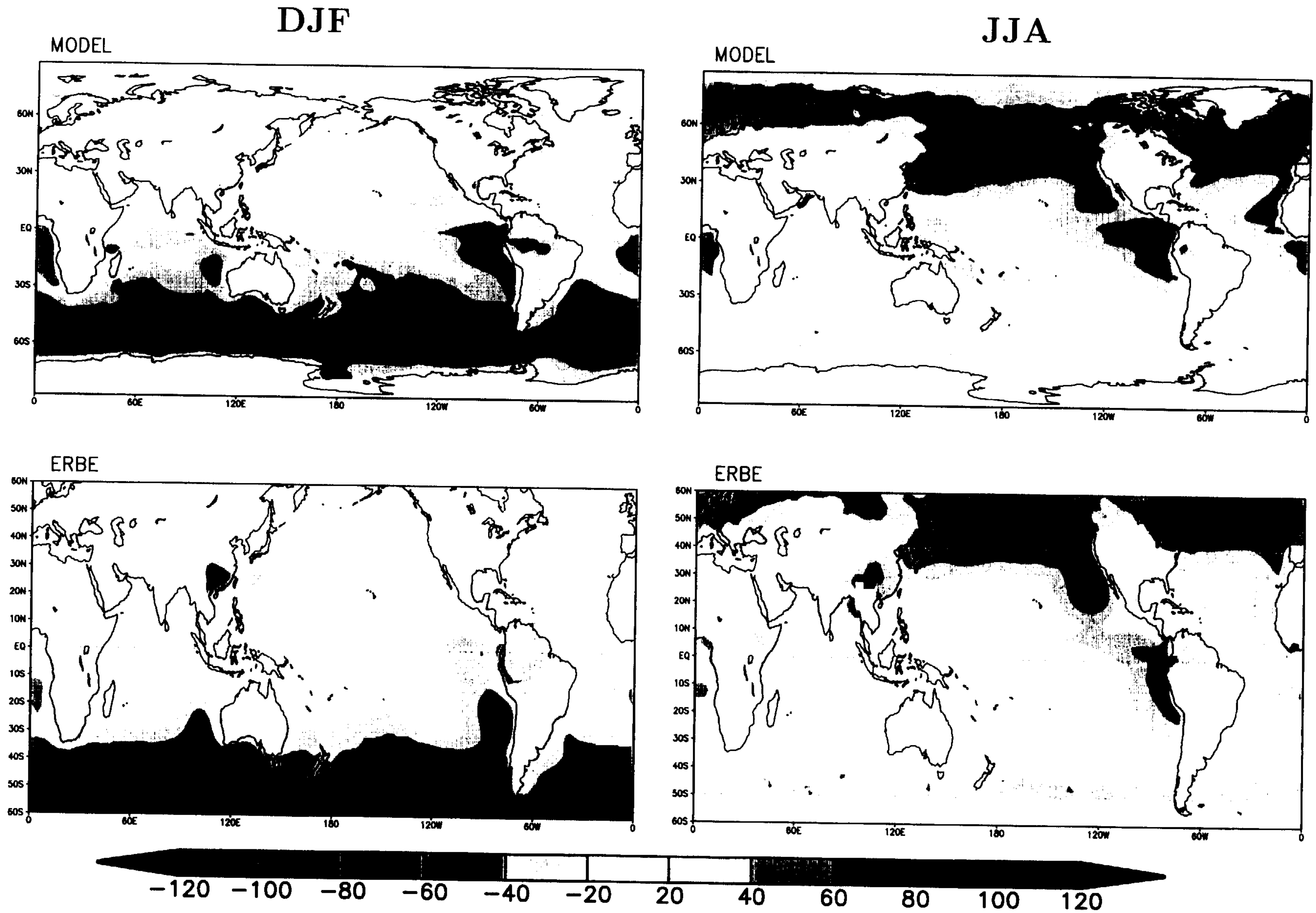

Figure 156: Net cloud radiative forcing (W m^{-2}). The comparison is for the ERBE period: January 1985 to December 1989.— Upper panels: Model; Lower panels: Reanalysis; Left panels: DJF; Right panels: JJA.

NET_CRF

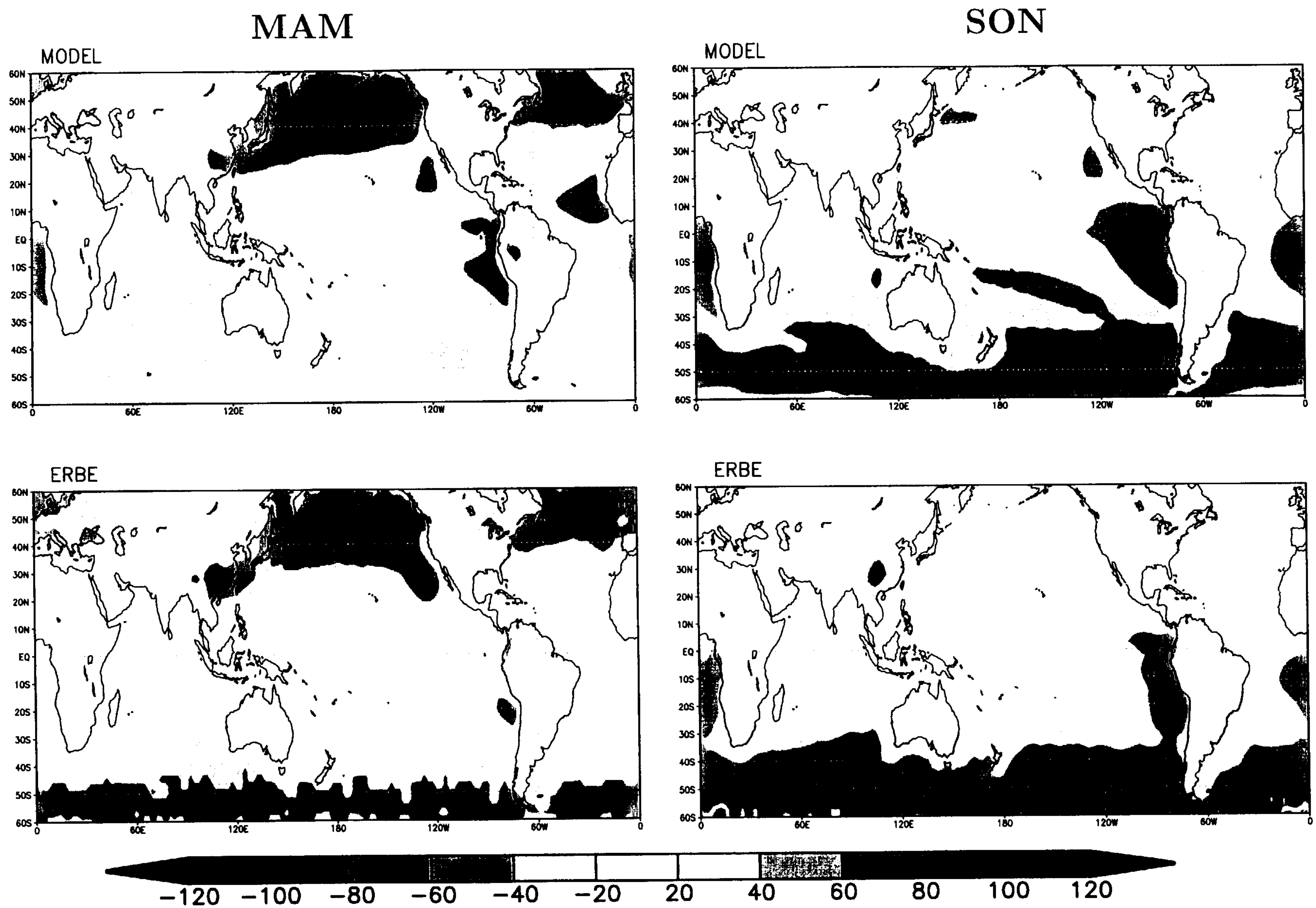

Figure 157: Net cloud radiative forcing (W m^{-2}). The comparison is for the ERBE period: January 1985 to December 1989.— Upper panels: Model; Lower panels: Reanalysis; Left panels: MAM; Right panels: SON.

$$\overline{OLR}_{MODEL} - \overline{OLR}_{ERBE}$$

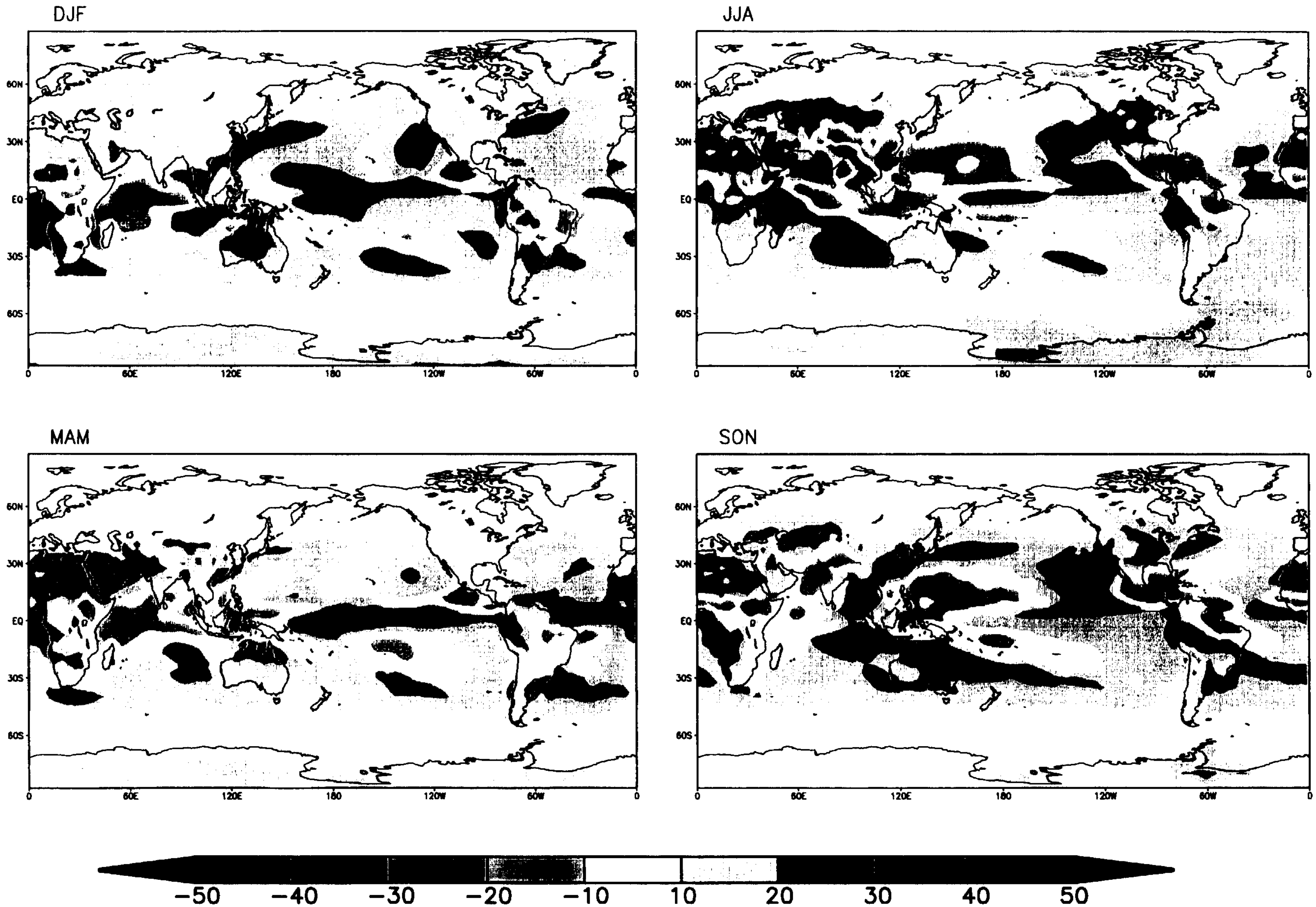

Figure 158: Outgoing longwave radiation bias (Model - ERBE) (W m^{-2}). The comparison is for the ERBE period: January 1985 to December 1989. .

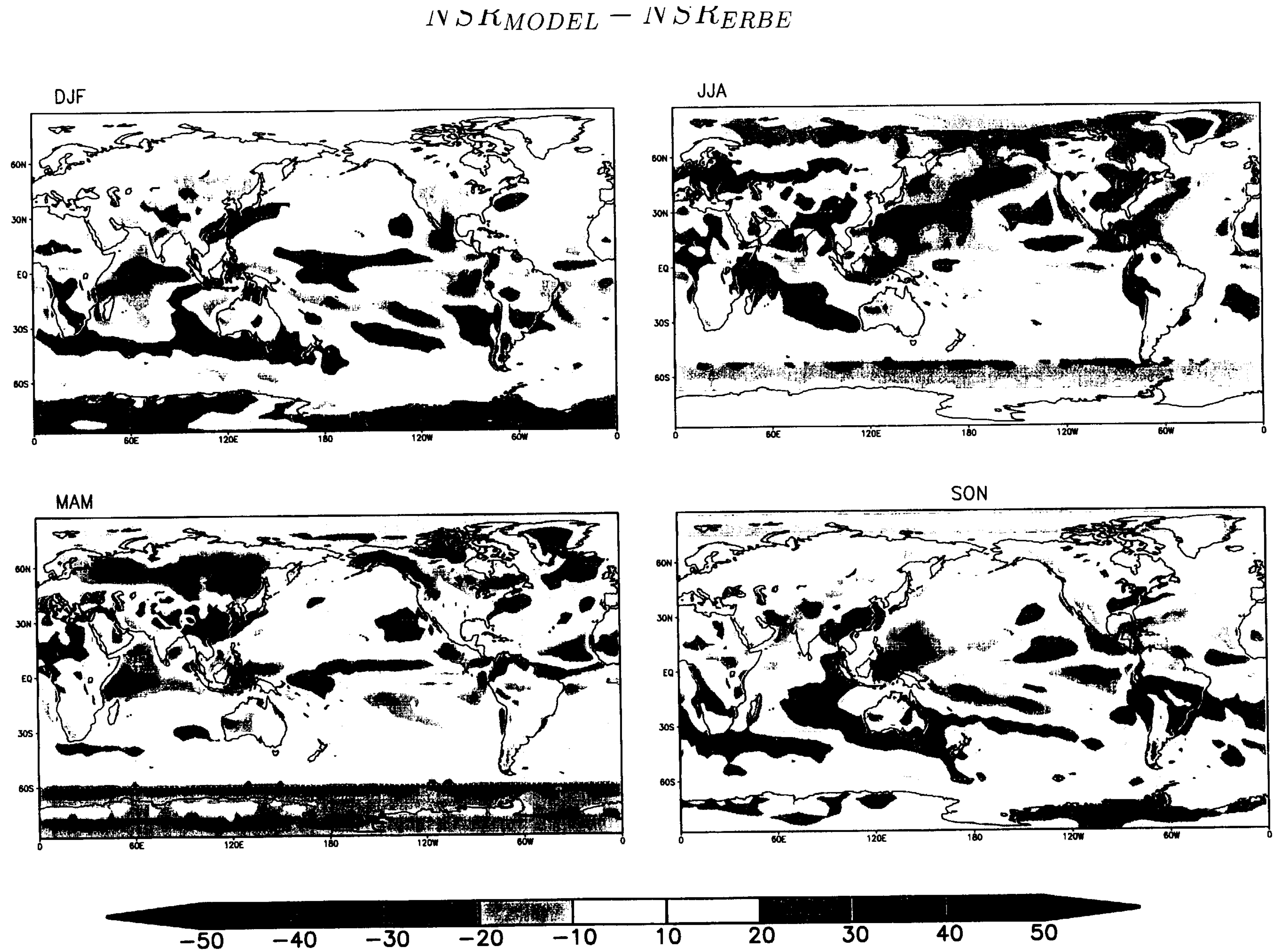

Figure 159: Net downward shortwave radiation bias (Model - ERBE) (W m^{-2}). The comparison is for the ERBE period: January 1985 to December 1989. .

$\overline{NET}_{MODEL} - \overline{NET}_{ERBE}$

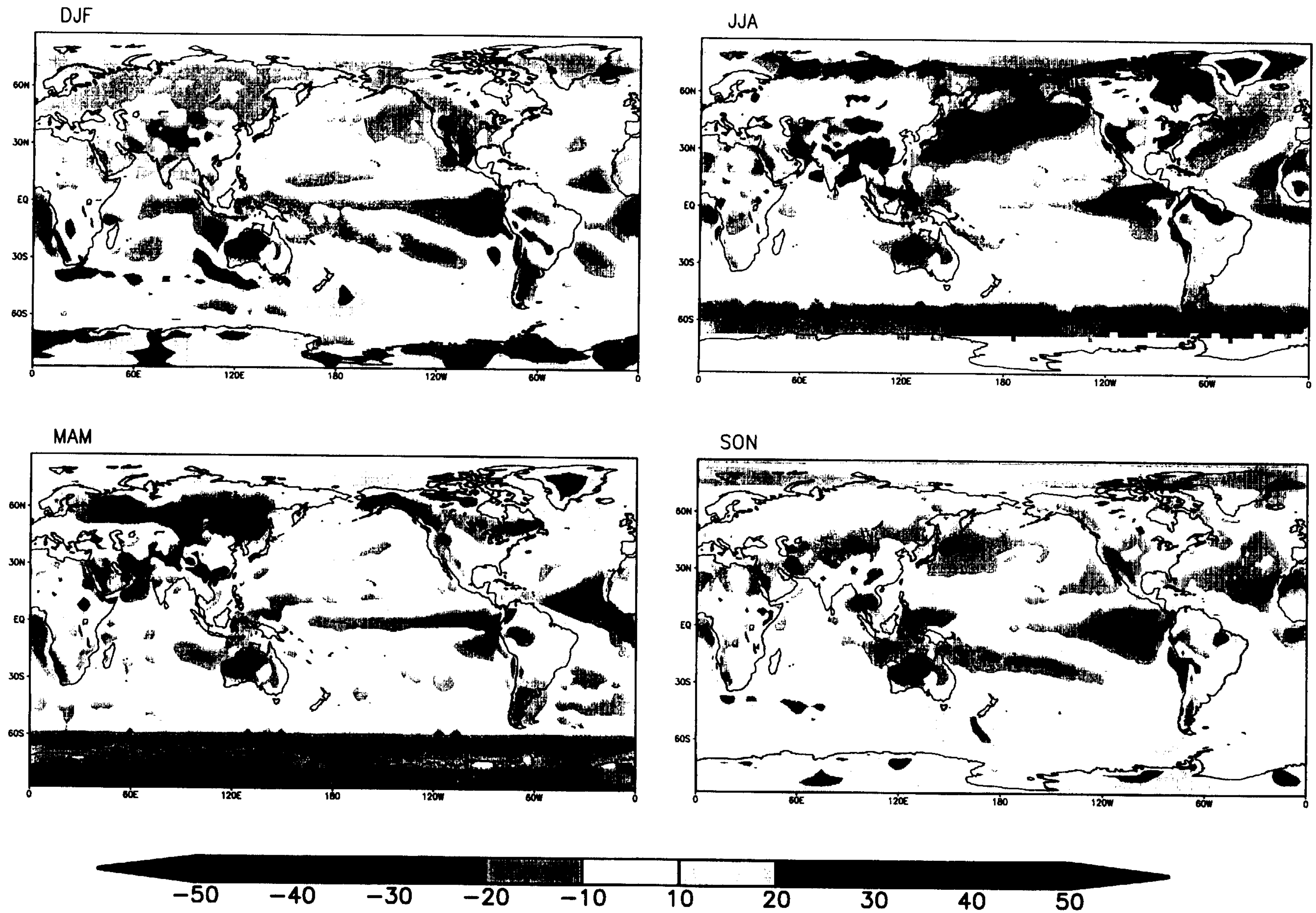

Figure 160: Net radiation bias (Model - ERBE) (W m^{-2}). The comparison is for the ERBE period: January 1985 to December 1989. .

This page left intentionally blank.

$\overline{\tau_x}$

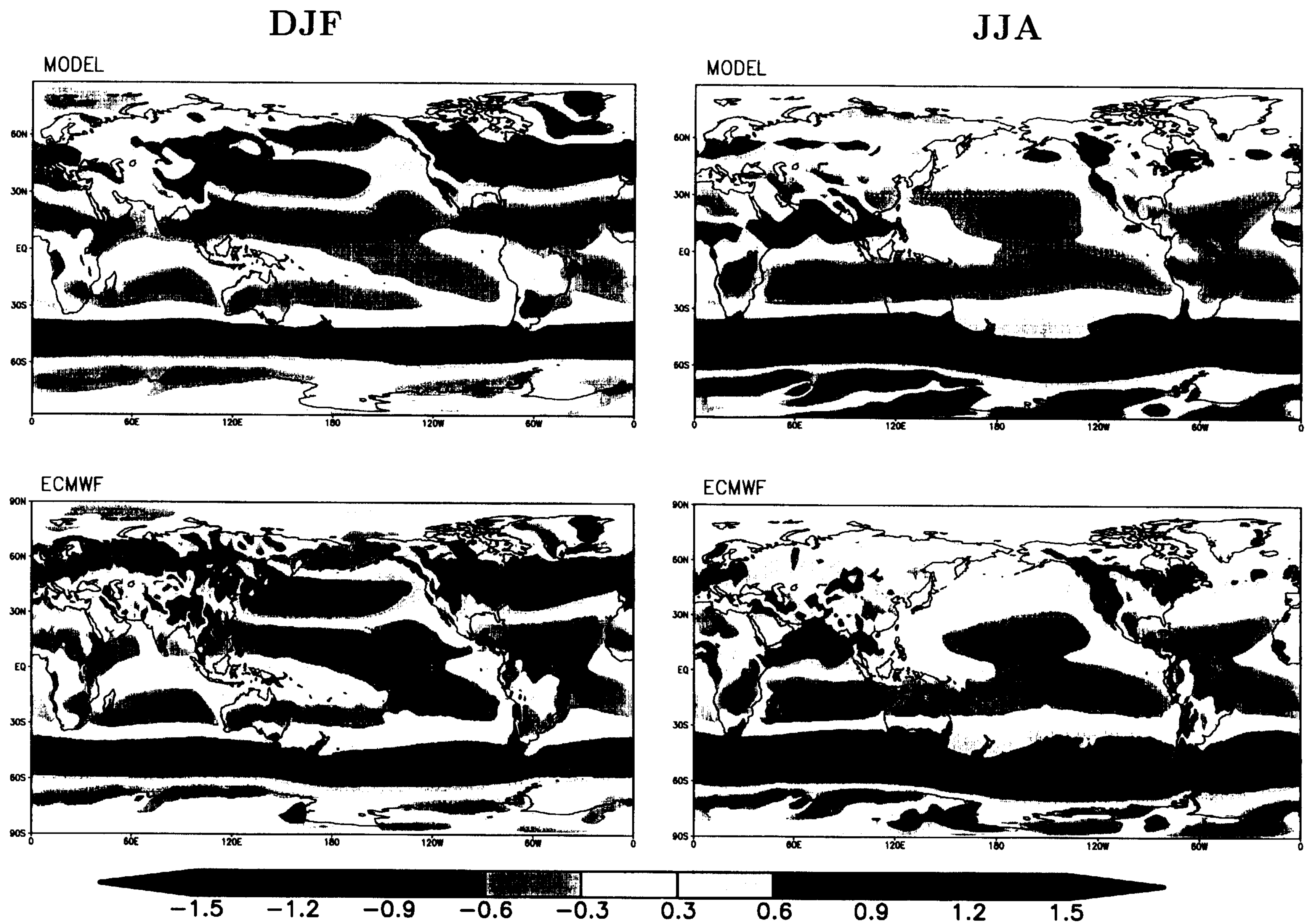

Figure 161: Zonal component of the surface wind stress (dynes cm^{-2}). — Upper panels: Model; Lower panels: Reanalysis; Left panels: DJF; Right panels: JJA. Results from the ECMWF re-analysis are for the 10-year period December 1979 to November 1989. Model results are for all 20 years.

$\overline{\tau_x}$

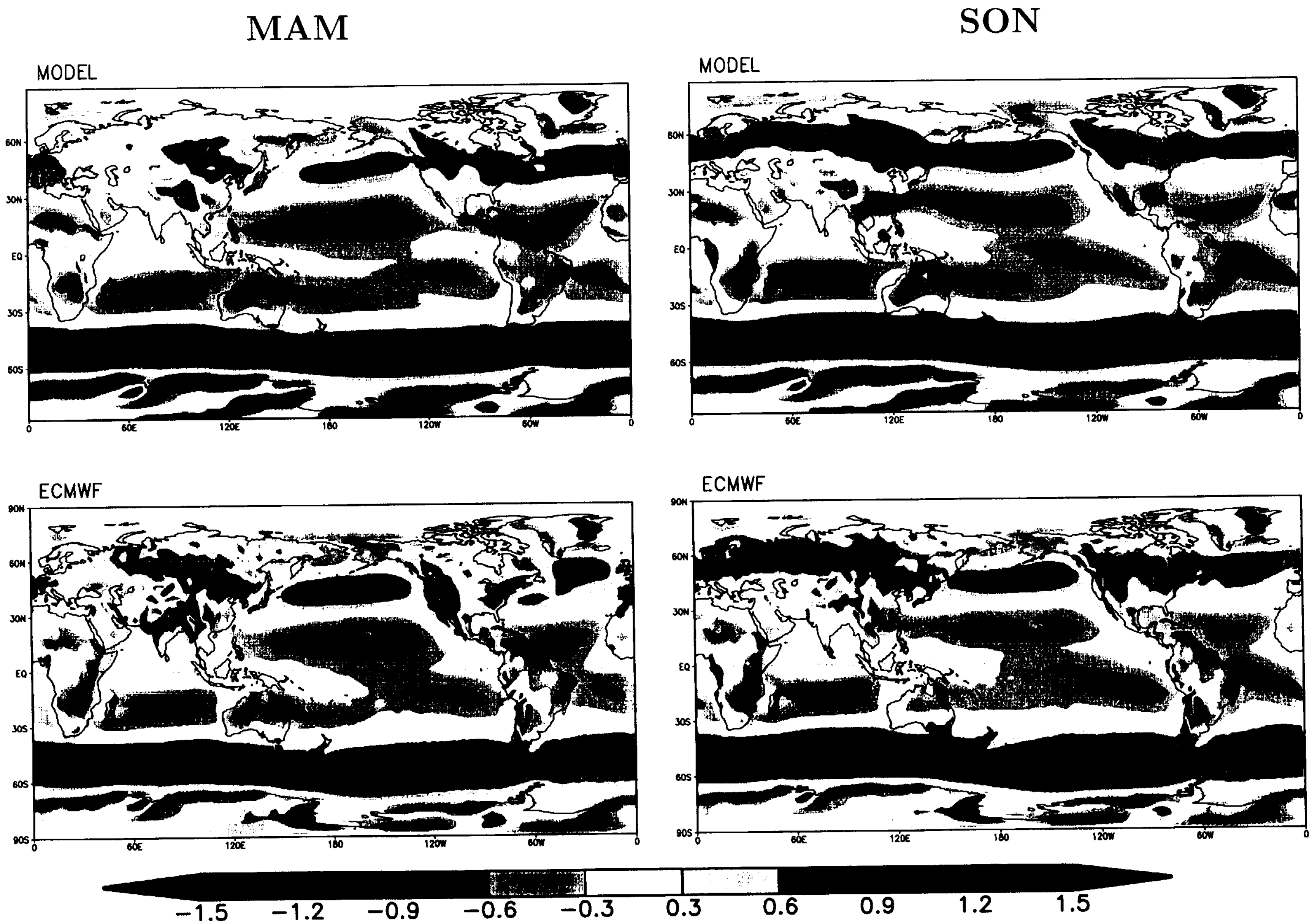

Figure 162: Zonal component of the surface wind stress (dynes cm^{-2}). — Upper panels: Model; Lower panels: Reanalysis; Left panels: MAM; Right panels: SON. Results from the ECMWF re-analysis are for the 10-year period December 1979 to November 1989. Model results are for all 20 years.

$\overline{\tau_y}$

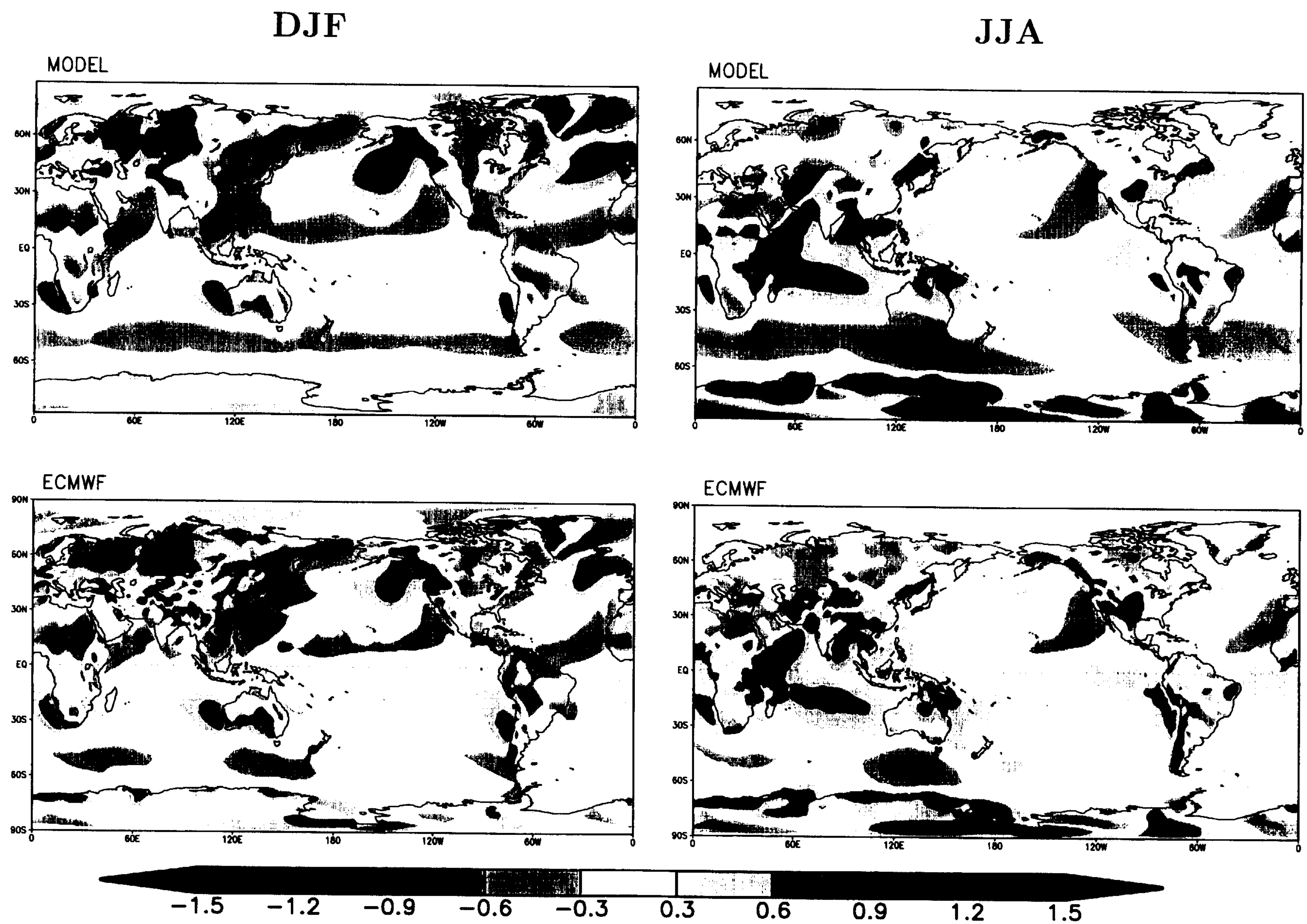

Figure 163: Meridional component of the surface wind stress (dynes cm^{-2}). — Upper panels: Model; Lower panels: Reanalysis; Left panels: DJF; Right panels: JJA. Results from the ECMWF re-analysis are for the 10-year period December 1979 to November 1989. Model results are for all 20 years.

$\overline{\tau_y}$

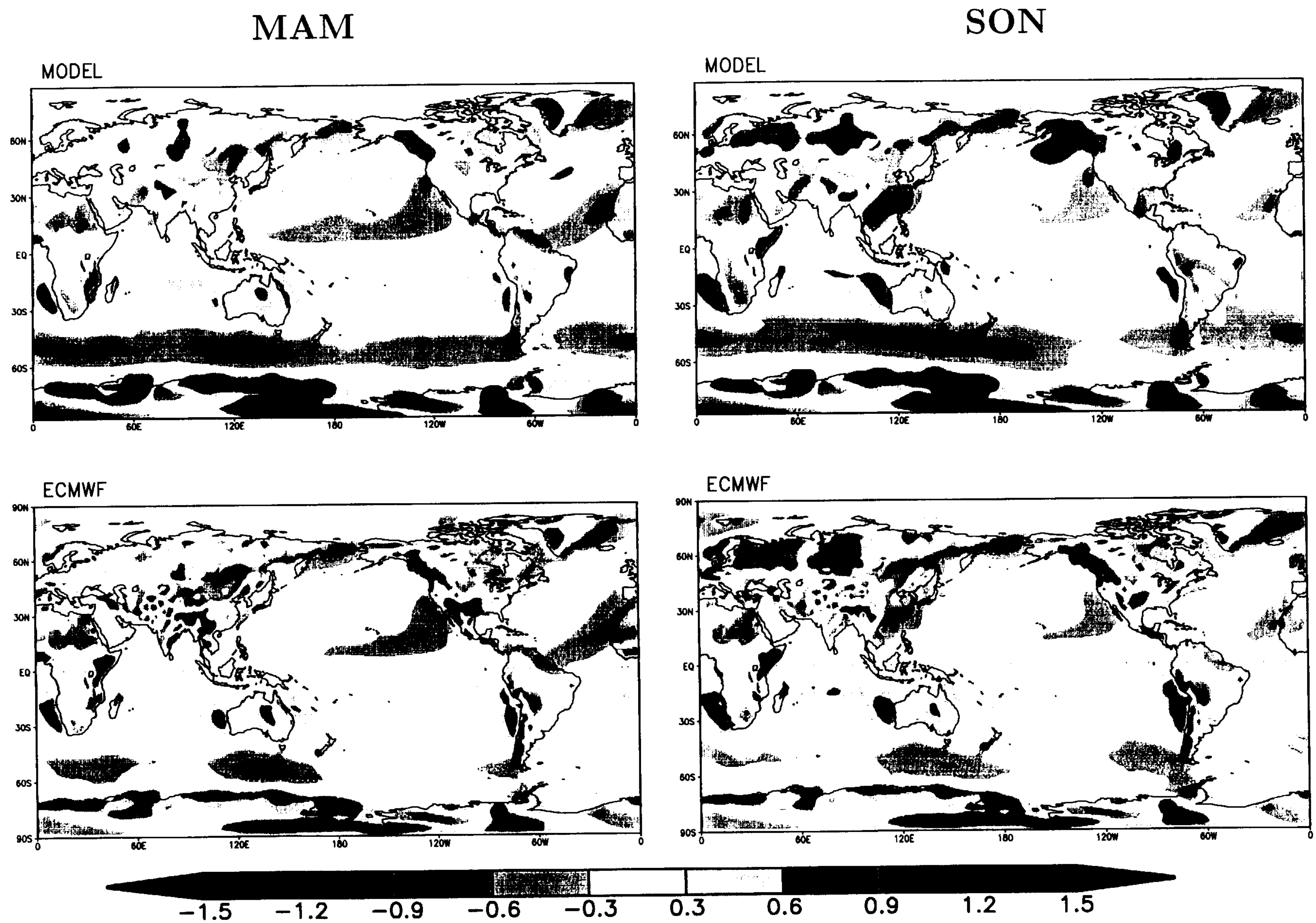

Figure 164: Meridional component of the surface wind stress (dynes cm^{-2}). — Upper panels: Model; Lower panels: Reanalysis; Left panels: MAM; Right panels: SON. Results from the ECMWF re-analysis are for the 10-year period December 1979 to November 1989. Model results are for all 20 years.

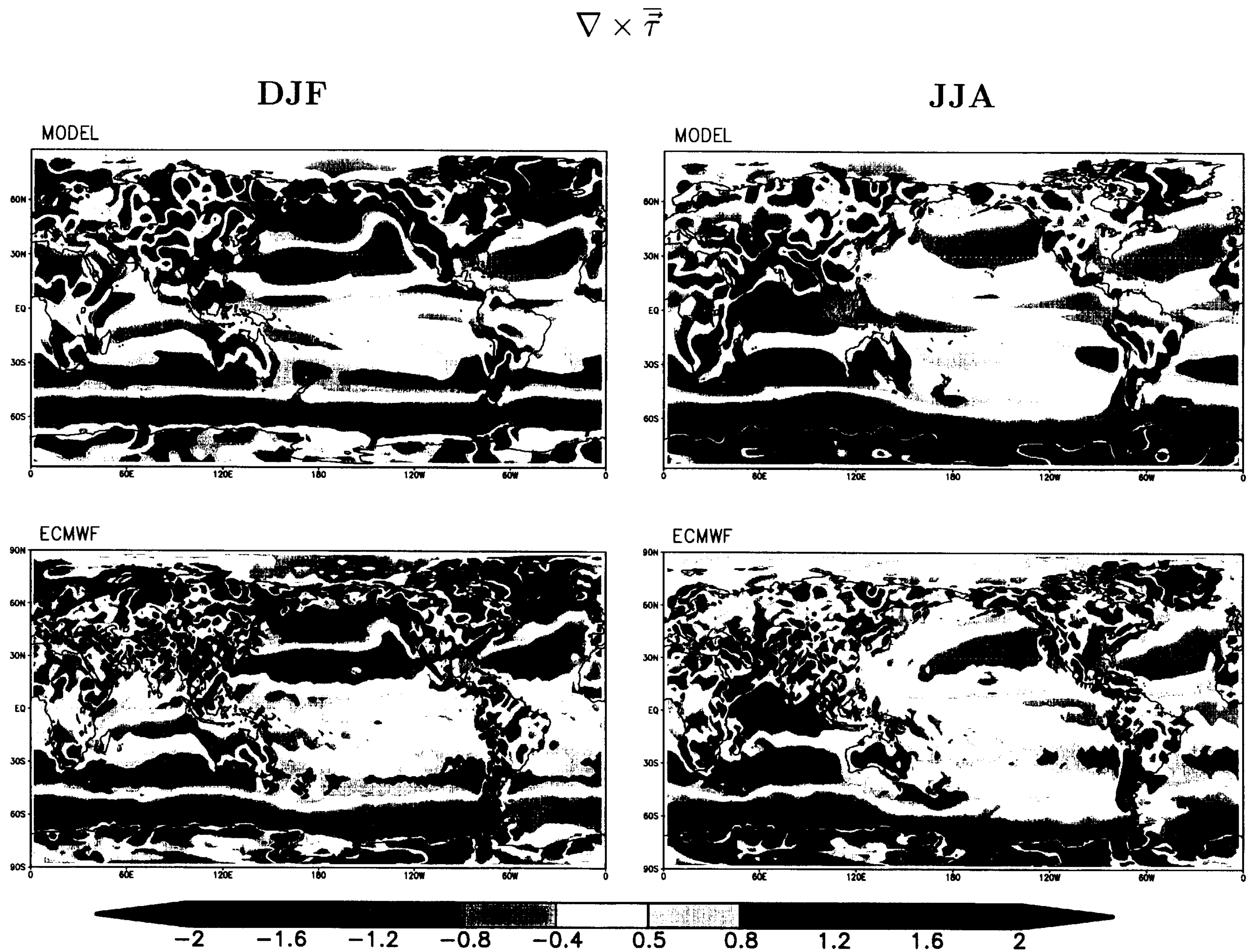

Figure 165: Curl of the surface wind stress (10^{-6} N m^{-3}). — Upper panels: Model; Lower panels: Reanalysis; Left panels: DJF; Right panels: JJA. Results from the ECMWF re-analysis are for the 10-year period December 1979 to November 1989. Model results are for all 20 years.

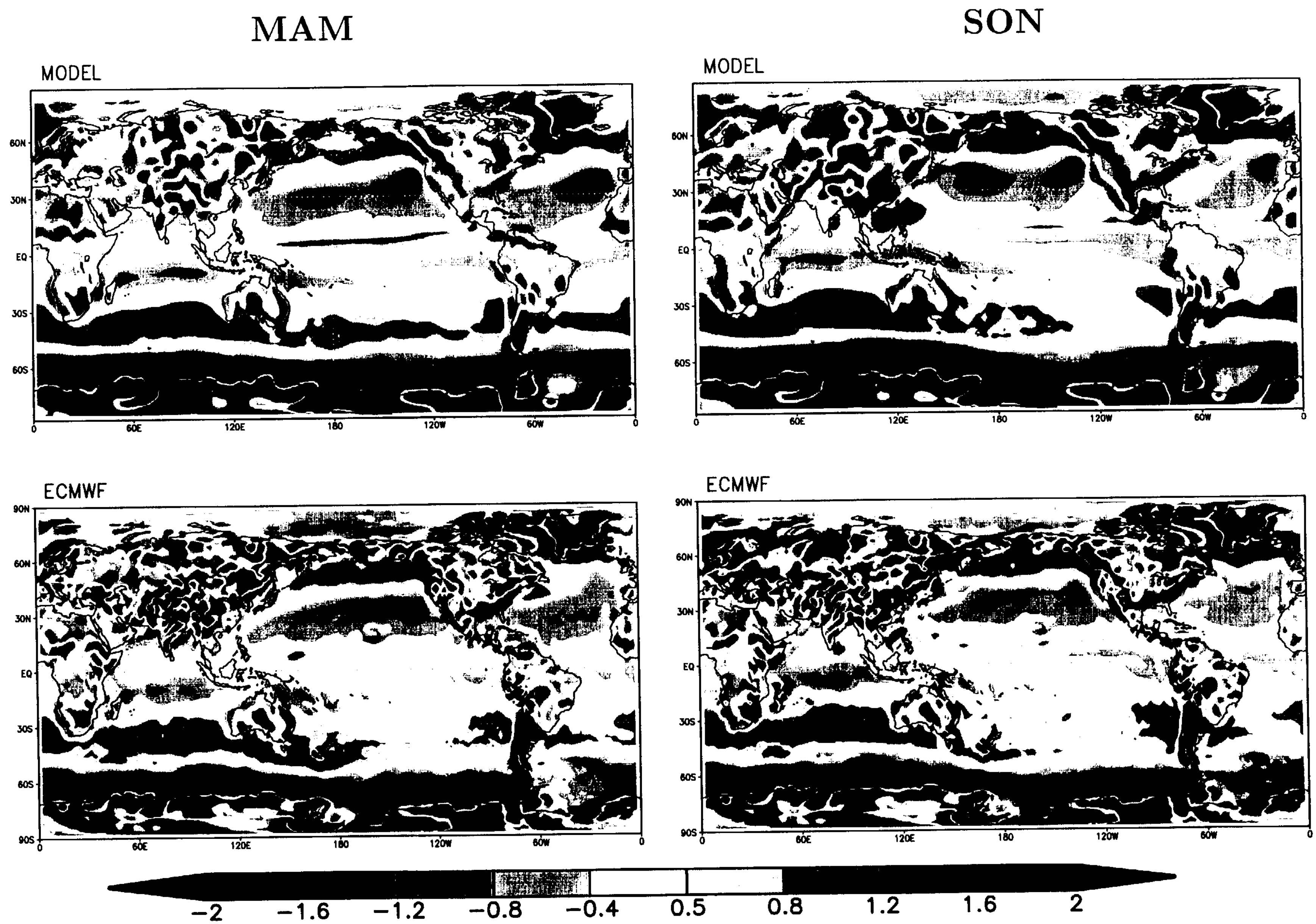

Figure 166: Curl of the surface wind stress (10^{-6} N m^{-3}). — Upper panels: Model; Lower panels: Reanalysis; Left panels: MAM; Right panels: SON. Results from the ECMWF re-analysis are for the 10-year period December 1979 to November 1989. Model results are for all 20 years.

$\overline{SHF}$

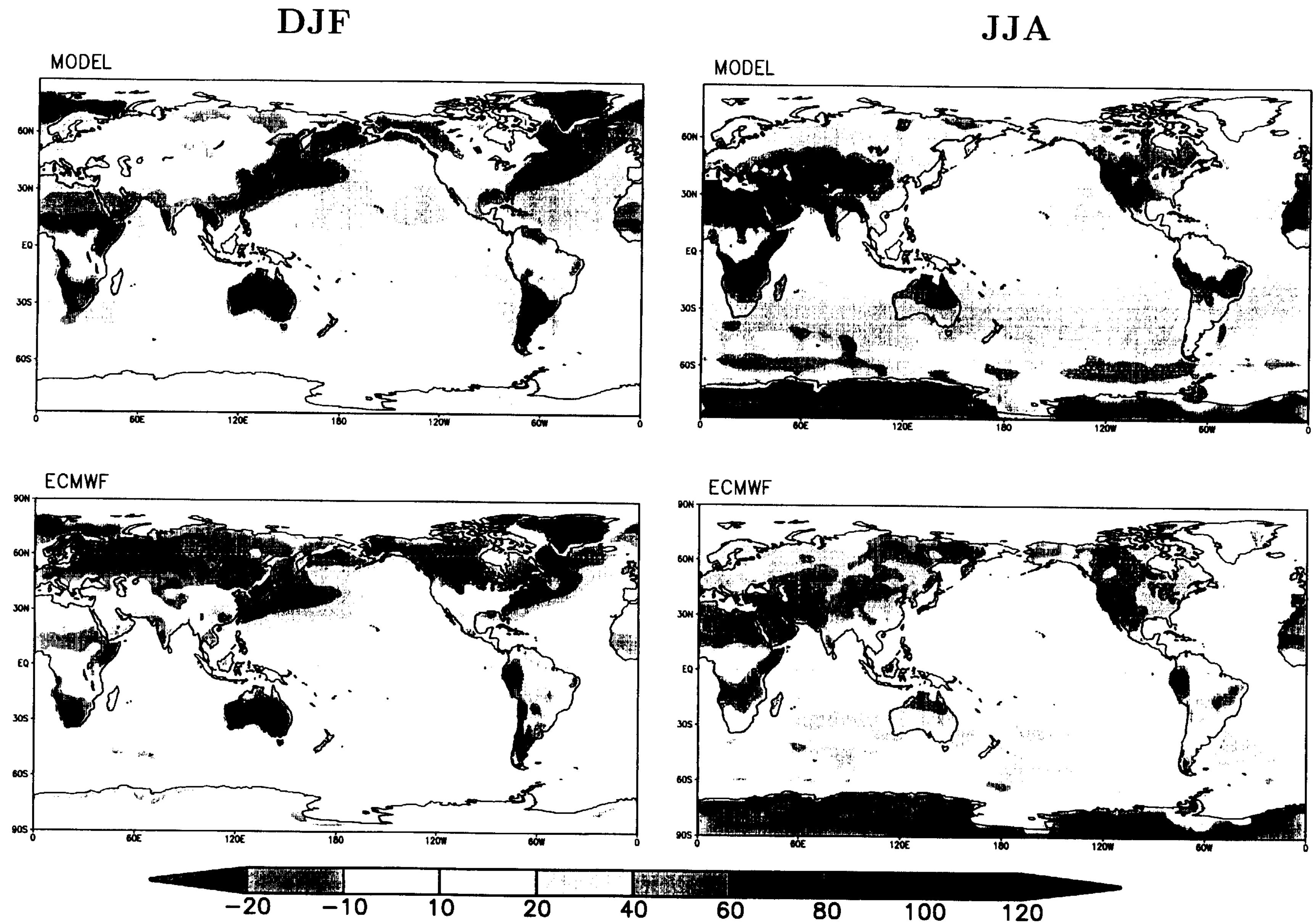

Figure 167: Surface sensible heat flux (W m^{-2}). — Upper panels: Model; Lower panels: Reanalysis; Left panels: DJF; Right panels: JJA. Results from the ECMWF re-analysis are for the 10-year period December 1979 to November 1989. Model results are for all 20 years.

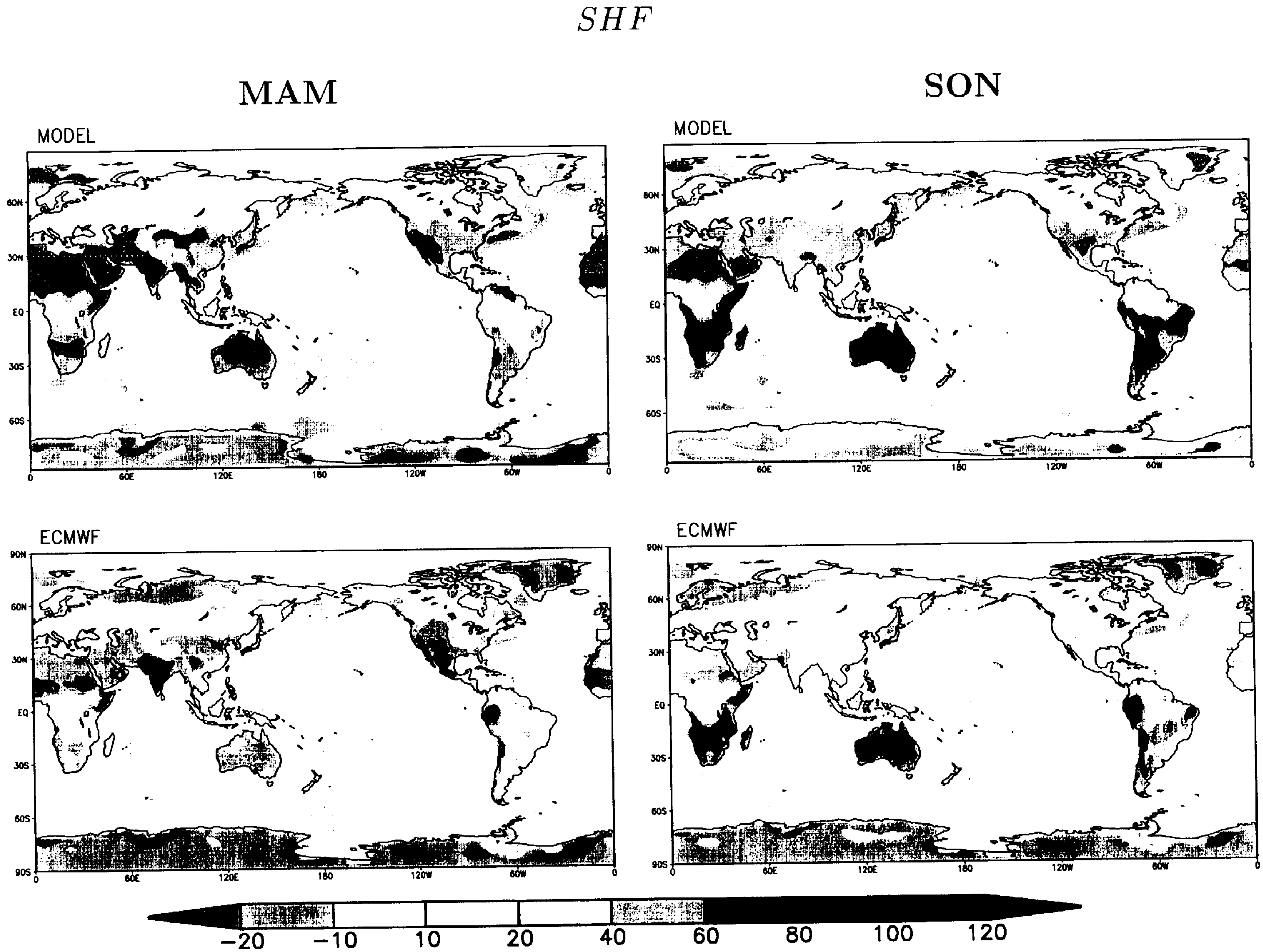

Figure 168: Surface sensible heat flux (W m^{-2}). — Upper panels: Model; Lower panels: Reanalysis; Left panels: MAM; Right panels: SON. Results from the ECMWF re-analysis are for the 10-year period December 1979 to November 1989. Model results are for all 20 years.

$\overline{LHF}$

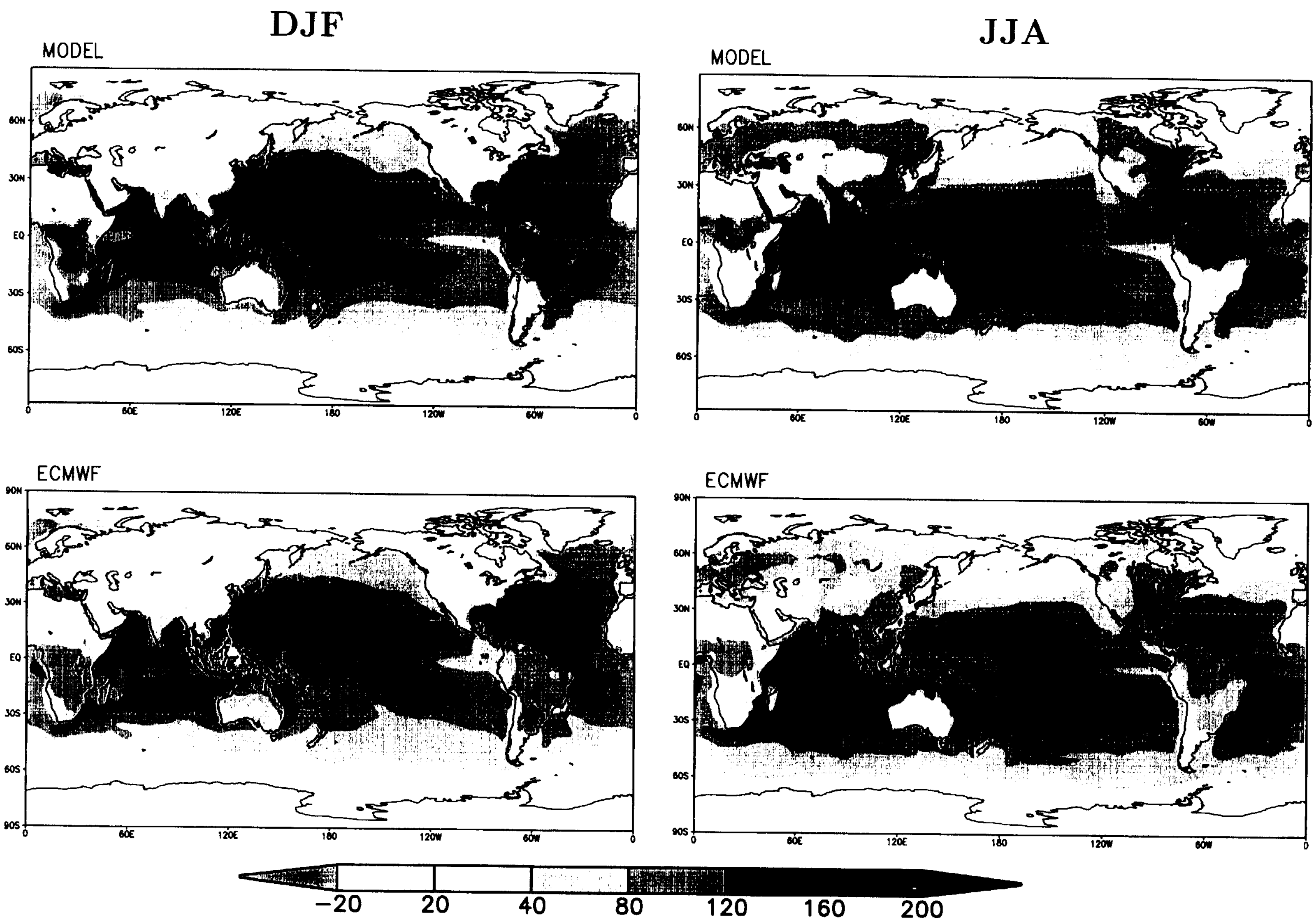

Figure 169: Surface latent heat flux (W m^{-2}). — Upper panels: Model; Lower panels: Reanalysis; Left panels: DJF; Right panels: JJA. Results from the ECMWF re-analysis are for the 10-year period December 1979 to November 1989. Model results are for all 20 years.

LHF

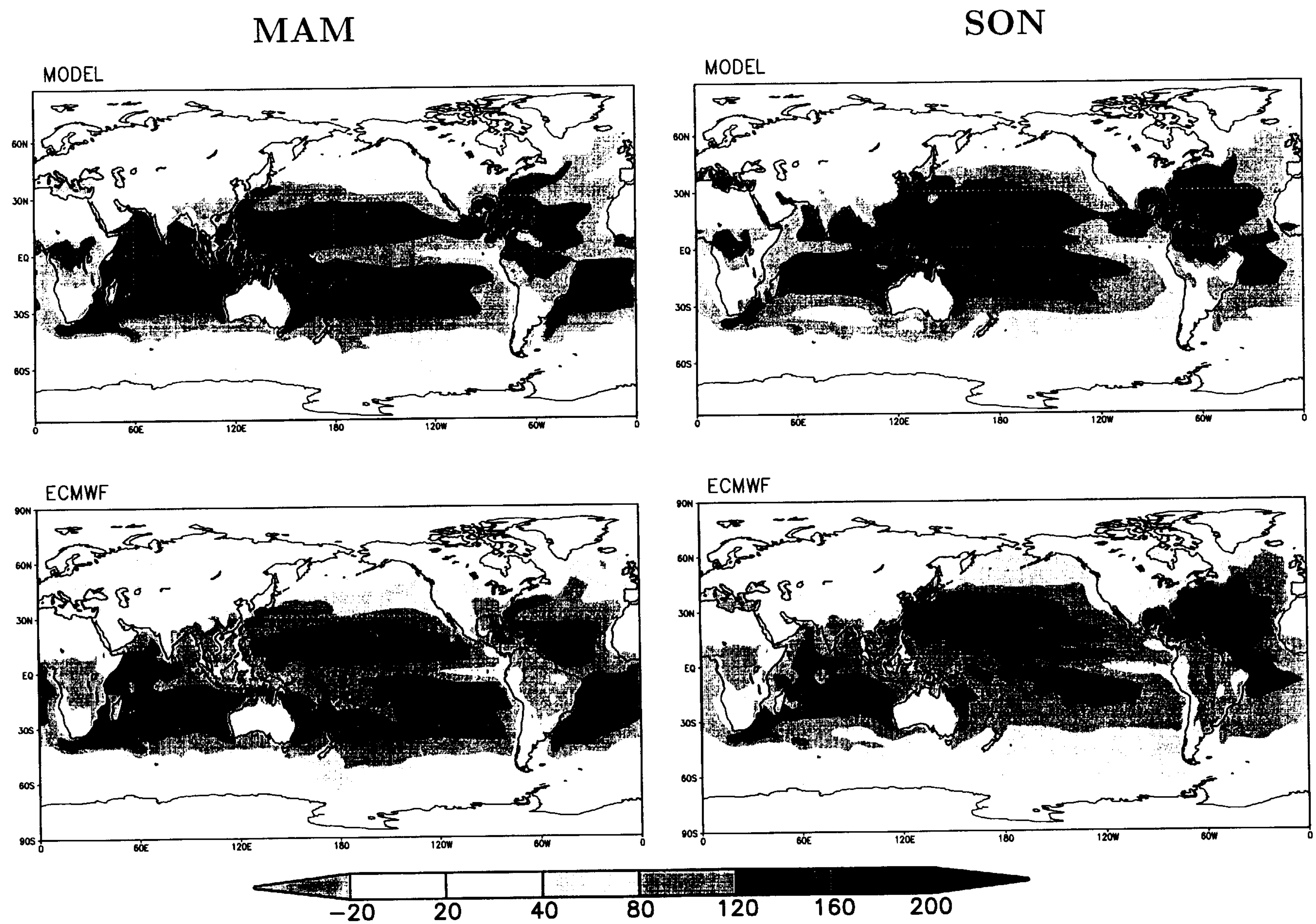

Figure 170: Surface latent heat flux (W m^{-2}). — Upper panels: Model; Lower panels: Reanalysis; Left panels: MAM; Right panels: SON. Results from the ECMWF re-analysis are for the 10-year period December 1979 to November 1989. Model results are for all 20 years.

Previous Volumes in This Series

Volume 9 *March 1996*	Energy and Water Balance Calculations in the Mosaic LSM **Randal D. Koster and Max J. Suarez**
Volume 10 *April 1996*	Dynamical Aspects of Climate Simulations Using the GEOS General Circulation Model **Lawrence L. Takacs and Max J. Suarez**
Volume 11 *May 1997*	Documentation of the Tangent Linear and its Adjoint Models of the Relaxed Arakawa-Schubert Moisture Parameterization Package of the NASA GEOS-1 GCM (Version 5.2) **Weiyu Yang I. Michael Navon, and Ricardo Todling**
Volume 12 *August 1997*	Comparison of Satellite Global Rainfall Algorithms **Alfred T.C. Chang and Long S. Chiu**
Volume 13 *December 1997*	Interannual Variability and Potential Predictability in Reanalysis Products **Wie Ming and Siegfried D. Schubert**
Volume 14 *August 1998*	A Comparison of GEOS Assimilated Data with FIFE Observations **Michael G. Bosilovich and Siegfried D. Schubert**
Volume 15 *June 1999*	A Solar Radiation Parameterization for Atmospheric Studies **Ming-Dah Chou and Max J. Suarez**
Volume 16 *November 1999*	Filtering Techniques on a Stretched Grid General Circulation Model **Lawrence Takacs, William Sawyer, Max J. Suarez, and Michael S. Fox-Rabinowitz**

REPORT DOCUMENTATION PAGE

Form Approved
OMB No. 0704-0188

1. AGENCY USE ONLY *(Leave blank)*	2. REPORT DATE	3. REPORT TYPE AND DATES COVERED
	July 2000	Technical Memorandum

4. TITLE AND SUBTITLE
Technical Report Series on Global Modeling and Data Assimilation
Volume 17—Atlas of Seasonal Means Simulated by the NSIPP 1 Atmospheric GCM

5. FUNDING NUMBERS
Code 970
971-622-24-47-26

6. AUTHOR(S)
Julio Bacmeister, Philip J. Pegion, Siegfried D. Schubert, and Max J. Suarez

7. PERFORMING ORGANIZATION NAME(S) AND ADDRESS (ES)
Oceans and Ice Branch
Goddard Space Flight Center
Greenbelt, Maryland 20771

8. PEFORMING ORGANIZATION REPORT NUMBER
2000–03740–0

9. SPONSORING / MONITORING AGENCY NAME(S) AND ADDRESS (ES)
National Aeronautics and Space Administration
Washington, DC 20546-0001

10. SPONSORING / MONITORING AGENCY REPORT NUMBER
TM-2000-104606, Vol. 17

11. SUPPLEMENTARY NOTES
J. Bacmeister: Universities Space Research Associates; P.J. Pegion: General Sciences Corporation, Laurel, Maryland

12a. DISTRIBUTION / AVAILABILITY STATEMENT
Unclassified–Unlimited
Subject Category:46
Report available from the NASA Center for AeroSpace Information,
7121 Standard Drive, Hanover, MD 21076-1320. (301) 621-0390.

12b. DISTRIBUTION CODE

13. ABSTRACT *(Maximum 200 words)*

This atlas documents the climate characteristics of version 1 of the NASA Seasonal-to-Interannual Prediction Project (NSIPP) Atmospheric General Circulation Model (AGCM). The AGCM includes an interactive land model (the Mosaic scheme), and is part of the NSIPP coupled atmosphere-land-ocean model. The results presented here are based on a 20-year (December 1979-November 1999) "AMIP-style" integration of the AGCM in which the monthly-mean sea-surface temperature and sea ice are specified from observations. The climate characteristics of the AGCM are compared with the National Centers for Environmental Prediction (NCEP) and the European Center for Medium-Range Weather Forecasting (ECMWF) reanalyses. Other verification data include Special Sensor Microwave/Imager (SSM/I) total precipitable water, the Xie-Arkin estimates of precipitation, and Earth Radiation Budget Experiment (ERBE) measurements of short and long wave radiation. The atlas is organized by season. The basic quantities include seasonal mean global maps and zonal and vertical averages of circulation, variance/covariance statistics, and selected physics quantities.

14. SUBJECT TERMS
Numerical Methods, Atmospheric Models, Regional Models, Climate Models
Atmospheric General Circulation

15. NUMBER OF PAGES
192

16. PRICE CODE

17. SECURITY CLASSIFICATION OF REPORT	18. SECURITY CLASSIFICATION OF THIS PAGE	19. SECURITY CLASSIFICATION OF ABSTRACT	20. LIMITATION OF ABSTRACT
Unclassified	Unclassified	Unclassified	UL